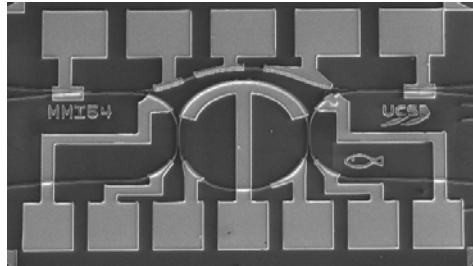


Research in Optoelectronics (A)



2009 Reprints of
Professor Larry A. Coldren
and Collaborators

*ECE Technical Report 10-01
Department of Electrical & Computer Engineering
University of California, Santa Barbara*

Research in Optoelectronics (A)

Reprints published in 2009

by

Professor Larry A. Coldren

and Collaborators

Published as

Technical Report # ECE 10-01

of

The Department of Electrical & Computer Engineering

The University of California

Santa Barbara, CA 93106

Phone: (805) 893-4486

Fax: (805) 893-4500

E-mail: coldren@ece.ucsb.edu

<http://www.ece.ucsb.edu/Faculty/Coldren/home.htm>

Introduction:

This is the 2009 edition of articles published by Professor Coldren's group at UC-Santa Barbara. It contains journal and conference publications in which Prof. Coldren was named a co-author. The majority of these works have originated from proposals generated within Coldren's group, but a few are due to efforts that originated elsewhere and were supported by Coldren and his group members. As in recent years the work has a focus on III-V compound semiconductor materials as well as the design and creation of photonic devices using these materials—mostly diode lasers and photonic integrated circuits (PICs). The work spans efforts from basic materials and processing technology, through device physics and design, to device formation, characterization, and insertion into systems demonstrations.

The reprints have been grouped into three areas: **I. Photonic IC Technology & Devices;** **II. Vertical-Cavity Surface-Emitting Lasers;** and **III. Cavity QED.** The vast majority of the work is in the first area, which has been further subdivided into *A. PIC Technology and Transmitters;* *B. Wavelength Converters, Routing, and Packet Switching;* *C. RF-Photonics and Analog PICs;* *D. Ring-Resonator-Based Filters and Logic Elements;* and *E. Optical-Phase-Locked-Loop PICs.* Each area contains materials research, device physics, device design and process development, device fabrication, and device characterization. In some cases devices are inserted into more advanced systems, so that their performance can be evaluated in a more rigorous environment. The epitaxial growth activity is strongly supported by Prof. DenBaars (MOCVD) and Prof. Gossard (MBE), who co-advise the students involved in these areas. Thus, their contributions have been invaluable to the research, even when they do not appear as co-authors on the device oriented papers.

The work was performed with funding from several grants from industry and government, some gifts funds from industry, and support from the Kavli Endowed Chair in Optoelectronics and Sensors. Specific projects included one on wavelength converters and photonic networks under the DARPA DoDN program (Prof. Blumenthal, PI); an analog receiver project sponsored by DARPA Phorfront (Prof. Bowers, PI); two projects to create very high-speed, high-efficiency optical sources for optical interconnects, one an STTR with Ziva Corp. and one an extension of the DARPA C2OI program, both to support our vertical-cavity surface-emitting laser work; a project on programmable optical filters supported by the DARPA-PhASER program, and an ONR sponsored program supporting ring-resonator-based digital optical processing.

The first group of reprints (*IA.*) summarizes our work on photonic IC technology in a number of overview talks as well as a couple focused more on an extension of our continuing transmitter PIC efforts centered around the widely-tunable Sampled-Grating Distributed-Bragg-Reflector (SG-DBR) Laser. This group consists of five conference papers, including one for a Plenary talk and two others for invited talks at major international venues.

The Second group of papers (*IB.*) contains six items that discuss our work on extending the widely-tunable transmitter technology to single-chip transceivers or wavelength converters, and then to arrays of these included in larger-scale photonic routing and switching chips.

Figure 1 illustrates the first monolithic tunable optical router (MOTOR) chip that consists of an array of eight widely-tunable wavelength converters connected to an arrayed-waveguide-grating-router (AWGR), which translates the converted wavelength at some input port to a different output port, much like a prism. Thus, by switching the wavelength of the incoming data in the 8 wavelength conversion stages an 8 x 8 space switch results, and this is achieved in an overall device footprint of 14.5 mm x 4.25 mm. This work was carried out in close collaboration with Prof. Blumenthal’s group.

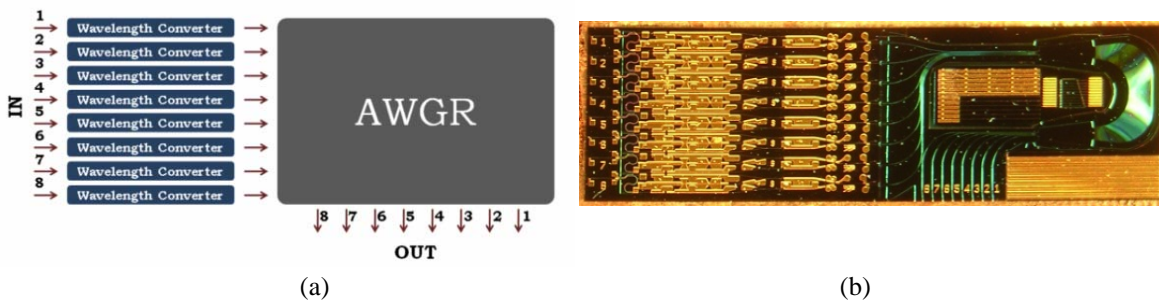


Figure 1. (a) Schematic overview of MOTOR architecture; (b) Photograph of fabricated device.

Work on the *RF-Photonics and Analog PICs (IC.)* continues to be a major thrust in Prof Coldren’s group in 2009 with most of the publications from the work on integrated coherent receivers for phase modulated signals using optical feedback to tracking modulators. These consist of a PIC that incorporates a pair of differentially-driven tracking modulators, a 3 dB coupler, and a differential detector pair together with a negative feedback path from the detectors back to the modulators, which may or may not include electronic amplification. The idea is to drive the detector output, whose amplitude is proportional to the phase difference between the LO and the input following the tracking modulators, to near zero, and then use the feedback signal required to do this as a measure of the magnitude of the phase difference existing before the tracking modulators. Figure 2 shows a schematic of the ‘all-optical’ receiver version in which no electronics is used in the feedback path.

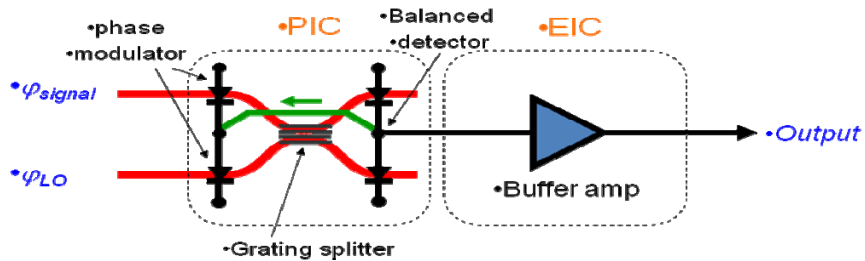


Figure 2. ‘All-optical’ coherent receiver for phase modulated signals. (No EIC in feedback path)

In 2009 the work shifted to using an etched trench for the 3 dB coupler to minimize its size, and flip-chip bonded electronics, both to minimize feedback delay. The papers in

this *Section I.C* culminate with copies of slides presented at an invited panel presentation, and these summarize much of the work presented in the other papers, as well as overview that in Prof. Coldren's group. Figure 3 shows a frustrated total internal reflection (FTIR) trench coupler receiver configuration together with a schematic of the flip-chipping concept. Again, the idea behind both is to minimize feedback delay

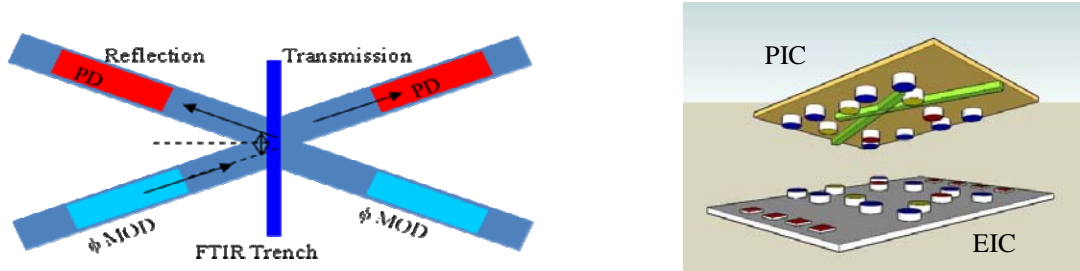


Figure 3. FTIR Trench coupler PIC configuration and flip-chipping concept.

Lasers and filters often use gratings for mirrors to form cavities, but it is also possible to use ring-resonator cavities. Prof. Coldren's group is involved in two programs that use this approach, and this is the subject of the three papers in *Section I.D*. The first program aims to make programmable lattice filters by coupling together a number of ring-resonator stages, which provide poles and zeros as infinite impulse response (IIR) stages, together with interferometer stages, which only provide zeros as finite impulse response (FIR) stages. A proposed lattice filter is shown in Fig. 4(a), and SEMs of the realized filter along with insets of the waveguide coupler and crosssection are shown in Figs. (b) and (c), respectively.

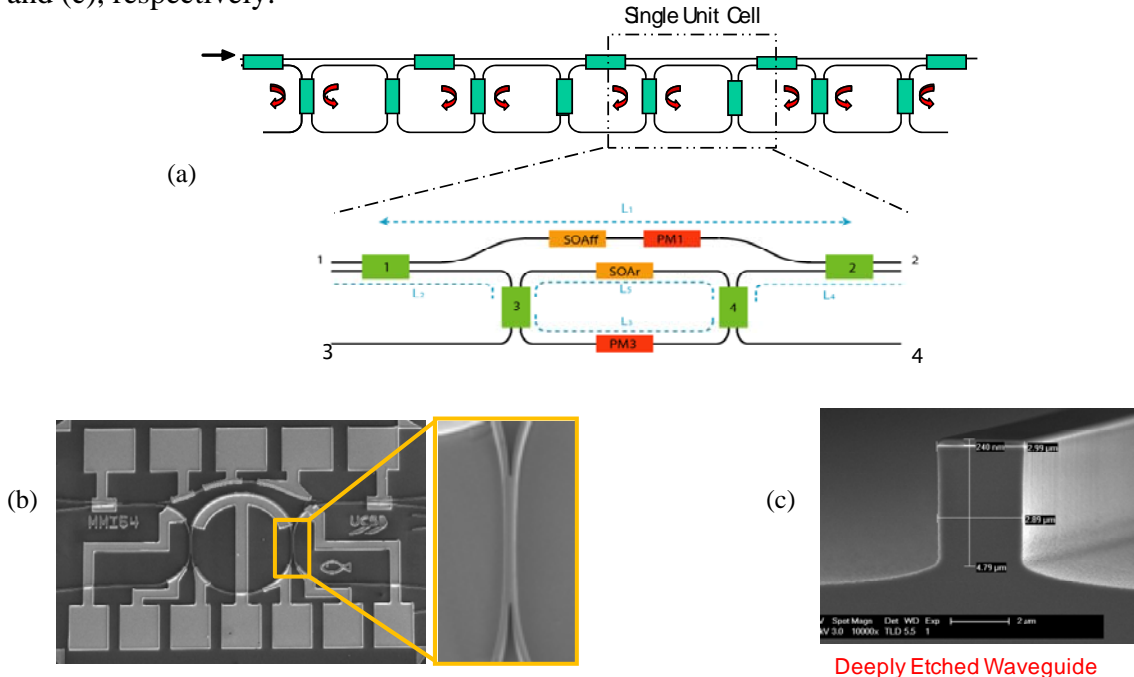


Figure 4. (a) Ring-resonator-based lattice filter and unit cell; (b) topview of fabricated filter unit cell together with blow-up of directional coupler; (c) deeply-etched waveguide crosssection.

Figure 5 illustrates pole and zero responses together with a combined pole and zero from the single unit cell depicted in Fig. 4(b).

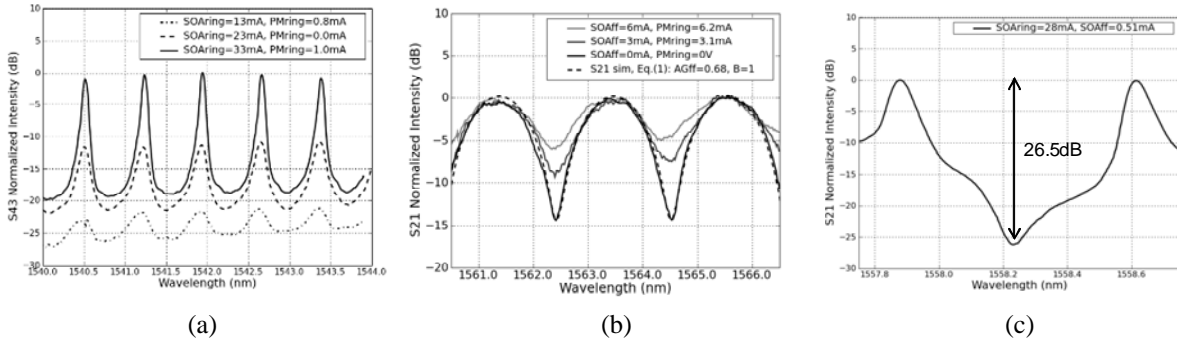


Figure 5. (a),(b) Isolated pole and zero responses tuned in amplitude by varying bias on feed-forward SOA and ring SOA respectively, the ring phase modulator is used to fix the filter in frequency. (c) Zero and pole are utilized simultaneously to enhance extinction ratio.

Triggerable bistable ring lasing operation has been demonstrated in the second project aimed at digital logic applications including fast A/D conversion. One paper documents that either a clockwise or counter-clockwise lasing mode can be triggered by varying the wavelength of a light pulse injected into the same end of the waveguide coupled to the resonator. Figure 6 summarizes that result. Injected light was -35dB below ring laser power; side-mode suppression of ring laser $\sim 25\text{ dB}$; extinction of unwanted (CW or CCW) mode $\sim 18\text{ dB}$.

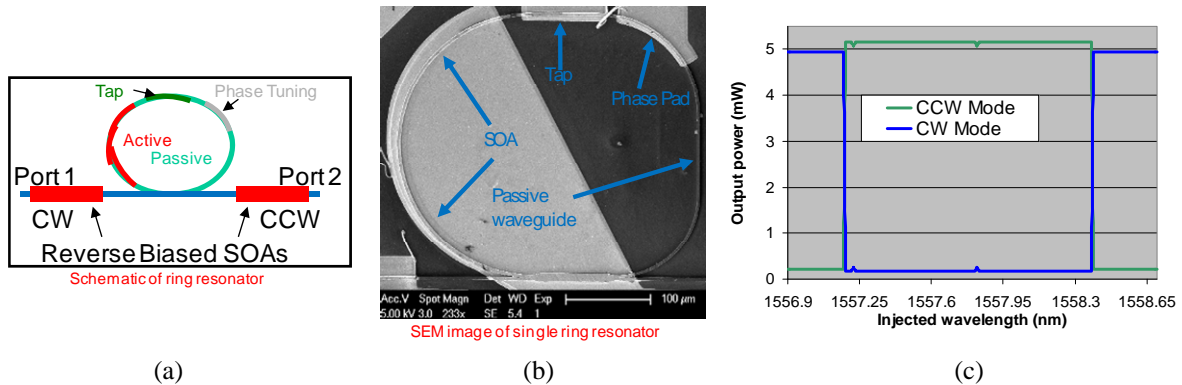


Figure 6. (a) Schematic of PIC; (b) photo; (c) outputs from detectors on coupling waveguide.

The work on *Optical-Phase-Locked-Loops* (OPLLs), in *Section I.E*, demonstrated the first integration of all of the photonic components necessary to phase lock two lasers together on one chip. This is the precursor to many future efforts in Prof. Coldren’s group on optical transmitters and receivers using OPLLs. Figure 7 summarizes the initial work with schematics of the PIC and the circuit, an SEM of the PIC, and two experimental results. The first experiment illustrated phase locking with no offset frequency; the second the frequency spectrum with a 5 GHz modulation applied to the on-chip optical phase modulator prior to the feedback detector positioned near the middle of the chip. The side bands visible at $\pm 300\text{MHz}$ from the central peak are due to the limited bandwidth of the feedback loop.

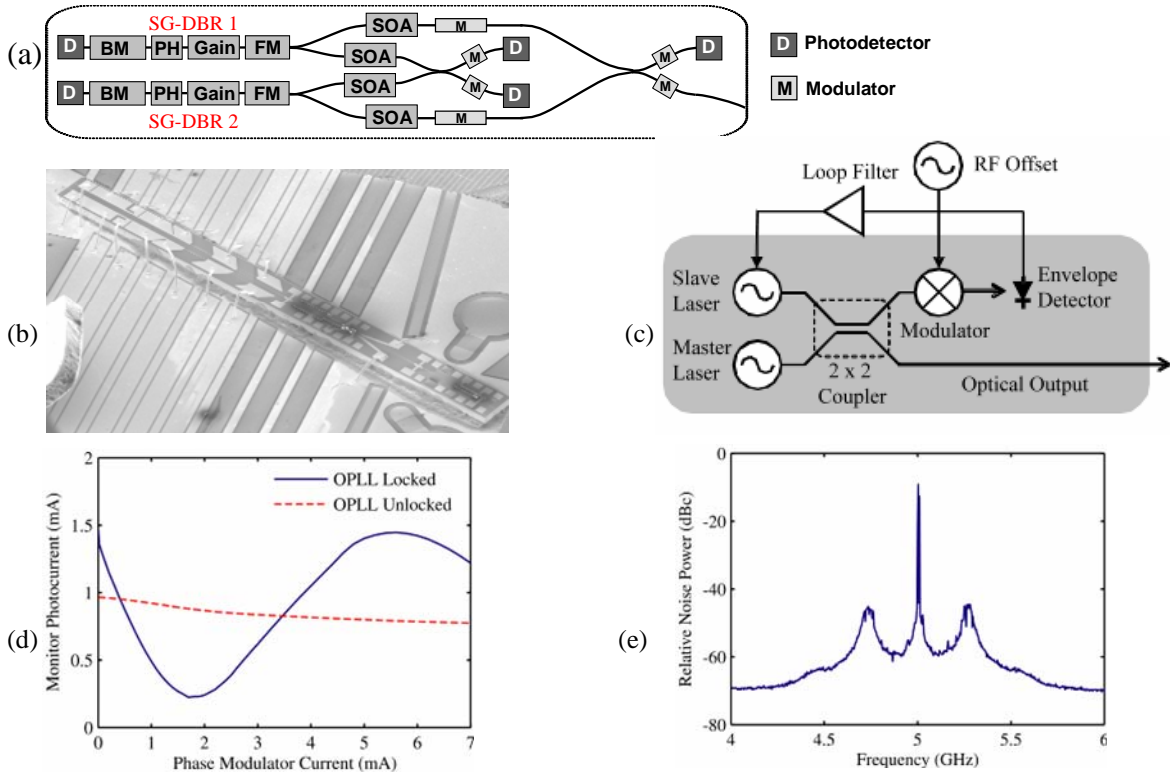


Figure 7. (a) Chip schematic); (b) chip SEM; (c) Circuit showing chip, feedback and offset modulation elements; (d) non-offset comparison of monitor current [detector on far right] as phase of reference laser is tuned [via the lowest central modulator]; (e) output spectrum for a 5GHz rf offset signal applied.

The publications in *Sections II* and *III* on Vertical-Cavity Surface-Emitting Lasers (VCSELs) and Cavity-QED effects, respectively, are really continuations of work already reported in previous years, so a detailed explanation of them will not be presented here, and the reader is referred directly to the papers. For summaries please see introductions from prior years.

However, the VCSEL work is continuing with a couple of new programs aimed at increasing the direct modulation bandwidth and efficiency even more than the record results that are reported in this issue as well as in the past.



Back Row: Leif Johansson, John Parker, Pietro Binetti, Chin-Han Lin, Yan Zheng, Chad Althouse, Sasa Ristic
Front Row: Joseph Chang, Abi Sivananthan, Erik Norberg, Rob Guzzon, Larry Coldren, Andy Hung, Jeannine Roson
Not Pictured: Ashish Bhardwaj

Professor Coldren's Group

I. Researchers

A. Bhardwaj	Visiting Scientist, UCSB
Pietro Binetti	Post Doctoral Researcher, UCSB
Yung-Jr Hung	Visiting Scientist from National Taiwan University of Science and Technology, UCSB
L. Johansson	Associate Research Engineer, UCSB
S. Ristic	Post Doctoral Researcher, UCSB

II. Students

C. Althouse	Ph.D. Program
Y. Chang	Ph.D. Program, now at Kaai Inc
C. Chen	Ph.D. Program, now at NTT Photonics Lab
M. Dummer	Ph.D. Program, now at Vixar Inc.
R. Guzzon	Ph.D. Program
J. Klamkin	Ph.D. Program, now at Lincoln Labs
U. Krishnamachari	Ph.D. Program
C. Lin	Ph.D. Program
S. Nicholes	Ph.D. Program, now at Aurrion
E. Norberg	Ph.D. Program
J. Parker	Ph.D. Program
A. Sivananthan	Ph.D. Program
N. Stoltz	Ph.D. Program, now at UCLA
A. Tauke-Pedretti	Ph.D. Program, now at Sandia National Labs
Y. Zheng	Ph.D. Program

III. Staff

D. Cohen	Principal Development Engineer, reports to Prof Nakamura
J. Roson	Center Assistant, OTC

Collaborators

I. Faculty

D. Blumenthal	UCSB
D. Bouwmeester	UCSB
J. Bowers	UCSB
S. DenBaars	UCSB
P. Petroff	UCSB
M. Rodwell	UCSB

II. Researchers

Y. Akulova	JDSU
M. Ayliffe	JDSU
J. Barton	Post Doctoral Researcher, UCSB (Blumenthal)
E. Burmeister	Ciena
J. English	Principal Development Engineer, UCSB Materials
G. Fish	JDSU
A. Hastings	Naval Research Lab
A. Jackson	Project Scientist, UCSB ECE
P. Koh	JDSU
M. Larson	JDSU
M. Masanovic	Post Doctoral Researcher, UCSB (Blumenthal)
G. Paloczi	JDSU
H. Poulsen	Post Doctoral Researcher, UCSB (Blumenthal)
K. Williams	Naval Research Lab

Collaborating Students

B. Jevremovic	UCSB (Blumenthal)
B. Koch	UCSB (Bowers)
G. Kurczveil	UCSB (Bowers)

V. Lal	UCSB (Blumenthal)
E. Lively	UCSB (Blumenthal)
J. Mack	UCSB (Blumenthal)
K. Nguyen	UCSB (Blumenthal)
N. Nunoya	UCSB (Bowers)
M. Piels	UCSB (Bowers)
M. Rakher	UCSB (Bouwmeester)
A. Ramaswamy	UCSB (Bowers)
B. Stamenic	UCSB (Blumenthal)

Table of Contents:

I. PIC Technology and Devices

Page

IA. PIC Technology and Transmitters

P.C. Koh, L.A. Johansson, Y.A. Akulova, G.A. Fish, G.T. Paloczi, M.Larson, M. Ayliffe, and L.A. Coldren, "Generation of 40 Gbps Duobinary Signals Using an Integrated Laser—Mach-Zender Modulator," OFC/NFOEC, OThN4, San Diego, CA (March 22-26, 2009)

L.A. Coldren, "Recent Advances in InP PICs," IPRM, PLE2, Newport Beach, CA (May 10-14, 2009) PLENARY

S.C. Nicholes, M.L. Masanovic, J. Barton, E.J. Norberg, E. Lively, B. Jevremovic, L.A. Coldren, and D.J. Blumenthal, "Novel Application of Quantum Well Intermixing Implant Buffer Layer to Enable High-Density Photonic Integrated Circuits in InP," IPRM, WB1.2, Newport Beach, CA (May 10-14, 2009)

L.A. Coldren, "Integrated Transmitters and Transceivers for High-End Applications in WDM Optical Networks," IPNRA, IWA3, Honolulu, HI, (July 12-17, 2009) INVITED PAPER

L.A. Coldren, "Technology and Applications for InP-based Photonic ICs," OIDA 18th Annual Forum, Santa Clara, CA (December 1-2, 2009) INVITED PAPER (slide copies included)

IB. Wavelength Converters, Routing, and Packet Switching

M. Masanovic, E. Burmeister, M. Dummer, B. Koch, S. Nicholes, B. Jevremovic, K. Nguyen, V. Lala, J. Bowers, L. Coldren, and D. Blumenthal, "Advanced photonic integrated technologies for optical routing and switching," SPIE Optoelectronic Integrated Circuits XI, 7219-17, San Jose, CA, (January, 28-29, 2009) INVITED PAPER

M.M. Dummer, J. Klamkin, A. Tauke-Pedretti, K. Nguyen, and L.A. Coldren, "Field-Modulated Packet Forwarding Chips for Label-Switched Optical Routing," OFC/NFOEC, OThG3, San Diego, CA (March 22-26, 2009)

S.C. Nicholes, M.L. Masanovic, B. Jevremovic, E. Lively, L.A. Coldren, and D.J. Blumenthal, "The World's First InP 8x8 Monolithic Tunable Optical Router (MOTOR) Operating at 40 Gbps Line Rate per Port," OFC/NFOEC, PDPB1, San Diego, CA (March 22-26, 2009)

M.M. Dummer, J. Klamkin, A. Tauke-Pedretti, and L.A. Coldren, "40 Gb/s Field-Modulated Wavelength Converters for All-Optical Packet Switching," *IEEE Journal of Selected Topics in Quantum Electronics*, **15**, (3), pp. 494- 503 (May/June 2009) INVITED PAPER

J.P. Mack, K.M. Nguyen, M.M. Dummer, E.F. Burmeister, H.N. Poulsen, B. Stamenic, G. Kurczveil, J.E. Bowers, L.A. Coldren, and D.J. Blumenthal, "40 Gb/s Buffered 2x2 Optical Packet Switching Using Photonic Integrated Circuits," CLEO, CMJJ6, (June 2-4, 2009)

S.C. Nicholes, M.L. Masanovic, E. Lively, L.A. Coldren, and D.J. Blumenthal, "An 8x8 Monolithic Tunable Optical Router (MOTOR) Chip in InP," IPNRA, IMB1, Honolulu, HI (July 12-17, 2009)

IC. RF-Photonics and Analog PICs

J. Klamkin, L.A. Johansson, A. Ramaswamy, N. Nunoya, S. Ristic, U. Krishnamachari, J. Chen, J.E. Bowers, S.P. DenBaars, and L.A. Coldren, "Highly Linear Integrated Coherent Receivers for Microwave Photonic Links," OFC/NFOEC, OMK4, San Diego, CA (March 22-26, 2009)

C.-H. Chen, J. Klamkin, S.C. Nicholes, L.A. Johansson, J.E. Bowers, and L.A. Coldren, "Compact Beam Splitters with Deep Gratings for Miniature Photonic Integrated Circuits: Design and Implementation Aspects," *Applied Optics*, **48**, (25), pp.F68-F75 (June 2009)

C.-H. Chen, A. Ramaswamy, L.A. Johansson, N. Nunoya, J. Klamkin, J.E. Bowers, and L.A. Coldren, "Linear Phase Demodulation using an Integrated Coherent Receiver with an Ultra-Compact Grating Beam Splitter," Device Research Conference, V.B-7, University Park, PA (June 22-24, 2009)

J. Klamkin, A. Ramaswamy, L.A. Johansson, N. Nunoya, J.E. Bowers, S.P. DenBaars, and L.A. Coldren, "Uni-Traveling-Carrier Balanced Photodiode with Tunable MMI Coupler for Optimization of Source RIN Suppression," Int. Top. Meet. Microwave Phot. (MWP), We.2.2, Valencia, Spain, (October 14-16, 2009)

A. Ramaswamy, N. Nunoya, M. Piels, L.A. Johansson, L.A. Coldren, J.E. Bowers, A.S. Hasings, K.J. Williams, J. Klamkin, "Experimental Analysis of Two Measurement Techniques to Characterize Photodiode Linearity," Int. Top. Meet. Microwave Phot. (MWP), Fr2.4, Valencia, Spain, (October 14-16, 2009)

L.A. Coldren, "Monolithic Integration on InP: Functionalities and Applications in RF Photonics," Int. Top. Meet. Microwave Phot. (MWP), Valencia, Spain, (October 14-16, 2009) INVITED PAPER (slide copies included)

ID. Ring-resonator-based Filters and Logic Elements

E.J. Norberg, R.S. Guzzon, S.C. Nicholes, J.S. Parker, and L.A. Coldren, "Programmable Photonic Filters Fabricated with Deeply Etched Waveguides," IPRM, TuB2.1, Newport Beach, CA (May 10-14, 2009)

E.J. Norberg, J.S. Parker, U. Krishnamachari, R.S. Guzzon, and L.A. Coldren, "InGaAsP/InP based Flattened Ring Resonators with Etched Beam Splitters," IPNRA, IWA1, Honolulu, HI (July 12-17, 2009)

J.S. Parker, Y. Hung, E.J. Norberg, R.S. Guzzon, and L.A. Coldren, "Single Port Optical Switching in Integrated Ring Resonators," IPNRA, IWA2, Honolulu, HI (July 12-17, 2009)

IE. Optical-Phase-Locked-Loop PICs

S. Ristic, A. Bhardwaj, M.J. Rodwell, L.A. Coldren, and L.A. Johansson, "Integrated Optical Phase-Locked Loop, OFC/NFOEC, PDPB3, San Diego, CA (March 22-26, 2009)

S. Ristic, A. Bhardwaj, M.J. Rodwell, L.A. Coldren, and L.A. Johansson, "Heterodyne Locking of an Integrated Optical Phase-Locked Loop," Int. Top. Meet. Microwave Phot. (MWP), Th1.5, Valencia, Spain, (October 14-16, 2009)

II. Vertical-Cavity Surface-Emitting Lasers (VCSELs) & MBE Technology

Y.-C. Chang and L.A. Coldren, "Efficient, High-Data-Rate, Tapered Oxide-Aperture Vertical-Cavity Surface-Emitting Lasers," *IEEE Journal of Selected Topics in Quantum Electronics*, **15**, (3), pp. 704-715 (May/June 2009) INVITED PAPER

Y.-C. Chang, L.A. Coldren, "High-efficiency, high-speed VCSELs for optical interconnects," *Applied Physics A*, **95**, (4), pp.1033-1037 (June 2009)

Y.-C. Chang, Y. Zheng, J.H. English, A.W. Jackson, and L.A. Coldren, "Wide-dynamic-range, fast-response CBr₄ doping system for molecular beam epitaxy," NAMBE, IX.5, Princeton, NJ (August 9-12, 2009)

III. Cavity QED

M. Rakher, N. Stoltz, L. Coldren, P. Petroff, and D. Bouwmeester, "Externally Mode-Matched Cavity Quantum Electrodynamics with Charge-Tunable Quantum Dots," *Physical Review Letters*, **102**, (097403), pp.1-4 (March 2009)

I. PIC Technology and Devices

A. PIC Technology and Transmitters

Generation of 40 Gbps Duobinary Signals Using an Integrated Laser—Mach-Zehnder Modulator

P.C. Koh⁺, L.A. Johansson^{*}, Y.A. Akulova⁺, G.A. Fish⁺, G.T. Paloczi⁺, M. Larson⁺, M. Ayliffe⁺ and L.A. Coldren^{*}

⁺JDSU, 7404 Hollister Ave, Goleta, CA 9311.

^{*}Department of Electrical and Computer Engineering, University of California, Santa Barbara, CA 93106.

Abstract: Generation of 40 Gbps duobinary signals is demonstrated using the intrinsic EO response of an Mach-Zehnder modulator integrated with a widely tunable laser over a wavelength range of 1537nm – 1569nm.

©2007 Optical Society of America

OCIS codes: (250.5300) Photonic Integrated Circuits; (060.2330) Fiber Optics Communications

1. Introduction

To meet growing transmission demand, 40 Gbps optical channel rate is proving increasingly attractive. This requires the development of low-cost optical transmitters. For short-distance interconnects, directly modulated VCSELs is emerging as an attractive potential source [1]. More complex modulation formats with high tolerance to fiber nonlinearities such as RZ-DQPSK [2] is attractive for long-haul transmission. For intermediate reach, where linear chromatic fiber dispersion is the dominant impairment, optical duobinary (ODB) is attractive for increased reach, compact channel width and direct detection.

ODB using LiNbO₃ modulators have been demonstrated up to 107 Gbps [3]. Semiconductor modulators are a more attractive option because of its potentially lower drive voltage, integration with lasers and compatibility with compact, low-cost packaging. 40 Gbps semiconductor Mach-Zehnder (MZ) modulators have been demonstrated both discrete [4] and integrated to a laser [5].

In this work we demonstrate an integrated 40Gbps duobinary transmitter consisting of a MZ modulator integrated with a widely tunable Sampled-Grating DBR laser. Unlike previous results where 10Gbps duobinary modulation was generated and transmitted using this type of device [6], this demonstration does not require a low-pass filter for the drive signal. Instead, the electro-optic (EO) response of the MZ modulator is designed such that a good return loss over a broad frequency band, and a sharp EO roll-off of ~50dB/decade, is used to form the duobinary optical signal when driven directly by binary drive signal.

2. Device and Experiment

The device used in this work consists of a sampled-grating DBR laser integrated to an SOA and a dual-drive MZ modulator. All sections of the device are integrated onto one single Indium-Phosphide chip. The sampled-grating DBR laser can be tuned throughout the C-band and the integrated SOA provides power leveling over this wavelength range and compensates for cavity and modulator losses. The MZ modulator consist of two optical waveguide segments with RF electrodes situated in-between two multimode interference (MMI) couplers. More details of this type of device can be found in [7].

In order to generate the 3 level electrical drive signals for the MZ modulator through Inter-Symbol-Interference (ISI), a low-pass electrical filter is normally used. This low-pass filter has a 3dB bandwidth of approximately 0.25xBitRate and with a 40-50dB/decade filter roll-off after the 3dB cut-off. Typically this is accomplished by a Bessel Thompson filter employing absorptive filter design, giving good S11 performance and simultaneously achieving a steep filter roll-off at ~40-50dB/decade. For our 40Gbps optical duobinary transmitter, we design the MZ modulator such that its EO response has a 3dB bandwidth of 10GHz, has a 40-50dB/decade roll-off after the 3dB cut-off, and is broadband impedance matched such that reflection of the 40Gbps input drive is minimized. This design approach eliminates the need for additional sharp electrical low-pass filter as generation of the ISI drive is performed by the modulator itself.

To achieve the design objectives mentioned above, both the EO response and return loss performance of our modulator need to be improved. Broadband impedance matching is necessary because of the relatively low modulator impedance of $\sim 26\text{-}29\Omega$ resulting from our fabrication process. In addition, RC time-constant limited EO response usually gives a 20dB/decade roll-off after the 3dB cut-off, hence sharper roll-off in the response will be needed in order to be used in a 40Gbps duobinary application. We achieved these objectives by using a distributed electrode design such that on-chip matching elements are introduced in the modulator electrodes. This increases the input impedance of the modulator to $\sim 37\Omega$, and at the same time, slows the electrical phase velocity such that a huge velocity mismatch now exists between the electrical signal and the optical wave. Velocities mismatch in electrical and optical domain then results in the required bandwidth, and increases the roll-off of the response after the 3dB cut-off.

To determine the suitability of the modulator for 40Gbps duobinary applications, frequency domain characterization is performed whereby the chip-on-carrier return loss S_{11} and electro-optic (EO) response are measured using a network analyzer. Fig.1 shows the experimental setup for time domain characterization of the Integrated-Laser-Mach-Zehnder (ILMZ) chip-on-carrier. The output of the pseudo-random pattern generator is used to drive a matched pair of 40Gbps drivers. Two phase tuners are used to equalize the delays of the RF signal paths from pattern generator to the probes tips. No low-pass filters are used for our experiments as the required duobinary signal is generated by the EO response of the MZ modulator itself. Without a 40Gbps differential encoder at our disposal, time-domain characterizations include eye diagram measurements at 0km (BTB), 10km and 12.5km of single-mode fiber across the 1537-1569nm tuning range.

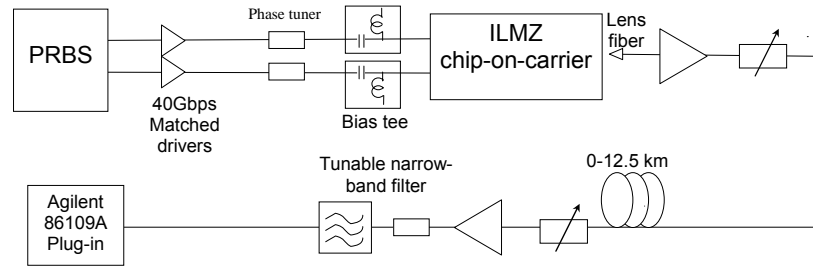


Fig. 1. Schematic of experimental arrangement used to generate 40 Gbps duobinary modulation using the integrated SGDBR laser – Mach-Zehnder modulator. Intrinsic MZ modulator EO response is used to generate the 40Gbps duobinary modulations.

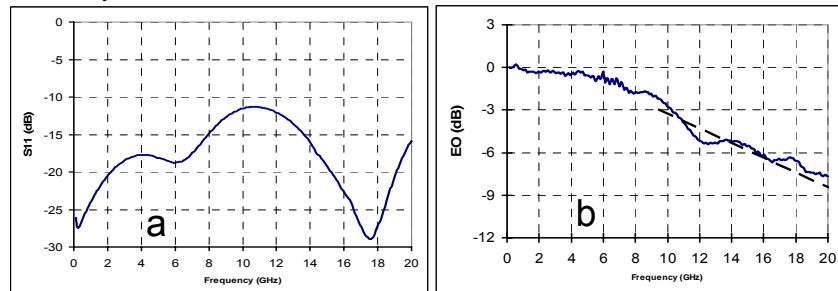


Fig. 2a: Return loss S_{11} of chip-on-carrier with a $750\mu\text{m}$ long modulator. Fig. 2b: Electro-optical response of chip-on-carrier with a $750\mu\text{m}$ long modulator.

3. Results

In Fig. 2a, the return loss S_{11} of the chip-on-carrier with a $750\mu\text{m}$ long modulator biased at -1.5V is plotted. The S_{11} plot shows that the return loss is below -15dB for most of the 20GHz band measured, indicating an excellent impedance matching. Broadband impedance matching beyond the $0.25\times\text{BitRate}$ band is desirable in our case as the input signal is a 40Gbps Non-Return-to-Zero signal. The small-signal EO response is measured with the MZ modulator bias at -1.5V and is shown in Fig. 2. The $750\mu\text{m}$ long MZ modulator gives a 3dB bandwidth 10.4GHz. A $\sim 50\text{dB/decade}$ roll-off of the modulator is obtained by fitting a line at the EO response as shown in Fig. 2. The high roll-off of the EO response is due to velocities mismatch of the electrical and optical signals as indicated previously. With good return loss, a bandwidth of $0.25\times\text{BitRate}$ and a sharp roll-off, the MZ modulator is suitable for 40Gbps duobinary transmitter application without additional electrical low-pass filter.

Fig. 3 plots the optical eye diagrams for transmit wavelengths of 1537nm, 1542nm, 1555nm and 1569nm, after transmission of 0km, 10km and 12.5km of fiber, using a PRBS word length of $2^{31}-1$. RF drive voltages of the modulator are 3.5Vpp, 3.95Vpp, 4.3Vpp and 4.3Vpp for wavelength channels of 1537nm, 1542nm, 1555nm and 1569nm respectively. The back-to-back eye diagrams show that the MZ modulator, with its sharp EO response roll-off, functions as a 40Gbps duobinary transmitter according to expectations. The device used in this experiment has input MMI that is input power dependent such that at short wavelength, the optical splitting ratio is severely unbalanced. Unequal splitting ratio results in residual chirp at short wavelength channels such that an “open” optical eye is not possible after fiber transmission. Nonetheless, for wavelength channels that do not suffer from this artifact, “open” optical eye diagrams are obtained after transmission of 10-12.5km of fiber.

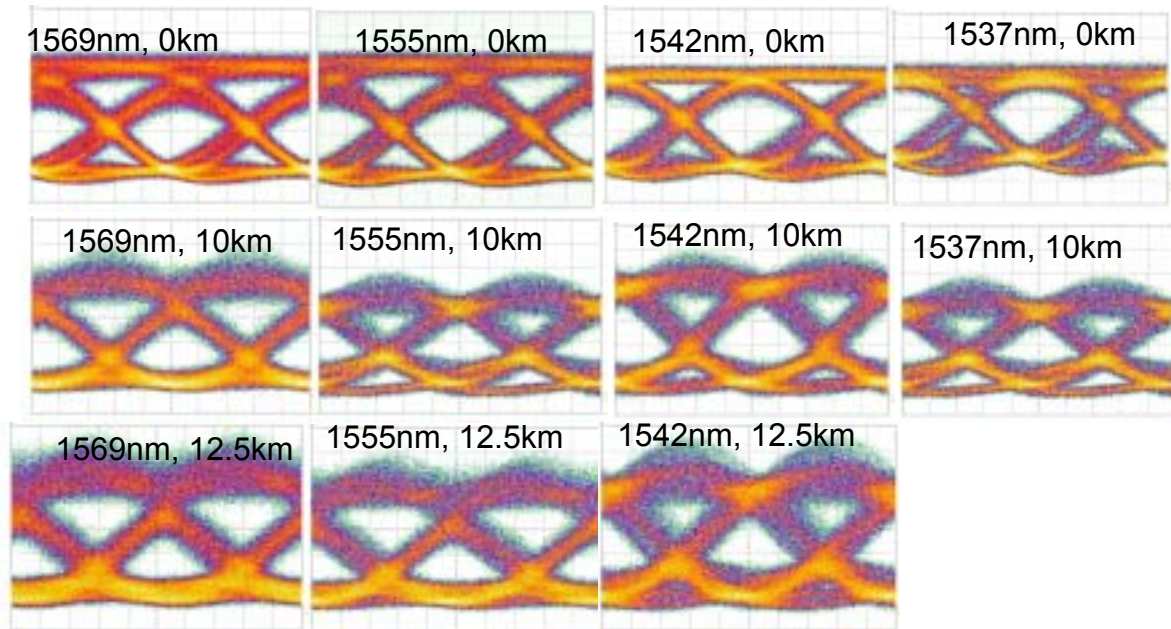


Fig. 3: Received optical eye diagrams at 1569nm, 1555nm, 1542nm, 1537nm after transmission through 0km, 10km and 12.5km fiber, respectively.

4. Conclusion

We demonstrate, for the first time, a 40Gbps duobinary transmitter using an integrated widely-tunable SGDBR laser and a Mach-Zehnder modulator. 40Gbps ODB eye diagrams are obtained for wavelength channels from 1537nm to 1569nm, using the intrinsic EO response of the modulator. This eliminates the need for an additional electrical low-pass filter. The modulator uses on-chip matching in the modulator electrodes to achieve good return loss over a 20GHz frequency band and a sharp 50dB/decade EO response roll-off. “Open” eye diagrams are obtained indicating a good potential for high transmission performance.

5. References

1. Y.-C. Chang, C.S. Wang, and L.A. Coldren, “High-Efficiency, High-Speed VCSELs with 35 Gb/s Error-Free Operation,” *Electronics Letters*, 43, (9), 1022-1023. (September 2007).
2. C. Fürst “43 Gb/s RZ-DQPSK DWDM field trial over 1047 km with mixed 43 Gb/s and 10.7 Gb/s channels at 50 and 100 GHz channel spacing,” *Proc. ECOC 2006 Cannes, France*, Sep. 2006.
3. P.J. Winzer, G. Raybon, M. Duelk, “107-Gb/s optical ETDM transmitter for 100G Ethernet transport,” *31st European Conference on Optical Communication*, 2005. Vol. 6, pp:1-2, 25-29 Sept. 2005.
4. A 40-Gb/s InGaAlAs–InAlAs MQW n-i-n Mach–Zehnder Modulator With a Drive Voltage of 2.3 V,” *IEEE Photonics Technology Letters*, Vol. 17, No. 1, pp. 46-48, January 2005.
5. J. S. Barton, M. L. Masanovic, A. Tauke-Pedretti, E. J. Skogen, and L. A. Coldren, “Monolithically-integrated 40Gbit/s widely-tunable transmitter using series push-pull Mach-Zehnder modulator SOA and sampled-grating DBR laser,” presented at *OFC/NFOEC 2005 Optical Fiber Communication Conference*, Mar 6-11 2005, Anaheim, CA, United States, 2005
6. L.A. Johansson, L.A. Coldren, P.C. Koh, Y.A. Akulova, G.A. Fish, “Transmission of 10 Gbps Duobinary Signals Using an Integrated Laser-Mach Zehnder Modulator,” *Optical Fiber communication/National Fiber Optic Engineers Conference*, 2008. *OFC/NFOEC 2008*. pp. 1-3, 24-28 Feb. 2008

Recent Advances in InP PICs

Larry A. Coldren

Electrical & Computer Engineering and Materials Depts., University of California, Santa Barbara, CA 93106
coldren@ece.ucsb.edu

Abstract: Within the past couple of years InP-based Photonic Integrated Circuits (PICs) have become the subject of aggressive development for commercial applications primarily for the telecommunications industry. Chips with hundreds of photonic components carry live traffic in the field, but questions remain about cost/volume/performance tradeoffs, as well as the need for common integration platforms and/or foundry services. Research efforts have been influenced by these issues.

1. Introduction

Small-scale PICs in InP have been researched for over two decades[1], and there have been a few successes that have had some commercial impact over the past decade or so. However, for many years success with hybrid integration techniques as well as limited market volumes has slowed the commercial adoption of PICs, except for a few limited examples. The classic success example is the so-called EML, the electro-absorption modulated (EAM) laser, usually consisting of a DFB laser integrated with a waveguide section at one end that has a slightly higher absorption energy so that it is nominally transparent[2,3]. A reverse bias to this section increases its optical absorption so that it can function as a high-speed modulator. Other PIC examples include various single-chip widely-tunable transmitter chips that have included integrated amplifiers, modulators, and monitoring detectors together with multiple-section lasers[4,5]. Larger-scale PICs with hundreds of components have been offered commercially only in the past few years[6]. Most of this work has involved chips with numerous parallel channels, which each might contain four or five elements, multiplexed together in a wavelength-division-multiplexed (WDM) transmitter or receiver[6,7]. Research efforts on larger-scale PICs have included work with more complex chains of components to provide a higher level of functionality within each channel[8,9].

This Plenary presentation will endeavor to mention representative examples of different classes of PICs that have been worked on in recent years. The emphasis at the IPRM will be on the materials and integration issues as well as some of the device/circuit tradeoffs. Partly due to necessity because of proprietary issues, and partly due to convenience, an overemphasis on our work at UCSB will result.

2. Integration Platforms

The most elementary of photonic ICs requires the ability to switch between active and passive optical waveguide sections without undue loss or reflections. Perhaps three or more waveguide types need to be abutted in such a 'seamless' manner to integrate all of the desired functionalities within some PIC. Figure 1 illustrates some examples of active-passive junctions along the axis of the optical waveguides.

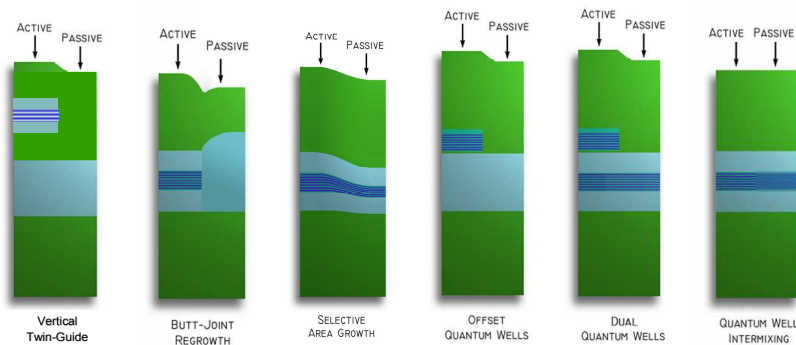


Fig. 1. Schematic waveguide cross sections of six active-passive integration platforms. All have been used in commercial products.

Pros and Cons of each active-passive junction include the following: the vertical twin guide allows for independent properties in the upper and lower guides, but a long coupling length is needed to accomplish the vertical light transfer; the butt-joint regrowth approach also allows for independent properties in the active and passive sections, but a critical alignment of the regrown waveguides is necessary; the selective area growth technique provides a scaling of the vertical dimensions to change the absorption edge of the quantum-wells, but the properties of each are still linked and the patterned growth results in some transition length as well as being critically dependent on the lateral diffusion properties of the precursors; the offset quantum-well approach only requires an unpatterned blanket

regrowth over a small step after etching away the active wells, but offsetting the gain results in a reduced net gain for the mode; the dual quantum-well case adds higher bandgap wells in the waveguide to provide better modulators in the ‘passive’ guide; the quantum-well intermixing approach can provide multiple bandgaps from a single growth with multiple diffusion steps, but only low saturation power SOAs are available without more growths.

In the lateral direction there are also many different possible waveguiding geometries that are more or less desirable for various PIC elements. These include surface ridge waveguides, buried heterostructures, buried ribs, deeply etched ridges, and the transitions between these. Many tradeoffs exist. High-index-contrast enables sharp bends, but it tends to bring higher losses. Active regions generally require high-quality epitaxial interfaces for low non-radiative recombination and high reliability, but this limits the fabrication options.

3. Example PICs

Figures 2-4 give recent examples of photonic ICs from some of our work at UCSB. Different integration platforms and lateral waveguide structures were used in each case. Figure 2 illustrates a photocurrent driven wavelength converter that integrates an all-photonic SOA-PIN receiver with a widely-tunable SGDBR laser—SOA—traveling-wave-EAM transmitter[10]. It uses the ‘dual quantum-well’ integration platform with a surface-ridge waveguide structure.

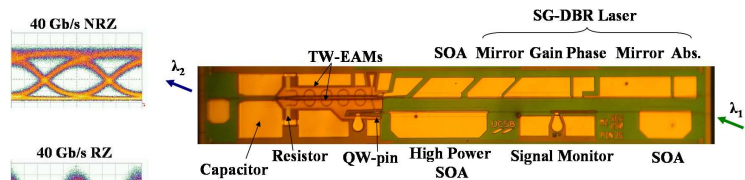


Fig. 2. Photocurrent-driven wavelength converter and outputs for both NRZ and RZ input data @ 40 Gb/s.

Figure 3 illustrates a chip which provides the fabric of an 8 x 8 all-photonic packet-switch[9]. In one of the most complex PICs ever created, 8 wavelength converters feed an 8 x 8 AWGR (which acts like a prism) that together enable any of 8 incoming channels to be switched to any of 8 output channels by switching the wavelength in the wavelength converters. In this case quantum-well intermixing is used for different bandgaps, and three different waveguides are employed in the different sections: surface-ridges, deeply-etched ridges, and buried ribs.

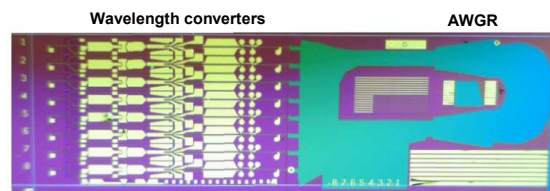


Fig. 3. 8 x 8 all-photonic space switch employing wavelength converters and a passive dispersive AWGR filter.

Figure 4 is a programmable integrated photonic lattice filter that incorporates three coupled ring resonators together with a Mach-Zehnder geometry[11]. Numerous FIR and IIR filter functions can be programmed. Illustrated is a repeating two pole response. In this case an offset-quantum-well layer structure and deeply-etched waveguides are used throughout.

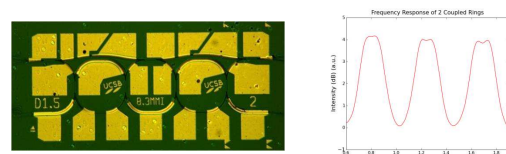


Fig. 4. Programmable lattice filter and 2-pole IIR response.

4. Acknowledgements

This work is supported by DARPA via the DODN and PhASER projects.

5. References:

- [1] R. F. Leheny, R. E. Nahory, M. A. Pollack, A. A. Ballman, E. D. Beebe, J. C. DeWinter, R. J. Martin, *Electron. Letts.* **16**, 353 (1980).
- [2] M. Suzuki, Y. Noda, H. Tanaka, S. Akiba, Y. Kushiuro, and H. Ishiki, *IEEE J. Lightwave Tech.*, **LT-5**, 1277-1285 (1987)
- [3] T. L. Koch and U. Koren, *IEEE J. Quantum Electronics*, **QE-27**, 641-653 (1991).
- [4] Y. A. Akulova, G. A. Fish, H. Xu, E. Hall, M. C. Larson, P. Abraham, H. Marchand, et al, *Proc. IPRA*, paper IWF4, San Diego (2005).
- [5] J. W. Raring, L. A. Johansson, E. J. Skogen, M. N. Sysak, H. N. Poulsen, S. P. DenBaars, and L. A. Coldren, *JSTQE*, **25** (1) 239-248 (2007).
- [6] R. Nagarajan, C. H. Joyner, R. P. Schneider, et al, “Large scale photonic integrated circuits,” *IEEE JSTQE*, **11** (1) 50-65 (2005).
- [7] D. F. Welsh, F. A. Kish, R. Nagarajan, C. H. Joyner, R. P. Schneider, Jr, J. G. Dominic, M. L. Mitchell, et al, “The realization of large-scale photonic integrated circuits and the associated impact on fiber-optic communication systems,” *IEEE JLT*, **24** (12) 4674-4683 (2006).
- [8] V. Lal, M. Masanovic, J. Summers, G. Fish, and D. Blumenthal, “Monolithic wavelength converters for high-speed packet-switched optical networks,” *IEEE JSTQE*, **13** (1) 49-57 (2007).
- [9] S. C. Nicholes, M. L. Mašanović, E. Norberg, E. Lively, B. Jevremović, L. A. Coldren, and D. J. Blumenthal, “Advanced epitaxial techniques for high-density photonic integrated circuits in InP,” *IPRM’09*, paper , Newport Beach, (May, 2009).
- [10] M. M. Dummer, J. Klamkin, A. Tauke-Pedretti, and L. A. Coldren, “A bit-rate transparent monolithically integrated wavelength converter,” *ECOC’08*, Invited paper Th.2.C.1, Brussels, (Sept., 2008)
- [11] E. J. Norberg, R. S. Guzzon, S. Nicholes and L. A. Coldren, “Programmable photonic filters fabricated with deeply etched waveguides,” *IPRM’09*, paper , Newport Beach, (May, 2009).

NOVEL APPLICATION OF QUANTUM WELL INTERMIXING IMPLANT BUFFER LAYER TO ENABLE HIGH-DENSITY PHOTONIC INTEGRATED CIRCUITS IN InP

Steven C. Nicholes^{*}, Milan L. Mašanović[†], Jonathon Barton[†], Erik J. Norberg[†], Erica Lively[†], Biljana Jevremović[†], Larry A. Coldren[†], and Daniel J. Blumenthal[†]

^{*}*Department of Materials*

[†]*Department of Electrical and Computer Engineering
University of California, Santa Barbara 93106*

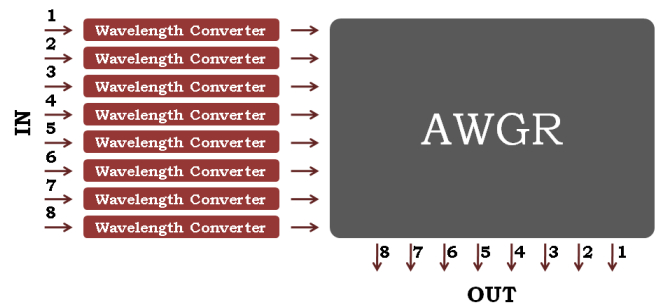
Abstract

We demonstrate a novel technique for free-carrier absorption reduction using an InP buffer layer with quantum well intermixing. Application of this technique enabled fabrication of monolithic tunable optical routers with more than 200 functions.

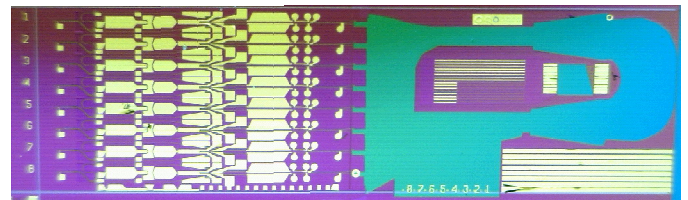
I. Introduction

Photonic integrated circuits (PICs) in InP provide an attractive alternative to discrete component systems, offering a reduction in overall system footprint, improved reliability, and reduced packaging costs. However, as on-chip component demands increase in both total number and functional requirements, novel approaches to epitaxial design and fabrication that minimize process complexity to achieve high device yields are desirable [1]. A number of device fabrication platforms have been reported that provide a path for active and passive component integration [2-4]. Each approach has advantages and disadvantages depending on the application, but should provide an optimal combination of high gain and low loss regions with a minimum number of regrowths for improved yield. For instance, with the offset quantum well platform, active and passive regions are defined by a simple wet etch, which minimizes fabrication complexity [2]. This approach only yields two band-edges and therefore limits the diversity of components that can be integrated on-chip. Alternatively, quantum-well intermixing (QWI) can provide multiple band-edges on-chip, but this requires additional post-growth processing [3]. Epitaxial regrowths have also been used to increase integration flexibility, such as butt-joint regrowths [4] for additional band-edges on chip and unintentionally doped (UID) InP regrowths for very low-loss propagation regions. However, these regrowth techniques increase cost and complexity and can result in a significant reduction in device yield.

Optical routers are one promising area in which the footprint and power benefits of photonic integration could make a significant impact [5]. In this paper, we discuss a new application for a bulk InP implant buffer layer used in QWI to realize a 640 Gbps, 8x8 monolithic tunable optical router (MOTOR). This method allows for reduced passive loss without a UID regrowth, thus improving device yield. The device contains more than 200 building blocks, representing



(a)



(b)

Fig. 1. a) Schematic overview of MOTOR architecture; (b) Photograph of fabricated device

the forefront of integration in terms of the total number of components and functional complexity.

II. Device Integration Approach

The MOTOR chip consists of an array of eight, 40 Gbps RZ, widely-tunable wavelength converters (WC) and an arrayed-waveguide grating router (AWGR) (Fig. 1). The WCs operate using cross phase modulation effects in a carrier-based, differential Mach-Zehnder interferometer (MZI) [6]. This approach to wavelength conversion uses an integrated differential-delay line to overcome carrier recovery time limits in semiconductor optical amplifiers (SOA) in the MZI at 40

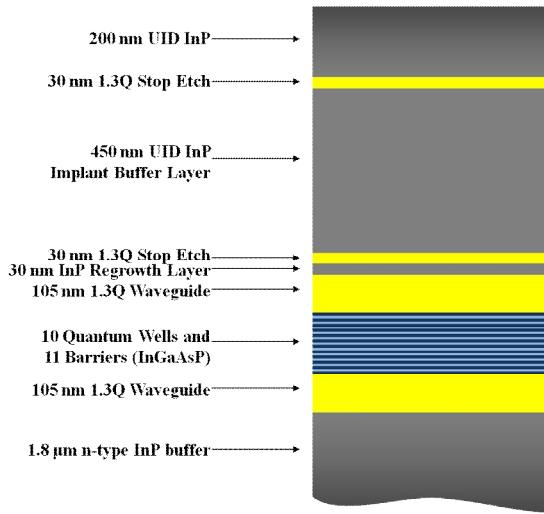


Fig. 2. Epitaxial base structure for quantum well intermixing

Gbps. The converted data are routed to a specific output port of the AWGR, based upon the new wavelength set by the WC [7]. The chip integrates active and passive components, such as SOAs, sampled grating (SG)-DBR lasers, variable optical attenuators (VOA), phase modulators, light couplers, waveguides and delay lines simultaneously, thus requiring a robust integration platform to properly place different band edges and reduce waveguide losses. To overcome this key challenge of integrating a low loss AWGR with the optimized active tunable wavelength converters, we use a QWI epitaxial design, three different waveguide architectures, and a novel, non-regrowth approach to reduce free-carrier absorption losses with the QWI implant buffer layer.

A. Epitaxial Platform and QWI Details

To define the active/passive regions of the chip, we utilize an impurity-free quantum well intermixing (QWI) process [3]. The initial base growth consists of ten compressively-strained (+0.9%) 6.5-nm InGaAsP quantum wells (QW) and eleven tensile-strained (-0.2%) 8.0-nm InGaAsP barriers centered in a quaternary waveguide (Fig. 2). This structure maximizes the optical overlap with the QWs, yielding an optical confinement factor (Γ) of $\sim 13\%$. Above the waveguide, a 450 nm unintentionally doped (UID) InP buffer layer is grown to collect the subsequent phosphorous implant for QWI. Selective intermixing of the wells and barriers for QWI. Selective intermixing of the wells and barriers for QWI is achieved through a rapid thermal anneal (RTA) process at 675°C to shift the as-grown peak PL wavelength from 1545 nm to 1420 nm as in [8]. A single, blanket, p-type regrowth is used later to define the waveguide cladding.

B. Waveguide Designs and Implementation

Because of the diversity of on-chip functions, three waveguide architectures are used in MOTOR: surface ridge waveguides, deeply etched ridge waveguides, and buried rib waveguides. All active components and most passive waveguide regions in the WCs employ a surface ridge design (Fig. 3a,d) for reasons explained below. This design is accomplished using a combination of dry and wet chemical etching. A 400-nm PECVD SiO_2 hard mask is defined above the cladding by photolithography and CHF_3 inductively-coupled plasma (ICP) dry etching. The InP ridge is etched to a depth of roughly $1.8\ \mu\text{m}$ in an ICP system using a $\text{Cl}_2\text{:H}_2$: Ar chemistry to achieve straight and smooth sidewalls [9].

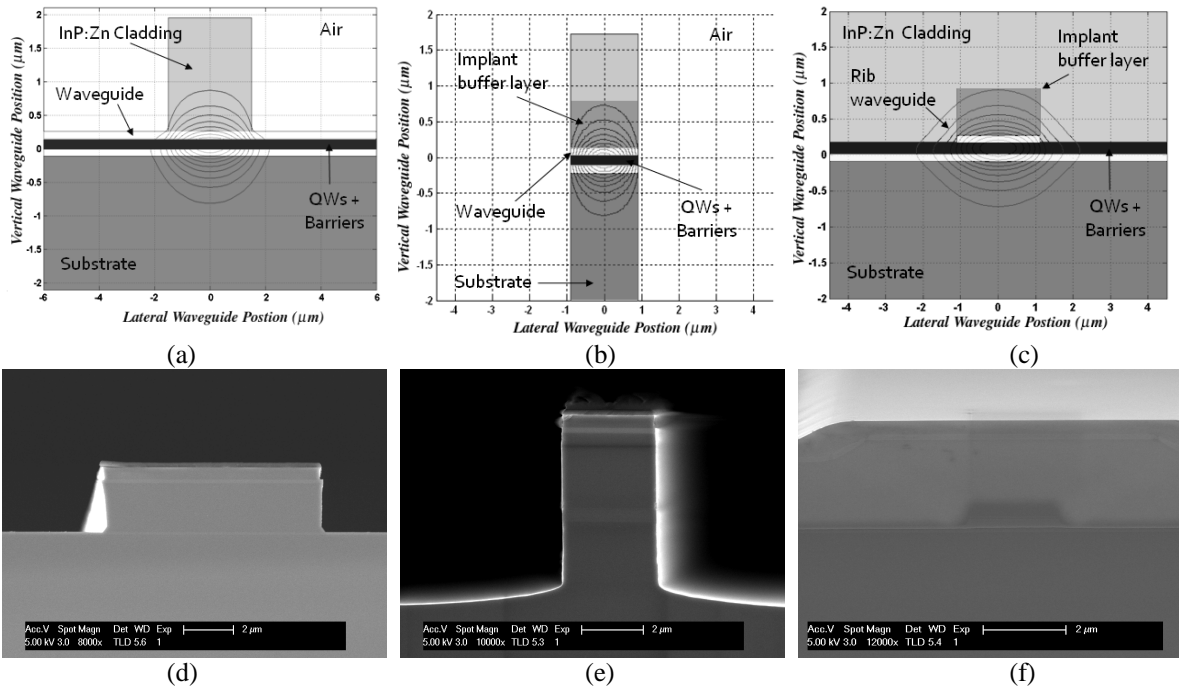


Fig. 3. Ridge architectures used in MOTOR: (a), (b), (c) show schematic cross-sections of epitaxial layers with the optical mode profile superimposed for surface ridge, deep ridge, and buried rib, respectively. (d), (e), (f) show corresponding SEM cross sections for surface ridge, deep ridge, and buried rib, respectively

Next, the surface ridge regions are wet etched another $\sim 0.6 \mu\text{m}$ in a 3:1 $\text{H}_3\text{PO}_4:\text{HCl}$ mixture. The quaternary waveguide below the cladding regrowth acts as a stop-etch layer. By etching the InP down to only the top of the waveguide, we avoid etching the QWs and eliminate surface recombination losses. Although the surface ridge waveguide is simple to fabricate, there is significant modal overlap with the Zn-doped cladding material above the waveguide, resulting in free-carrier absorption losses.

The device also utilizes a deeply etched waveguide for the differential-delay line to accommodate a compact structure with tight bend radii (Fig. 3b,e). This region is fabricated by two separate dry etches. The first $1.8\text{-}\mu\text{m}$ etch is accomplished simultaneously with the dry-etch step of the surface ridge waveguide. The delay line region is masked with photoresist during the surface ridge wet etch, due to the crystallographic nature of the wet etch chemistry. Following the surface ridge wet etch, a lift-off process with photoresist and 350 nm PECVD SiO_2 is used to open the delay line region. A $2\text{-}3 \mu\text{m}$ deep dry etch through the waveguide (using identical etch conditions) is then performed.

In the AWGR, a 70-nm rib waveguide is etched into the upper portion of the waveguide prior to the cladding regrowth, which subsequently buries it (Fig. 3c,f). The rib allows for large bend radii in the AWGR with low scattering losses since the waveguide is only partially etched.

C. Novel Use for Quantum Well Intermixing Buffer Layer

In our previously reported work on QWI [2,8], the undoped implant buffer layer grown above the waveguide is used only for QWI purposes. The thickness of this layer is designed to ensure that the 100-keV phosphorous implant generates vacancies above the waveguide, avoiding damage to the QW region. After intermixing is complete, the layer is typically removed by wet etching. Here, however, we deliberately leave the buffer layer in certain regions of the chip, creating a UID setback layer between the optical mode and the Zn dopant atoms in the p-type cladding in order to reduce optical scattering losses. At $1.5 \mu\text{m}$, the absorption loss as a function of Zn concentration has been shown to be high, according to the following [10]:

$$\alpha = 20(p/10^{18} \text{ cm}^{-3}) \text{ cm}^{-1}. \quad (1)$$

where α is the loss in cm^{-1} and p is the Zn concentration. By leaving the implant buffer layer in passive sections, the Zn doping in the cladding is pushed further away from the optical mode and a significant reduction in loss can be achieved without comprising the quality of active components. Furthermore, a 200-nm sacrificial InP layer is grown above the implant buffer layer during the initial epitaxial growth to protect the buffer layer from implant damage and ensure a high-quality regrowth interface (Fig. 2).

Both the deeply etched waveguide and the buried rib waveguide designs are well suited to using the implant buffer layer in this manner. As shown in Fig. 3b, because the deep etch process etches completely through the waveguide

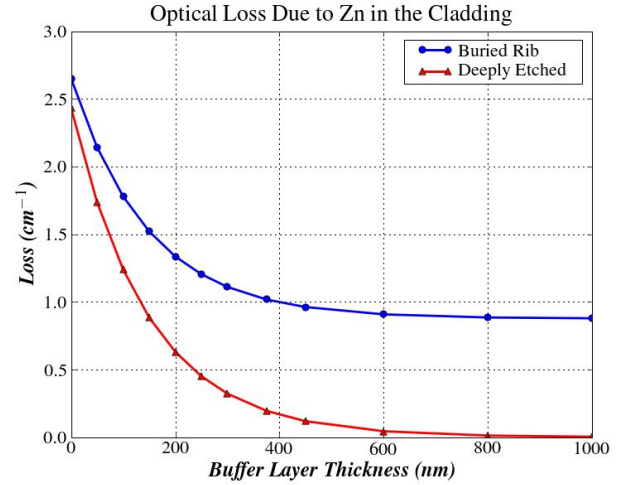


Fig. 4. Effect of the implant buffer layer thickness on the scattering loss due to Zn doping in a buried rib and deeply etched waveguide (model assumes no Zn diffusion)

region, the optical mode can only interact with Zn-doped material directly above the waveguide. Therefore, the presence of an undoped InP setback layer is expected to provide a major improvement in optical loss. In the buried rib region (Fig. 3c), however, the mode is not tightly confined and expands laterally outside of the rib region. Leaving the buffer layer directly above the rib will only reduce optical loss over a portion of the mode volume. Because the lateral portion of the mode remains in the Zn-doped cladding, the expected reduction in optical loss is not as great as that in the deeply etched waveguide.

To verify this reduction in loss, we used Eqn. 1 with 3D beam propagation methods to simulate the expected loss due to Zn in the cladding as a function of implant buffer layer thickness. Our cladding regrowth utilized a graded doping profile to ensure the formation of a p-i-n junction across the QWs while minimizing the concentration of Zn near the optical mode. Using these doping concentrations and neglecting Zn diffusion during the regrowth, we can approximate the reduction in scattering loss due to the presence of the buffer layer. Fig. 4 shows the relationship between loss and buffer layer thickness. As anticipated, loss in the deeply etched region drops off more quickly than in the buried rib structure, as there is no lateral mode interaction with Zn dopant atoms. This result also shows that there is no measurable advantage to increase the implant buffer layer beyond its current thickness of 450 nm . The magnitude of these loss values will be larger in the actual sample due to diffusion effects, but the general trends should be unchanged.

This technique cannot be readily applied to the surface ridge waveguide, however, because the surface ridge is finished by wet-etching. In order to facilitate removal of the implant buffer layer before the cladding regrowth, a quaternary stop etch layer is included directly below the buffer (Fig. 2). If the implant buffer layer was left in the surface ridge region, the wet etch would stop on this quaternary layer instead of the waveguide, resulting in a detrimental reduction

in optical confinement in these regions.

III. Device Performance

The AWGR region was first characterized using amplified spontaneous emission (ASE) generated by forward biasing SOAs in the WC and measuring the output in an optical spectrum analyzer. Fig. 5 shows the ASE spectrum from input channel #3 at every output channel of the AWGR. The free spectral range was measured to be 11.1 nm. Next, wavelength-based switching was examined by tuning the SG-DBR to an allowed wavelength for each output port (Fig. 5). Output powers of more than -5 dBm were measured in the OSA. These powers are reasonable given the long propagation length of the AWGR region and fiber coupling losses.

Measurements of the MZI transfer function in the WC show more than 25 dB of extinction in the MZI for multiple input ports (Fig. 6). Input WCs #1 and #5 had ridge defects in the MZI and thus data are not shown for these ports. This level

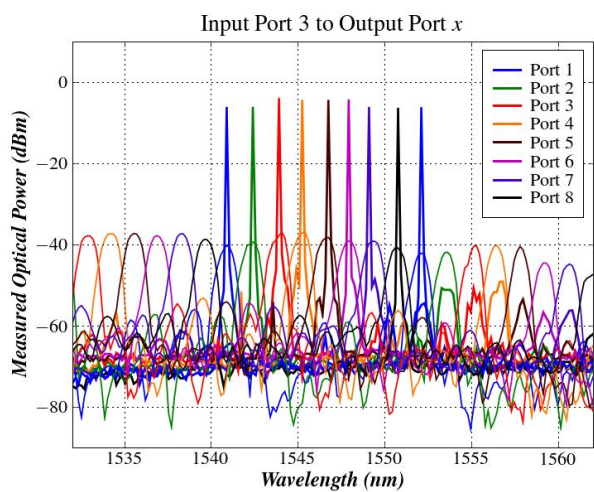


Fig. 5. Wavelength switching using the SG-DBR of input channel #3 and measuring at each output port (superimposed on ASE spectra from all output ports)

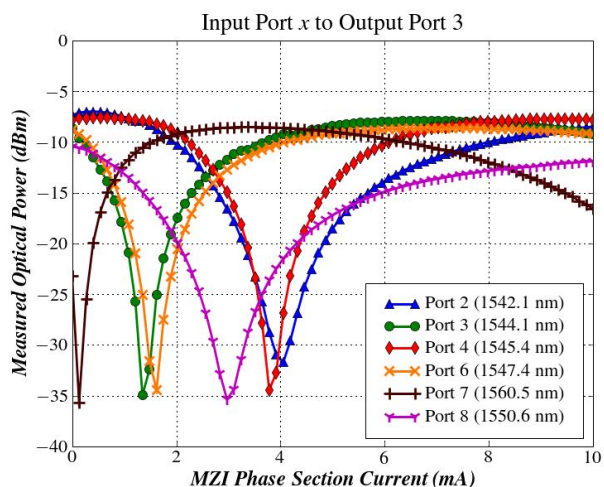


Fig. 6. MZI transfer functions for six of the eight input wavelength converters measured from output port #3

of extinction indicates that there is sufficient phase swing in the MZI to perform wavelength conversion of the input data.

IV. Conclusion

We demonstrate a new technique to reduce free-carrier absorption in passive regions of large-scale PICs by exploiting an InP implant buffer layer used for quantum well intermixing. The buffer layer, which is typically removed everywhere, was left in deeply etched and buried rib waveguide regions to provide an undoped setback layer between the optical mode and the Zn-doped cladding. In addition to a reduction in optical loss, this method eliminates the need for an additional UID regrowth in the AWGR region, thus improving device yield. Using this method, we fabricated the first 8x8 monolithic tunable optical router capable of 40 Gbps operation per channel with more than 200 integrated functions.

Acknowledgements

This work was supported by DARPA MTO and the Army under the DOD-N LASOR Project (W911NF-04-9-0001). Device fabrication was done in the UCSB nanofabrication facility, part of the NSF funded NNIN network.

References

- [1] R. Nagarajan, *et al.*, "Large-scale photonic integrated circuits," *IEEE J. Sel. Topics Quantum Electron.*, vol. 11, pp. 50, Jan./Feb. 2005.
- [2] M.N. Sysak, J.W. Raring, J.S. Barton, M. Dummer, D.J. Blumenthal, and L.A. Coldren, "A single regrowth integration platform for photonic circuits incorporating tunable SGDBR lasers and quantum-well EAMs," *Photonics Technology Letters*, vol.18, no.15, pp.1630-1632, Aug. 2006.
- [3] E.J. Skogen, J.S. Barton, S.P. Denbaars, and L.A. Coldren, "A quantum-well-intermixing process for wavelength-agile photonic integrated circuits," *Journal of Selected Topics in Quantum Electronics*, vol.8, no.4, pp. 863-869, Jul/Aug 2002.
- [4] J. J. M. Binsma, M. van Geemert, F. Heinrichsdorff, T. van Dongen, R. G. Broeke, and M. K. Smit, "MOVPE waveguide regrowth in InGaAsP/InP with extremely low butt joint loss," in *Proc. IEEE/LEOS Symp. (Benelux Chapter)* Brussels, Belgium, Dec. 2001.
- [5] D. Wolfson, V. Lal, M. Masanovic, H.N. Poulsen, C. Coldren, G. Epps, D. Civello, P. Donner, and D.J. Blumenthal, "All-optical asynchronous variable-length optically labelled 40 Gbps packet switch," *Optical Communication*, 2005. ECOC 2005. 31st European Conference on, vol.6, no., pp. 49-50 vol.6, 25-29 Sept. 2005.
- [6] V. Lal, M.L. Masanovic, J.A. Summers, G. Fish, and D.J. Blumenthal, "Monolithic Wavelength Converters for High-Speed Packet-Switched Optical Networks," *Selected Topics in Quantum Electronics, IEEE Journal of*, vol.13, no.1, pp.49-57, Jan.-feb. 2007.
- [7] M. Smit and C. van Dam, "PHASAR-Based WDM-Devices: Principles, Design and Applications," *Journal of Selected Topics in Quantum Electronics*, vol 2, no. 2, 236-250, 1996.
- [8] J. Raring *et al.*, "Advanced integration schemes for high-functionality high-performance photonic integrated circuits," presented at the *Proc. SPIE*, San Jose, CA, Jan. 23-25, 2006, Paper 61260H.
- [9] F. Karouta, B. Docter, E. Kok, E.-J. Geluk, J. Van der Tol, and M. Smit, "High Aspect Ratio Etching and Application in InP-Based Photonic Integrated Circuits," *Meet. Abstr. - Electrochem. Soc.* 802, 2050 (2008).
- [10] H. C. Casey Jr. and P. L. Carter, "Variation of intervalence band absorption with hole concentration in p-type InP," *Appl. Phys. Lett.*, vol. 44, no. 1, pp. 82-83, 1984.

Integrated Transmitters and Transceivers for High-End Applications in WDM Optical Networks

Larry A. Coldren

*Electrical & Computer Engineering and Materials Depts., University of California, Santa Barbara, CA 93106
coldren@ece.ucsb.edu*

Abstract: Integration platforms initially developed for widely-tunable lasers have recently been extended to encompass more complex single-chip transmitters as well as single-chip transceivers or wavelength converters by incorporating optical amplifier-photodiode receivers with these transmitters. Results from these and other InP-based photonic ICs will be presented.

© 2009 Optical Society of America

OCIS codes: 250.5300; 250.3140; 130.0250; 060.1155

1. Introduction

Photonic integration on InP is beginning to reach a maturity that enables hundreds of interacting components to be successfully fabricated on a single chip. Several commercial firms now sell products into the fiber optic communications market that use chips containing dozens of individual optical elements [1]. At least one uses chips that contain hundreds of optical elements in its products [2,3]. Billions of no-failure device-hours have been documented in the field with such photonic integrated circuits (PICs).

Nevertheless, some still question the reasons for monolithic integration versus the hybrid approaches that have been used with success for many years. The desire to have 'known-good-die' prior to the expensive packaging step is compelling to some, and the promise of low cost PIC components can not always be assumed because of limited volumes for any one design. Universal integration platforms that can produce a wide range of chips are necessary. The history to date for high-end applications has been that the PIC wins if and only if it can *perform* as well as the hybrid circuit. Distortions can not be introduced; sensitivity (range) can not be sacrificed. So, the issue with photonic integration inevitably becomes the identification of an integration platform that is simple and robust enough to be high-yield, but at the same time deliver high-performance across a wide range of photonic elements. The system *cost* must be much lower to take the risk, but this result seems to be emerging, so the cost/size/power reductions afforded by the use of PIC solutions may at long last be realized, and one might expect to observe an acceleration of their use with an associated further advance down the cost curve for them. Perhaps some might even accept slight performance compromises in some systems' architectures if the price is right!

This paper will introduce the integration platforms developed at UCSB, initially for the four-section Sampled-Grating Distributed-Bragg-Reflector (SGDBR) laser alone[4], and later for the SGDBR integrated with various other elements, such as semiconductor-optical-amplifiers (SOAs), electro-absorption modulators (EAMs), Mach-Zehnder modulators (MZMs), multi-mode interference (MMI) couplers, photodetectors (PDs), and arrayed-waveguide-routers (AWGRs). It will then discuss results from transmitters formed with the SGDBR and some of these elements. The paper will then move on to transceivers/wavelength converters using all-photonic high-gain, high-saturation power SOA-PD receivers together with a particular transmitter. Finally, some recent work with arrays of wavelength converters integrated with an AWGR to create a space switch will be briefly introduced.

2. Integration Platforms

One of the main issues in integrating various photonic waveguide elements together is to match up the different waveguides at the interface between the sections. It is generally important to have no reflections and very low loss on transmission. Perhaps three or more waveguide types need to be abutted in such a 'seamless' manner to integrate all of the desired functionalities within some PIC. Several approaches have been used and the key ones will be reviewed in the presentation [5]. These include 1) a vertical twin guide structure, 2) a butt-joint regrowth approach, 3) a selective area growth technique, 4) an offset quantum-well approach, 5) a dual quantum-well modification of that, and 6) a quantum-well intermixing approach.

In the lateral direction there are also many different possible waveguiding geometries that are more or less desirable for various PIC elements. These include surface ridge waveguides, buried heterostructures, buried ribs, deeply etched ridges, and the transitions between these. Many tradeoffs exist. High-index-contrast enables sharp bends, but it tends to bring higher losses. Active regions generally require high-quality epitaxial interfaces for low non-radiative recombination and high reliability, but this limits the fabrication options.

3. Widely-Tunable Integrated Transmitters

As mentioned in the introduction, many of the basic integration techniques were developed in the process of developing the SGDBR structure in the 1990s, and these were refined by Agility Communications, Inc., which was formed in 1998 to commercialize the technology. Figure 1(a) illustrates an early SGDBR-SOA-EAM transmitter developed by Agility that used the offset quantum-well integration platform [6]. Figures 1(b,c,d,&e) show various aspects of a recent UCSB SGDBR-SOA-TW/EAM transmitter that incorporates a 'dual QW' wafer structure and a velocity-matched traveling-wave (TW) electrode structure to provide more-efficient, higher-bandwidth modulator performance [7]. Good 40 Gb/s eyes that gave error-free operation over a wide wavelength range are shown.

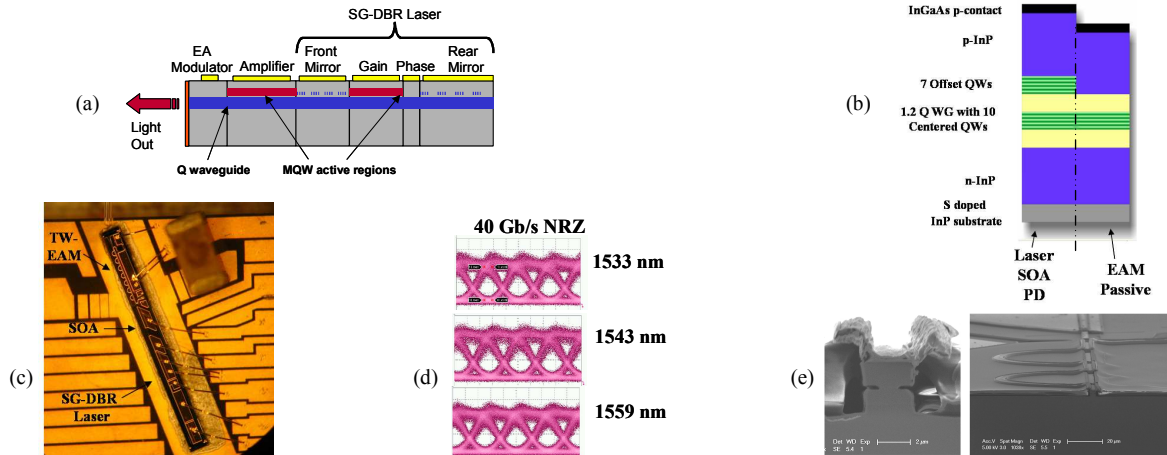


Fig. 1. (a) Vintage SGDBR-SOA-EAM using off-set QW platform [6]; (b) dual-QW layer structure; (c) mounted SGDBR-SOA-TW/EAM; (d) digital eyes across at several wavelengths; (e) TW/EAM waveguide cross section and top-view perspective [7].

Analogous transmitters have also been constructed with Mach-Zehnder modulators in place of the EAMs. These have the advantage of having manageable chirp, although in InP there is always a mix of absorption and phase modulation that complicates the matter. Nevertheless, very good results have been reported [8].

4. Integrated Widely-Tunable Transceivers/Wavelength Converters

Figure 2 illustrates a single-chip all-photonic transceiver (operated as a wavelength converter) in which an input signal of nearly arbitrary data rate and various intensity modulation formats over some wavelength range can be converted (and regenerated to some extent) to a desired output wavelength [9]. The transmitter stage is similar to that shown in Fig. 1; the receiver stage consists of a two-stage high-gain, high-saturation-power SOA preceding a high-saturation current photodiode (PD). The photocurrent from the PD directly modulates the TW-EAM of the transmitter, so that no rf needs to be coupled on or off of the chip, and no optical filters are necessary. A separate absorber is used for data monitoring if so desired. It was developed for use in all-optical networking experiments.

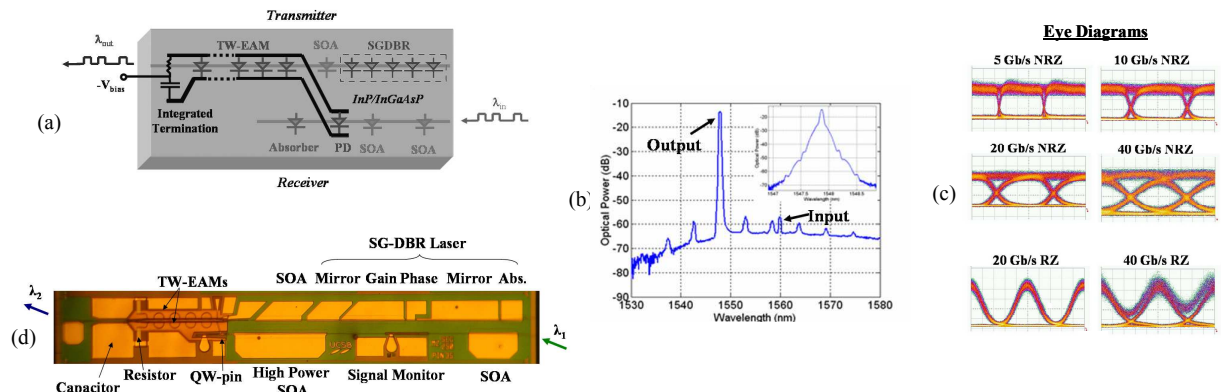


Fig. 2. (a) Functional schematic of all-photonic transceiver; (b) unfiltered unmodulated (and inset modulated @ 40Gb/s - expanded across 1.7 nm) output spectrum; (c) digital eyes for RZ and NRZ modulation from 5-40 Gb/s; (d) photo of transceiver with SGDBR-SOA-TW/EAM transmitter and two-stage SOA—PD receiver[9].

Figure 3 illustrates a different widely-tunable 40 Gb/s transceiver operated as a wavelength converter (WC). In this case the transmitter section uses a traveling-wave Mach-Zehnder modulator (TW/MZM) instead of a TW/EAM [10]. Such devices primarily use phase modulation instead of absorption modulation, and they can be designed to manage chirp, so that transmission distances can be greatly extended. In fact, in this case the TW/MZM uses a series-connected design for higher impedance, so that the photocurrent can generate a higher electric field for better efficiency.

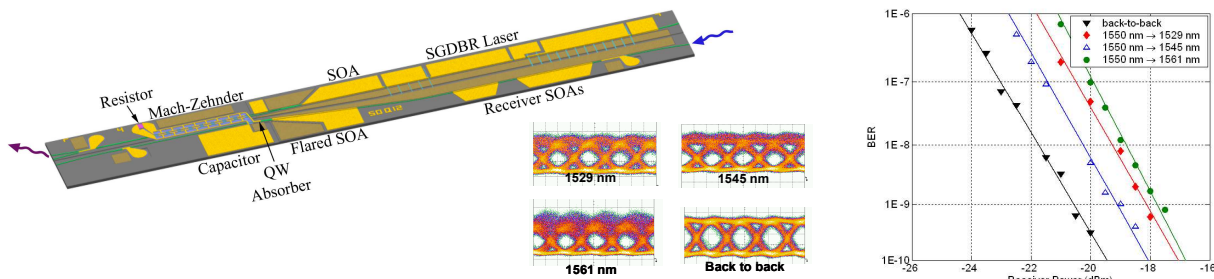


Fig. 3. All-photonic widely-tunable wavelength converter that integrates an SGDBR-SOA-TW/MZM transmitter with a two-stage SOA-PD receiver. NRZ-Eye diagrams and bit-error-rate @ 40Gb/s illustrated for 1550 nm input data across 32 nm. Power penalties similar for different input wavelengths. Equivalent circuit is similar to Fig. 2 (a) except MZM diodes connected in series push/pull across PD [10].

5. A Monolithic Tunable Optical Router

Figure 3 illustrates a chip which provides the fabric of an 8 x 8 all-photonic packet-switch that operates to 40 Gb/s. It uses nonlinear cross-phase modulation in SOAs within a Mach-Zehnder wavelength converter structure as shown in the figure instead of the photocurrent-driven transceivers discussed in Section 4 [11]. In one of the most complex PICs ever created, 8 of these wavelength converters feed an 8 x 8 AWGR that together enable any of 8 incoming channels to be switched to any of 8 output channels by controlling the wavelength switching in the wavelength converters. In this case quantum-well intermixing is used for different bandgaps, and three different waveguides are employed in the different sections: surface-ridges, deeply-etched ridges, and buried ribs [12].

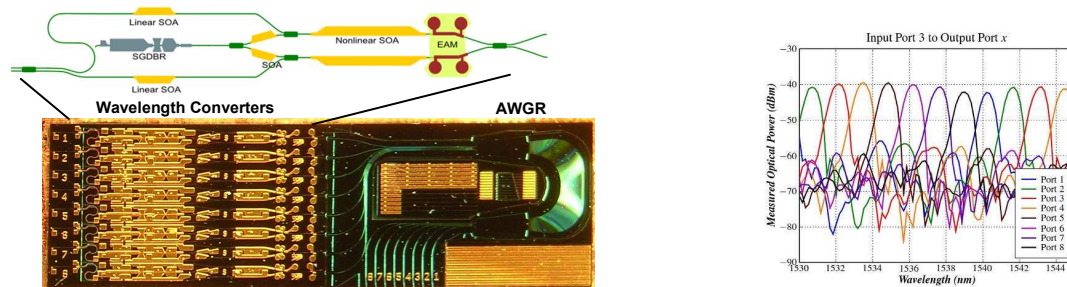


Fig. 3. (Left) Photo of 8 x 8 tunable optical space switch consisting of 8 wavelength converters integrated to an 8 x 8 AWGR. Above the photo is a schematic of the tunable SOA-based wavelength converter including EAM label re-write. (right) AWGR filter characteristic.

6. Acknowledgements

This work was supported by DARPA via the DODN project.

7. References:

- [1] See for example: http://www.semiconductor-today.com/news_items/NEWS_2007/SEPT_07/JDSU_100907.htm
- [2] R. Nagarajan, C.H. Joyner, R.P. Schneider, et al, "Large scale photonic integrated circuits," *IEEE-JSTQE*, **11** (1) 50-65 (2005).
- [3] D.F. Welsh, F.A. Kish, R. Nagarajan, C.H. Joyner, et al, "The realization of large-scale PICs ...," *IEEE-JLT*, **24** (12) 4674-4683 (2006).
- [4] V. Jayaraman, Z. Chuang, L. Coldren, "Theory, design, and performance of extended tuning range ...," *IEEE-JQE*, **29** (6) 1824-1834 (1993).
- [5] For a discussion & refs. see: J.W. Raring & L.A. Coldren, "40 Gb/s widely-tunable transceivers," *IEEE-JSTQE*, **13** (1) 3-14 (2007).
- [6] Y. Akulova, G. Fish, et al, "Widely-tunable EA-modulated SGDBR laser," *IEEE/LEOS Annual Meeting*, paper MM3, La Jolla (2001).
- [7] M. Dummer, J. Klamkin, J. Mack, L. Coldren, "Widely-tunable 40 Gb/s transmitter ...," *Proc. IPNRA*, paper IMA2, Boston (2008).
- [8] A. Tauke-Pedretti, M. Sysak, et al, "40 Gb/s series-push-pull MZ-transmitter on a dual QW ...," *IEEE-PTL*, **18** (18) 1922-1924 (2006).
- [9] M. Dummer, J. Klamkin, A. Tauke-Pedretti, L. Coldren, "A bit-rate transparent ... integrated WC," *ECOC'08*, Th.2.C.1, Brussels, (2008).
- [10] A. Tauke-Pedretti, M. Dummer, et al, "Separate absorption and modulation MZ-WC," *IEEE-JLT*, **26** (1) 91-98 (2008).
- [11] V. Lal, et al, "Monolithic WCs for high-speed packet-switched optical networks," *IEEE-JSTQE*, **13** (1) 49-57 (2007).
- [12] S. Nicholes, M. Mašanović, et al, "Advanced epitaxial techniques for high-density PICs in InP," *IPRM'09*, Newport Beach, (May, 2009).



Technology and Applications for InP-based Photonic ICs

OIDA
December 1, 2009

Larry A. Coldren

with contributions from

S. Nicholes, L. Johansson, S. Ristic, E. Norberg, R. Guzzon,
& other UCSB students, researchers, and faculty

ECE and Materials Departments

University of California, Santa Barbara, CA 93106

coldren@ece.ucsb.edu

State-of-the Art Electronic Terabit IP Router

UCSB

- **Problem:** Bandwidth demands scaling faster than both silicon and cooling technologies

Maximum configuration for CRS-1: 92 Tbps

→ 72 line card shelves 8 fabric shelves



Cisco CRS-1 Router

Some of our Earliest and Latest Functional PICs

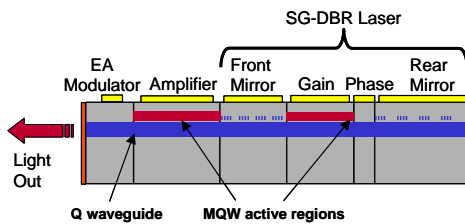
SGDBR-SOA-Modulator PIC (the earliest)

UCSB

SGDBR X: Foundation of PIC work at UCSB

"Multi-Section Tunable Laser with Differing Multi-Element Mirrors," US Patent # 4,896,325 (January 1990)

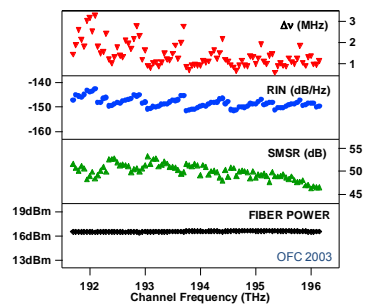
(UCSB'90-- → Agility'99-'05 → JDSU'05→)



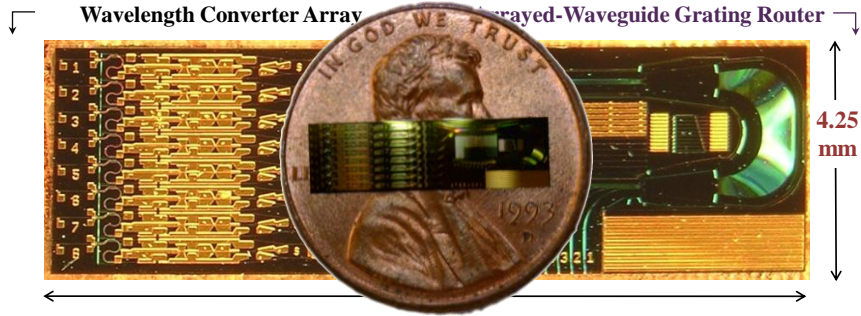
6 section InP chip

- SOA external to cavity provides power control
- Both EAM and MZ modulators integrated

JDSU-ILMZ recently released as TOSA



Recent PIC: MOTOR Chip (the latest)

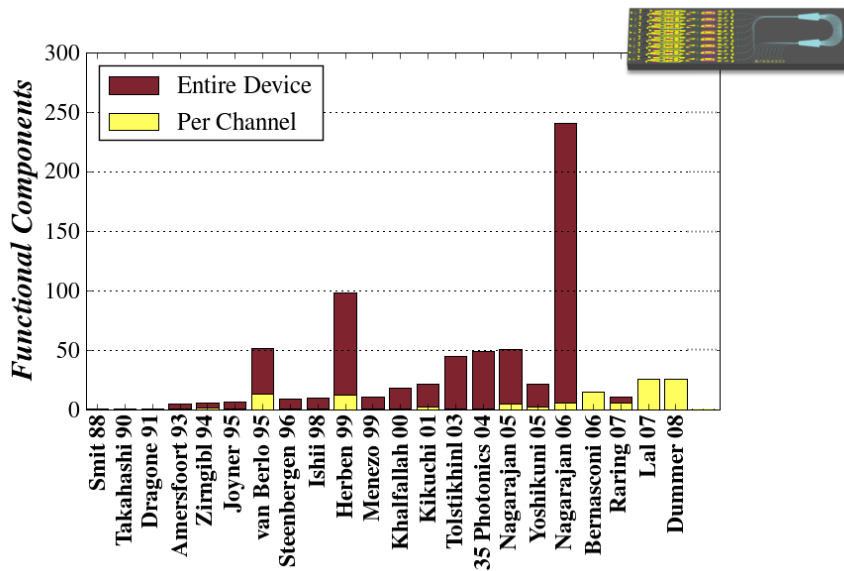


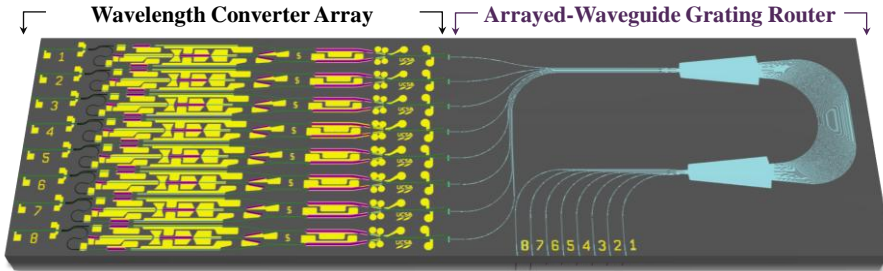
- A monolithic tunable optical router (MOTOR) chip to function as the switch fabric of an all-optical router
 - Line rate: 40 Gbps / channel
 - Total capacity: 640 Gbps
 - Error-free operation
- Photonic integration technologies designed for high-yield, large-scale applications



Steven C. Nicholes, M. L. Mašanović, E. Lively, L. A. Coldren, and D. J. Blumenthal, *IPNRA '09*, Paper IMB1 (July, 2009) also *JLT*, (Jan. 2010) in press.

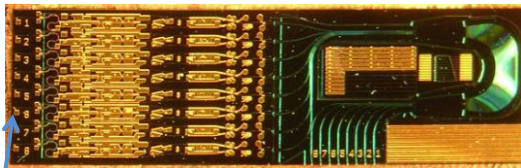
Leading Edge of Monolithic Integration





Benefits of integrated solution:

Size	<ul style="list-style-type: none"> • Smaller device footprint • Smaller rack space for increased bandwidth
Power	<ul style="list-style-type: none"> • No power required in passive AWGR (free switching—no transistors) • Lower power consumption with all-optical approach
Cost	<ul style="list-style-type: none"> • Reduced packaging and system costs • Fewer fiber alignments
Performance	<ul style="list-style-type: none"> • Increased reliability



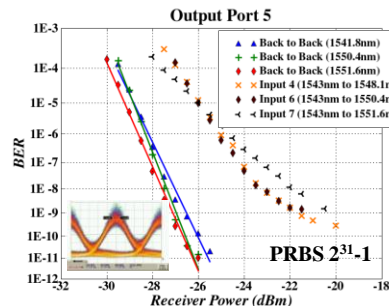
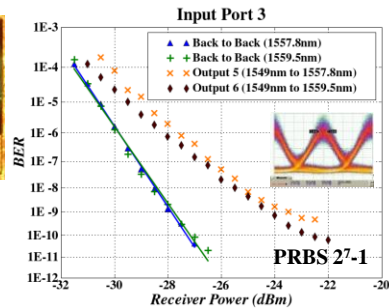
PRBS Data at λ_1 IN

Data at λ_2 OUT to BERT

Key Results: WC

- BER 1E-9 achieved for conversion and routing
- Power penalty (BER 1E-9):
 - 10 Gbps NRZ **1.3 dB**
 - 40 Gbps RZ:
 - PRBS 2⁷-1 **3.5 dB**
 - PRBS 2³¹-1 **4.5 dB**
 - Extinction **11.2 dB**

No AR coatings; low P_{sat} Preamp SOAs

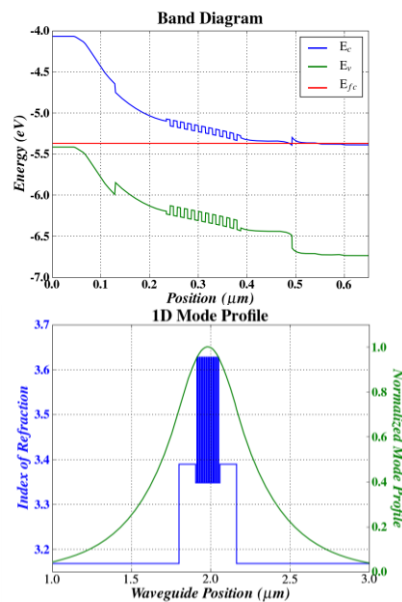


Integration Strategy

Integration Platform

UCSB

- Strategy:
 1. Centered MQW base structure
 2. Quantum-well intermixing for active/passive definition
 3. Single blanket cladding regrowth
- Trade-offs:
 1. Limited total number of regrowths → need multiple waveguide architectures
 2. Efficient active diodes → higher passive losses due to Zn in cladding
 3. Efficient high-gain, low-saturation power elements → nonlinear preamplifiers
 4. Polarization sensitivity

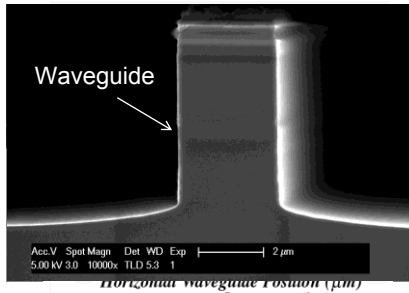


Multiple Waveguide Architectures

- Need multiple waveguide designs to integrate diverse range of components



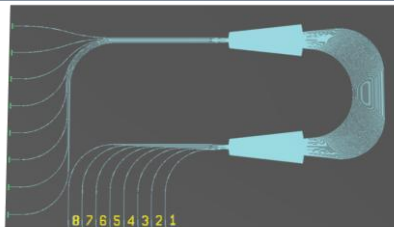
Waveguides



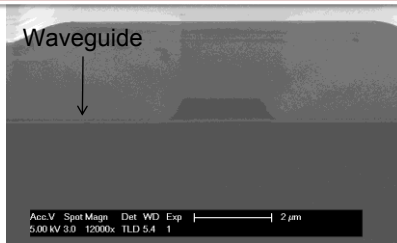
Deep Etched Ridge

- Ridge defined through waveguide cladding and stops at waveguide layer
 - Dry etch only
 - Dry etch selective "cleanup" wet etch
- Sharp bends possible
- Wet etch is crystallographic → no bends over 15°

Multiple Waveguide Architectures



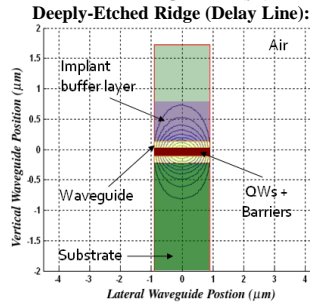
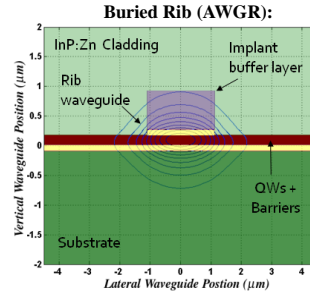
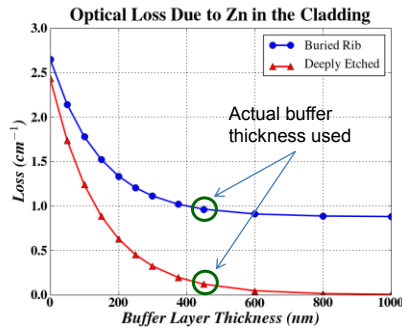
Need short mode transition elements to maximize coupling between waveguide regions



- Partial etch into upper waveguide prior to cladding regrowth, which buries it
 - Low index contrast
 - Larger footprint
 - Dry etch due to high-angle bends

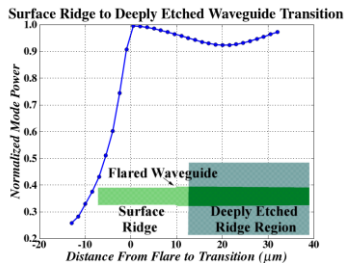
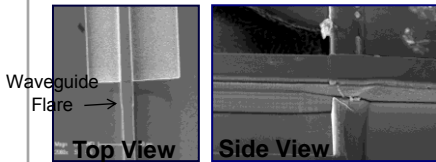
Horizontal Waveguide Position (μm)

- Use QWI implant buffer to provide undoped setback layer between optical mode and Zn atoms
- Simulated *reduction* in optical loss:
 - Deeply-etched Buried rib
 - No lateral mode interaction with Zn doped cladding



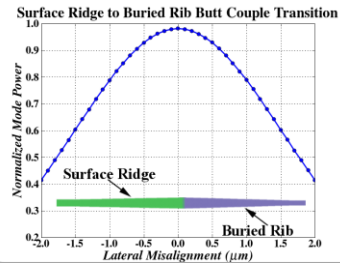
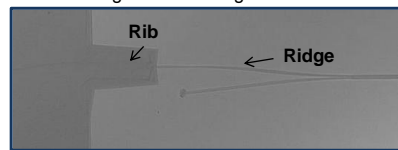
Surface-to-Deep Ridge Transition

- “Mode matching” transition [1]
 - Surface ridge flares and tapers before deep ridge section
 - No lateral misalignment issues



Surface-to-Buried Rib Transition

- Flared/tapered butt-couple transition
 - Surface ridges flares and butt couples to tapering rib waveguide
 - Fairly tolerant to lateral and longitudinal misalignment

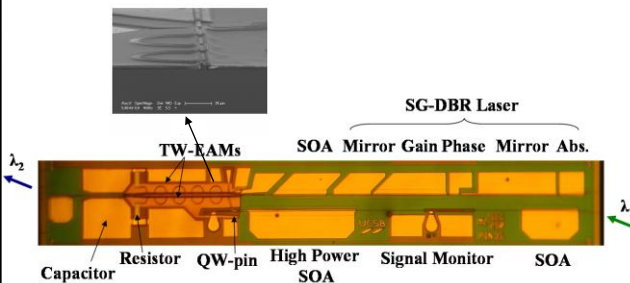
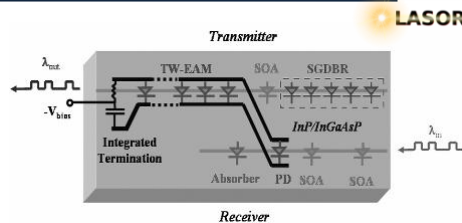


Other PICs

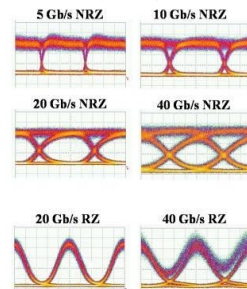
Transceiver/wavelength-converter: 2-stage-SOA-PIN & SGDBR-TW/EAM

UCSB

- Data format and rate transparent 5-40Gb/s
- No filters required (same λ in and out possible)
- On-chip signal monitor
- Two-stage SOA pre-amp for high sensitivity, efficiency and linearity
- Traveling-wave EAM with on chip loads
- Only DC biases applied to chip—photocurrent
- directly drives EAM
- 40 nm wavelength tuning range



Eye Diagrams



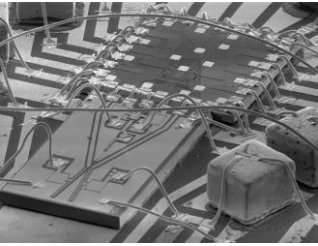
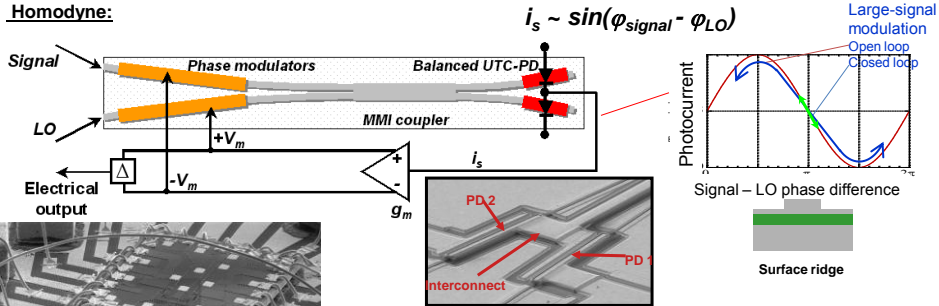
M. Dummer et al. Invited Paper Th.2.C.1, ECOC 2008.

Coherent Receiver for Phase Modulated Signals

OPLL—NEED for PICs & close integration/EICs



Homodyne:



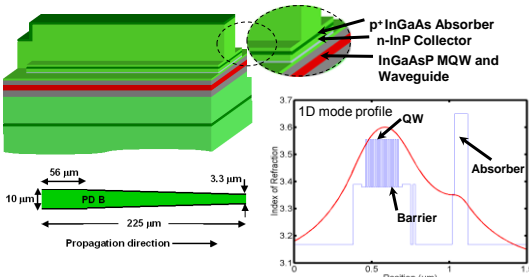
Close collaboration with NGST

- Signal mixed with LO to demodulate optical phase
 - Detected photocurrent signal-LO phase difference
 - Response is sinusoidal
- With feedback, output reduced by the loop gain: $1/(1+T)$
 - Hybrid integrated EIC provides amplification
 - Operation within linear regime
 - NEED VERY SHORT FEEDBACK PATH

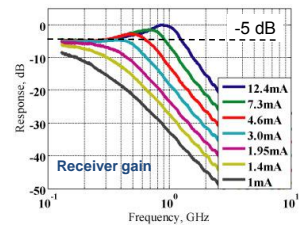


L.A. Johansson, H.F. Chou, A. Ramaswamy, L. A. Coldren, and J.E. Bowers, "Coherent optical receiver for linear optical phase demodulation," *Proc. MTT-S Microwave Sym.*, Tu3D-01 (June, 2007).

Integrated Coherent Receiver Results

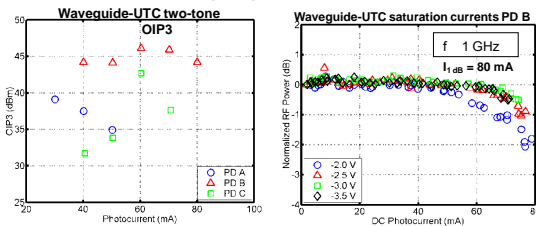


1.4 GHz OPLL BW—Loop delay limited
SFDR = 131 dB-Hz^{2/3} @ 300 MHz

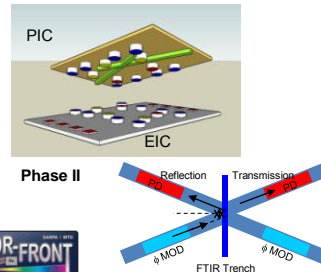


A. Ramaswamy, et al, *JLT*, 26 (1) pp209-216 (Jan., 2008).

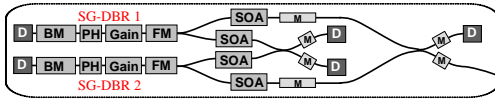
→ Record OIP3 for waveguide PD
46.1 dBm at 60 mA (PD B)



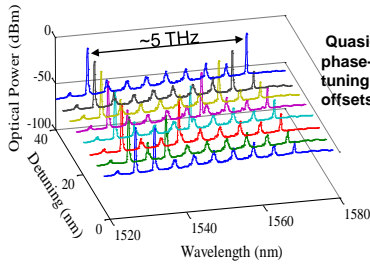
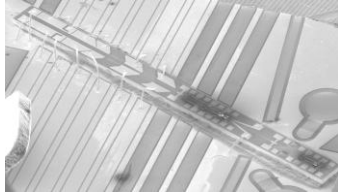
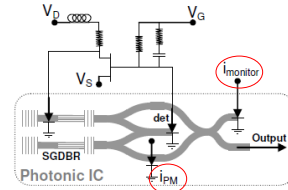
J. Klamkin, et al, *JSTQE*, 44 (4) pp354-359 (Apr., 2008).



Phase-Locked SGDBRs/OPLL

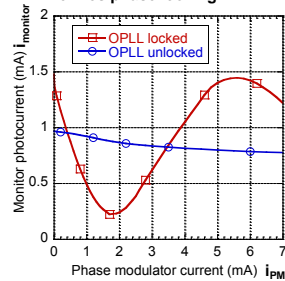


D Photodetector
M Modulator



Quasi-continuous phase-locked digital tuning up to 5 THz offsets possible

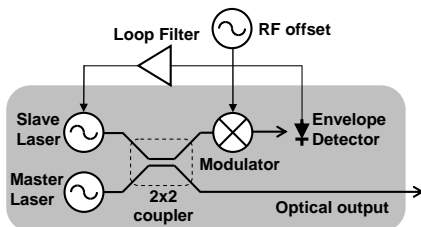
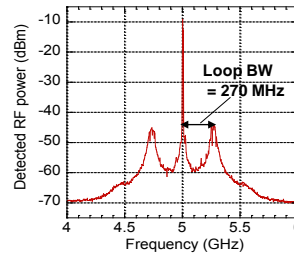
Coherent interference at monitor verifies phase locking



S. Ristic, et al, *OFC '09*, PDPB3, San Diego, (Mar., 2009)

OPLL'd SGDBRs—Heterodyne

- ▶ EA modulator used to generate 5 GHz offset frequency
- ▶ Slave laser locked to modulation sideband
- ▶ Coherent beat observed
 - 0.03 rad² phase error variance in +/-2GHz BW estimated from captured spectrum
- ▶ Up to 20 GHz offset locking demonstrated

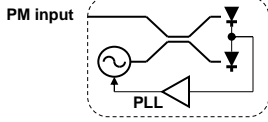


Ristic et al: *JLT* v.28 no.4, 2010, in press, also at *MWP2009*, paper Th 1.5



Additional OPLL Applications/Challenges

Coherent receiver



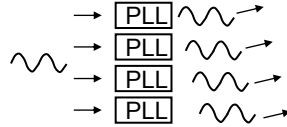
Costa's Loop for BPSK, QPSK demodulation

No requirement for complex DSP circuits

Challenge: Develop receivers for high speed (>100Gbaud) or high constellations (n-QAM)

Matched with development of coherent sources

LIDAR



Very rich/challenging area

Locking tunable lasers

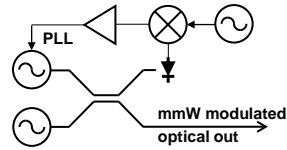
Arrays of locked OPLLs

Swept microwave reference

Time / Phase encoding of directed output

Need for rapid scanning and locking rates

mmW / THz generation



Locking of two tunable lasers

Requires Integration of high-speed UTC photodiode

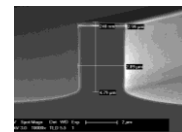
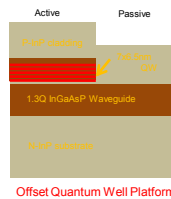
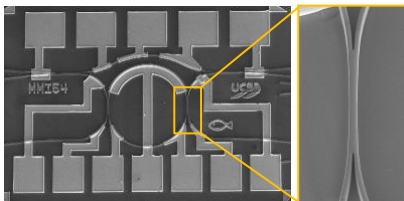
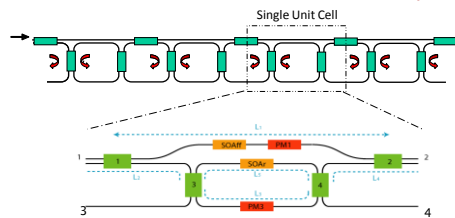
Speed determined by UTC photodiode and feedback electronics: Can be very high

Combined with antenna designs for complete TRX links with free-space path

All require close integration of electronics with photonics

Programmable Photonic Lattice Filters

- Demonstrate programmable poles and zeros from a single unit cell that can be cascaded to form complex lattice filters
- Incorporate SOAs and Phase Modulators to control filter parameters



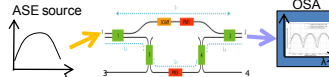
See E.J. Norberg, R.S. Guzzon, S. Nicholes, J.S. Parker, and L. A. Coldren, "Programmable photonic filters fabricated with deeply etched waveguides," *IPRM '09*, paper TuB2.1, Newport Beach (May, 2009)

Single Unit Cell – Isolated Zero

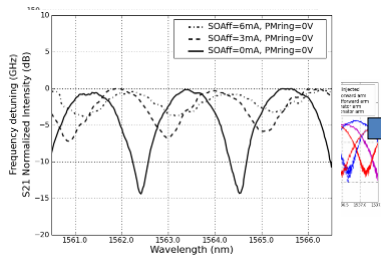
- FIR filter response synthesized with MZI
 - Ring SOA reversed bias – no optical feedback from resonator
- SOA on feed forward arm used to tune zero amplitude
 - 14dB maximum extinction ratio (ER)
 - Parasitic frequency shift due to current injection in SOA
 - Use phase modulators (PM) to align filter response
- Phase modulators used to tune filter in frequency
 - 270GHz (110 of FSR) total tunability of MZI response



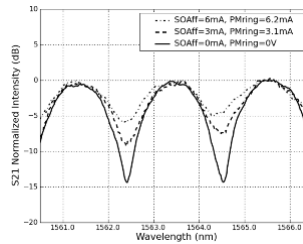
SEM of Single Unit Cell Filter



Schematic of measurement



S21 MZI response depends on current (Wavelength)

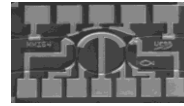


S21 MZI response – with PM

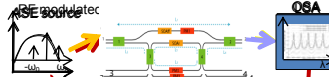


Single Unit Cell – Pole and Zero

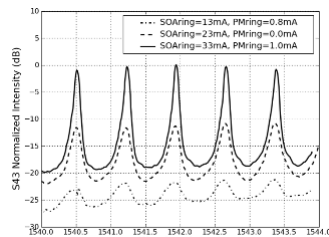
- IIR filter response synthesized with ring resonator
 - S43 or S21 with feed forward SOA reversed biased
- SOA in ring resonator used to tune pole amplitude
 - 18dB of ER, FWHM 0.067nm (7.9GHz), Q 23,000, 50 GHz frequency tunability
- RF filter response measured with Lightwave Component Analyzer
 - Characteristic π phase shift
- Enhancing ER by utilizing both zeros and poles
 - 25dB extinction by placing zero in between poles



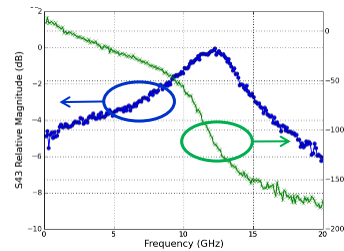
SEM of Single Unit Cell Filter



Schematic of measurement



S43 Pole response tuned in amplitude

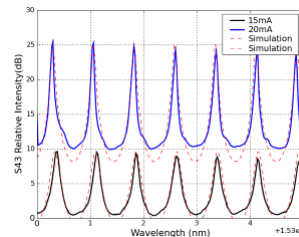
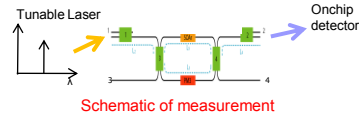


S43 Pole response

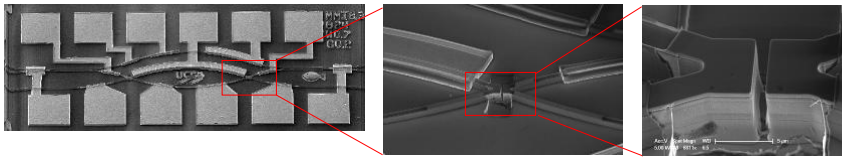


Flattened Ring Unit Cell

- Resonator in/out coupling with Etched Beam Splitters (EBS)
 - EBS coupled ring resonator in InGaAsP demonstrated for the first time
- Pole response
 - E.g. Biased 20mA (I_{th} 23mA)
 - FWHM of 7GHz, Q 27500
- EBS power splitting ratio
 - R 55 60 , T 2.9 3.2
 - Back calculated from resonator response and measured relative splitting ratio



Measured and Simulated Resonator Pole Response – Varied Ring SOA Current (curves shifted for clarity)



Summary

- Illustrated medium-scale highly-functional PIC integration technology requiring only one blanket regrowth.
 - Indicated usefulness of quantum-well intermixing for integrating high-confinement active regions with low-loss passive regions.
 - Demonstrated efficient, robust techniques to integrate very different lateral waveguides together.
- This technology provided largest and most complex PIC ever (at least for UCSB).
 - Performance adequate for many digital photonic switching functions
 - Prior work has shown that the addition of one more blanket regrowth can greatly enhance the performance of such PICs
- Illustrated other functional InP-based PICs
 - All-photonic transceivers using photocurrent-driven modulators
 - Coherent receiver using an optical phase-locked loop for phase-modulated rf-photonics
 - Locking of SGDBRs for mmW - THz generation using an OPLL other possibilities
 - Programmable photonic lattice filters

I. PIC Technology and Devices

B. Wavelength Converter, Routing, and Packet Switching

Advanced photonic integrated technologies for optical routing and switching

Milan L. Mašanović^a, Emily Burmeister^a, Matthew M. Dummer^a, Brian Koch^a,
Steven C. Nicholes^b, Biljana Jevremović^a, Kim Nguyen^a, Vikrant Lal^a,
John E. Bowers^a, Larry A. Coldren^{ab}, and Daniel J. Blumenthal^a

^a Department of Electrical and Computer Engineering;

^b Department of Materials

University of California Santa Barbara, CA, USA

ABSTRACT

In this paper, we report on the latest advances in implementation of the photonic integrated circuits (PICs) required for optical routing. These components include high-speed, high-performance integrated tunable wavelength converters and packet forwarding chips, integrated optical buffers, and integrated mode-locked lasers.

Keywords: Photonic integrated circuits, optical routers, wavelength converters, optical buffers, mode-locked laser

1. INTRODUCTION

Consumer demand for speed and bandwidth over the Internet Protocol (IP) and other networks is at an all-time high and is steadily increasing. The continued scaling of current commercial electronic routers requires increasing power consumption and footprint. All-optical packet switching and routing technologies^{1,2} hold the potential to provide more efficient power and footprint scaling with increased router capacity. The all-optical approach eliminates the need to convert input optical signals into the electrical domain, thus reducing the demand for electronic switch fabric capacity with increased throughput.

This paper covers the latest advances in photonic integrated circuit (PIC) optical packet switching and routing technologies investigated under the DARPA/MTO and Army DOD-N program sponsored LASOR project¹. The goal of this project is to demonstrate the world's first 1 Tbps capable label switched optical router. In the LASOR architecture, 40 Gbps optical packets are routed based on the packet's wavelength and 10 Gbps optical labels. Integration of the switching and routing function onto PICs allows for advanced routing functions to be realized in the optical domain while offering advantages of integration including reduced footprint and power requirements. Each PIC building block of the LASOR router uses advanced processing and epitaxial techniques to combine a large number of diverse components on-chip, including tunable lasers, amplifiers, detectors, and waveguide delays.

2. WIDELY TUNABLE ALL-OPTICAL PACKET FORWARDING CHIPS

The conversion of the input payload to a new wavelength and the encoding of the new optical labels for output packets are handled in LASOR optical router by a packet forwarding chip (PFC). The all-optical PFCs include a number of functions: (1) fast-switching and widely tunable lasers; (2) optically controlled gate used to convert the input data onto the CW laser signal; and (3) a modulator, required to write new labels preceding the outgoing labels.

To achieve fast wavelength tuning in excess of 40 nm, a sampled-grating DBR laser (SG-DBR) is incorporated into the PFC chips.

The optical gating functionality needed for wavelength conversion are achieved by one of two methods—carrier modulation through the use of non-linear effects in semiconductor optical amplifiers (SOAs) or electric field-based modulation through a photodiode-EAM interaction. Neither of these approaches require electronic data processing or amplification. In the carrier-modulated approach, the absorption of the input signal and the modulation of the CW output signal occur coincidentally at the same waveguide (coincident absorption and modulation—CAM, Figure 1). In the field-modulated approach, the absorption and modulation functions are

separate and occur at different waveguides (separate absorption and modulation—SAM, Figure 2). Although each scheme has certain advantages and disadvantages, both approaches have been successfully used to demonstrate error free 40 Gbps wavelength conversion and full packet switching.⁴⁻⁸

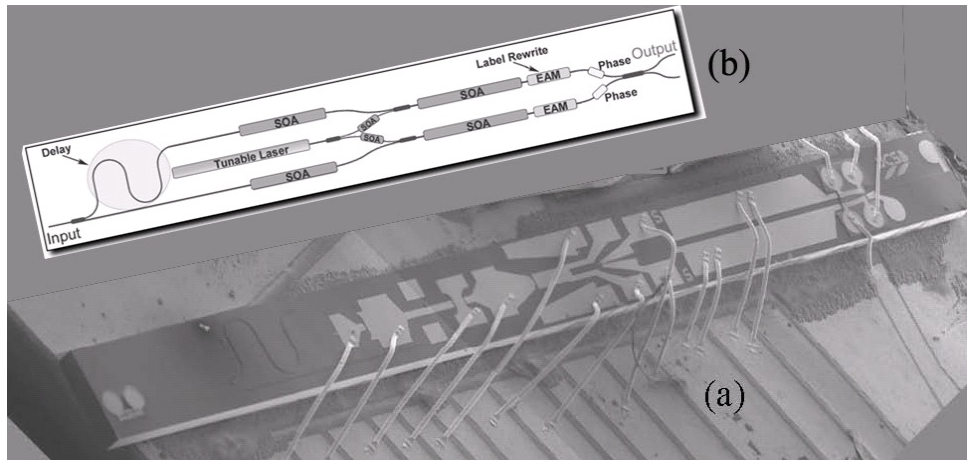


Figure 1 - 40 Gbps packet forwarding chip (a) Schematic representation of nonlinear SOA-based CAM device; (b) Optical micrograph of a fabricated CAM device.

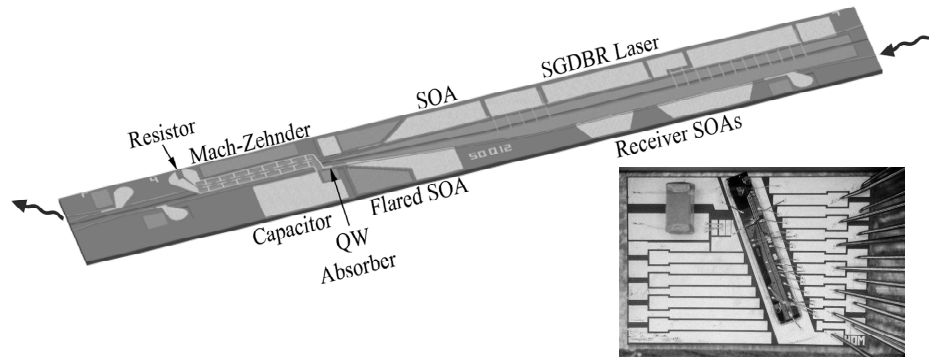


Figure 2 - 40 Gbps packet forwarding chip – Schematic representation of the Mach-Zehnder modulator field-modulated SAM device and an optical micrograph of a chip on carrier.

2.1 Coincident Absorption and Modulation PFCs

In our PFC design, wavelength conversion is accomplished by exploiting cross phase modulation effects in a differential delay Mach-Zehnder interferometer (MZI) (Figure 1). The device consists of a widely tunable SGDBR laser monolithically integrated with a MZI-SOA wavelength converter. The delay helps overcome bandwidth limitations stemming from the finite carrier lifetime in a saturated SOA. Additionally, a phase modulator is included in the MZI-SOA region for label rewrite functionality. Using this configuration, successful optical switching of 40 Gbps payloads and 10 Gbps labels has been accomplished.^{2,4} The overall device footprint is 7 mm x 0.5 mm. 40 Gbps RZ wavelength conversion has been demonstrated for CAM SOA-based devices using both SG-DBR lasers and AWGR-based discretely tunable lasers as a CW source.^{4,9}

In this configuration, an external filter is required to remove the input signal from the PFC output. However, a multistage MZI-SOA wavelength converter with on-chip filtering has also been demonstrated to eliminate this requirement.¹⁰ Although the CAM-based device affords robust packet forwarding with only 1 dB power penalty,⁴ it does involve a more complex epitaxial growth scheme.

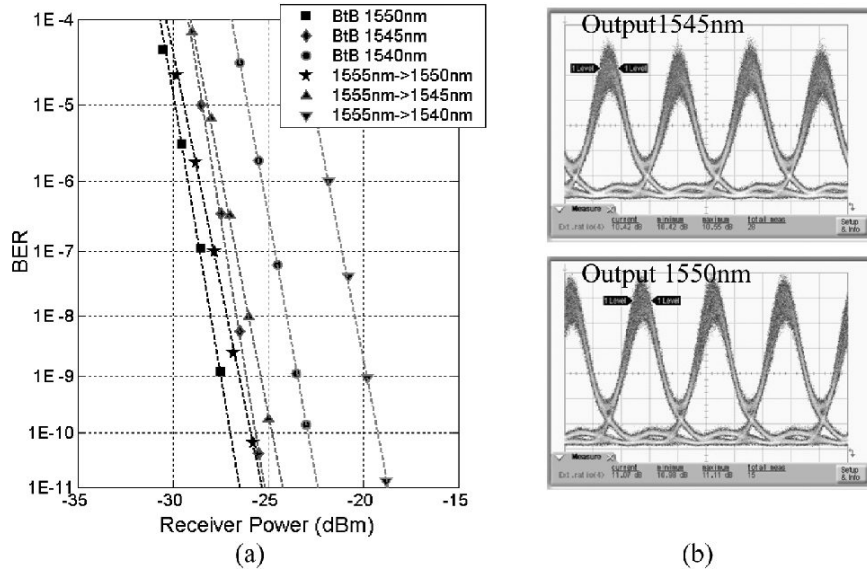


Figure 3 – CAM PFC: (a) Bit error rate results for 40 Gbps RZ wavelength conversion; (b) Eye diagram for an output wavelength of 1550 nm.

Since the structure requires both linear SOAs at the input (for input signal amplification) and nonlinear SOAs in the MZI (for cross phase modulation), a simple epitaxial base structure with a single active band edge cannot provide the most optimized components. Instead, post-growth techniques such as quantum well intermixing (QWI) or multiple epitaxial regrowths must be employed. For the device in Reference 4, the linear SOAs were realized in the initial base structure growth with quantum wells (QW) grown directly above the waveguide. Because the QWs are offset from the peak of the optical mode, the SOA saturation output power is increased, but its gain is decreased. The nonlinear SOAs in the MZI were realized by first removing the QWs and waveguide from the MZI and then using a butt-joint regrowth to grow a bulk SOA in their place. Alternatively, QWI can be used with a base structure consisting of QWs centered in the waveguide (for maximum gain and low saturation powers) to define the nonlinear MZI SOAs.¹¹ However, the preamplifier SOAs are then limited in length (and gain) in order to ensure that the input SOAs do not saturate and distort the input signal. Another advantage of QWI is that a second active band edge detuned from the as-grown gain peak can be defined to create more efficient phase modulators.

2.2 Separate Absorption and Modulation PFCs

Two different SAM PFC designs capable of 40 Gbps operation have also been demonstrated as part of the LASOR project.⁵⁻⁸ Both approaches combine a transmitter and receiver architecture on a single chip, shown in Figure 2 and Figure 5. The photocurrent in a receiver-side photodiode is used to drive a modulator on the transmitter side of the chip using a traveling wave electrode without any need for electrical amplification. One advantage of separating the absorption and modulation regions is that the need for output filtering of the input signal is eliminated.

The first design approach uses a Mach-Zehnder modulator (MZM) on the transmitter side. MZMs are an attractive option due to their ability to produce zero or negative chirp, high extinction ratios, and short gate opening times. Operating the MZM in a series-push-pull fashion places the two arms of the Mach-Zehnder in series along the microwave signal path, effectively halving the devices capacitance and providing an increase in bandwidth. With this approach, wavelength conversion across the 32 nm laser tuning range showed less than a 2.5 dB power penalty (Figure 3).⁵ Furthermore, this device allows conversion back to the input wavelength (which is not possible with the CAM device) with no increase in power penalty.

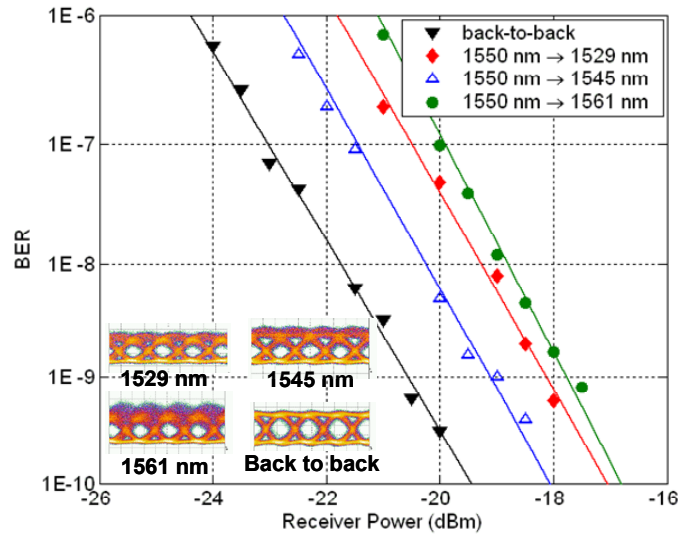


Figure 4 – Bit error rate measurements for 40 Gbps RZ input data for the Mach-Zehnder SAM wavelength converter

As designed, this device does not include an EAM for label encoding and thus cannot be used as a PFC. However, the platform used for this device is optimized for monolithic integration of a wide variety of components so an EAM could be included for 10 Gbps label writing in future designs.

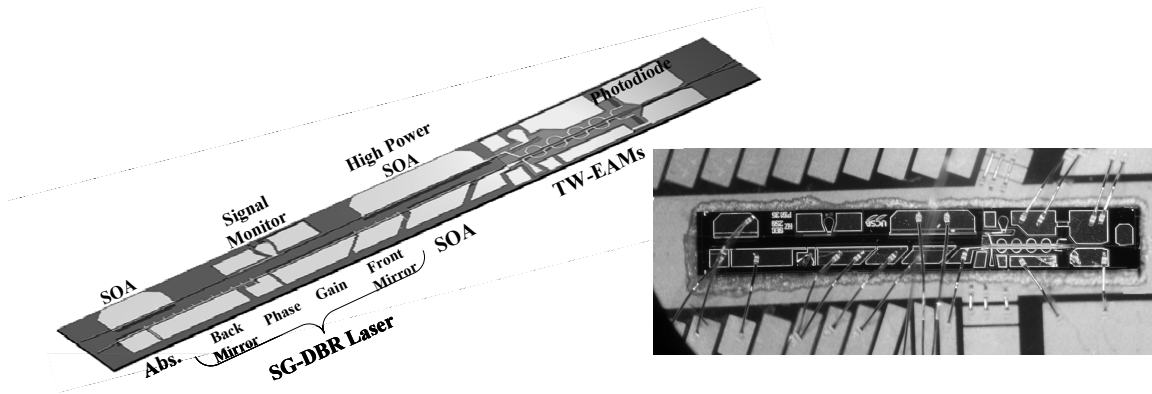


Figure 5 - 40 Gbps packet forwarding chip – Schematic representation of the traveling wave EAM field-modulated SAM device and an optical micrograph of a chip on carrier.

The second SAM-based wavelength converter approach we investigated utilized a traveling wave (TW) EAM modulator on the transmitter side (Figure 5).^{6,7} The modulator structure (Figure 6) employs an undercut, deeply etched ridge waveguide with a thin intrinsic region. Undercutting the active region provides a significant reduction in diode capacitance without the increase in series resistance that would accompany a narrower, lithographically defined ridge width. Furthermore, by deeply etching through the waveguide, there is a reduction in fringing capacitance to ground. The traveling wave electrode has also been optimized by using a periodically loaded microstrip lines, as shown in Figure 7, designed to velocity match the electrical and optical waves along the modulator. This design increases the characteristic impedance by a factor of two to 40 Ω , improves the return loss by 10 dB at 20 GHz, and provides an optical bandwidth of 30 GHz for a 400 μm device.⁸

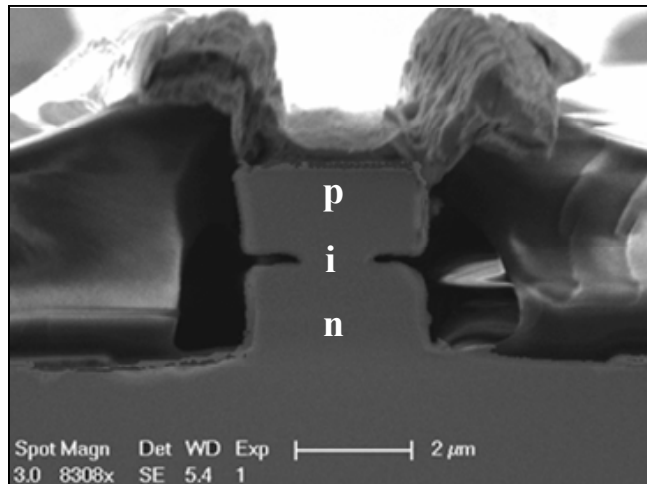


Figure 6 – Travelling wave modulator cross section, showing the undercut waveguide design

Compared to the CAM and SAM-MZM based wavelength converters described above, the TW-EAM wavelength converter demonstrates true bit rate transparency up to 40 Gbps in both RZ and NRZ data formats⁶. Using a bias of -3.8 V on the modulator, NRZ output extinction ratios were 8.9, 9.4, 9.5, and 8.1 dB for 5, 10, 20, and 40 Gbps data rates, respectively. For RZ data rates of 20 and 40 Gbps and a modulator bias of -4.5 V, output extinction ratios of 11.5 and 10.8 dB were measured, respectively. This wavelength converter design was also extended to include 10 Gbps label encoding by incorporating a second TW-EAM on-chip, making the device a true packet forwarding chip.

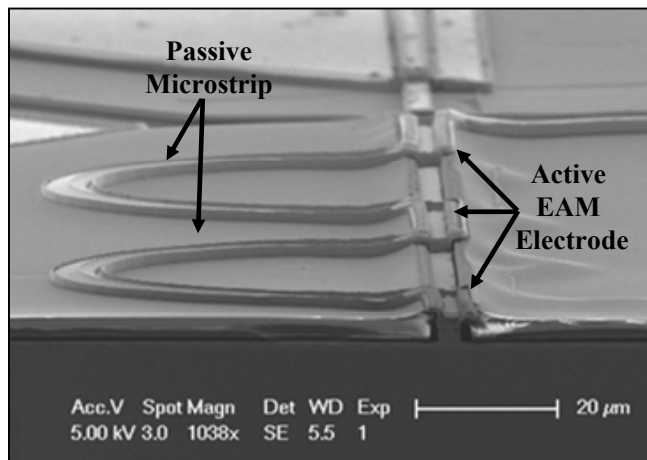


Figure 7 - Periodically loaded microstrip lines, designed to provide better matching in group velocities between the optical and electrical signals

The results of packet forwarding experiments using TW-EAM PFCs will be reported in detail elsewhere, but packet recovery rates of 100% for simultaneous conversion of payloads and headers has been achieved.

In addition to bit-rate transparency, the TW-EAM PFC has a number of advantages. First, it offers a smaller overall device footprint (4.1 mm x 0.55 mm). Second, it requires only a single blanket p-type cladding regrowth. However, the fabrication process for the TW-EAM is more complex than that of the CAM device (due to the undercut modulator and the incorporation of integrated resistors and capacitors) and it also demonstrates a smaller input power dynamic range.

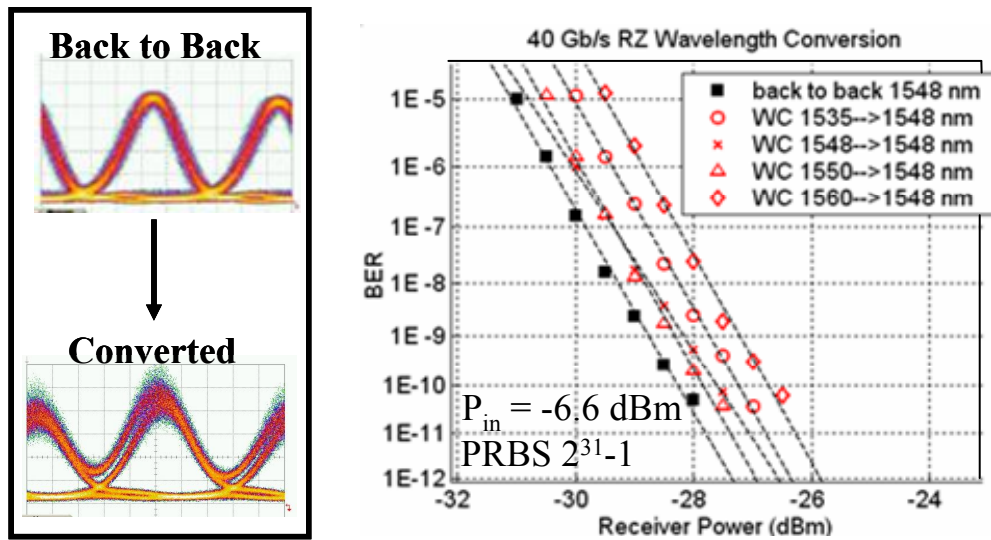


Figure 8 - Bit error rate measurement results for 40 Gbps RZ input data for the traveling wave EAM SAM wavelength converter

2.3 Integrated Optical Buffers

In order for all-optical routing functions to become viable, technologies for optical buffering to eliminate potential contention between packets must be developed and improved. Specifically, these optical buffers must be compact, easily integratable with other router functions, and bit-rate scalable to 40 Gbps or more. They should also be able to store packets of at least 40 bytes with guard bands of less than a few nanoseconds. Ideally, the buffer should be transparent to the packet length and provide the ability to easily vary storage times.

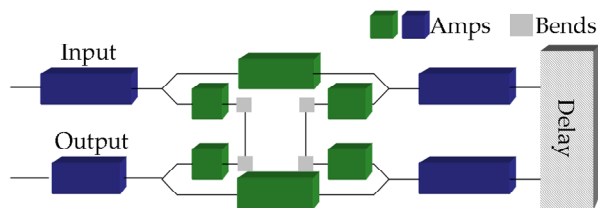
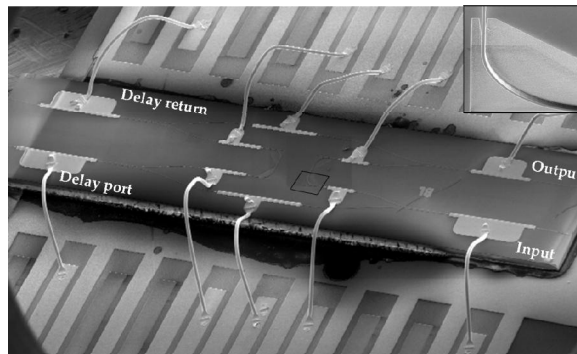


Figure 9 - Schematic of 2x2 switch with amplifiers (bottom) SEM image of the switch affixed and wire-bonded to a submount (top)

Most optical buffers attempt to meet these varied goals by using either feedback or feed-forward techniques with one-by-two or two-by-two switches, and while reasonable storage times have been demonstrated, no

practical integrated solutions have emerged.¹¹ We recently reported a recirculating buffer design capable of providing dynamically variable storage time based on a two-by-two InP-based switch.¹²

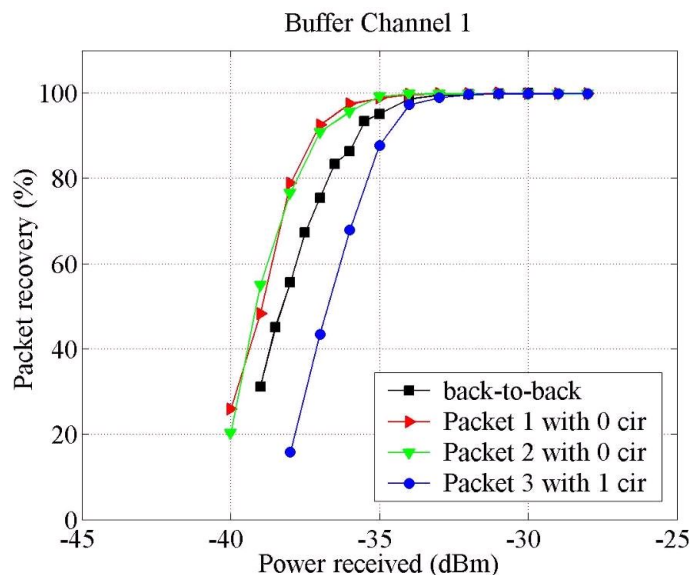


Figure 10 – Packet recovery rate as function of received power for buffer tested at 40 Gbps RZ

The device is based on an SOA gate matrix switch—one of the most promising options for recirculating buffers due to its inherent high extinction ratios and fast switching capacity (Figure 9). The amplifiers range in length from 200 μm for the switching amplifiers to 650 μm for the chip input/output and delay line input/output amplifiers. The overall gain is designed to be greater than the total loss by only a few dB so there is slight gain during the first few circulations until the amplified spontaneous emission (ASE) builds up to sufficiently high levels that it detracts from the signal gain.

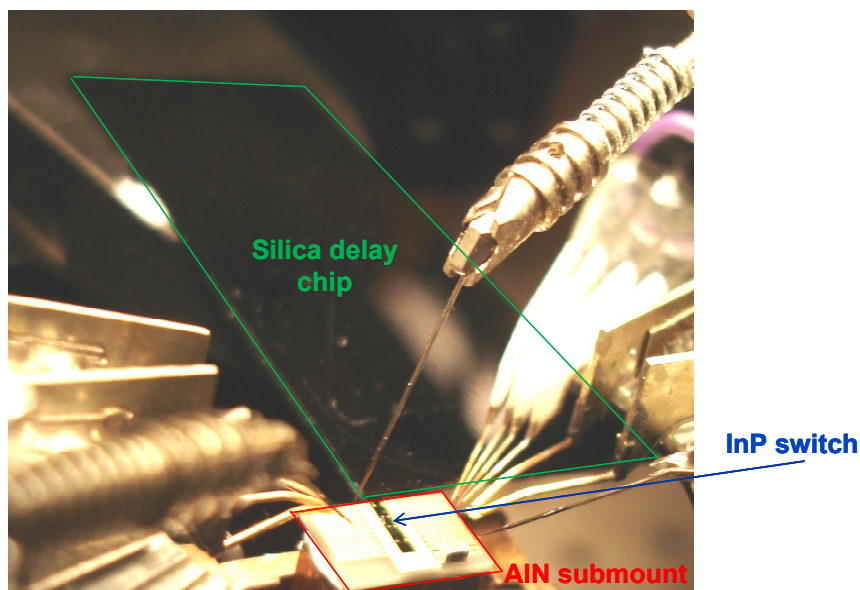


Figure 11 – Photograph of the optical buffer used in LASOR architecture – InP switch and the silica delay line chip

Additionally, to ensure that there are no crossing waveguides and that the chip input/output ports are on the opposite side of the chip as the delay line input/output ports, deeply etched 90° bends are included in the device. Since the rest of the device uses surface ridge waveguides, there is some loss associated with the transition to the deeply etched waveguide regions.

Error-free buffering has been demonstrated using this configuration for 40 Gbps data with less than a 1 dB power penalty and an input power dynamic range of greater than 15 dB.¹³ The delay loop was accomplished using 450 cm of fiber (or 23 ns). A more compact solution is possible by replacing the fiber delay with a silicon or silica-on-silicon waveguide delay chip, Figure 11. A hybrid optical buffer with a low loss silicon waveguide delay line and an integrated silicon evanescent gate matrix switch of wafer-bonded InGaAsP/InP amplifiers has also been demonstrated.¹⁴

Using an all-III-V device, packet recovery experiments using 40-byte packets at 40 Gbps have shown that up to 184 ns of storage is possible with a packet recovery of over 98% (Figure 10). For up to four circulations in the buffer, the dynamic range has been shown to be error-free over an input power range of 8 dB. Additionally, the buffer exhibited more than 40 dB extinction, an overall chip gain (input fiber to output fiber) of approximately 2 dB, and sub-nanosecond gate switching times. The main limitation of this method of optical buffering is the build-up of ASE in the recirculation loop due to the SOAs in the gate matrix. If a 5 nm filter is placed in the delay line, the maximum storage time is increased to 230 ns.

2.4 Monolithic Mode Locked Lasers

3R regeneration capabilities are essential for a high-performance, all-optical router. Mode-locked lasers (MLL) are an attractive choice for pulse shaping and optical clock recovery, offering significant jitter reduction, tunable output pulse widths, amplification, without the need for fast electronics.^{15,16} To our knowledge, we have demonstrated the first MLL with integrated SOAs and two, lithographically-defined DBR mirrors (instead of cleaved mirrors) for precise determination of the mode-locking frequency (Figure 12). The integration of SOAs onto the chip allow for lower input powers and higher output powers, without any significant deterioration of output pulse quality and a 10 dB increase in output power. Furthermore, this MLL design can be further integrated into more complex 3R PICs.

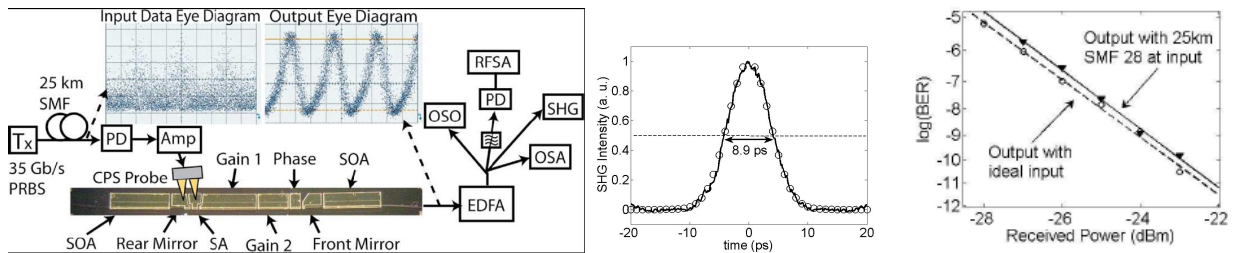


Figure 12 - (left) Experimental setup for hybrid clock recovery, with eye diagrams of the input and output signals and photograph of the device. The recovered clock appears to have high jitter because of poor OSO triggering. The actual jitter is 1.14 ps (middle) SHG trace of the output pulses. The solid line is the data and the open circles are a Gaussian fit (right) Bit error rates of the output clock that has been gated by the input data and sent to the receiver with a normal input and with input signal degradation

Both hybrid¹⁵ and all-optical¹⁶ optical clock recovery have been demonstrated using this PIC. In the hybrid case, the input optical data signal is converted to an electrical signal that is used to modulate the saturable absorber (SA) in the MLL. Using an intentionally degraded, 35 Gbps 2³¹-1 PRBS signal the device had a pulsewidth of 6.3 ps, an output power of 8.3 dBm, and over 12 dB of extinction. The jitter in the input signal was reduced from 2.23 to 1.14 ps. The output pulse width was measured with a second-harmonic-generation (SHG) autocorrelator and could be varied between 3.5 and 8.9 ps by changing the bias conditions (Figure 12). Bit error rates with the output clock gated by the input data and sent to a receiver with input signal degradation is also shown in Figure 12. Packet injection was also examined with a locking time of 800 ps to 3 ns depending on biasing conditions, indicating that packet clock recovery is also possible.

For all-optical clock recovery, the data is coupled directly into the input SOA adjacent to the rear mirror of the MLL. Over a 3 ps difference (between 6.7 and 10 ps) in the full width at half maximum (FWHM) of the output pulse could be achieved by tuning the bias conditions on the laser. All optical clock recovery with varying output pulse widths was thus

possible for a 35 Gbps RZ input data stream (Figure 9b). The relatively narrow output clock pulsewidth is ideal for gating applications.

Although the device was designed for 35.0 GHz operation due to system measurement limitations, it could easily be adjusted to perform at 40 GHz or more with a highly precise locking frequency. More interestingly, this design could be integrated directly with a PFC chip (either the CAM or SAM style) to create a fully integrated 3R regenerator.

2.5 Conclusions

Significant advances have been made towards the realization of highly integrated all-optical router PIC technology. Specifically, both SOA-based and field-effect-based wavelength converters with error-free 40 Gbps packet forwarding capability have been demonstrated. The TW-EAM based PFC also demonstrate bit-rate transparency up to 40 Gbps and can operate in both RZ and NRZ formats. We have also demonstrated the best performance to the best of our knowledge of optical buffering in an approach that is suitable for monolithic integration. Finally, we have made important advances towards a fully integrated 3R regenerator. Using an MLL with integrated SOAs, all-optical clock recovery with tunable output pulsewidths has been demonstrated. Since each of these technologies has been demonstrated in an InP platform, it may eventually be possible to integrate all of these building blocks simultaneously to realize a single-chip, all-optical router.

ACKNOWLEDGMENTS

This work is supported by DARPA and the Army under contract #W911NF-04-9-0001.

REFERENCES

1. Blumenthal, D., Olsson, B.-E., Rossi, G., Dimmick, T., Rau, L., Masanovic, M., Lavrova, O., Doshi, R., Jerphagnon, O., Bowers, J., Kaman, V., Coldren, L., and Barton, J., "All-optical label swapping networks and technologies," *Lightwave Technology, Journal of* **18**, 2058-2075 (2000).
2. Wolfson, D., Lal, V., Masanovic, M., Poulsen, H., Coldren, C., Epps, G., Civello, D., Donner, P., and Blumenthal, D., "All-optical asynchronous variable-length optically labelled 40 gbps packet switch," *Optical Communication, 2005. ECOC 2005. 31st European Conference on* **6**, 49-50 vol.6 (2005).
3. Gripp, J., Stiliadis, D., Simsarian, J. E., Bernasconi, P., Grange, J. D. L., Zhang, L., Buhl, L., and Neilson, D. T., "Iris optical packet router (invited)," *J. Opt. Netw.* **5**(8), 589-597 (2006).
4. Lal, V., Masanovic, M. L., Summers, J. A., Fish, G., and Blumenthal, D. J., "Monolithic wavelength converters for high-speed packet-switched optical networks," *Selected Topics in Quantum Electronics, IEEE Journal of* **13**, 49-57 (2007).
5. Tauke-Pedretti, A., Dummer, M., Sysak, M., Barton, J., Klamkin, J., Raring, J., and Coldren, L., "Separate absorption and modulation mach-zehnder wavelength converter," *Lightwave Technology, Journal of* **26**, 91- 98 (2008).
6. Dummer, M. M., Klamkin, J., Tauke-Pedretti, A., and Coldren, L. A., "A bit-rate-transparent monolithically integrated wavelength converter," in [*European Conference on Optical Communications (ECOC), Brussels Belgium*], (2008).
7. Dummer, M., Klamkin, J., Tauke-Pedretti, A., and Coldren, L., "40 gb/s widely tunable wavelength converter with a photocurrent-driven high-impedance tw-eam and sgdr laser," *Semiconductor Laser Conference, 2008. ISLC 2008. IEEE 21st International* , 145-146 (2008).
8. Dummer, M., Klamkin, J., Norberg, E., Raring, J., Tauke-Pedretti, A., and Coldren, L., "Periodic loading and selective undercut etching for high-impedance traveling-wave electroabsorption modulators," *Optical Fiber communication/National Fiber Optic Engineers Conference, 2008. OFC/NFOEC 2008.* (2008).
9. Bernasconi, P., Zhang, L., Yang, W., Sauer, N., Buhl, L., Sinsky, J., Kang, I., Chandrasekhar, S., and Neilson, D., "Monolithically integrated 40-gb/s switchable wavelength converter," *Lightwave Technology, Journal of* **24**, 71-76 (2006).
10. Summers, J., Masanovic, M., Lal, V., and Blumenthal, D., "Design and operation of a monolithically integrated two-stage tunable all-optical wavelength converter," *Photonics Technology Letters, IEEE* **19**, 1248-1250 (2007).

11. M. L. Mašanović, V. Lal, E. Skogen, J. Barton, J. Summers, J. W. Raring, L. A. Coldren, and D. J. Blumenthal, "Cross-phase modulation efficiency in offset quantum well and centered quantum well semiconductor optical amplifiers," *IEEE Photon. Technol. Lett.*, vol. 17, no. 11, pp. 2364–2366, (2005).
12. Burmeister, E., Blumenthal, D., and Bowers, J., "A comparison of optical buffering technologies," *Optical Switching and Networking* **5**(1), 10 - 18 (2008). Special Section: Photonics in Switching (2006).
13. Burmeister, E., Mack, J., Poulsen, H., Klamkin, J., Coldren, L., Blumenthal, D., and Bowers, J., "Soa gate array recirculating buffer for optical packet switching," *Optical Fiber communication/National Fiber Optic Engineers Conference, 2008. OFC/NFOEC 2008. Conference on*, 1-3 (2008).
14. Burmeister, E. and Bowers, J., "Integrated gate matrix switch for optical packet buffering," *Photonics Technology Letters, IEEE* **18**, 103-105 (2006).
15. Park, H., Mack, J. P., Blumenthal, D. J., and Bowers, J. E., "An integrated recirculating optical buffer," *Opt. Express* **16**(15), 11124-11131 (2008).
16. Koch, B. R., Barton, J. S., Masanovic, M., Hu, Z., Bowers, J. E., and Blumenthal, D. J., "Monolithic mode-locked laser and optical amplifier for regenerative pulsed optical clock recovery," *Photonics Technology Letters, IEEE* **19**, 641-643 (2007).
17. Koch, B., Barton, J., Masanovic, M., Hu, Z., Bowers, J., and Blumenthal, D., "35 gb/s monolithic all-optical clock recovery pulse source," *Optical Fiber Communication and the National Fiber Optic Engineers Conference, 2007. OFC/NFOEC 2007.1-3* (2007).

Field-Modulated Packet Forwarding Chips for Label-Switched Optical Routing

Matthew M. Dummer, Jonathan Klamkin, Anna Tauke-Pedretti, Kimchau N. Nguyen and Larry A. Coldren

Department of Electrical and Computer Engineering, University of California, Santa Barbara, CA 93106

dummer@enr.ucsb.edu

Abstract: We demonstrate a single-chip 40 Gb/s wavelength converter based on an SG-DBR laser and field-modulated optical gate. This device also performs 10 Gb/s label encoding for all-optical packet forwarding.

©2008 Optical Society of America

OCIS codes: (230.7405) Wavelength conversion devices, (140.3600) Lasers, tunable (250.7360) Waveguide modulators.

1. Introduction

Wavelength division multiplexing (WDM) has become the enabling technology for utilizing the available bandwidth (BW) in fiber optic links. However, as BW usage increases, the capacity of the network nodes must be scaled to accommodate larger amounts of data received and transmitted through each fiber. The capacity of today's OEO routing architecture will soon approach its limit in terms of processing and buffering requirements, as well as overall power dissipation. To resolve these issues, next generation WDM networks will necessitate that much of the routing functionality be performed in the optical domain. One proposed method is all-optical label switching, which allows individual IP packets to be optically routed by dynamic wavelength assignment [1]. Labels which are written onto each payload are identified using a look-up table to control the output wavelength of a tunable wavelength converter. This type of architecture allows for minimal electronic processing and can support very high bit rates, since only the labels must be electronically recovered at each node.

In this work, we present a novel packet forwarding chip (PFC) which can be used as the core component for label-switched routing. This device performs wavelength conversion of data up to 40 Gb/s and additionally has the capability to write, or rewrite labels at 10 Gb/s. Wavelength conversion is accomplished by a field modulation technique, which combines a high-power receiver with an electroabsorption modulator (EAM) to create a high-speed optical gate. The EAM modulates the output of an on-chip tunable laser to transcribe the input data signal onto the selected output wavelength of an on-chip tunable laser. A second EAM is also integrated in this device to allow external modulation for label encoding to the same output wavelength.

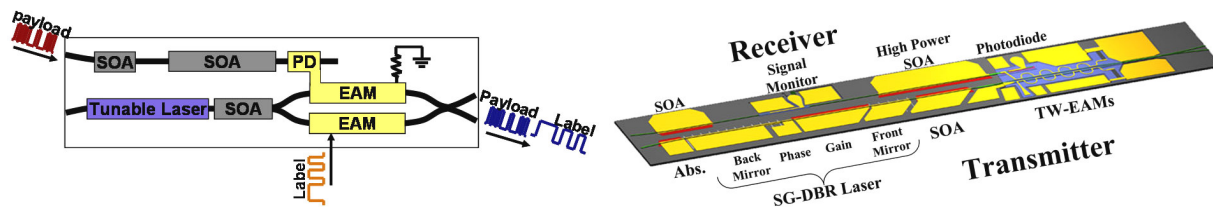


Fig. 1. (left) Field modulated PFC diagram depicting wavelength conversion and label writing functions. (right) Schematic of fabricated device showing integrated components. Footprint is 4.0 mm x 0.55 mm.

Although similar packet forwarding chips using SOA-based wavelength conversion have previously been demonstrated [2], the field-modulated approach offers a number of advantages for optical routing applications. These include increased network transparency, conversion to a similar (or the same) wavelength as the input signal, and elimination of optical filtering requirements at the output. Furthermore, field-modulated wavelength converters have demonstrated the potential for 2R, or 3R regeneration [3], which will be beneficial for cascaded optical routing through multiple nodes.

2. PFC design

The PFC is a highly-complex photonic integrated circuit that requires multiple components with diverse functionalities on a single chip. The device is separated into two ridge-waveguide regions which differentiate between the receiving and transmitting functions of the device. The receiver side consists of two SOA preamplifiers followed by a high-power photodiode (PD). The transmitter side consists of a widely tunable sampled grating (SG)-

DBR laser, followed by an output SOA and two parallel EAMs. The SG-DBR laser light is coupled through both EAMs using a 1x2 MMI splitter followed by a 2x2 MMI combiner at the output. Figure 1 shows a basic diagram of the PFC architecture as well as a device schematic showing each of the components drawn to scale.

This device was fabricated using a dual quantum well integration platform [4] on a S-doped InP substrate. The layer structure consists of a single waveguide core with two multi-quantum-well (MQW) stacks. An offset MQW provides gain for the active components while the centered MQW is designed to provide modulation efficiency. The offset MQW is selectively removed from passive regions prior to a single blanket regrowth of the p-type InP cladding and p-contact layer. Wavelength conversion relies on directly driving the EAM with the PD photocurrent; therefore achieving high output saturation power in the receiver is very important. To improve the receiver saturation characteristics, the PFC uses a laterally flared waveguide SOA design followed by an offset MQW-PD [5]. In this device, the receiver is capable of 20 dB of gain with 32 mA of DC photocurrent generation at the 1-dB gain-compression output power. We have implemented an advanced traveling wave (TW) design in the EAMs to achieve very high BW. Both the converting and label-writing EAM make use of periodic microstrip electrodes and selectively undercut waveguide geometry to raise the characteristic impedance and improve velocity matching [6]. The absorption-edge of the centered MQW (10 wells) has been chosen to be 1470 nm to achieve low passive loss but high modulation efficiency when biased. Under reverse bias, the 250 μm long modulator achieves 10-14 dB/V modulation efficiency across 30 nm of tuning from the SG-DBR laser. Integrated thin film resistors (25 Ω) are also included to terminate the EAMs and simplify biasing.

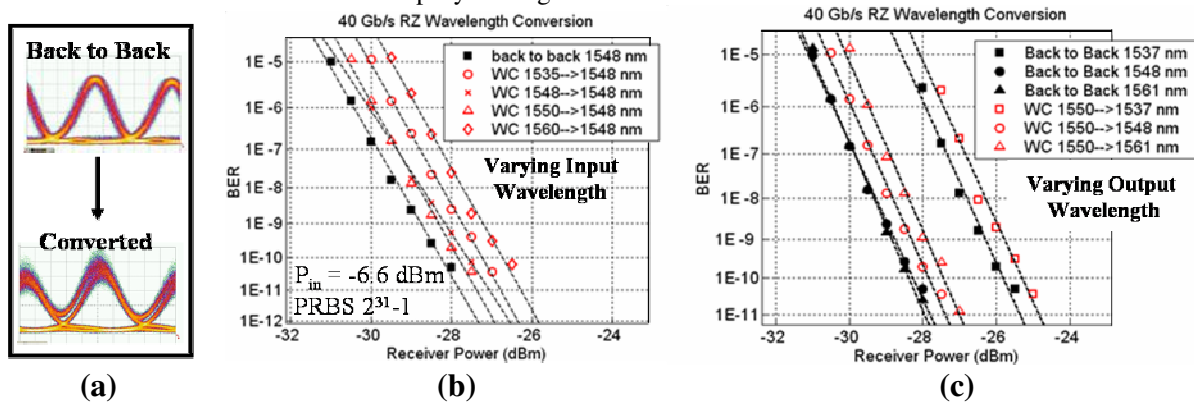


Fig 2. (a) 40 Gb/s back-to-back (1550 nm) and wavelength converted eye diagrams (1550 \rightarrow 1548 nm) (b) Wavelength converted BER measurements for varying input wavelength and (c) varying output wavelength compared with back-to-back transmission.

3. Wavelength Conversion Performance

The wavelength conversion performance of the PFC has been evaluated by bit error rate (BER) measurements using 40 Gb/s RZ data. The receiver SOAs were biased to 8 kA/cm^2 , which was determined to give the highest saturation power. The SG-DBR gain section and output SOA were biased to 5.5 kA/cm^2 and the mirror currents were tuned to achieve the desired output wavelength. The PD-EAM gate bias was chosen to be between -3.5 V and -5.0 V, determined by the maximum slope efficiency of the EAM at each output wavelength. The optimal input power into the device was found to be a trade off between achieving the maximum photocurrent swing and minimal pattern dependence caused by receiver saturation. For RZ data, the optimal input power was determined to be -6.6 dBm, which is slightly below the 1-dB compression point of the receiver. Using this input power, BER measurements were performed for varying input wavelengths to and varying output wavelengths from the PFC. Figure 2 shows the BER measurements for the wavelength converted signals compared with back-to-back transmission. The back-to-back data was taken at the same wavelength as the output of the PFC to eliminate the wavelength dependence in the measurement setup. For 25 nm of input tuning, and 22 nm output tuning, error free operation was achieved with less than 2 dB power penalty compared with the back-to-back. This includes the case of conversion to the input wavelength (1548 nm \rightarrow 1548 nm). The power penalty shows a minimum when the input wavelength corresponds to the gain peak of the receiver SOAs (1550 nm). The output extinction ratio of the converted signal was measured to be between 10 and 12 dB in all cases. The facet-to-facet conversion efficiency, defined as the ratio of output power to input power, was measured to be between -3 dB and -8 dB. The lowest conversion efficiency occurred at the shortest output wavelength (1537 nm), due to higher passive loss. The total power dissipation measured for the PFC during 40 Gb/s RZ PRBS wavelength conversion was 1.5 W.

4. Label Writing Performance

Demonstrations of optical label writing have been performed using PRBS data to modulate the EAM in the other transmitter arm of the PFC. The slower modulation rate of 10 Gb/s NRZ was chosen so that labels could be more easily processed by control electronics in the router architecture. A 2.0 V peak-to-peak drive signal was applied by directly contacting the chip with a ground-signal-ground probe. Again, the DC bias for the EAM was adjusted to take advantage of the maximum modulation efficiency for each wavelength. Figure 3 shows the BER for the 10 Gb/s modulation for varying output wavelengths, along with corresponding eyes diagrams. The output extinction ratio was measured to be 9-10 dB and the output power was -6 to -6.5 dBm. Less than 1 dB power penalty over the output tuning range was observed.

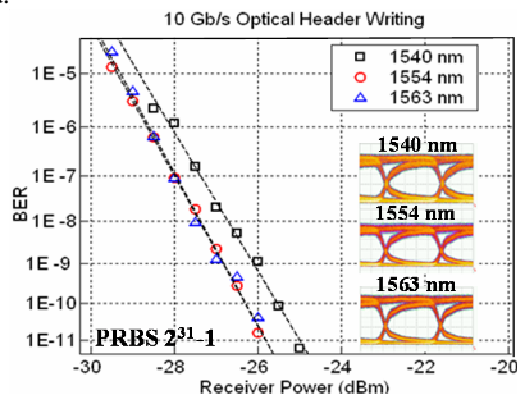


Fig 3. BER measurements for 10 Gb/s NRZ optical label writing for varying SG-DBR wavelengths. Insets show corresponding eye diagrams with 2.0 V peak-to-peak drive.

5. Conclusion

This work has discussed the design and performance of the first field-modulated packet forwarding chip, which can be used for label-switched optical routing. This device demonstrates error free wavelength conversion at 40 Gb/s for over 22 nm of input and output wavelength tuning, with less than 2 dB power penalty compared with back-to-back transmission. Output extinction ratios of greater than 10 dB were measured. This device also enables 10 Gb/s label encoding, with greater than 9 dB extinction for a 2.0 V drive. Future work is focused on dynamic characterization of this device including fast wavelength switching and label encoding of individual packets to demonstrate wavelength selected routing.

The authors acknowledge the funding support of the DARPA/MTO/ARL DOD-N program under the LASOR project award number W911NF-04-9-0001.

References

- [1] Blumenthal, D.J. et al. "All-optical label swapping networks and technologies," *J. of Lightwave Technol.* Vol. 18, pp. 2058-2075 (2000)
- [2] Lal, V. et al. "Monolithic wavelength converters for high-speed packet-switched optical networks" *J. of Lightwave Technol.* Vol. 13 pp. 49-57 (2007)
- [3] Sysak, M.N et al. "Optical 2R and 3R signal regeneration in combination with dynamic wavelength switching using a monolithically integrated, widely tunable photocurrent driven wavelength converter," *Proc. European Conf. on Optical Communication Th3.4.1* (2006)
- [4] Sysak, M.N. et al. "A single regrowth integration platform for photonic circuits incorporating tunable SGDBR lasers and quantum-well EAMs" *Photon. Technol. Lett., IEEE* vol. 18, pp 1630-1632, (2006)
- [5] Tauke-Pedretti, A et al." High saturation power and high gain integrated photoreceivers" *Photon. Technol. Lett., IEEE* vol. 17, pp 2167-2169, (2005)
- [6] Dummer, M. M. et al "Periodic Loading and Selective Undercut Etching for High-Impedance Traveling-Wave Electroabsorption Modulators," *Proc. Optical Fiber Communications Conf* (2008)

The World's First InP 8x8 Monolithic Tunable Optical Router (MOTOR) Operating at 40 Gbps Line Rate per Port

Steven C. Nicholes^{*}, Milan L. Mašanović[†], Biljana Jevremović[†],
Erica Lively[†], Larry A. Coldren^{†,*}, and Daniel J. Blumenthal[†]

^{*}Department of Materials

[†]Department of Electrical and Computer Engineering

University of California, Santa Barbara 93106

Email: snicholes@engineering.ucsb.edu

Abstract: We demonstrate the first InP monolithic tunable optical router with error-free 40 Gbps operation per port. The device has eight wavelength converters and an 8x8 arrayed-waveguide grating router, yielding more than 200 on-chip functional elements.

©2009 Optical Society of America

OCIS codes: (250.5300) Photonic integrated circuits; (130.0250) Optoelectronics

1. Introduction

Advanced photonic integrated circuits (PIC) in InP are a critical technology for next-generation optical networks [1,2]. In addition to a reduced device footprint and the elimination of component-to-component coupling losses, PICs also provide a path to scale networks to higher bandwidths with a lower power consumption requirement than that of electronic routers. Although devices like advanced transmitters and wavelength converters that exploit these benefits have been realized [3-5], there have only been a few demonstrations of large-scale integration in InP [2].

In this paper, we report on the world's first 8-channel monolithic tunable optical router (MOTOR) operating at 40 Gbps per port. The InP/InGaAsP device integrates an array of 8 tunable wavelength converters (WC) with a low-loss passive 8x8 arrayed-waveguide grating router (AWGR) and functions as a wavelength-based switching element. The MOTOR chip requires a very high level of integration with more than 200 integrated functional elements.

2. Device Design

A schematic of the overall MOTOR chip is shown in Fig. 1a. The details of a single input channel are shown in Fig. 1b. Each individual tunable wavelength converter has a high degree of complexity, consisting of a sampled-grating DBR (SG-DBR) laser, semiconductor optical amplifiers (SOAs), passive phase shifters, an integrated differential delay line, MMIs, and variable optical attenuators. The SG-DBR is operated in the continuous wave regime and consists of five sections: an active gain section, front and back tuning mirrors, a phase tuning pad, and an active absorber. For wavelength conversion, the CW light generated by the on-chip SG-DBR laser is used inside an SOA-based, differentially-delayed Mach-Zehnder interferometer (MZI). In the MZI region, nonlinear (i.e., highly saturable) SOAs are used so that input pulses deplete the carriers in the SOA causing cross phase modulation of the SG-DBR generated light. Additionally, two SOAs are used to amplify the input data signal before the MZI, and two

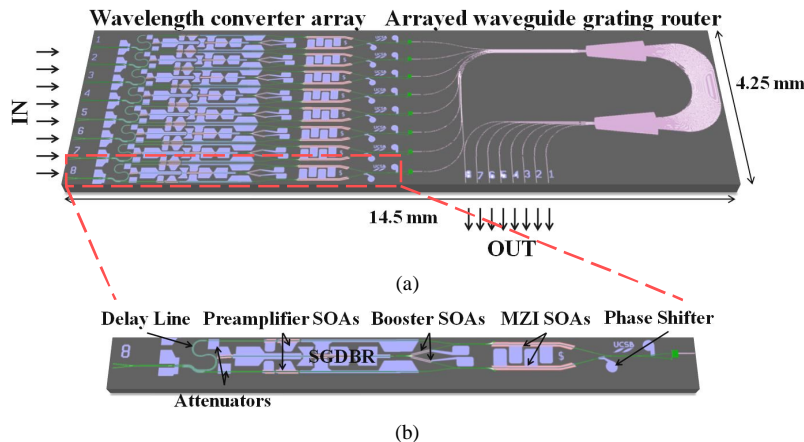


Figure 1. Schematic of the MOTOR chip: (a) overall device; (b) close-up of the wavelength converter design.

SOAs are used to boost the output power of the SG-DBR, one in each branch of the MZI. The differential integrated delay line is used to overcome carrier recovery time limits at 40 Gbps in the MZI SOAs. Low power penalty wavelength conversion at 40 Gbps in the RZ data format using a stand-alone device similar to Fig. 1b was demonstrated previously [3]. The output of the wavelength converter is connected to the AWGR, which passively routes the converted signal based on the new wavelength of the data, as set by the SG-DBR [6].

The integration platform supports both active and low-loss elements using a novel, single regrowth, quantum-well intermixing approach. This platform allowed us to reduce absorption losses in the AWGR and delay line regions by exploiting an undoped InP setback layer in the passive sections of the device [7] while optimizing active functions. The chip has 3 different waveguide types: a surface ridge waveguide design in the wavelength converter section, a high-contrast deeply etched waveguide in the delay line for compactness, and a buried rib waveguide in the AWGR region for low scattering losses. The epitaxial structure consisted of 10 compressively-strained quantum wells (QW) centered in a quaternary waveguide. Quantum-well intermixing was used to blue-shift the band-edge of all passive regions. The completed chip was soldered to a copper mount and held at 16°C during operation.

3. AWGR Performance

The performance of the AWGR was characterized using on-chip light sources and an optical spectrum analyzer (OSA). First, amplified spontaneous emission (ASE) was generated by forward biasing the MZI SOAs on a single WC, and the output of each egress port was fiber coupled to the OSA (Fig. 2a). The free spectral range (FSR) of the AWGR was measured to be 11.1 nm. Next, the MZI SOAs of each WC were biased and the resulting spectrum was measured from a single output port (Fig. 2b). By changing the biasing conditions on the front and back mirrors of the SG-DBR, the laser can be tuned to any of the allowed output wavelengths of a given port in order to achieve full channel switching (Fig. 2c). Lastly, the single-channel crosstalk of the AWGR was found to be 16 dB or more.

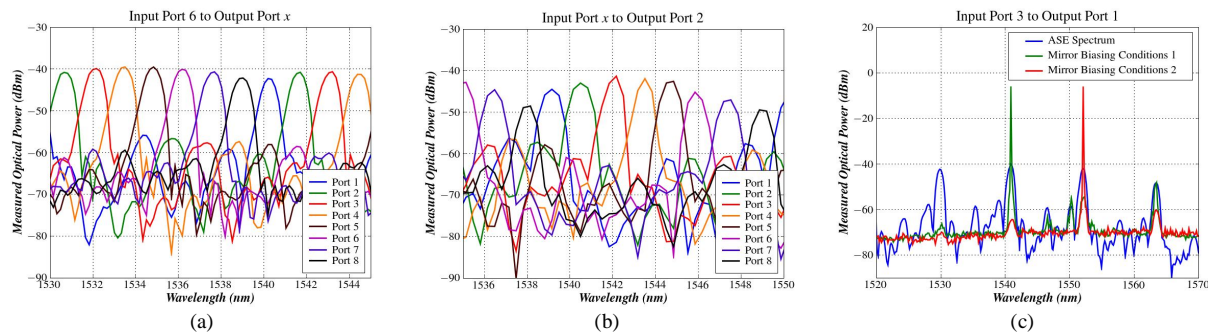


Figure 2: Output response of the integrated AWGR: (a) measured optical output from all output ports using input WC port #3; (b) measured optical output from output port #2 using each input WC port; and (c) lasing spectra for different biasing conditions using the SG-DBR of input WC port #3 superimposed on the ASE spectrum for that channel, all measured from output port #1.

4. Wavelength Conversion and Routing Results

The MOTOR chip was tested during single-channel operation using PRBS $2^{31}-1$ data at 40 Gbps. The RZ data signal was amplified with an erbium doped fiber amplifier (EDFA) and was transmitted through an attenuator to control the power level, a 5-nm filter to remove ASE, and a polarizer to ensure TE polarization before it was coupled into the chip. The fiber-coupled output was passed through a 5-nm filter to remove the original input signal and was transmitted to a preamplified receiver. Bit-error-rate (BER) measurements were made using a 40 Gbps SHF BERT.

Fig. 3 shows the BER and eye diagrams for multiple input channels while monitoring a constant output port (Input WCs #1 and #5 each had a ridge defect near the MZI, and Input WC #2 had a shorted preamplifier and thus data are not shown for these channels). Additionally, Fig. 4 shows the BER results for two different output ports using a constant input channel and open eye diagrams for all eight output ports. These results indicate error-free operation. The measured power penalties at a BER of 10^{-9} for the conversion and routing process range from approximately 4.3 to 6.9 dB (depending on the input port).

The noise floor and high power penalty are likely attributable to two main factors. First, the tested MOTOR chip was not antireflective (AR) coated. Given the high output powers of the centered gain regions, it is probable that minor reflections exist in the device during operation. Second, to minimize regrowth quantity and complexity, the input preamplifier SOAs are made from the centered QW band-edge. Because there is a relatively high modal overlap with the centered wells, the output saturation power of the SOA is low. In order to provide enough gain to

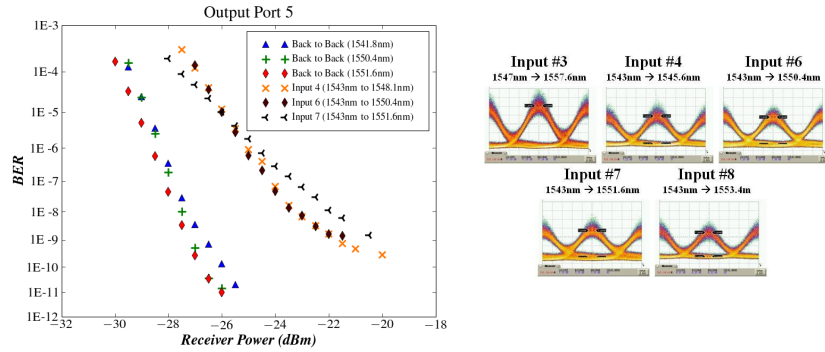


Figure 3. 40 Gbps BER measurements and eye diagrams for various input ports monitored at output port #5.

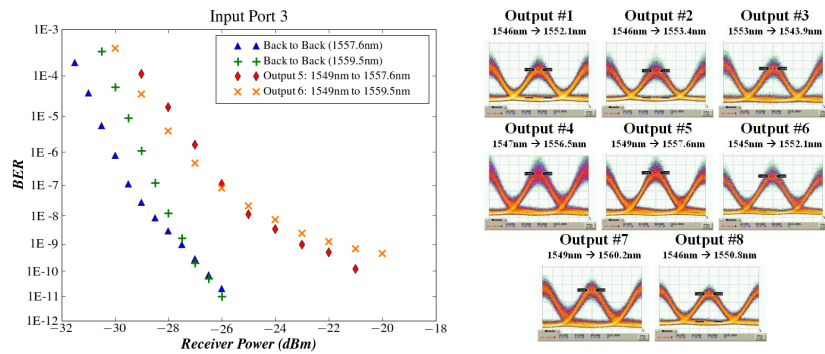


Figure 4. 40 Gbps BER measurements and eye diagrams for input port #3 and various output ports.

the input signal to deplete the MZI SOAs of carriers and modulate the MZI, the preamplifier SOAs had to operate in the nonlinear regime. This resulted in pattern distortion effects and an increased BER. Future MOTOR designs with AR coatings and an optimized preamplifier structure with combined centered and offset QWs are planned to address these issues.

5. Conclusion

We report demonstration of the world's first InP 8x8 monolithic tunable optical router (MOTOR) capable of error-free 40 Gbps operation per port. The device represents one of the most densely-integrated InP chips ever reported, with more than 200 integrated functions and power penalty as low as 4.3 dB at 40 Gbps. Improved power penalty is expected with future designs employing AR coatings and optimized preamplifier SOAs.

6. Acknowledgements

This work was supported by the DARPA MTO and the Army under the DOD-N LASOR Project (W911NF-04-9-0001). Device fabrication was done in the UCSB nanofabrication facility, part of the NSF funded NNIN network.

7. References

- [1] D. Wolfson *et al.*, "All-optical asynchronous variable-length optically labelled 40 Gbps packet switch," in *Optical Communication, 2005. EOC 2005*, Vol.6, pp. 49-50.
- [2] R. Nagarajan *et al.*, "Large Scale Photonic Integrated Circuits", *JSTQE*, **11**, 50-65, (2005).
- [3] V. Lal *et al.*, "Monolithic Wavelength Converters for High-Speed Packet-Switched Optical Networks," *JSTQE*, **13**, 47-57 (2007).
- [4] M. Masanovic *et al.*, "Widely Tunable Monolithically Integrated All-Optical Wavelength Converters in InP," *JLT*, **23**, 1350-1362 (2005).
- [5] M. Dummer *et al.*, "40 Gb/s widely tunable wavelength converter with a photocurrent-driven high-impedance TW-EAM and SGDBR laser," in *Semiconductor Laser Conference, 2008. ISLC 2008*, pp. 145-146.
- [6] M. Smit and C. van Dam, "PHASAR-Based WDM-Devices: Principles, Design and Applications", *JSTQE*, **2**, 236-250 (1996).
- [7] S. Nicholes *et al.*, "Novel Application of Quantum Well Intermixing Implant Buffer Layer to Enable High-Density Photonic Integrated Circuits in InP", in *Conf. on Indium Phosphide and Related Materials (IPRM, Newport Beach, CA, 2009)*, Paper WB1. 2.

40 Gb/s Field-Modulated Wavelength Converters for All-Optical Packet Switching

Matthew M. Dummer, *Student Member, IEEE*, Jonathan Klamkin, *Student Member, IEEE*,
Anna Tauke-Pedretti, *Member, IEEE*, and Larry A. Coldren, *Fellow, IEEE*

(Invited Paper)

Abstract—We present a high-functionality photonic integrated circuit that performs field-modulated wavelength conversion. This device incorporates an on-chip sampled grating distributed Bragg reflector laser for wide tunability. Wavelength conversion is accomplished using a preamplified semiconductor optical amplifier photodiode receiver interconnected with a traveling-wave modulator to form a high-speed optical gate. This paper discusses the design and performance of this device, as well as its potential for optical packet switching applications. Error-free wavelength conversion is demonstrated at 40 Gb/s with 1–3 dB power penalty compared with back-to-back transmission over 22 nm of input and output tuning. Output extinction in all cases is greater than 9 dB, and conversion efficiency ranges from –2 to –6 dB over the tuning range. This device additionally demonstrates the capability for external 10 Gb/s modulation, which can be used for optical label encoding.

Index Terms—Electroabsorption, semiconductor amplifiers, traveling-wave devices, tunable lasers, undercut etching, wavelength conversion.

I. INTRODUCTION

THE WIDESPREAD use of wavelength-division multiplexing (WDM) has greatly increased the capacity in today's fiber optic networks. As WDM networks continue to grow in complexity, methods for dynamic wavelength management, and especially wavelength conversion, have become increasingly important. Wavelength conversion allows for effective resolution of signal contention in high traffic networks, allowing for better utilization of available network bandwidth [1]. Furthermore, wavelength converters have been proposed as the key switching elements for all-optical routing in next-generation networks.

The capacity of today's optical–electronic–optical (OEO) routing architecture is rapidly approaching its limit in terms of processing and buffering requirements, as well as overall power dissipation. To resolve these issues, future networks will necessitate that many of the routing functions be performed in the optical domain. One solution that has been offered is all-optical label switching, which allows individual IP packets to

be optically routed by dynamic wavelength assignment [2]. In this type of routing architecture, individual labels that accompany each payload are identified by the node, and the destination of the packet is determined using a lookup table. The output of a wavelength converter is then tuned to the proper wavelength to route the packet through an arrayed waveguide grating to the desired port. This type of architecture allows for minimal electronic processing and can support very high bit rates, since only the labels must be electronically recovered at each node.

Making the leap to optically packet switched networks will require an efficient and scalable technology for performing high-speed wavelength conversion. Photonic integrated circuits (PICs) are an attractive solution for achieving high functionality with low cost. Compared with discrete optical components, such as PICs offer small footprint, simplified packaging, low optical loss, and reduced power dissipation, all of which are necessary for a viable wavelength conversion technology.

Of particular interest are PICs that incorporate a widely tunable laser source on chip. To date, two different methods for single-chip wavelength conversion have been demonstrated. The first of these is a carrier-modulated approach, which takes advantage of nonlinearity in a semiconductor optical amplifier (SOA) to achieve cross-gain modulation (XGM) or cross-phase modulation (XPM) between an input data signal and the on-chip continuous-wave (CW) signal [3]. The switching speed of these devices is limited by the carrier lifetime in the saturated SOA, which typically limits the operating bandwidth to 10 Gb/s. However, more recently, differential interference techniques have been used to demonstrate 40 Gb/s in a monolithic device [4], [5].

An alternative approach to wavelength conversion is based on modulation of the electric field, as opposed to modulation of the carrier density in the SOA case. Field-modulated devices make use of an interconnected photodiode (PD) and either an electroabsorption modulator (EAM) or Mach–Zehnder modulator (MZM) to form a high-speed optical gate. Such optical gates have been used to demonstrate wavelength conversion at data rates as high as 100 Gb/s [6]. The field-modulated approach offers a number of advantages for optical routing applications. These include increased network transparency, conversion to a similar (or the same) wavelength as the input signal, and elimination of optical filtering requirements at the output. Furthermore, field-modulated wavelength converters have demonstrated the potential for 2R, or 3R regeneration [7], which will be beneficial for cascaded optical routing through multiple nodes.

Manuscript received November 1, 2008; revised February 10, 2009. First published May 8, 2009; current version published June 5, 2009. This work was supported by the Defense Advanced Research Projects Agency (DARPA) MTO-LASOR under Grant W911NF-04-9-0001.

The authors are with the Department of Electrical and Computer Engineering and the Department of Materials, University of California Santa Barbara, Santa Barbara, CA 93106 USA (e-mail: dummer@engineering.ucsb.edu).

Color versions of one or more of the figures in this paper are available online at <http://ieeexplore.ieee.org>.

Digital Object Identifier 10.1109/JSTQE.2009.2017279

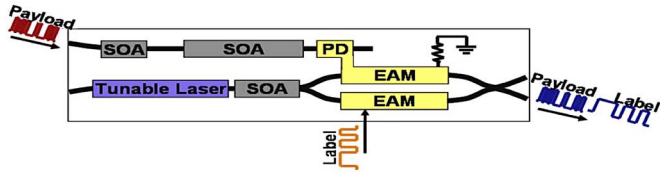


Fig. 1. Schematic diagram of the device design depicting both wavelength conversion and label writing functionalities.

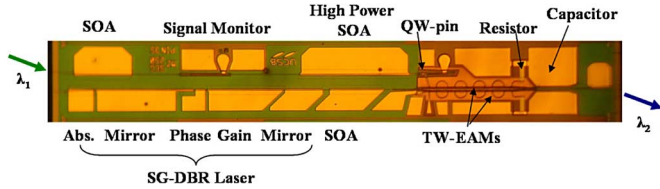


Fig. 2. Photograph of fabricated wavelength converter. The total footprint is $4.1 \text{ mm} \times 0.55 \text{ mm}$.

In previous monolithic devices, 10 Gb/s operation has been demonstrated using an EAM [8], and 40 Gb/s operation has been demonstrated with a series push-pull MZM [9]. This paper presents the first demonstration of monolithic 40 Gb/s wavelength conversion using an electroabsorption-based device. Error-free operation with less than 3 dB power penalty is achieved over 22 nm of input and output tuning range.

For efficient utilization of bandwidth in optical packet switching, it is desirable for the optical label to be encoded on the same carrier wavelength as its corresponding payload. Therefore, we have designed this device with the capability to encode 10 Gb/s labels as well, using a separate modulation region. Over the same wavelength range, 10 Gb/s transmission is demonstrated error-free.

II. DEVICE ARCHITECTURE AND FUNCTIONALITY

This wavelength converter incorporates all of the elements of a widely tunable transceiver onto a single InP chip. The device is comprised of two separate waveguide regions that are responsible for the receiver and transmitter functionality. A schematic depicting the general layout of the wavelength converter is shown in Fig. 1. On the receiver side, there are two SOA preamplifiers followed by a high-power p-i-n PD. The transmitter side contains a widely tunable sampled grating distributed Bragg reflector (SG-DBR) laser, consisting of a gain and phase section between two SG mirrors, followed by an output SOA. The light from the SG-DBR laser is divided into two parallel traveling-wave EAMs using a 1×2 multimode interference (MMI) splitter. One of the EAMs is directly connected to the PD to form a high-speed optical gate to perform wavelength conversion. The other EAM can be electrically driven to function as a transmitter for encoding labels onto individual IP payloads. The two EAM branches are combined again by a 2×2 MMI before being emitted from the chip. The parallel EAM configuration allows the wavelength conversion and label-writing functions to take place independent of one another, with a simple bias configuration. A picture of the final fabricated device is shown in Fig. 2.

The operation of the optical gate for wavelength conversion can be described by a three-step process, as shown in Fig. 3.

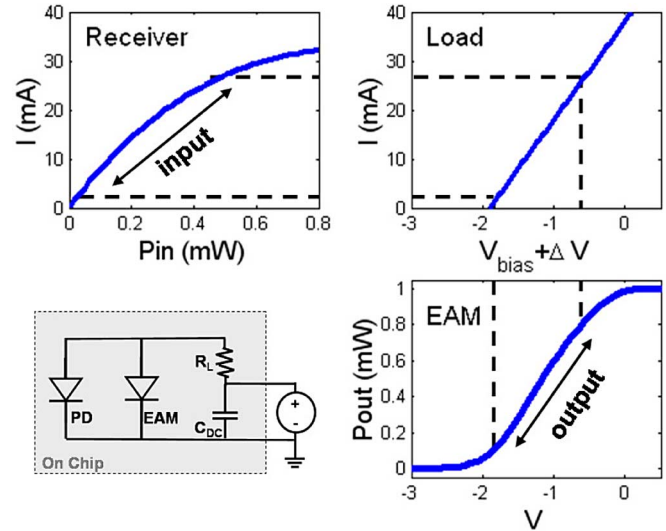


Fig. 3. Example of the three-part transfer function for the field-modulated optical gate. Circuit diagram is shown in the lower left.

First, the input signal, which is optically preamplified by the receiver SOAs, is incident on the PD to generate photocurrent. This current is dissipated by a load resistor, which provides the transimpedance to change the voltage across the EAM. The corresponding change in electric field reduces the absorption in the EAM from its normally “OFF” state, thereby opening the gate. In this way, the input signal can be transcribed onto any new output wavelength within the tuning range of the SG-DBR. The efficiency of the gate is dependent on the gain of the receiver and the extinction characteristics of the EAM, as well as the resistor value selection. The individual component performance will be further discussed in Section IV.

For this device, a thin-film load resistor has been integrated onto the chip. A dc-blocking capacitor is also incorporated to allow for simple reverse biasing of the PD and EAM with a single dc voltage. The on-chip termination allows wavelength conversion to be performed without any external microwave circuitry or bias tees, and greatly simplifies packaging and operation [8]. The bias configuration is shown in Fig. 3. A similar resistor and capacitor are also used to terminate the label-writing EAM.

III. DUAL QUANTUM WELL INTEGRATION PLATFORM

As described before, this field-modulated wavelength converter requires the integration of four types of optical components with diverse functionalities. These include the gain elements, i.e., laser and amplifier, and the absorption elements, i.e., modulator and PD. In addition, low-loss passive regions are also desirable for transporting signals between the components. Therefore, a versatile integration platform is essential for achieving optimal device performance. In this case, we have adopted a dual quantum well (DQW) integration platform as described in [10].

The epitaxial layer structure consists of a single InGaAsP waveguide core surrounded by upper and lower InP cladding layers shown in Fig. 4. Within the core, there are two different multiquantum well stacks. An upper set of seven offset quantum

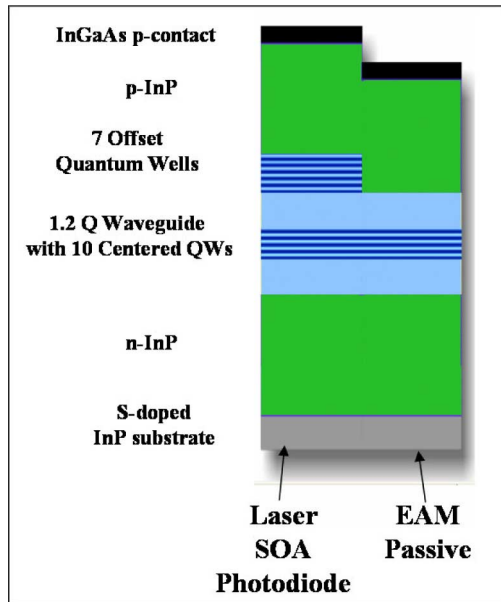


Fig. 4. DQW integration platform. The layer structure chosen for each region of the chip is denoted.

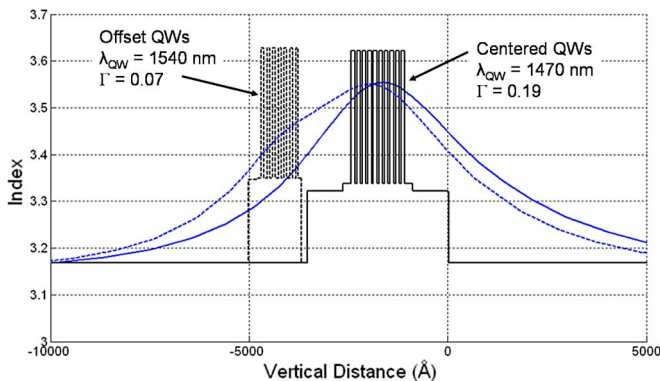


Fig. 5. Index and optical mode profile for the "active" (dotted) and "passive" (solid) regions of the device.

wells (OQWs) with a band edge corresponding to 1540 nm is used to provide optical gain. A second set of ten quantum wells centered in the core (CQW) is detuned 70 nm from the operating wavelength ($\lambda_{QW} = 1470$ nm) and is used to provide modulation efficiency under reverse bias. Active and passive regions of the device are defined by selectively removing the OQWs prior to regrowth of the upper InP cladding. A simulation of the optical mode profile in both the active and passive sections is shown in Fig. 5.

The DQW platform is advantageous because it can be implemented with only a single blanket regrowth, and therefore, allows for relatively simple fabrication and high yield. However, because this platform provides only two distinct bandgap regions within the chip, there are inherent tradeoffs in performance for each of the device components. For example, because both the SOAs and the laser make use of the same OQW gain material, a compromise must be made between the laser gain and amplifier saturation power. Similarly, because the CQWs

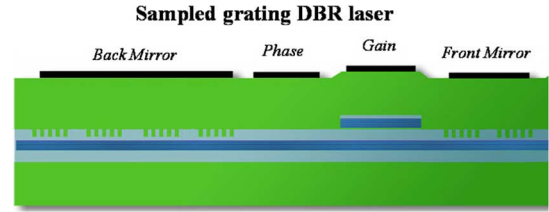


Fig. 6. Schematic of the SG-DBR laser cross section showing the waveguide structure of the gain, phase, and mirror sections.

are present throughout the entire wafer, the band edge of these wells must be carefully chosen to balance modulation efficiency of the EAM under reverse bias with passive waveguide loss in the unbiased regions. Finally, the DQW does not allow for an optimal PD structure to achieve both high bandwidth and high saturation power. While the best reported high-power PDs typically make use of bulk absorbing in conjunction with an intricate doping scheme, as in untraveling carrier (UTC) [11], [12] or partially depleted absorbers (PDAs) [13], this is not possible without an additional regrowth. For simplicity, we have instead chosen to implement a QW pin detector by using the offset gain region under reverse bias as the absorbing medium. By proper design of the device geometry, these PDs are capable of high-bandwidth operation (40 Gb/s) and good responsivity (1.00 A/W).

IV. INTEGRATED COMPONENTS AND CHARACTERIZATION

The performance of each of the integrated components has been optimized within the limits of the DQW platform. Here, we discuss the design and the characterization of these components, and their overall impact on the performance of the wavelength converter.

A. SG-DBR Laser

The SG-DBR laser was chosen for this paper because of its robust fabrication process and ease of integration. The laser consists of a 550- μm -long active gain section and a 50- μm -long phase section, surrounded by two mirrors, as shown in Fig. 6. The mirrors make use of periodic gratings, patterned by holographic lithography, to obtain a comb-like reflectivity spectrum. Because the sampling period differs between the front and back mirrors, current injection can be used to shift the relative reflectivity of each of the mirrors to select out a single supermode. This principle allows for Vernier-based tuning to achieve lasing over a wide wavelength range [14].

Fig. 7 shows the measured *LIV* characteristic for the integrated laser. The optical power was measured on chip by reverse biasing the output SOA. The threshold current for the device is 45 mA, and 19 mW of power is possible when biased up to 150 mA. The 400- μm -long output SOA additionally produces up to 6 dB of gain. However, it is typically driven with a lower current to limit the amplified spontaneous emission (ASE) contribution. The laser demonstrates continuous tuning over the range of 1524–1564 nm, as shown by the overlaid supermode spectra in Fig. 8. The fiber-coupled output power after the modulation

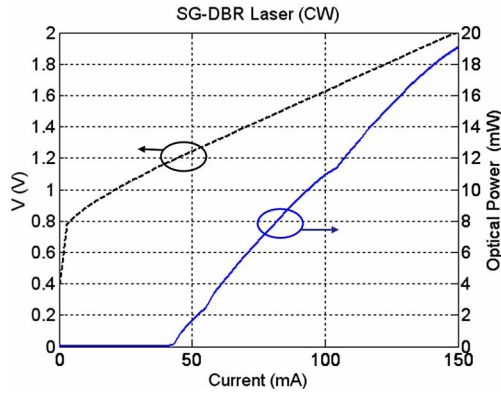
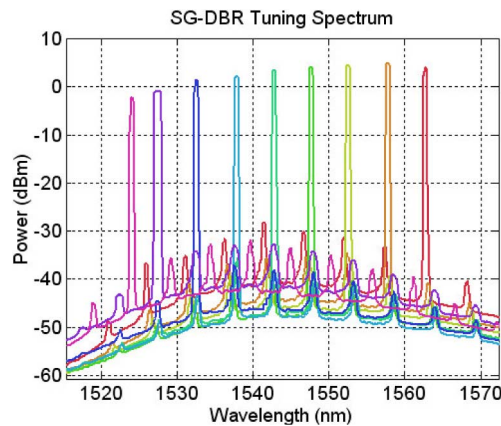
Fig. 7. SG-DBR laser *LIV* characteristic.

Fig. 8. Overlaid output spectra of nine supermodes from the SG-DBR laser.

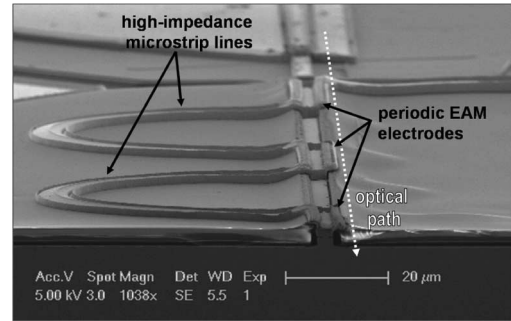
region ranges from -2 to 4 dBm, and greater than 30 dB side-mode suppression is observed over the entire tuning range.

B. Traveling-Wave EAMs

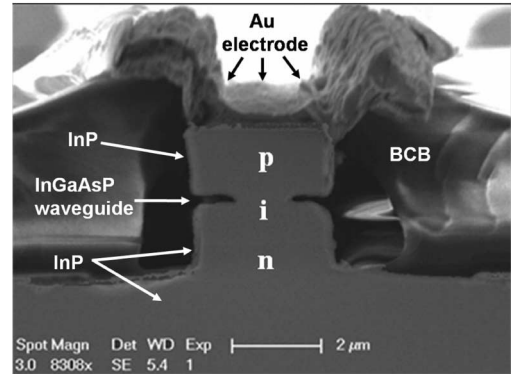
For the modulators in this paper, we have implemented a traveling-wave (TW) electrode design such that the electrical signal copropagates with the optical wave to achieve coherent interaction along the device length. With this configuration, it is possible to surpass the traditional RC frequency limitation of the device so that very high bandwidth can be achieved. In a TW-EAM, the instantaneous forward traveling voltage on the electrode is directly proportional to the characteristic impedance Z_0

$$V^+ = Z_0 I_{\text{photo}}. \quad (1)$$

Therefore, for the given amount of photocurrent from the PD (I_{photo}), it is advantageous to raise Z_0 to achieve a higher drive voltage, and consequently, improve the modulation efficiency. Here, we have implemented two techniques for raising the characteristic impedance, both of which involve reducing the capacitance per length of the TW-EAM. The first is selective undercut etching of the modulator waveguide to reduce the underlying junction capacitance [15], [16]. This requires first transitioning from a surface ridge waveguide into a deeply etched structure in



(a)



(b)

Fig. 9. SEMs of a high-impedance TW-EAM structure. (a) Periodic microstrip electrode design. The modulator has been cleaved halfway along the length. (b) Cross section of the ridge waveguide with selectively undercut intrinsic region for low capacitance.

the modulator region. A lateral selective wet etch with sulphuric acid and hydrogen peroxide is then used to reduce the width of the InGaAsP intrinsic region. In this case, the EAM waveguide width has been reduced from $3 \mu\text{m}$ down to $1.1 \mu\text{m}$ wide, as shown in the SEM cross section in Fig. 9.

The second technique that has been utilized is periodic loading of the transmission-line structure. By alternating between high-impedance microstrip sections and capacitively loaded modulation sections, a higher average impedance can be achieved [17]. The EAMs in this paper are designed with five $50 \mu\text{m}$ stages for a total modulation length of $250 \mu\text{m}$. The periodic electrode, as shown in Fig. 9, uses a 1:3 ratio of loaded to unloaded sections. The lengths of the electrical and optical paths through the EAM are designed such that the propagation times are equal to provide effective velocity matching. Together with the undercut etched waveguide, the periodic electrode structure effectively doubles the characteristic impedance of the TW-EAM from 20 to 40Ω . The integrated load resistor value (25Ω) is intentionally lower than Z_0 to create a resonant reflection that leads to an enhancement in the frequency response. From previously fabricated modulator test structures, we estimate the 3-dB bandwidth of the TW-EAM to be >45 GHz.

The dc extinction of the TW-EAM has been measured across the tuning range of the SG-DBR laser. Fig. 10 shows the extinction characteristics for varying reverse bias. The peak modulation efficiency ranges from 10 to 14 dB/V over 30 nm of

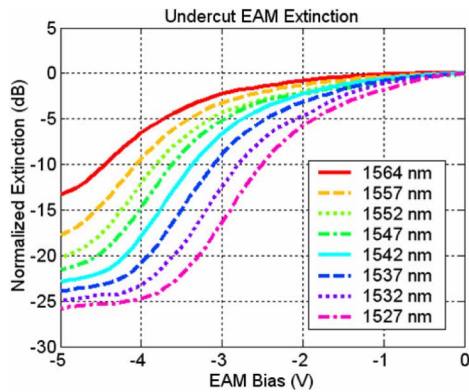


Fig. 10. DC extinction characteristic for the 250- μm TW-EAM over the tuning range of the SG-DBR.

wavelength tuning. The efficiency is the highest at the shortest wavelength, where the detuning from the absorption edge of the CQW is the least. However, the shorter wavelengths also incur higher insertion loss. The modal passive waveguide loss in the device has been measured to be between 4 and 11 cm^{-1} (1.74–4.78 dB/mm) for wavelengths from 1562 to 1528 nm. The undercut waveguide structure in the EAM adds an additional 7 cm^{-1} (3.0 dB/mm) of modal loss. This is possibly due to increased overlap of the mode with the zinc-doped upper InP cladding in this region, which results in higher absorption.

C. SOA-PD Receiver

Since there is no electronic amplification of signals in this device, wavelength conversion relies on directly driving the EAM with the photocurrent from the PD. Therefore, achieving high saturation power in the SOAs and PD is very important for generating high voltage swing and minimal pattern dependence caused by slow carrier lifetimes. The two-section receiver SOA uses a short (400 μm) gain stage followed by a long (800 μm) high-power stage. The two-stage design enables independent biasing of the two amplifiers so that the input power into the second stage can be adjusted to achieve the maximum output without signal degradation. A signal monitor pad between the two SOAs offers the possibility for implementing automatic gain control with an external feedback circuit, although this has not yet been demonstrated.

The low confinement factor (0.07) of the OQW gain region is beneficial for providing SOAs with high saturation power. To further increase the saturation power in the second stage, the width of the waveguide is flared to reduce the optical power density as the total power increases. By linearly flaring the the ridge from 3 to 12 μm wide, the saturation power can be increased by 4 dB [18]. In this case, the 1-dB output compression power of the second receiver SOA is 16.3 dBm.

Under reverse bias, the OQW material provides a modal absorption coefficient of 450 cm^{-1} , which allows for short PDs with high quantum efficiency. However, using QWs as the absorbing medium in the PD introduces the possibility of space charge accumulation under high-power illumination. To improve the saturation power of the QW-PD, the front end of

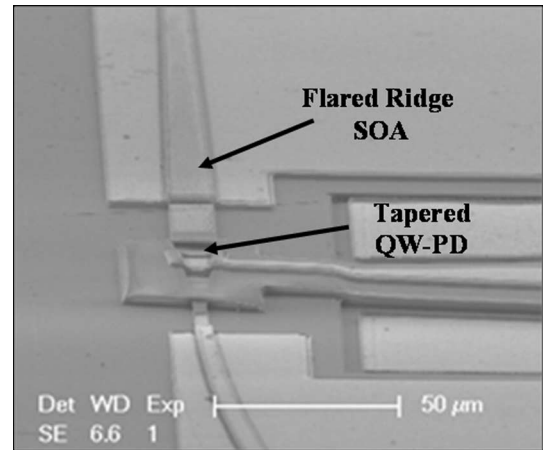


Fig. 11. SEM of the receiver depicting the flared ridge SOA followed by the high-power QW PD.

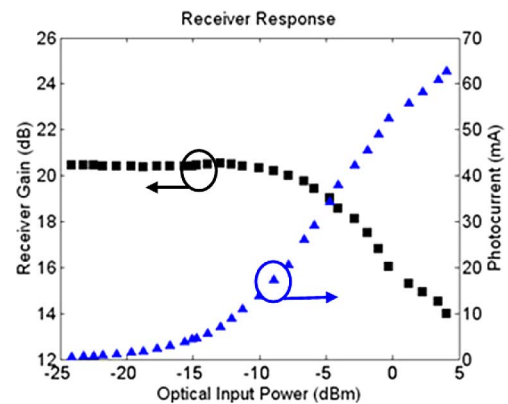


Fig. 12. Measured receiver gain and generated photocurrent as a function of input power.

the detector is kept wide, similar to the SOA, to reduce the optical power density. As the power is absorbed along the length, the waveguide is tapered to reduce the total capacitance. An SEM of the receiver structure depicting the flared and tapered waveguide is shown in Fig. 11. For the 35- μm -long PD, tapered from 9 to 5 μm , the bandwidth is greater than 20 GHz and -3 V bias is sufficient to maintain unsaturated operation with 20 mA of average photocurrent.

Because the gain material is comprised of compressively strained QWs, the receiver is highly polarization sensitive. Therefore, the input polarization was adjusted to TE orientation in all experiments. Fig. 12 shows the gain and photocurrent generated by the receiver for a 1550-nm CW input signal. For dc biases of 70 and 310 mA on the two SOAs and -3.0 V on the QW pin PD, the total gain of the receiver is about 20 dB. The maximum photocurrent observed is greater than 60 mA. However, at this operating point, the SOA gain has significantly rolled off due to saturation. The 1-dB gain compression point occurs at an input power of -6 dBm. This corresponds to 32 mA of linear dc photocurrent available for driving the TW-EAM.

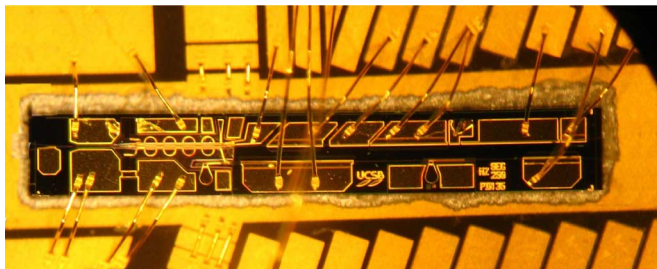


Fig. 13. Photograph of DUT mounted and wirebonded to an AlN carrier.

V. WAVELENGTH CONVERSION EXPERIMENTS

A series of wavelength conversion experiments have been performed to characterize the overall device performance. For these experiments, the device was soldered to an aluminum nitride carrier and wirebonded such that a single dc probe card could be used to apply all dc biases (Fig. 13). A $0.22\text{-}\mu\text{F}$ capacitor was mounted on the carrier and placed in parallel with the on-chip capacitor to improve the low-frequency response of the optical gate circuit. Input and output signals were coupled to and from the chip using conically tipped lensed fibers. The temperature of the copper test stage was maintained at 13°C during these experiments to achieve the optimal gain in the SOAs.

A. Small-Signal Response

Although this device was designed for large-signal digital modulation, small-signal measurements are useful for characterizing the microwave circuit design and observing the carrier dynamics within the receiver. Fig. 14 shows the normalized optical-to-optical small-signal response for conversion from 1548 to 1554 nm. The transmitter and receiver were biased such that the average photocurrents in the EAM and PD were 8.5 and 20 mA, respectively. Over the measurement range, a broadband inductive peak is observed due to the high-impedance electrode design in the EAM. For reverse biases greater than 3 V, there is no degradation in the response up to 20 GHz. For less than 3 V reverse bias, the corresponding applied field in the PD is insufficient to quickly sweep the generated carriers out of the junction. The accumulation of localized space charge can be recognized by the resulting degradation in the device bandwidth. The small resonance in the response at 1 GHz is caused by the inductance of the wirebond used to bias the optical gate [8].

B. Digital Performance

The wide bandwidth of this device makes it well suited for high-speed digital operation. To characterize the large signal behavior, we have examined the bit error rate (BER) performance using pseudorandom bit sequences (PRBSs) at 40 Gb/s with nonreturn-to-zero (NRZ) format. The experimental setup used for these digital wavelength conversion measurements is shown in Fig. 15. PRBS data generated by a BER tester (BERT) was used to modulate an optical transmitter, and was passed through an erbium-doped fibre amplifier (EDFA), optical filter, polarization controller, and attenuator, before being coupled into the device under test (DUT). The converted output signal

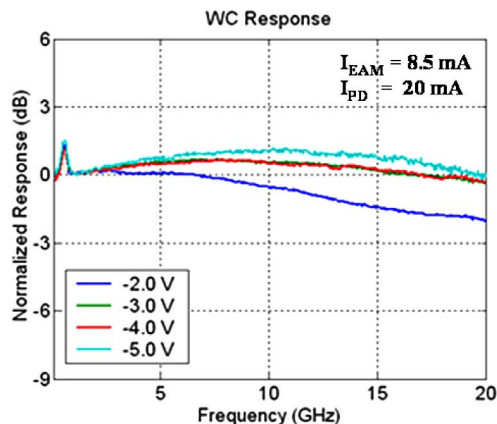


Fig. 14. Small-signal optical-to-optical response of the wavelength converter.

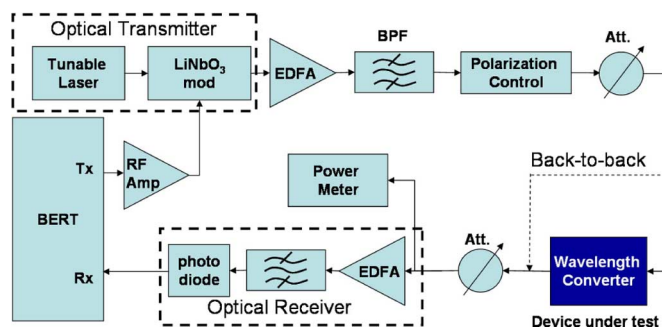


Fig. 15. Measurement setup for characterization of the wavelength conversion performance. BER of converted signal is compared to back-to-back transmission for varying power into the optical receiver.

was passed through a second attenuator, followed by an optically preamplified receiver that was connected back to the error analyzer of the BERT. The attenuator following the DUT was used to reduce the power into the receiver to a level at which errors could be recorded. The resulting BER for each received power was then compared with back-to-back transmission to compute a power penalty. The word length in these experiments was limited to $2^7 - 1$ because of pattern-dependent effects in the measurement setup.

Before measuring the BER over the wavelength tuning range, the optimal input power and operating conditions for the device were determined. The optimal bias point for the receiver SOAs was found to be 9 kA/cm^2 , which corresponded to the highest gain and saturation power. The laser gain section and the transmitter SOA were biased with lower current density (5.8 and 2.5 kA/cm^2 , respectively) to limit the EAM photocurrent and reduce thermal crosstalk. The bias of the optical gate was chosen to take advantage of the highest modulation slope efficiency for the output wavelength of the SG-DBR. Using these conditions, the input power into the device was varied to determine the best BER, as shown in Fig. 16(a), for wavelength conversion from 1550 to 1548 nm. From this measurement, we have extracted the power penalty measured at a BER of 10^{-9} between back-to-back and the wavelength-converted signals, as shown in Fig. 16(b). Also measured were the extinction ratio of the output signal and the wavelength conversion efficiency, defined

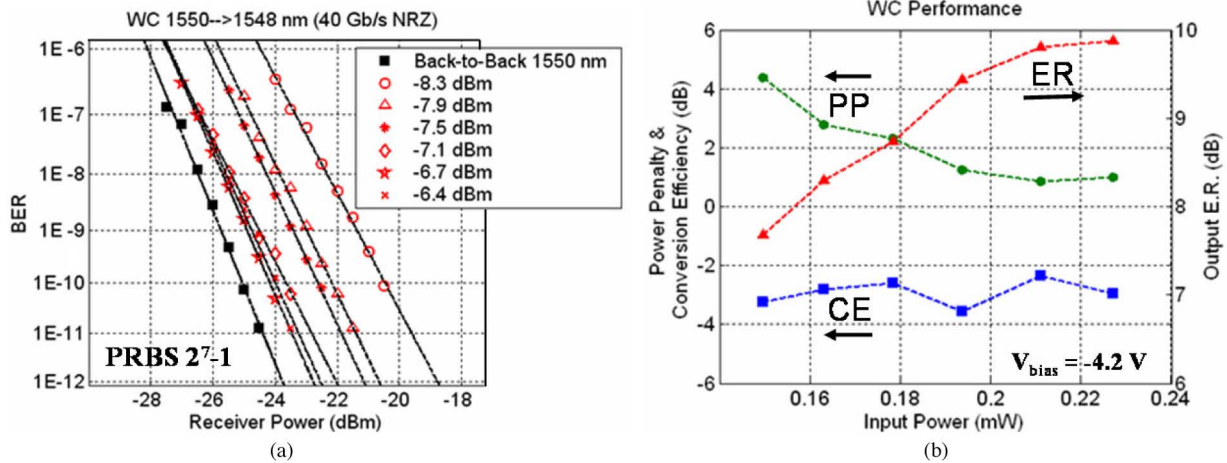


Fig. 16. (a) 40 Gb/s BER measurements for wavelength conversion from 1550 to 1548 nm for varying optical input power compared with back-to-back transmission. (b) Measured power penalty (PP) at BER of 10^{-9} , output extinction ratio (ER), and facet-to-facet conversion efficiency (CE) at each input power.

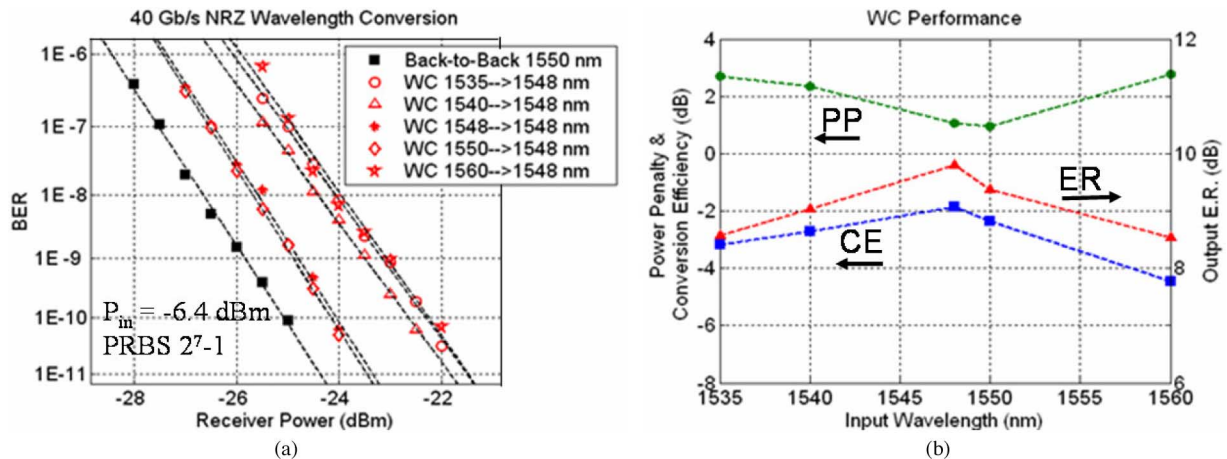


Fig. 17. (a) 40 Gb/s BER measurements for varying input wavelength and constant output wavelength for input power of -6.4 dBm. (b) Measured power penalty (PP), output extinction ratio (ER), and conversion efficiency (CE) versus input wavelength.

as the ratio of power between the converted signal and the input signal at each facet. Since no mode converters were present in this design, the fiber coupling loss added an additional 4 dB of loss at each facet.

The dynamic range measurements show that the output extinction ratio increases with input power, resulting in a reduction in the power penalty. As the input power approaches the 1-dB saturation point of the receiver SOA, the output extinction begins to level off due to the reduced gain. Input powers above -6.4 dBm were not tested with these bias conditions to avoid damaging the PD, since failure has been observed at 200 mW of dissipated power. Operation with input powers as high as $+5$ dBm was possible by adjusting the bias of the first SOA stage to reduce the total gain. This, however, resulted in significant reduction in conversion efficiency.

Wavelength conversion performance was evaluated as a function of input wavelength. Fig. 17(a) shows the resulting BER measurements for varying input wavelength with -6.4 dBm input power. Error-free wavelength conversion was observed over the range of 1535–1560 nm. The measured power penalty,

extinction, and conversion efficiency are shown in Fig. 17(b). Less than 3 dB power penalty is observed over the tuning range compared with back-to-back transmission. This includes the case of conversion back to the same wavelength (1548 nm to 1548 nm). The device exhibits the best performance when the input wavelength corresponds to the gain peak of the receiver. This results in a power penalty of 1 dB and a conversion efficiency of -2 dB.

BER measurements of wavelength conversion to varying output wavelengths have also been performed. Fig. 18 shows the BER measurements for three output wavelengths: 1537, 1548, and 1559 nm. For these measurements, the back-to-back data were compared at the same wavelength as the output from the device to eliminate the wavelength dependence in the measurement setup. The bias of the optical gate was adjusted to achieve the lowest power penalty at each wavelength. Error-free transmission was observed in all three cases with less than 1 dB power penalty. Fig. 19 shows the converted 40 Gb/s eye diagrams, which were taken at the lowest power penalty for each wavelength. The output extinction and bias condition are listed

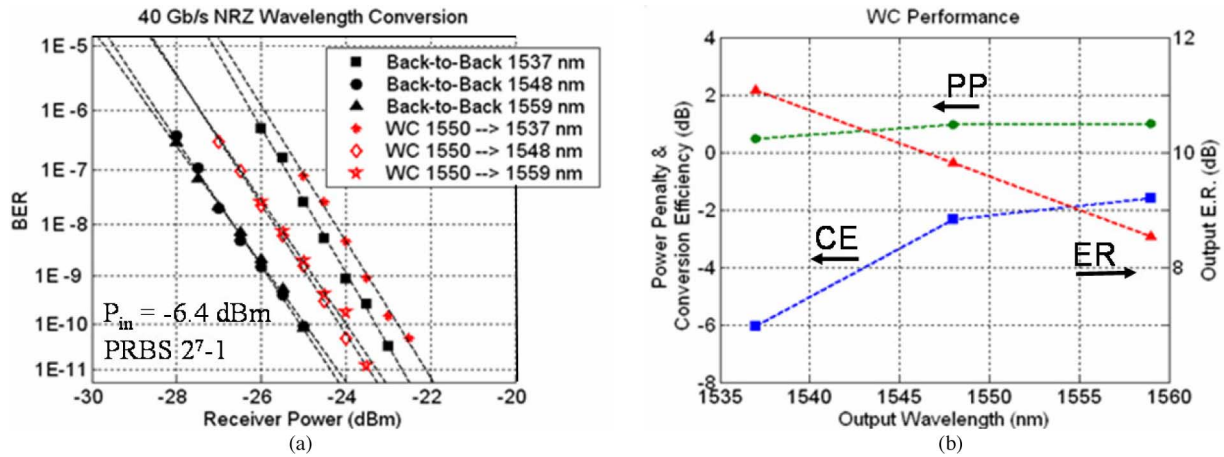


Fig. 18. (a) 40 Gb/s BER measurements for fixed input wavelength and varying output wavelength for input power of -6.4 dBm. (b) Measured power penalty (PP), output extinction ratio (ER), and conversion efficiency (CE) versus output wavelength.

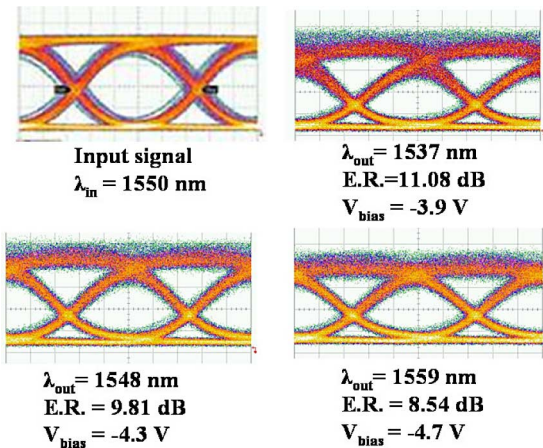


Fig. 19. 40 Gb/s NRZ input and wavelength-converted eye diagrams corresponding to the BER measurements in Fig. 18. Gate bias and output extinction are listed.

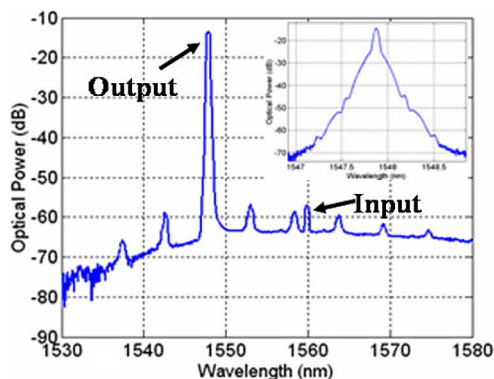


Fig. 20. Output optical spectrum from the wavelength converter demonstrating 45 dB input suppression. Inset shows higher resolution plot of the output signal with 40 Gb/s modulated data spectrum.

for each case. The summary of performance in Fig. 18(b) exemplifies the tradeoff introduced by the wavelength dependence of the EAM. For shorter wavelengths, the modulation efficiency is higher, which produces greater extinction. However, the passive optical loss is also increased, which leads to lower output power,

TABLE I
OPERATING CONDITIONS AND TOTAL POWER DISSIPATION

	V (V)	I (mA)	P (mW)
SG-DBR Gain	1.7	115	195.5
Trans. SOA	1.6	60	96
Rec. SOA 1	2.1	100	210
Rec. SOA 2	2.1	300	630
Mirrors / Phase	1.3	50	65
PD	-4.2	28	117.6
EAM 1	-4.2	12	50.4
EAM 2	-4.2	12	50.4
Load Resistor	1	40	40
Total			1454.9

and hence lower conversion efficiency. The opposite result occurs for the longer output wavelength; however, in all cases, the total power penalty remains relatively constant.

The optical spectrum of the converted output signal is shown in Fig. 20 for input and output wavelengths of 1560 and 1548 nm, respectively. Because of the spatial separation of the input and output signals within the device, the input suppression ratio at the output is greater than 40 dB. As shown in Fig. 20, the input power level is on the same order as the side-mode suppression of the SG-DBR laser.

The total power dissipation of the device has also been calculated. The normal operating conditions and the power contribution from each component on the chip are listed in Table I. During wavelength conversion of PRBS data, the total power dissipation is slightly lower than 1.5 W. For no input signal, or for bursts of data with short duty cycles, the power dissipation is reduced to around 1.35 W due to lower average photocurrent generated in the optical gate.

VI. LABEL WRITING

The capability of optical label writing with this device has been demonstrated using PRBS data to modulate the EAM in the other transmitter arm. A modulation rate of 10 Gb/s was chosen, since this slower data rate would be more easily processed in a realistic optical router. A 2.0-V peak-to-peak drive signal was

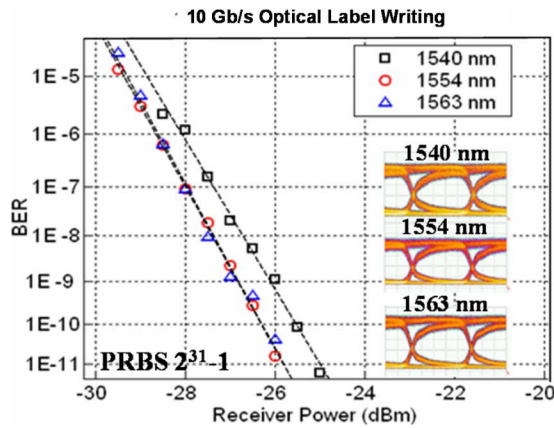


Fig. 21. BER measurements for external modulation of label-writing EAM at 10 Gb/s. Eye diagrams at each wavelength are shown.

applied by directly contacting the chip with a ground–signal–ground probe. Again, the dc bias for the EAM was adjusted to take advantage of the maximum modulation efficiency for each wavelength. Fig. 21 shows the BER for the 10 Gb/s modulation for varying output wavelengths. Less than 1 dB power penalty over the output tuning range was observed. The corresponding eyes diagrams demonstrate an output extinction ratio greater than 9 dB in all cases, and the output power was -6 to -6.5 dBm.

VII. CONCLUSION

This paper has presented a monolithic widely tunable wavelength converter based on a field-modulation technique. The device integrates a tunable SG-DBR laser, high saturation power SOAs, and high-speed EAM and PD, using a single regrowth fabrication process. The device geometry of each of the integrated components has been optimized to achieve efficient 40 Gb/s operation. The integrated receiver demonstrates >20 dB of gain and is capable of producing >30 mA of unsaturated photocurrent. The EAMs in this paper have demonstrated greater than 10 dB/V modulation efficiency over a wide optical bandwidth of 30 nm. Selective undercut etching and periodically loaded transmission lines have been used to double the characteristic impedance of the modulator for higher speed and increased voltage swing. Wavelength conversion has been demonstrated for 25 nm of input tuning and 22 nm output tuning, with 3 and 1 dB power penalty, respectively. The output extinction ratio of the converted signal was greater than 8 dB for all cases, with as high as -2 dB conversion efficiency. Conversion back to the same wavelength was demonstrated, as well as >40 dB input signal suppression at the output. This device also has been used for 10 Gb/s data transmission, which demonstrates potential for use in optical packet switched networks. Future work is focused on fast wavelength tuning to demonstrate packet routing as well as dynamic label encoding with simultaneous wavelength conversion. These experiments will confirm the viability of this wavelength converter in all-optical routing applications.

REFERENCES

- [1] S. Yoo, "Wavelength conversion technologies for WDM network applications," *J. Lightw. Technol.*, vol. 14, no. 6, pp. 955–966, Jun. 1996.
- [2] D. Blumenthal, B.-E. Olsson, G. Rossi, T. Dimmick, L. Rau, M. Masanovic, O. Lavrova, R. Doshi, O. Jerphagnon, J. Bowers, V. Kaman, L. Coldren, and J. Barton, "All-optical label swapping networks and technologies," *J. Lightw. Technol.*, vol. 18, no. 12, pp. 2058–2075, Dec. 2000.
- [3] M. Masanovic, V. Lal, J. Summers, J. Barton, E. Skogen, L. Rau, L. Coldren, and D. Blumenthal, "Widely tunable monolithically integrated all-optical wavelength converters in InP," *J. Lightw. Technol.*, vol. 23, no. 3, pp. 1350–1362, Mar. 2005.
- [4] V. Lal, M. Masanovic, J. Summers, L. Coldren, and D. Blumenthal, "Performance optimization of an InP-based widely tunable all-optical wavelength converter operating at 40 Gb/s," *IEEE Photon. Technol. Lett.*, vol. 18, no. 4, pp. 577–579, Feb. 2006.
- [5] P. Bernasconi, W. Yang, L. Zhang, N. Sauer, L. Buhl, I. Kang, S. Chandrasekhar, and D. Neilson, "40 Gbit/s RZ wavelength converter in a monolithically integrated chip with a tunable laser," *Electron. Lett.*, vol. 41, no. 12, pp. 701–702, 2005.
- [6] T. Yoshimatsu, S. Kodama, K. Yoshino, and H. Ito, "100-Gb/s error-free wavelength conversion with a monolithic optical gate integrating a photodiode and electroabsorption modulator," *IEEE Photon. Technol. Lett.*, vol. 17, no. 11, pp. 2367–2369, Nov. 2005.
- [7] M. Sysak, J. Raring, L. Johansson, H. Poulsen, J. Barton, D. Blumenthal, and L. Coldren, "Optical 2R and 3R signal regeneration in combination with dynamic wavelength switching using a monolithically integrated, widely tunable photocurrent driven wavelength converter," presented at the Eur. Conf. Opt. Commun. (ECOC), Cannes, France, Sep. 2006, Paper Th3.4.1.
- [8] M. M. Dummer, M. N. Sysak, A. Tauke-Pedretti, J. W. Raring, J. Klamkin, and L. A. Coldren, "Widely tunable separate absorption and modulation wavelength converter with integrated microwave termination," *J. Lightw. Technol.*, vol. 26, no. 8, pp. 938–944, Apr. 2008.
- [9] A. Tauke-Pedretti, M. Dummer, M. Sysak, J. Barton, J. Raring, J. Klamkin, and L. Coldren, "Monolithic 40 Gbps separate absorption and modulation Mach–Zehnder wavelength converter," in *Proc. Opt. Fiber Commun. Conf. (OFC) Postdeadline Papers*, Anaheim, CA, Mar. 2007, Paper PDP36.
- [10] M. Sysak, J. Raring, J. Barton, M. Dummer, D. Blumenthal, and L. Coldren, "A single regrowth integration platform for photonic circuits incorporating tunable SGDBR lasers and quantum-well EAMs," *IEEE Photon. Technol. Lett.*, vol. 18, no. 15, pp. 1630–1632, Aug. 2006.
- [11] Y. Muramoto, K. Kato, M. Mitsuhashi, O. Nakajima, Y. Matsuoka, N. Shimizu, and T. Ishibashi, "High-output-voltage, high speed, high efficiency uni-travelling-carrier waveguide photodiode," *Electron. Lett.*, vol. 34, no. 1, pp. 122–123, 1998.
- [12] N. Li, X. Li, S. Demiguel, X. Zheng, J. Campbell, D. Tulchinsky, K. Williams, T. Isshiki, G. Kinsey, and R. Sudharsanan, "High-saturation-current charge-compensated InGaAs-inp uni-traveling-carrier photodiode," *IEEE Photon. Technol. Lett.*, vol. 16, no. 3, pp. 864–866, Mar. 2004.
- [13] S. Demiguel, X. Li, N. Li, H. Chen, J. Campbell, J. Wei, and A. Anselm, "Analysis of partially depleted absorber waveguide photodiodes," *J. Lightw. Technol.*, vol. 23, no. 8, pp. 2505–2512, Aug. 2005.
- [14] V. Jayaraman, Z.-M. Chuang, and L. Coldren, "Theory, design, and performance of extended tuning range semiconductor lasers with sampled gratings," *IEEE J. Quantum Electron.*, vol. 29, no. 6, pp. 1824–1834, Jun. 1993.
- [15] Y.-J. Chiu, T.-H. Wu, W.-C. Cheng, F. Lin, and J. Bowers, "Enhanced performance in traveling-wave electroabsorption modulators based on undercut-etching the active-region," *IEEE Photon. Technol. Lett.*, vol. 17, no. 10, pp. 2065–2067, Oct. 2005.
- [16] T. Yamanaka, K. Tsuzuki, N. Kikuchi, E. Yamada, Y. Shibata, H. Fukano, H. Nakajima, Y. Akage, and H. Yasaka, "High-performance InP-based optical modulators," in *Proc. 2006 Nat. Fiber Opt. Eng. Conf. Opt. Fiber Commun. Conf.*, Anaheim, CA, 3 pp.
- [17] R. Lewen, S. Irmscher, U. Westergren, L. Thylen, and U. Eriksson, "Segmented transmission-line electroabsorption modulators," *J. Lightw. Technol.*, vol. 22, no. 1, pp. 172–179, Jan. 2004.
- [18] A. Tauke-Pedretti, M. Dummer, J. Barton, M. Sysak, J. Raring, and L. Coldren, "High saturation power and high gain integrated photoreceivers," *IEEE Photon. Technol. Lett.*, vol. 17, no. 10, pp. 2167–2169, Oct. 2005.



Matthew M. Dummer (S'06) received the B.S. degree in electrical engineering in 2002 from the University of Minnesota, Minneapolis, and the M.S. and Ph.D. degrees in electrical engineering in 2004 and 2008, respectively, from the University of California Santa Barbara (UCSB), Santa Barbara.

His thesis research focused on the development of high functionality photonic integrated circuits for wavelength conversion and optical routing. He also specialized in fabrication of high-power semiconductor optical amplifiers, and photodiodes, as well as traveling-wave circuit design for electroabsorption modulators. In 2008, he joined Vixar Inc. in Minneapolis, where he is currently working on the development of visible and long-wavelength vertical cavity surface emitting lasers (VCSELs).



Jonathan Klamkin (S'04) received the B.S. degree in electrical and computer engineering in 2002 from Cornell University, Ithaca, New York, the M.S. degree in electrical and computer engineering and the Ph.D. degree in materials from the University of California Santa Barbara (UCSB), Santa Barbara, in 2004 and 2008, respectively.

His thesis work focused on a novel coherent integrated receiver for highly linear microwave photonic links. In 2008, he joined the Electro-Optical Materials and Devices Group at MIT Lincoln Laboratory as a member of the Technical Staff. His research interests include the design, growth, fabrication, and characterization of widely-tunable semiconductor lasers, high power photodetectors, optical intensity and phase modulators, and semiconductor optical amplifiers for InP based photonic integrated circuits.



Anna Tauke-Pedretti (S'02–M'08) received the B.S. degree in physics and electrical engineering in 2001 from the University of Iowa, Iowa City, and the M.S. and Ph.D. degrees in electrical and computer engineering from the University of California Santa Barbara, Santa Barbara, in 2002 and 2007, respectively.

Her dissertation research involved the design, fabrication and testing of InP-based photonic integrated circuits for high-speed wavelength conversion. She has also developed monolithic high-speed transmitters and high-saturation power pre-amplified receivers. In 2008, she joined Sandia National Laboratories, Albuquerque, NM as a Senior Member of Technical Staff where she continues to work on the development of novel photonic integrated circuits.



Larry A. Coldren (S'67–M'72–SM'77–F'82) received the Ph.D. degree in electrical engineering from Stanford University, Stanford, CA in 1972.

He was engaged in research at Bell Laboratories for 13 years, where he was initially involved in the field of waveguided surface-acoustic wave signal processing devices and coupled-resonator filters and later developed tunable coupled-cavity lasers using novel reactive-ion etching (RIE) technology that he created for the new InP-based materials. In 1984, he joined the University of California Santa Barbara (UCSB), Santa Barbara, where he is currently the Fred Kavli Professor of optoelectronics and sensors and the Director of the Optoelectronics Technology Center, and was engaged in research on multiple-section tunable lasers, thus inventing, in 1988, the widely tunable multielement mirror concept. During the late 1980s, he also developed efficient vertical-cavity multiple-quantum-well modulators, which led to novel vertical cavity surface-emitting laser (VCSEL) designs that provided unparalleled levels of performance. In 1990, he cofounded Optical Concepts, later acquired as Gore Photonics, to develop novel VCSEL technology. In 1998, he cofounded Agility Communications to develop widely tunable integrated transmitters. His current research interests include developing new photonic integrated circuit (PIC) and VCSEL technology, including the underlying materials growth and fabrication techniques, creation of vertical and in-plane GaN-based emitters, efficient all-epitaxial InP-based VCSELs, and a variety of PICs incorporating numerous optical elements for widely tunable integrated transmitters, receivers, and wavelength converters. He has authored or coauthored more than 700 papers, five book chapters, one textbook, and is a holder of 36 patents.

Prof. Coldren has presented dozens of invited and plenary talks at major conferences. He is a Fellow of the Optical Society of America and the Institute of Electrical Engineers, and a member of the National Academy of Engineering. He was the recipient of the 2004 John Tyndall Award.

40 Gb/s Buffered 2x2 Optical Packet Switching Using Photonic Integrated Circuits

John P. Mack, Kimchau N. Nguyen, Matt M. Dummer, Emily F. Burmeister, Henrik N. Poulsen, Biljana Stamenic, Geza Kurczveil, John E. Bowers, Larry A. Coldren, and Daniel J. Blumenthal

Electrical and Computer Engineering Department, University of California, Santa Barbara

jmack@ece.ucsb.edu

Abstract: Contention resolution and forwarding of labeled optical packets at 40 Gb/s is demonstrated utilizing multiple InP based optical buffers and monolithic wavelength converters. Layer-2 packet recovery measurements are presented.

©2009 Optical Society of America

OCIS codes: (060.1810) Buffers, couplers, routers, switches, and multiplexers; (060.6719) Switching, packet

1. Introduction

Optical packet switching provides a means of communication that is high bit rate, transparent, and scalable [1]. In label switched optical packet switching, forwarding information and data are separated into lower bit rate headers and high bit rate payloads [2]. This allows for the use of low frequency electronics for processing headers and payload envelope information while transparently forwarding high bit-rate payloads optically at low switching speeds. Optical packet switches must operate asynchronously making optical buffering a necessary functionality for contention resolution to avoid temporal collisions of packets simultaneously destined for the same output port [3, 4]. Buffering of 40 Gb/s payloads has been shown previously utilizing an integrated 2x2 InP switch matrix with fiber delay lines [5]. Switches must also be able to dynamically route packets to different output ports. Wavelength converters (WCs) offer a scalable and fast switching solution. A monolithic wavelength converter based on a PD-EAM gate and SGDBR laser has been demonstrated to operate at any bit rate up to 40 Gb/s in both NRZ and RZ formats [6].

We demonstrate optical packet buffering utilizing packaged compact InP switches with fiber delay lines that erase 10 Gb/s headers and re-circulate 40 Gb/s payloads for contention resolution. Buffered 40 Gb/s payloads are then dynamically forwarded through the use of monolithic fast switching PD-EAM based wavelength converters. Buffering and forwarding decisions are made based on output destinations extracted from 10 Gb/s headers and envelopes of 40 Gb/s payloads.

2. Principle of Operation and Experimental Implementation

The basis of optical buffering, forwarding, and electronic lookup for a 2x2 optical data router is shown in Fig. 1. Transmitted optical packets occupy a timeslot (Ts) of 64 ns which consist of 128 bit NRZ headers at 10 Gb/s, 40 byte RZ payloads at 40 Gb/s, and 43.2 ns guard bands. The optical headers contain a label field that indicates the output port. The stream contains three packets and the labels alternate output port requests B, A, B respectively at a wavelength of 1560nm as shown in Fig. 2. The transmitted signal is split into two identical streams and injected to input A and input B of the system. The packet stream is optically tapped and the data enters a clock/data recovery circuit (CDR) and payload envelope detector (PED). In this experiment, a 10 GHz clock from the transmitter was used as the input of the clock recovery circuit so that the system was synchronous. Recovered headers and envelopes are sent to an FPGA based electronic channel processor (ECP) to determine the output port destination of the payloads based on the optical label and to provide a precise time reference for the payloads. The ECPs then forward the recovered payload envelopes as output port requests to a central arbiter for electronic lookup. The FPGA based arbiter uses a lookup table to determine contention and buffer control by comparing port requests and buffer queue signals. Based on the lookup table, the arbiter generates buffer control signals which pass a packet through, load a packet into the buffer, re-circulate a packet in the buffer, or unload a packet from the buffer. The arbiter also generates WC control signals which are used to switch wavelengths in order to forward packets. The buffer and WC control signals are then sent to the corresponding ECPs which forward the signals to the buffers and WCs. The buffers consist of packaged 2x2 InP switches driven by current DACs and RF opamp circuits. The fiber delay line, equivalent to 64ns, includes an attenuator, band pass filter and polarization controller. The buffers erase labels by turning SOAs off before the payloads and gating the payloads for buffering. Buffer A circulates packets 1, 2, 3 for 1, 0, 0 timeslots and buffer B circulates packets 1, 2, 3 for 0, 1, 1 timeslots respectively as shown in Fig. 2. The wavelength converters are

switched by modulating the front mirror of the SGDBR laser. WC A converts packets 1, 2, 3 to 1554, 1560, 1554 nm and WC B converts packets 1, 2, 3 to 1559, 1553, 1559 nm respectively as shown in Fig. 3. Band pass filters with a band width of 1.2 nm are used to simulate an arrayed waveguide grating (AWG). Here, the filters are tuned to 1560 nm for input A and 1553 nm for input B destined for output A and tuned to 1554 nm for input A and 1559 nm for input B destined for output B. New labels would then be written in front of the forwarded payloads.

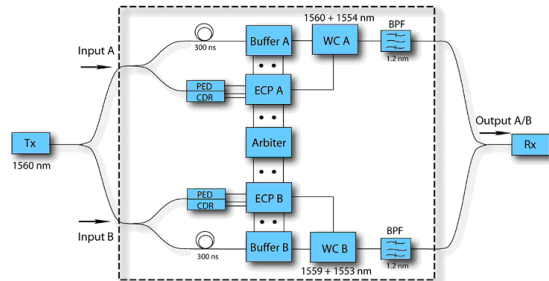


Fig. 1. Buffers, wavelength converters, and electronic lookup of a 2x2 optical packet switch

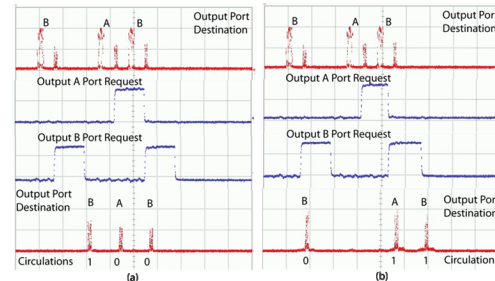


Fig. 2. Input packet stream, port request signals, and buffered payloads (a) channel A (b) channel B

3. Performance Measurements

Layer-2 packet recovery measurements were conducted for buffered packets that are dynamically wavelength converted. Packet recovery is a necessary measurement when small packets are used and rearranged but misaligned at the bit level. Packet recovery is defined as successful recovery of the entire 64 bit payload identifier followed by an 8 bit control field inside the payload. Curves were taken for back-to-back that contain headers and payloads as well as a stream that contained payloads only. Measurements were then taken for each buffered, converted, and filtered output separately. Greater than 92% packet recovery was achieved for all buffered and converted payloads. The large offset in curves is caused by the difference in duty cycles of the measured signals, insertion loss of the buffers, and extinction of the converted payloads as well as the use of a pre-amplified receiver.

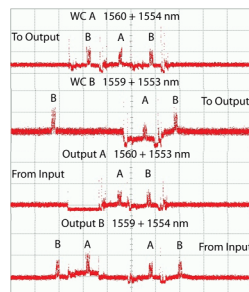


Fig. 3. Converted payloads of WC A/B and output A/B

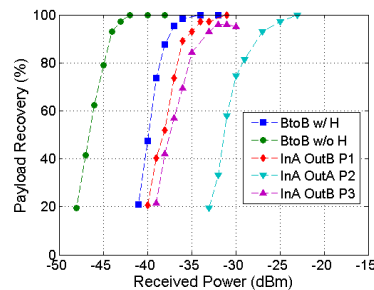


Fig. 4. Packet recovery for buffered and converted payloads from channel A.

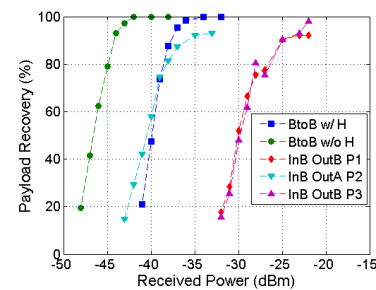


Fig. 5. Packet recovery for buffered and converted payloads from channel B.

4. Conclusions

Multiple packaged optical buffers and monolithic wavelength converters are used to demonstrate dynamic optical buffering and forwarding at 40 Gb/s. Forwarding and buffering decisions are determined for 40 Gb/s payloads from 10 Gb/s labels with greater than 92% packet recovery demonstrated.

4. Acknowledgement

This work is supported by DARPA/MTO and ARL under LASOR award #W911NF-04-9-0001.

5. References

- [1] G.I. Papadimitriou *et al.*, "Optical switching: switch fabrics, techniques, and architectures," *J. Lightw. Technol.*, vol. 21, no. 2, pp. 284-404, Feb. 2003.
- [2] S.J.B. Yoo, "Optical packet and burst switching technologies for the future photonic internet," *J. Lightw. Technol.*, vol. 24, no. 12, pp. 4468-4492, Dec. 2006.
- [3] D. Wolfson *et al.*, "All-optical asynchronous variable-length optically labeled 40 Gb/s switch," in *Proc. ECOC 2005*, Paper Th. 4.5.1.
- [4] D. K. Hunter *et al.*, "Buffering in optical packet switches," *J. Lightw. Technol.*, vol. 16, pp. 2081-2094, Dec. 1998.
- [5] E.F. Burmeister *et al.*, "SOA gate array recirculating buffer for optical packet switching," in *Proc. OFC 2008*, Paper OWE4.
- [6] M.M. Dummer *et al.*, "A bit-rate-transparent monolithically integrated wavelength converter," in *Proc. ECOC 2008*, Paper Th.2.C.1.

An 8x8 Monolithic Tunable Optical Router (MOTOR) Chip in InP

Steven C. Nicholes^{*}, Milan L. Mašanović[†], Erica Lively[†], Larry A. Coldren^{†,*}, and Daniel J. Blumenthal[†]

^{*}Department of Materials

[†]Department of Electrical and Computer Engineering
University of California, Santa Barbara 93106

Email: snicholes@engineering.ucsb.edu

Abstract: We demonstrate 10 Gbps error free operation through multiple ports of an InP monolithic tunable optical router consisting of eight input wavelength converters and an 8x8 passive arrayed-waveguide grating router.

1. Introduction

All-optical routing technologies are an attractive alternative to traditional electronic-based routing because of the potential to reduce power dissipation and the number of OEO interfaces [1]. Full on-chip switching functions can be realized by integrating wavelength converters and passive routers. This level of integration has the potential to reduce: (1) the overall device footprint; (2) discrete component-to-component coupling losses; and (3) packaging costs. Such benefits have been realized previously with the development of monolithically integrated all-optical wavelength converters [2,3].

We demonstrate the first reported 8x8 monolithic tunable optical router (MOTOR) in InP. Each MOTOR input port consists of a wavelength converter (WC) that is tunable across the C-band. The output of each wavelength converter is connected to the input of a passive 8x8 arrayed-waveguide grating router (AWGR) that performs channel switching to a certain output port based on the input wavelength. This switch requires the dense integration of more than 200 functional building blocks, including sampled-grating DBR (SG-DBR) lasers, multiple semiconductor optical amplifiers (SOAs), phase modulators, and an AWGR, representing one of the most complex InP photonic integrated circuits reported to date.

2. Device Design and Integration

As shown in Figure 1, the MOTOR chip consists of an array of eight widely-tunable WCs and an AWGR, resulting in an overall device footprint of 14.5 mm x 4.25 mm. Wavelength conversion is achieved through cross phase modulation effects in an SOA-based, differential Mach-Zehnder interferometer (MZI) [4]. 10 Gbps wavelength conversion in the NRZ format is accomplished by sending data into one branch of the MZI, with the input to the other branch turned off (i.e., the preamplifier SOA on this branch is not biased). The new wavelength of the converted data, which is set by the CW signal from an SG-DBR, determines the subsequent routing in the AWGR as explained in [5].

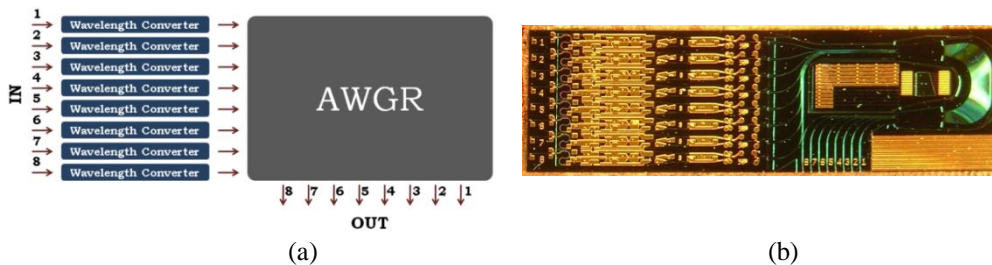


Figure 1: (a) Schematic overview of MOTOR architecture; (b) Photograph of fabricated device (area in the center of the AWGR consists of test structures that are not involved in device operation).

To realize the MOTOR chip, a platform consisting of multiple quantum wells (MQW) centered in the device waveguide was selected. Because of the high overlap of the optical mode with the MQW region, high gain regions that are ideal for the SG-DBR laser and the MZI SOAs can be achieved. However, the increase in gain comes at the expense of saturation power. While this is ideal to increase the nonlinear response of the MZI SOAs, the reduced

saturation power is problematic for the input preamplifier SOAs, whose length and overall gain are thus limited. For active/passive definition, quantum well intermixing was used to shift the as-grown MQW bandedge from 1545nm to 1420nm in all passive sections as described in [6]. The wavelength converters employ a surface ridge architecture, where a combination of dry and selective wet etching was used to etch ridges down to the top of the waveguide. An integrated delay line at the WC input [4] was fabricated exclusively by dry etching. To minimize the loss in the AWGR region, a buried rib waveguide structure was utilized. The loss in this region was further reduced by leaving an undoped implantation buffer layer (used in intermixing, but typically removed immediately thereafter) above the etched rib to create a setback from the Zn doped cladding as described in [7]. The advantage of this method is that it reduces optical loss in the AWGR region without the need of a special UID regrowth to bury the rib and separate the optical mode from Zn dopant atoms. As a result, the MOTOR chip required only a single, low-risk, blanket, p-type cladding regrowth. Minimizing the number and complexity of regrowth steps is essential to increase component yield.

3. Device Results

The MOTOR chip was tested using PRBS $2^{31}-1$ data streams at 10 Gbps. Only a single channel was tested at a given time. However, the single-channel crosstalk of the AWGR was measured to be 16 dB or greater (depending on the output port). The chip was soldered directly to a copper submount for efficient heat sinking. The submount was held at a temperature of 16°C for all experiments. The size of the chip prohibited sensible wire-bonding, so the metal pads were each directly probed.

Figure 2 shows wavelength converted eyes for six of the eight input ports. Although the individual SOAs worked on Inputs #1 and #5, these devices had a random material defect in the ridge near the MZI that prevented them from functioning as WCs. Figure 3 shows wavelength converted eyes out of every output port using a single input channel.

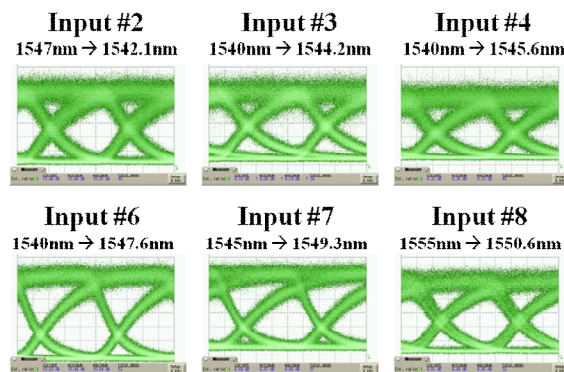


Figure 2: 10 Gbps eyes for the six working input channels measured out of output port #3.

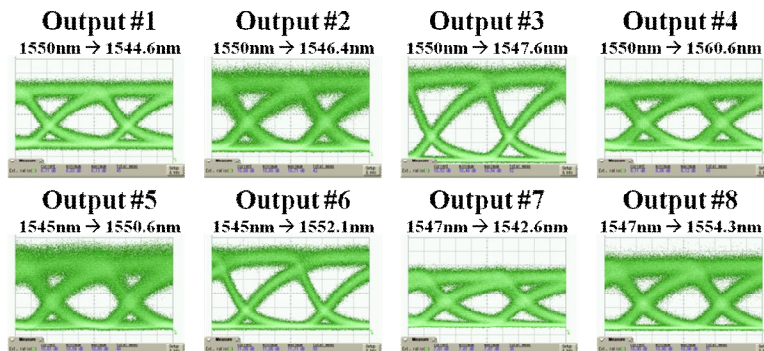


Figure 3: 10 Gbps eyes using input channel #6 measured out of every output port.

Finally, BER measurements were performed in order to determine the power penalty associated with 10 Gbps operation. Figure 4 shows BER curves for converted data along with back-to-back measurements for two of the six working input channels. The power penalty associated with the conversion at a BER of 10^{-9} ranges from 3.2 to 4.4 dB. One factor that contributes to this power penalty is the lack of antireflective (AR) coatings on the chip. Additionally, the preamplifiers have a low saturation power due to the centered MQW design, and this causes pattern dependence at longer pattern lengths. By employing an AR coating and an improved preamplifier design as in [8], this power penalty could be reduced.

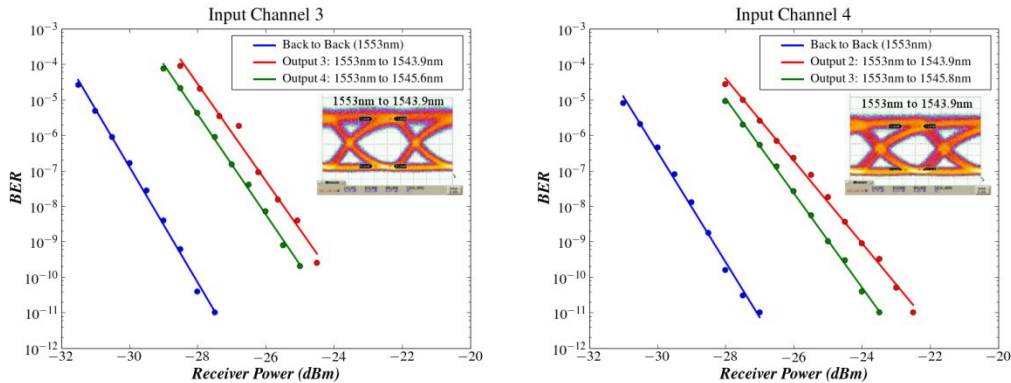


Figure 4: BER measurements for input channels 3 and 4. BERs are measured from two different output ports for each input port. Power penalties at a BER of 10^{-9} range from 3.2 to 4.4 dB.

4. Conclusions

Using a QWI platform with several ridge architectures, we have demonstrated a monolithic tunable optical router (MOTOR) in InP, consisting of eight input wavelength converters a passive AWGR. We have demonstrated error-free operation at 10 Gbps using six of the eight input channels and every output channel with a power penalty of 3.2 to 4.4 dB.

5. Acknowledgements

This work was supported by the DARPA MTO DOD-N Program under the LASOR Project (W911NF-04-9-0001). A portion of this work was done in the UCSB nanofabrication facility, part of the NSF funded NNIN network.

6. Reference

- [1] D. Blumenthal *et al.*, "All-optical label swapping networks and technologies," *JLT*, **18**, 2058-2075 (2000).
- [2] V. Lal *et al.*, "Quantum-well-intermixed monolithically integrated widely tunable all-optical wavelength converter operating at 10 Gb/s", *PTL*, **17**, 1689-1691, 2005.
- [3] M. Masanovic *et al.*, "Widely Tunable Monolithically Integrated All-Optical Wavelength Converters in InP," *JLT*, **23**, 1350-1362 (2005).
- [4] V. Lal *et al.*, "Monolithic Wavelength Converters for High-Speed Packet-Switched Optical Networks," *JSTQE*, **13**, 47-57 (2007).
- [5] M. Smit and C. van Dam, "PHASAR-Based WDM-Devices: Principles, Design and Applications", *JSTQE*, **2**, 236-250 (1996).
- [6] J. Raring *et al.*, "Advanced integration schemes for high-functionality high-performance photonic integrated circuits," in *Photonics Packaging and Integration VI*, Vol. 6126, (SPIE, San Jose, CA, 2006), Paper 61260H.
- [7] S. Nicholes *et al.*, "Novel Application of Quantum Well Intermixing Implant Buffer Layer to Enable High-Density Photonic Integrated Circuits in InP", in *Conf. on Indium Phosphide and Related Materials (IPRM, Newport Beach, CA, 2009)*, Paper WB1. 2.
- [8] J. Raring *et al.*, " Demonstration of high saturation power/high gain SOAs using quantum well intermixing based integration platform," *EL*, **41**, 1345-1346 (2005).

I. PIC Technology and Devices

C. RF-Photonics and Analog PICs

Highly Linear Integrated Coherent Receivers for Microwave Photonic Links

Jonathan Klamkin¹, Leif A. Johansson², Anand Ramaswamy², Nobuhiro Nunoya²,
Sasa Ristic², Uppili Krishnamachari², Janet Chen², John E. Bowers², Steven P.
DenBaars^{1,2}, Larry A. Coldren^{1,2}

¹Materials Department, University of California, Santa Barbara, CA 93106

²Electrical and Computer Engineering Department, University of California, Santa Barbara, CA 93106

Email: klamkin@engineering.ucsb.edu

Abstract: A coherent receiver with feedback was developed to linearly demodulate the phase of an analog signal. The receiver demonstrates a spur-free dynamic range of $125 \text{ dB}\cdot\text{Hz}^{2/3}$ at a signal frequency of 300 MHz.

©2009 Optical Society of America

OCIS codes: (250.5300) Photonic Integrated Circuits; (250.3140) Integrated Optoelectronic Devices

1. Introduction

Phase modulation can be used to improve the signal-to-noise ratio (SNR) and spur-free dynamic range (SFDR) of microwave photonic links because phase modulation is not limited in input modulation swing and is inherently linear using certain electro-optic devices [1]. To overcome the inherent nonlinearity of a traditional interferometer-based phase demodulator, a balanced receiver with feedback to a reference tracking phase modulator was developed (Fig. 1). The feedback reduces the phase difference between the signal and local oscillator. This effectively reduces the signal swing of the demodulator thereby suppressing the interferometer nonlinearities and leading to an improvement in SFDR. Balanced detection has several advantages such as the ability to suppress common mode relative intensity noise of the laser source as well as amplifier noise. Additionally, considering that most 2x1 combiners inherently exhibit a loss of 3 dB, a higher SNR can be achieved with balanced detection because the detected signal power is increased. Additionally, push pull drive to symmetric tracking phase modulators can be used to overcome the nonlinear characteristics of the integrated tracking phase modulator. For stable operation at high frequency the delay of the feedback loop must be kept short, therefore a monolithic approach is required to realize a compact receiver architecture. A similar feedback approach was demonstrated in [2] whereby an attenuation-counter-propagating phase modulator was employed, which is free of propagation delay.

The monolithic photonic integrated circuit (PIC) developed here consists of a high power balanced uni-traveling-carrier photodiode (UTC-PD), a compact 2x2 multimode interference (MMI) coupler, and multi-quantum well reference phase modulators. This PIC is hybrid integrated with an electronic integrated circuit (EIC) that provides transconductance amplification of the feedback signal for increased loop gain.

2. Device Design

For the integrated UTC-PDs, novel concepts such as absorption profile modification, charge compensation, and partially depleted absorption were incorporated to realize high saturation current and high linearity [3]. PD A

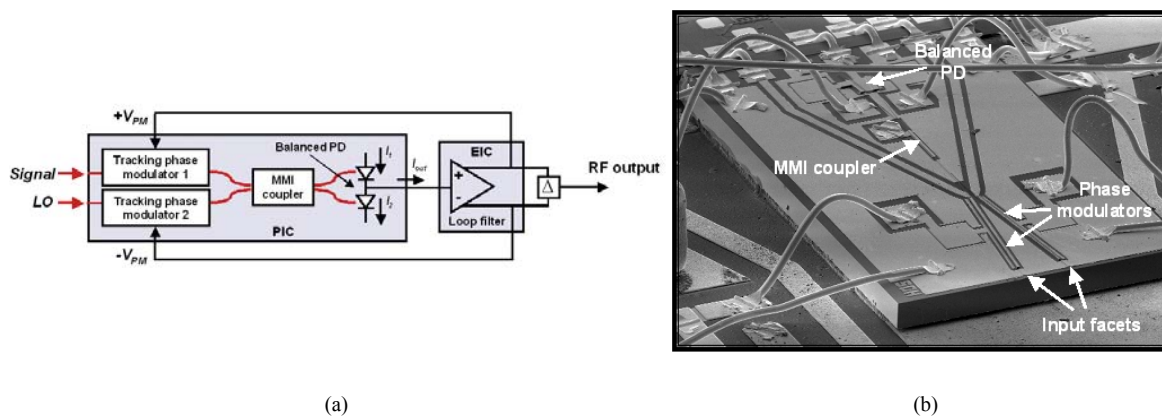


Figure 1. (a) Schematic of coherent integrated receiver with feedback and push-pull drive to tracking phase modulators. (b) Plan view SEM image of a PIC mounted on a carrier with an EIC (EIC out of view).

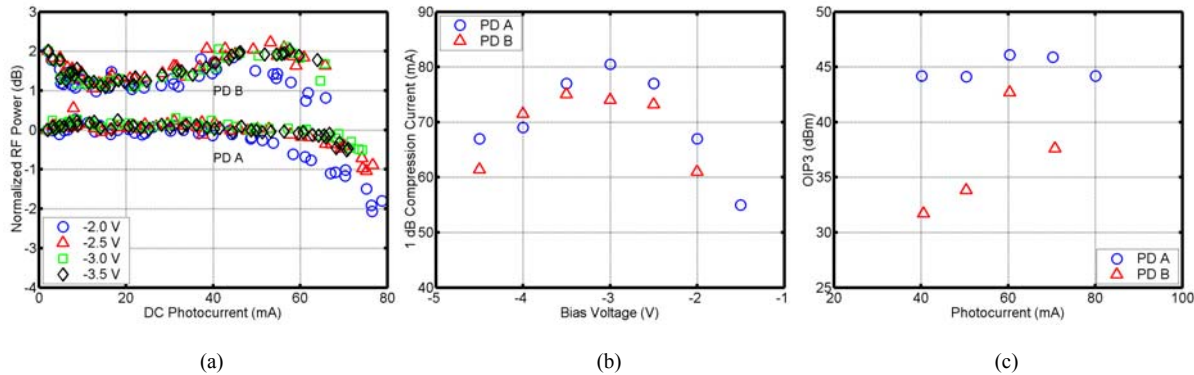


Figure 2. (a) Normalized RF power as a function of DC photocurrent at 1 GHz. The data for PD A is normalized to 0 dB and that for PD B to 2 dB. (b) 1-dB compression current as a function of bias voltage. (c) Two-tone OIP3 as a function of photocurrent.

incorporated a low overlap of the optical mode with the absorber layer resulting in a long absorption profile and low front-end saturation. PD B incorporated a collector doping of $3 \times 10^{16} \text{ cm}^{-3}$ and a low and graded absorber doping. Both general interference surface ridge (SR) MMI couplers and restricted interference deep ridge (DR) MMI couplers were explored, the latter for reducing the loop delay. Current injection tuning was incorporated into the

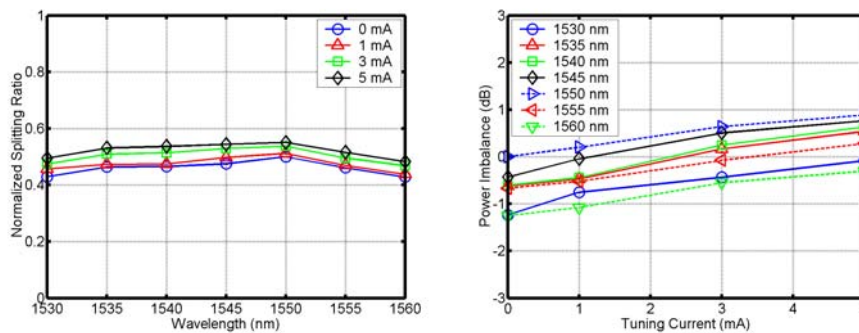


Figure 3. (a) Normalized splitting ratio as a function of input wavelength for various tuning currents. (b) Power imbalance as a function of tuning current for various wavelengths.

MMI couplers for fine tuning the output power splitting ratio [4]. The quantum well (QW) design of the reference phase modulators was optimized for realizing low V_π , low insertion loss, low absorption modulation, and improved linearity. Modulator A consisted of 28 compressively strained QWs, and 29 tensile strained barriers. The QW width was 50 Å, and the barrier width was 70 Å. The difference in energy between the QW and barrier in the conduction band was 97.3 meV. Modulator B contained 22 compressively strained QWs, and 23 tensile strained barriers. The QW width was 100 Å, the barrier width was 50 Å, and the conduction band energy difference was 69.6 meV. The PICs also incorporated quantum well intermixing (QWI) to shift the band edge of the QWs in the passive regions post growth to eliminate the tradeoff between phase modulation efficiency and passive loss.

3. Results and Discussion

Figure 2 shows the measurement results for the PDs. The peak 1 dB compression current for PD A and PD B was 80.5 mA and 75 mA respectively. The two-tone OIP3 for these PDs at 60 mA was 46.1 dBm and 42.7 dBm respectively. PD A was also measured at 80 mA and demonstrated an OIP3 of 44.2 dBm. The tuning properties of the SR MMI couplers were also characterized (Fig. 3). The output power splitting could be fine tuned to 3-dB splitting over a broad wavelength range with low levels of injected current. The efficiency, loss, and phase change were measured for the phase modulators (Fig. 4). The $V_\pi \cdot L$ of modulator A was 1.52 V·mm and that of modulator B was 1.29 V·mm. The loss incurred between 0 V and V_π and the insertion loss was 1.2 dB and 1.03 dB for modulator A, and 7.0 dB and 1.8 dB for modulator B. The ratio of the linear to cubic coefficient (A_1/A_3) was 19.5 for modulator A and 36.5 for modulator B.

OMK4.pdf

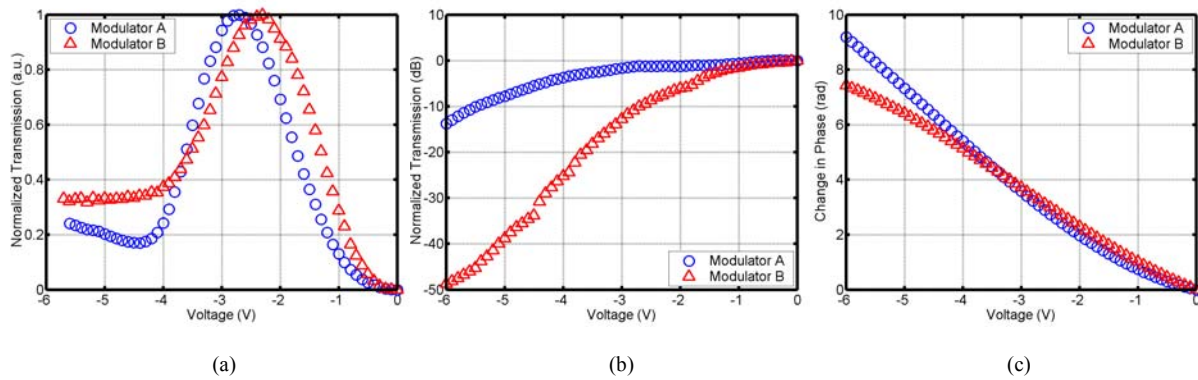


Figure 4. (a) Normalized MZM transmission, (b) normalized EAM transmission, and (c) phase change as a function of bias voltage.

The PIC and EIC were hybrid integrated on a common ceramic carrier. The chips were electrically connected with a series of wirebonds, which transport the differential output signal of the balanced PD from the PIC to the EIC, and the tracking phase modulator drive signal from the EIC to the PIC. Figure 5 shows the experimental setup used to characterize the integrated receivers and the results of SFDR measurements. Using the SR coherent receiver in a link experiment, the demonstrated SFDR for signal frequencies of 300 MHz, 500 MHz, and 1 GHz was $125 \text{ dB}\cdot\text{Hz}^{2/3}$, $121 \text{ dB}\cdot\text{Hz}^{2/3}$, and $113 \text{ dB}\cdot\text{Hz}^{2/3}$ respectively. Using a DR coherent receiver with QWI for low passive loss, and efficient phase modulators, the projected SFDR was improved by 6 dB.

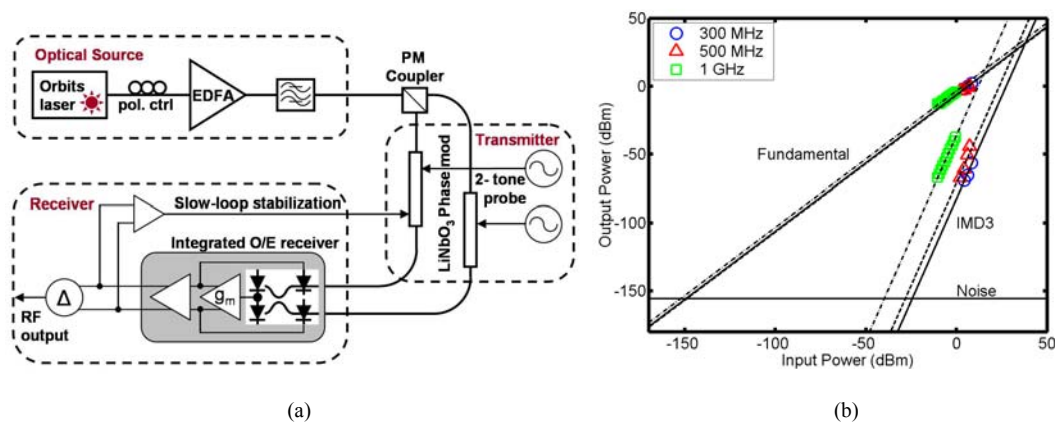


Figure 5. (a) Analog link experimental test setup. (b) SFDR measurements for different input signal frequencies.

4. Conclusions

A novel coherent receiver with feedback was developed to suppress the nonlinearities of an interferometer-based phase demodulator so that the advantages of phase modulation could be realized. When used in a link experiment, this receiver demonstrated up to a 14 dB improvement in SFDR compared to open loop operation (no feedback).

5. Acknowledgement

The authors acknowledge Northrop Grumman Space Technology for providing the EIC. This work was supported by the DARPA PHOR-FRONT program under USAF contract FA8750-05-C-0265.

6. References

- [1] L. A. Johansson, et al., *International Microwave Symposium (IMS)*, 2007.
- [2] Y. Li, P. R. Herczfeld, *Journal of Lightwave Technology*, vol. 24, pp. 3709-3718, 2006.
- [3] J. Klamkin, et al., *Device Research Conference (DRC)*, 2008.
- [4] J. Leuthold and C. H. Joyner, *Journal of Lightwave Technology (JLT)*, vol. 19, pp. 700-707, 2001.

Compact Beam Splitters with Deep Gratings for Miniature Photonic Integrated Circuits: Design and Implementation Aspects

Chin-Hui Chen,^{1,*} Jonathan Klamkin,² Steven C. Nicholes,³ Leif A. Johansson,¹
John E. Bowers,¹ and Larry A. Coldren^{1,3}

¹*Department of Electrical and Computer Engineering, University of California Santa
Barbara, Santa Barbara, CA, 93106, USA*

²*MIT Lincoln Laboratory, Lexington, MA, 02420, USA*

³*Department of Materials, University of California Santa Barbara,
Santa Barbara, CA, 93106, USA*

**Corresponding author: janet@ece.ucsb.edu*

We present an extensive study of an ultra-compact grating-based beam splitter suitable for photonic integrated circuits (PICs) which have stringent density requirements. The 10 μm long beam splitter exhibits equal splitting, low insertion loss, and also provides a high extinction ratio in an integrated coherent balanced receiver. We further present the design strategies for avoiding mode distortion in the beam splitter, and discuss the optimization of the widths of the detectors in order to improve insertion loss and extinction ratio of the coherent receiver circuit. In our study, we show that the grating-based beam splitter is a competitive technology having low fabrication complexity for ultra-compact PICs. © 2009 Optical Society of America

OCIS codes: 230.1360, 130.3120.

1. Introduction

In past few decades considerable attention has been given to waveguide beam splitters in optical integrated devices. With increasing demands on PIC performance, compactness requirements are becoming more stringent, similar to their electronic counterparts. For some applications with optical feedback circuits, such as optical phase-locked loops [1], the

system stability greatly relies on ultra-short loop delays.

Conventional directional couplers with dimensions of millimeters or more have become less attractive due to the chip size requirements. The size of a conventional surface ridge multimode interference (MMI) beam splitter is usually limited by lithographic resolution of the gap between access waveguides since the interaction length is proportional to square of its width. Moreover, long curves and S-bends are also necessary in order to separate the access beams for fiber coupling or integration with other components. Such fundamental attributes hinder the progress of device downsizing. Though significant efforts have been made to achieve interference lengths on the order of $100\ \mu\text{m}$ [2–5]; these components typically pay the price of higher insertion loss and lower fabrication tolerance. Alternatively other advanced technologies such as photonic crystals [6–9] and air trenches [10, 11] have been used to construct beam splitters in the submicron range. However, the performance of these beam splitters, unfortunately, is sensitive to process variations, and their applications are limited by fabrication complexity and low throughput.

The criteria for designing an ultra-compact beam splitter must also include the relative sizes of other integrated components. In present PIC technologies, the overall device sizes and the propagation lengths in a feedback loop are still dominated by the sizes of other elements such as modulators, detectors and connecting waveguides, which are typically hundreds of microns long or more. Therefore, it is beneficial to reduce the size of the beam splitter from millimeters to several microns for the purpose of minimizing the total device footprint and the signal propagation delay, but there is only a minor improvement to advance from microns to submicron range.

In this paper we present a comprehensive study of a proposed grating-based beam splitter [12, 13] which uses a $10\ \mu\text{m}$ -long ultra-compact strong interference region for equal splitting. This beam splitter is carried out by well-established and robust fabrication steps that enable potentially large throughput, and is compatible with existing integration platforms. The orientation of the splitter allows input beams to be coupled from opposing facets, which is advantageous in simplifying fiber alignment and packaging. These key advantages make the grating-based beam splitter a desirable and yet practical solution compared with other advanced technologies.

2. Beam Splitter Design

The goal of this work is to realize an integrated beam splitter with equal splitting, low insertion loss, short propagation length, as well as a high degree of interference between the incoming lights. Fig. 1(a) and 1(b) show the configuration of the compact 2×2 grating-based beam splitter with integrated modulators and photodetectors which are used in this work to obtain the data presented below.

2.A. Design Issues and Key Features

The grating region splits an incoming beam into transmissive (undiffracted) and reflective (diffracted) beams. Similar to Bragg diffraction in planar phase gratings [14], geometric and diffraction beam walk-off plus unequal mode distortion, however, arise in the case of oblique incidence of a finite beam onto a relatively thick grating region. The oblique multiple reflections from a series of grating grooves widen the reflective beams, and this widening becomes more pronounced with larger angles. On the other hand, the mode distortion is due to the continuous energy exchange between the diffracted and undiffracted beams during the interference process [14]. As a result, the interference extinction ratio between the two output beams could be severely decreased if falling into the degraded regime. Qualitatively speaking, it is important to keep the input angle near normal incidence and to arrange the beam size comparable to or wider than the grating length at the grating region.

In order to avoid the mode degradation, three design features are implemented. First, we design a quasi free space region surrounding the gratings for the purpose of expanding the beams within the shortest propagation distance. The beams diverge freely in the lateral direction without seeing the waveguide boundary and are only confined in the transverse direction in this region. Broadening a beam width wider than the grating length helps alleviate the mode distortion. We utilize a beam propagation method to simulate the mode expansion behavior in this region compared to one using a linear flaring. As shown in Fig. 2, the slope of beam widths to propagation distances in the quasi free space case is about 5 to 12 times larger than the linear cases, depending on the designated percentage of mode transfer. The beam divergence in a quasi free space region is shown to be much faster than the one in a conventional linear adiabatic tapering. This feature minimizes the traveling distance from the input waveguides to the output detectors and therefore keeps a compact device footprint and a small signal path in a feedback loop. In addition, it is also beneficial to reduce the detector front end saturation.

Second, we design input waveguides to have a small incident angle in order to eliminate

the beam walk-off. The lower bound of the incident angle is limited by the asymptotic line of the Gaussian beam divergence in the quasi free space region, which is determined by

$$\Theta \cong \frac{w(z)}{z} = \frac{\lambda}{\pi w_o}, \quad (1)$$

where $w(z)$ is the beam width at z distance along propagation, w_o is the beam waist, and λ is the beam wavelength in the waveguide. The asymptotic angle is calculated to be 2.89° in our design. Although a small incident waveguide angle helps relieve the beam walk-off effect, the trade-off is the long distance used to distinguish the beams on the same side of the gratings. A waveguide angle of 10° from normal incidence to the grating grooves is selected instead of one that close to the asymptotic angle. It is simulated to still be small enough to avoid mode distortion and to be sufficiently large to differentiate the beams within reasonably short total propagation length.

Third, we design a strongly reflective Bragg grating for 1550 nm wavelength in order to achieve the targeted reflection with an ultrashort coupling length. Fig. 3(a) illustrates the cross-section of the grating region with a maximal coupling coefficient (κ) by replacing the multiple quantum well (MQW) slab waveguide periodically with regrown InP material (Fig. 3(b)) to achieve a high reflectivity. It allows the grating grooves to interfere with the beams symmetrically in the vertical plane along the propagation direction; therefore, implies a small scattering loss. More details are given in the following paragraphs.

2.B. Models

The design principle of the grating-based beam splitter is further analyzed by both a horizontal model and a vertical FDTD model. Since in the quasi free space region the beam is only confined in the vertical (transverse) dimension, decomposing the problem into two 2-D models, horizontal (x-z plane) and vertical (y-z plane) ones, should not lose its generality but rather reduces the complexity and saves computing resources. In the horizontal model, the time monitor is used to mimic the functionality of the detector by recording the power flow along the propagation direction. We first study the case of one input with equal splitting as shown in Fig. 4(a) and 4(b). With the input beam equally bisected into transmission and reflection parts by the grating region, the second input is then introduced symmetrically in the model. Fig. 5 and Fig. 6 show the interference phenomenon resulting from the phase difference of the two input beams. The simulated numerical results are also shown in Table 1. They demonstrate that more than a 16 dB extinction ratio is theoretically achievable with the selected 10° incident angle at equal splitting.

The exact centered-MQW waveguide layer structure with a total thickness of 3695 Å is constructed in a FDTD vertical model. The radiation losses caused by different grating etch depth is studied as shown in Fig. 7. For shallow etch depths, the corrugated grating can be seen as small perturbation which is usually studied by coupled-mode theory, and its radiation loss is negligible. As the etch depth gets deeper, the mismatch increases between the unperturbed waveguide mode and the grating Bloch mode. The transverse displacement originates from the asymmetric material index that the mode experiences in the grating region. The loss passes through a maximum at an etch depth of around half the waveguide thickness, and the loss rolls off with deeper grooves. When the etch depth is deeper than the entire slab waveguide thickness, a symmetric waveguide is created and thus the radiation loss is reduced [15, 16].

3. Device Fabrication and Experiments

The integrated receiver as shown in Fig. 1(a) consists of a balanced uni-traveling-carrier photodiode (UTC-PD), a compact 2×2 grating-based beam splitter, and MQW phase modulators. The device is grown on an InGaAsP/InP integration platform with the UTC-PD structure grown above the waveguide. After defining the UTC-PD, deep gratings grooves are formed before the p-cladding and p-contact layer regrowth.

The gratings are patterned on a SiO₂ hard mask using holographic exposure and then transferred to the semiconductor by methane/hydrogen/argon (MHA)-based reactive ion etching (RIE) with hybrid oxygen cycling [17]. The maximal index contrast in the grating region can be achieved by etching the grating grooves through the entire slab waveguide layer. For the slab waveguide thickness used on our integration platform, grating grooves with an aspect-ratio of almost 3 : 1 are needed for an operating wavelength around 1.55 μm. As discussed in the previous section, the deeply etched grating region ensures a minimal total grating length and a low scattering loss. It is also equally important to have a high quality p-cladding regrowth over the grating region to keep the loss low. The fabricated gratings as shown in Fig. 3(b) shows no apparent air voids, which suggests low scattering losses at the regrowth interface. One note worth mentioning is that the grating structure with controlled dimensions is achieved without the need for costly electron beam lithography. It is a robust, well-developed, low cost and high throughput process, and is also compatible with other fabrication steps without obvious additional cost.

To realize our design goals — equal splitting and a short signal path — key design parameters are shown in Fig. 8. The distance between the modulator and the detector is kept the same for all cases and thus the beam divergence is virtually the same. The diverged

beam widths at different propagation distances are arranged to be $3 \mu\text{m}$ at the input end from the modulator, $10 \mu\text{m}$ at the grating region, and $12 \mu\text{m}$ at the detector front end. In order to study the grating reflectivity and mode distortion effects, we investigated a total of nine combinations of three different grating lengths ($5 \mu\text{m}$, $10 \mu\text{m}$, and $15 \mu\text{m}$) and three different detector widths ($7 \mu\text{m}$ (S), $12 \mu\text{m}$ (M), and $23 \mu\text{m}$ (L)). The middle grating length is selected to match the beam width at the grating region, and the middle detector width is selected to match the beam width at the detector front end. All detectors are $100 \mu\text{m}$ long, which is sufficient to absorb most of the incident light.

4. Results and Discussion

4.A. Splitting Performance

The peak splitting efficiency at the Bragg wavelength for both the FDTD simulations and experimental data are listed in Table 1 and Table 2. The FDTD simulation data in the case of a time monitor with a width equal to $Det L$ are the same as the case of infinite width. Thus the width of $Det L$ is considered wide enough to capture all the incoming light and should be independent of mode distortion.

The measured splitting spectra of all nine combinations are shown in Fig. 9 and the peak reflectivity of each case is also plotted in Fig. 10. The splitting ratios of $L_g = 5 \mu\text{m}$ and $L_g = 10 \mu\text{m}$ cases show little dependence on detector widths. It is very consistent with the simulation results, and it further confirms that the mode distortion has only marginal effects for a thin grating case. On the other hand, when the grating length becomes larger than the interacting beam width, as the case of $L_g = 15 \mu\text{m}$, the measured splitting ratios differ from each other for different detector widths. The beam walk-off effect and the mode distortion are more pronounced in this regime, which results in unequal distortion in transmissive and reflective beams, as explained in [14].

In Fig. 10 we show the well-known tanh-relation [18] between reflectivity and the product of $\kappa \cdot L_g$ with some reasonable assumptions as described below. For an ideal square grating, the reflective coefficient (r_g) and coupling coefficient (κ) can be expressed as follows:

$$|r_g| = \tanh(\kappa \cdot L_g), \quad (2)$$

$$\kappa = \frac{2\Delta n}{\lambda_o}, \quad (3)$$

where Δn is the index contrast between the two alternating layers and λ_o is the Bragg wavelength in vacuum. Here we have made two assumptions to better fit the tanh-curve to

our data:

$$\kappa_{eff} = \eta \cdot \kappa, \quad 0 \leq \eta \leq 1 \quad (4)$$

$$|r_g|_{eff} = \alpha \cdot \tanh(\kappa_{eff} \cdot L_g), \quad 0 \leq \alpha \leq 1 \quad (5)$$

Eq. (4) assumes the effective coupling coefficient to be $\eta = 77\%$ of the ideal κ , and Eq. (5) assumes that the reflectivity saturates at $\alpha = 80\%$ of the total incident light. Since the ideal κ is calculated for a rectangular grating profile, the value of η is reasonable when we account for the profile roundup due to processing imperfection such as mask erosion and element exchange during regrowth, as well as the barely etched-through grating grooves. The saturation in the curve for longer gratings can be explained by the fact that the overlap between the grating thickness and the mode profile in the transverse plane is not unity and some parts of the incident wave are transmitted through the deep grating region without experiencing interference [15].

4.B. Insertion loss

The measured insertion loss data shown in Fig. 11 include information about: (1) the propagation loss from the modulator to the detector; (2) the detector mismatch loss; (3) the grating loss. Presumably the propagation loss should be identical in all cases since the waveguide geometry is intentionally kept the same.

If we exclude the mismatch loss for the case of *Det-L* as discussed before, the insertion loss should only include the constant propagation loss and the grating loss. The material propagation loss is measured from a separate measurement to be 0.5 dB, and therefore the grating scattering loss should be not greater than 1.5 dB if the waveguide scattering loss is also taken into account. In this case, the insertion loss only exhibits slight dependence on the grating length within the range of interest. The insertion loss of the grating lengths $L_g = 5 \mu\text{m}$ and $10 \mu\text{m}$ for the case of *Det-M* are very similar to those of *Det-L*, which implies that most of the incident beams are still within a range equal to *Det-M*. As for the case of $L_g = 15 \mu\text{m}$, the loss difference between *Det-M* and *Det-L* can be seen as an evidence of mode distortion since some light is not captured by *Det-M* due to mode deformation by the thick grating. Lastly for the case of *Det-S*, another 3 to 4 dB loss for all three grating lengths is observed. Since it is designed to be narrower than the beam width on purpose as explained below, a mismatch-induced excitation loss indeed shows up as expected.

4.C. Extinction ratio

The extinction ratio between the constructive and destructive interferences of two beams that come from the two nominally identical MQW phase modulators is also characterized. The simulated and experimental data of extinction ratios are also shown in Table 1 and Table 2. We can easily see that the case of $L_g = 10 \mu\text{m}$ has the greatest extinction ratio among all three grating lengths because of the most equal splitting and therefore best cancelation. The price of the mismatch loss for the case of *Det-S* is paid back in the extinction ratio as it exhibits the greatest extinction ratio among three detector widths. Because the thick grating distorts the transmissive and reflective beams differently, a narrow detector at the center of the beam should only capture the portions that interfere most effectively. This clearly demonstrates the trade-off between mismatch loss and extinction ratio.

According to the discussion above, one may design a compact grating-based beam splitter with a proper choice of detector width to have both low insertion loss and high extinction ratio. As demonstrated in this work, high extinction ratio and low insertion loss as well as nearly equal splitting are achievable with a $10 \mu\text{m}$ long grating and a $12 \mu\text{m}$ wide photo detector.

5. Conclusion

In this paper, we present a comprehensive study of a proposed ultra-compact grating-based beam splitter. The fabricated devices experimentally validated our theoretical analysis and simulation data with a high degree of consistency. The design variety of nine different combinations demonstrates the properties of splitting ratio, insertion loss, and extinction ratio. It also provides guidance for a future design. The tradeoff between insertion loss and extinction ratio by varying the detector width is also clear.

An ultra-compact beam splitter with equal splitting, approximately 14 dB extinction ratio, and as low as 2 dB insertion loss has been achieved with only $10 \mu\text{m}$ long interference region. The grating-based beam splitter is proven to be attractive for compact PICs that require a small loop delay, a minimal device size and low fabrication complexity.

Acknowledgments

This work was supported by DARPA via the PHOR-FRONT program under the United States Air Force Contract. A portion of this work was done in the UCSB nanofabrication facility, part of the NSF funded NNIN network.

References

1. A. Ramaswamy, L. Johansson, J. Klamkin, C. Sheldon, H. Chou, L. Rodwell, M.J. Coldren, and J. Bowers, "Coherent receiver based on a broadband optical phase-lock loop," in "Optical Fiber communication/National Fiber Optic Engineers Conference, OFC/NFOEC," (2007).
2. L. Spiekman, Y. Oei, E. Metaal, F. Green, I. Moerman, and M. Smit, "Extremely small multimode interference couplers and ultrashort bends on InP by deep etching," *Photonics Technology Letters, IEEE* **6**, 1008–1010 (1994).
3. Y. Ma, S. Park, L. Wang, and S. T. Ho, "Ultracompact multimode interference 3-db coupler with strong lateral confinement by deep dry etching," *Photonics Technology Letters, IEEE* **12**, 492–494 (2000).
4. C. Janz, B. Keyworth, W. Allegretto, R. Macdonald, M. Fallahi, G. Hillier, and C. Roldand, "Mach-Zehnder switch using an ultra-compact directional coupler in a strongly-confining rib structure," *Photonics Technology Letters, IEEE* **6**, 981–983 (1994).
5. D. Levy, K. H. Park, R. Scarmozzino, J. Osgood, R.M., C. Dries, P. Studenkov, and S. Forrest, "Fabrication of ultracompact 3-db 2x2 MMI power splitters," *Photonics Technology Letters, IEEE* **11**, 1009–1011 (1999).
6. C.-C. Chen, H.-D. Chien, and P.-G. Luan, "Photonic crystal beam splitters," *Appl. Opt.* **43**, 6187–6190 (2004).
7. T. F. Krauss, "Planar photonic crystal waveguide devices for integrated optics," *physica status solidi (a)* **197**, 688–702 (2003).
8. Y. Zhang, Y. Zhang, and B. Li, "Optical switches and logic gates based on self-collimated beams in two-dimensional photonic crystals," *Opt. Express* **15**, 9287–9292 (2007).
9. P. Pottier, S. Mastroiacovo, and R. M. De La Rue, "Power and polarization beam-splitters, mirrors, and integrated interferometers based on air-hole photonic crystals and lateral large index-contrast waveguides," *Opt. Express* **14**, 5617–5633 (2006).
10. Y. Lin, N. Rahmanian, S. Kim, and G. Nordin, "Fabrication of compact polymer waveguide devices using air-trench bends and splitters," in "Southeastcon, 2008. IEEE," (2008), pp. 421–426.
11. Y. Lin, N. Rahmanian, S. Kim, and G. P. Nordin, "Compact and high efficiency polymer air-trench waveguide bends and splitters," (*SPIE*, 2007), vol. 6462, p. 64620V.
12. C.-H. Chen, M. Sysak, J. Klamkin, and L. Coldren, "Ultra-compact grating-based 2 x 2 beam splitter for miniature photonic integrated circuits," in "Lasers and Electro-Optics Society, 2007. LEOS 2007. The 20th Annual Meeting of the IEEE," (2007), pp. 784–785.
13. C.-H. Chen, J. Klamkin, L. A. Johansson, and L. A. Coldren, "Design and implementation of ultra-compact grating-based 2 x 2 beam splitter for miniature photonic integrated

- circuits,” in “Optical Fiber communication/National Fiber Optic Engineers Conference, 2008. OFC/NFOEC 2008. Conference on,” (2008), pp. 1–3.
14. M. R. Wang, “Analysis and observation of finite beam Bragg diffraction by a thick planar phase grating,” *Appl. Opt.* **35**, 582–592 (1996).
 15. J. Ctyroky, S. Helfert, and R. Pregla, “Analysis of a deep waveguide Bragg grating,” *Optical and Quantum Electronics* **30**, 343–358 (1998).
 16. M. Palamaru and P. Lalanne, “Photonic crystal waveguides: Out-of-plane losses and adiabatic modal conversion,” *Appl. Phys. Lett.* **78**, 1466–1468 (2001).
 17. J. E. Schramm, D. I. Babic, E. L. Hu, J. E. Bowers, and J. L. Merz, “Fabrication of high-aspect-ratio inp-based vertical-cavity laser mirrors using $\text{CH}_4/\text{H}_2/\text{O}_2/\text{Ar}$ reactive ion etching,” *Journal of Vacuum Science & Technology B: Microelectronics and Nanometer Structures* **15**, 2031–2036 (1997).
 18. S. Corzine, R. Yan, and L. Coldren, “A tanh substitution technique for the analysis of abrupt and graded interface multilayer dielectric stacks,” *Quantum Electronics, IEEE Journal of* **27**, 2086–2090 (1991).

Table 1. FDTD simulations on splitting and extinction ratio.

$W_d \backslash L_g$	Rx	Ext	Rx	Ext	Rx	Ext
	5 μm		10 μm		15 μm	
7 μm (<i>S</i>)	21.97 %	10.19 dB	53.86 %	21.15 dB	75.20 %	9.90 dB
12 μm (<i>M</i>)	21.64 %	10.03 dB	51.71 %	17.29 dB	70.71 %	9.53 dB
23 μm (<i>L</i>)	21.62 %	10.00 dB	51.34 %	16.05 dB	68.91 %	8.72 dB

Table 2. Experimental data on splitting and extinction ratio.

$W_d \backslash L_g$	Rx	Ext	Rx	Ext	Rx	Ext
	5 μm		10 μm		15 μm	
7 μm (<i>S</i>)	19.52 %	–	50.89 %	18.00 dB	70.25 %	–
12 μm (<i>M</i>)	18.41 %	–	48.03 %	13.88 dB	64.61 %	9.56 dB
23 μm (<i>L</i>)	20.66 %	–	48.98 %	–	57.37 %	7.91 dB

List of Figures

1	13
2	Comparison of field 1/e width of quasi free space expansion and linear flaring along propagation direction. Different mode expansion speeds in linear flaring give different power transfer percentages (e.g. 90 %, 95 % and 99 %).	13
3	14
4	14
5	FDTD simulation of the grating splitter with two inputs in different phase relations.	15
6	The simulated power at two output ports versus the phase difference of two inputs. The input power of each beam is set to one.	15
7	The FDTD simulated loss versus grating etch depth in the vertical model. Total slab waveguide thickness is 3695 μm	16
8	Beam divergence in the quasi free space region. The beam waist is 3 μm at the input from modulator, 10 μm at the grating region, and 12 μm at the detector front end. Different detector widths are also illustrated in blue (S), red (M), and green (L).	16
9	Measured splitting spectra of nine different combinations with different detector widths and different grating lengths. Red (lower) lines represent the reflection and blue (upper) lines represent the transmission.	17
10	Photocurrent splitting ratio versus grating length. Lines are from modeling and circles are the measured data.	17
11	Measured insertion loss data versus grating lengths.	18

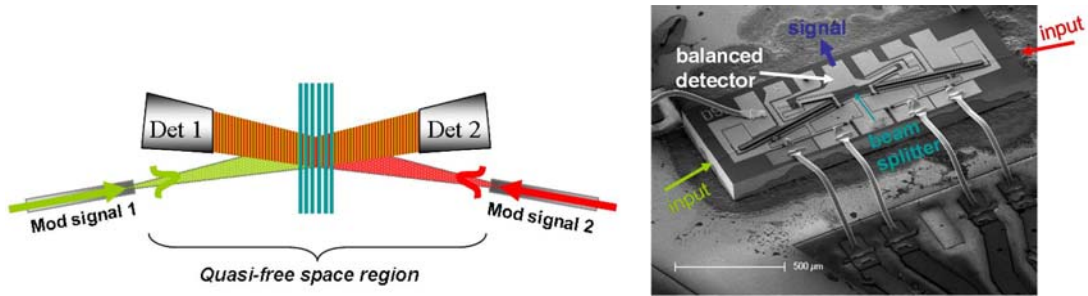


Fig. 1. (a) Schematic top view of 2x2 grating-based beam splitter which is integrated with two modulators and two photodetectors. Waveguide boundary (not shown) is far away from the diverged beams in the quasi free space region.

(b) SEM of integrated compact beam splitter on carrier. Two fiber coupled incoming beams are illustrated with arrows in red and green.

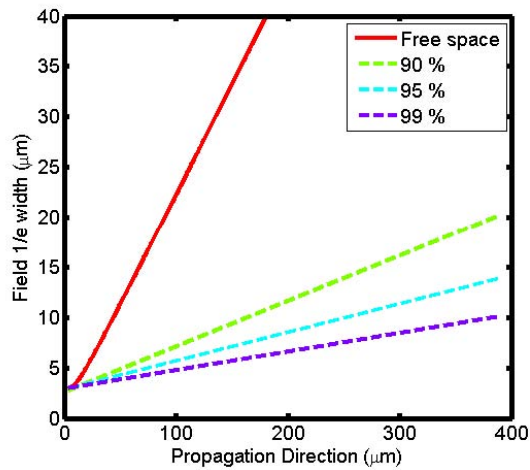


Fig. 2. Comparison of field 1/e width of quasi free space expansion and linear flaring along propagation direction. Different mode expansion speeds in linear flaring give different power transfer percentages (e.g. 90 %, 95 % and 99 %).

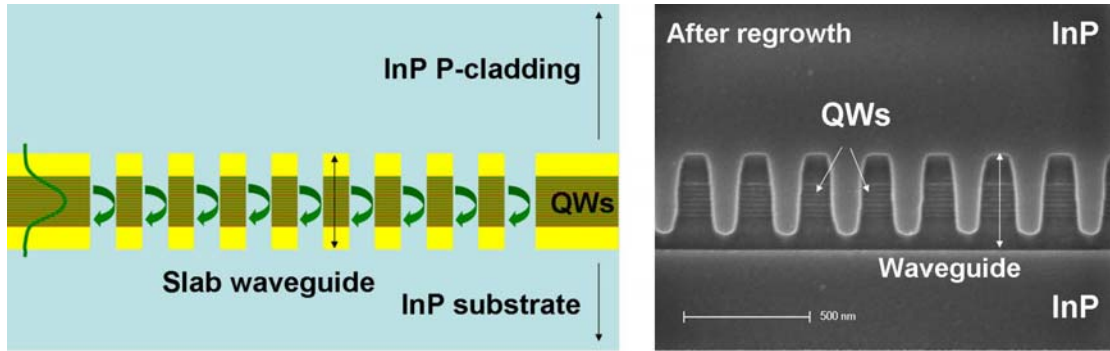


Fig. 3. (a) Schematic side view of the grating region. The beam is only confined in vertical direction. (b) Regrown gratings cross-section. The slab waveguide layer which contains multiple centered quantum wells can be clearly seen. No obvious air void is observed at the regrowth interface.

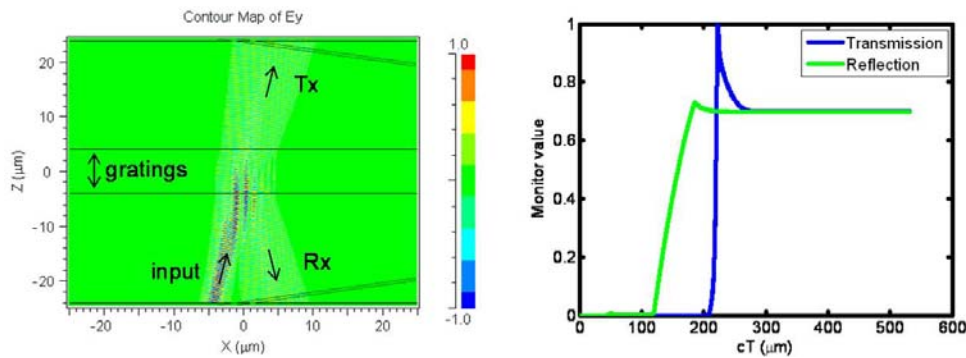


Fig. 4. FDTD simulation of the Bragg grating splitter with one input at equal splitting condition. (a) FDTD color-coded contour plot of the optical field. (b) Time monitor outputs at transmission and reflection versus time in units of cT (μm) where c is the speed of light in vacuum.

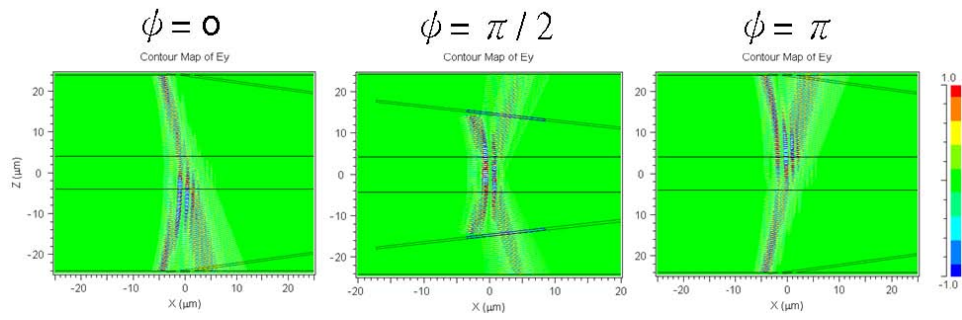


Fig. 5. FDTD simulation of the grating splitter with two inputs in different phase relations.

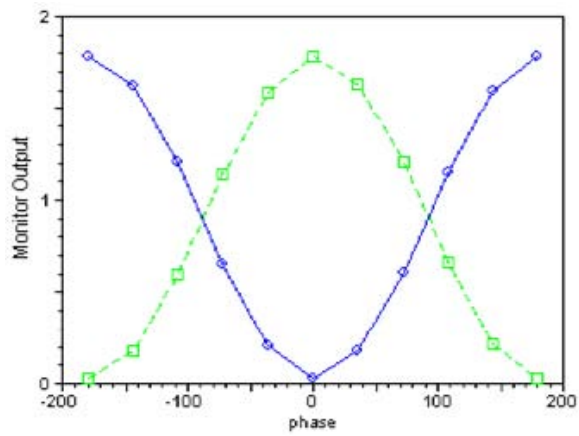


Fig. 6. The simulated power at two output ports versus the phase difference of two inputs. The input power of each beam is set to one.

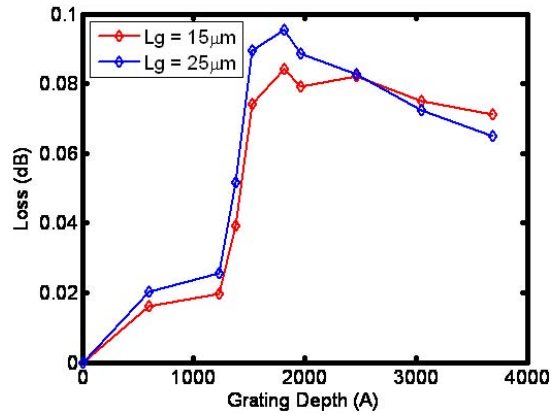


Fig. 7. The FDTD simulated loss versus grating etch depth in the vertical model. Total slab waveguide thickness is 3695 Å.

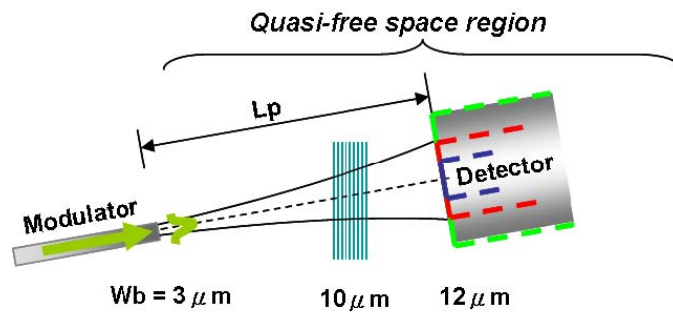


Fig. 8. Beam divergence in the quasi free space region. The beam waist is 3 μm at the input from modulator, 10 μm at the grating region, and 12 μm at the detector front end. Different detector widths are also illustrated in blue (S), red (M), and green (L).

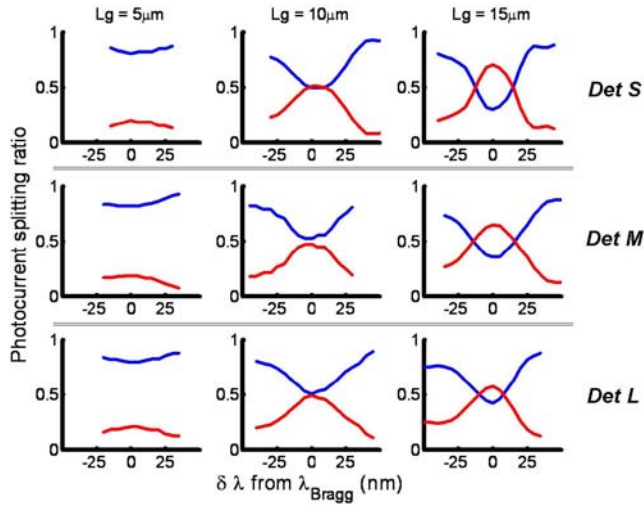


Fig. 9. Measured splitting spectra of nine different combinations with different detector widths and different grating lengths. Red (lower) lines represent the reflection and blue (upper) lines represent the transmission.

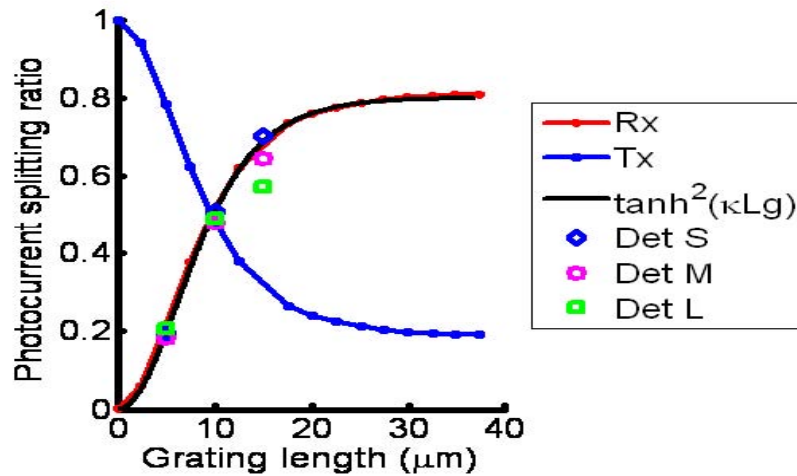


Fig. 10. Photocurrent splitting ratio versus grating length. Lines are from modeling and circles are the measured data.

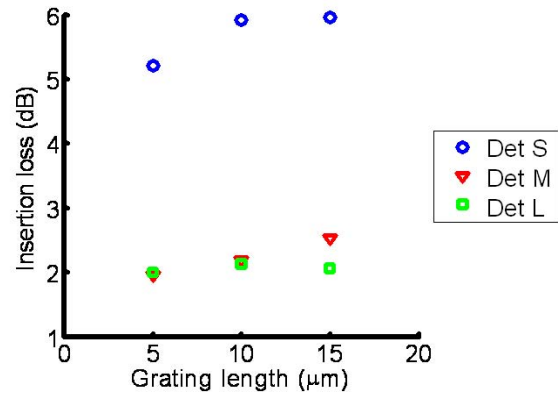


Fig. 11. Measured insertion loss data versus grating lengths.

Linear Phase Demodulation using an Integrated Coherent Receiver with an Ultra-Compact Grating Beam Splitter

**Chin-Hui Chen, Anand Ramaswamy, Leif A. Johansson, Nobuhiro Nunoya,
Jonathan Klamkin, John E. Bowers, and Larry A. Coldren**

ECE and Material Dept., University of California at Santa Barbara, Santa Barbara, CA 93106, USA

Phone: +1-805-893-7163, Fax: +1-805-893-4500, Email: janet@ece.ucsb.edu

With phase modulation, it is possible to realize high dynamic range analog optical links, provided the transmitted radio frequency (RF) signal can be linearly demodulated. The linearity of traditional interferometer-based phase demodulators, however, is often limited by their sinusoidal response. To achieve high linearity, negative feedback is introduced to suppress non-linearities arising from the phase demodulation process [1]. High feedback gain reduces the net phase swing across the demodulator such that it operates within the linear regime. Additionally, both the signal and the noise are reduced by the same feedback factor, so there is no penalty in signal-to-noise ratio (SNR) [1]. The challenge is to make a receiver incorporating feedback that is operable at high frequencies. Because high loop gain as well as a wide bandwidth is required for efficient phase tracking, the physical delay in the feedback path must be kept sufficiently short in order to prevent the loop from oscillating. Previously, we have demonstrated an ultra-compact grating-based beam splitter [2], which divides the incoming optical beams in a region, over 30 times shorter than a conventional surface-ridge Multimode Interference (MMI) beam splitter. This key feature leads to a significant reduction in loop delay.

In this paper, for the first time, we demonstrate the closed-loop operation of an integrated coherent receiver with the grating-based beam splitter. Fig. 1 shows both the schematic and the SEM photo of the integrated receiver with a direct interconnect (providing feedback) between the output of a balanced photodetector pair and a pair of optical phase modulators. The drive voltage to the modulator pair is obtained through the integration of the detector current across the capacitance of the detector and the modulator, and hence, the level of this drive voltage is proportional to the detected photocurrent level. When the photocurrent is sufficiently high to provide adequate loop gain, the integrated receiver can closely track signal phase. Consequently, the demodulated signal is very linear.

The integrated receiver consists of a balanced pair of uni-traveling-carrier photodiodes, multiple quantum well phase modulators, and a compact 2x2 grating-based beam splitter fabricated on an InGaAsP/InP platform. Deeply-etched periodic structures form a strongly reflective grating and enable an ultra-short splitting region. A symmetric waveguide grating in the vertical dimension is created when the etch depth is deeper than the thickness of the entire slab waveguide and thus, the radiation loss can be minimized.

We used an experimental analog optical link to characterize the linearity of the receiver. Details of the experimental setup are discussed in [3]. In Fig. 2(a) the signal-to-interference ratio (SIR) is 24.56 dB when the tracking modulators are turned off (feedback is negligible). When the modulators are turned on the SIR is 50 dB – an improvement of over 25 dB (Fig. 2(b)). Additionally, by measuring the noise floor we can determine the Spur Free Dynamic Range (SFDR) of the receiver (Fig. 3(a)). The measured noise floor (-130 dBm/Hz) is significantly higher than the calculated shot noise floor (-172.09 dBm/Hz) because of ASE noise from the optical source. Fig. 3(a) shows both noise floors. Assuming high loop gain and hence, complete phase tracking at 100 MHz and estimating the modulator V_{π} to be 4.37V, the resulting shot noise limited SFDR is 117.7 dB \cdot Hz^{2/3}. The closed loop SFDR is expected to decrease as a function of frequency because at higher frequencies there is not enough loop gain for accurate phase tracking. Fig. 3(b) shows the SFDR at 1 GHz to be 11 dB lower than the SFDR at 100 MHz. Also, at higher bias voltages the SFDR decreases because of a combination of modulator non-linearity and reduced photocurrent.

This work was supported by the DARPA PHOR-FRONT under US Air Force Contract FA8750-05-C-0265.

[1] Chou et al. COTA, 2006. [2] Chen et al. OFC, 2008. [3] Ramaswamy et al. JLT 26(1), 2008

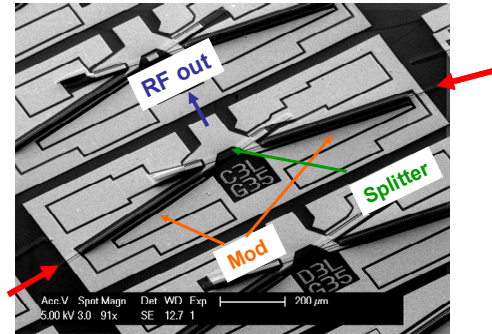
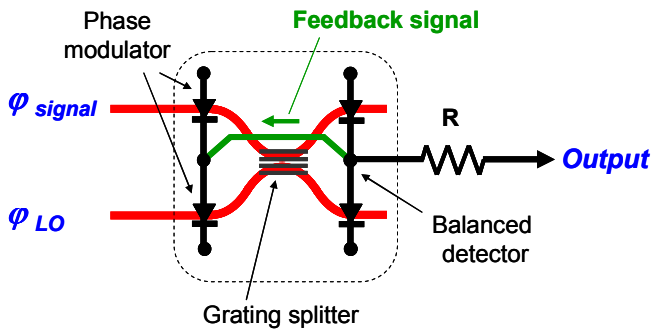
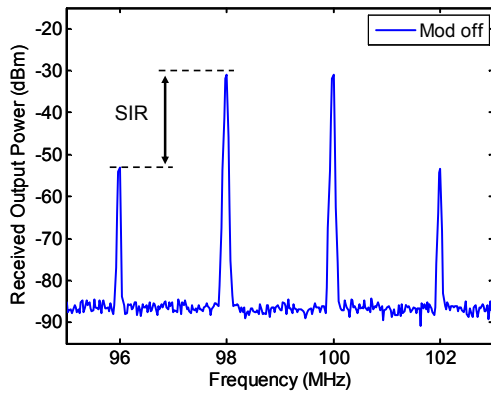
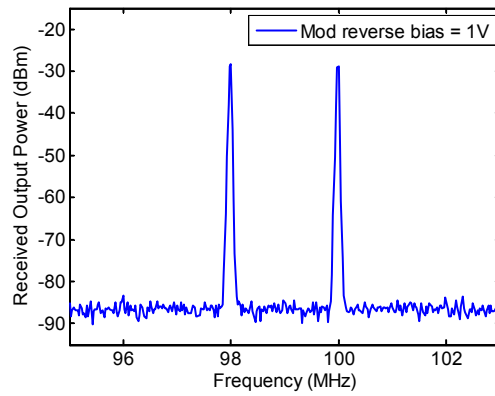


Fig. 1 Schematic and SEM of the integrated all-photonic receiver.

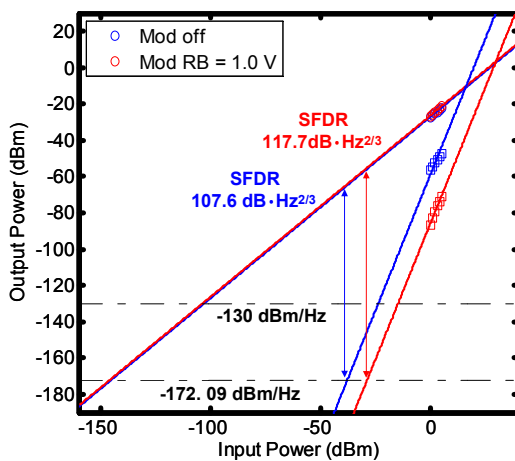


(a)

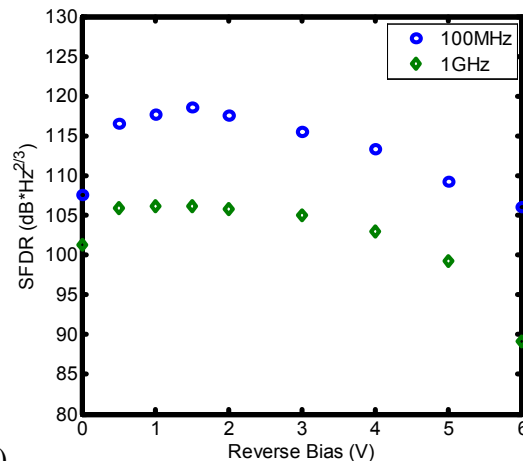


(b)

Fig. 2 Receiver output power spectra at 100 MHz, 10 mA photocurrent. (a) Modulator turned-off. (b) Modulator reverse-bias at 1 V.



(a)



(b)

Fig. 3 (a) The two-tone measurement at 100 MHz with modulator off and reverse bias at 1 V. (b) Shot noise limited SFDR results versus different modulator reverse biases at 100 MHz and 1 GHz.

Uni-Traveling-Carrier Balanced Photodiode with Tunable MMI Coupler for Optimization of Source Laser RIN Suppression

Jonathan Klamkin*, Anand Ramaswamy, Leif A. Johansson, Nobuhiro Nunoya,
John E. Bowers, Steven P. DenBaars, Larry A. Coldren
Materials Department and Electrical and Computer Engineering Department
University of California, Santa Barbara, CA USA

*Now with Lincoln Laboratory, Massachusetts Institute of Technology, Lexington, MA USA
Email: klamkin@ll.mit.edu

Abstract—A balanced uni-traveling-carrier (UTC) waveguide photodiode (PD) has been fabricated and characterized. The balanced PD incorporates a multimode interference (MMI) coupler as a light combiner/splitter with tunability of the output power splitting ratio. The individual UTC-PDs demonstrate a 1 dB compression current of 80.5 mA and a third-order output intercept point of 46.1 dBm at 60 mA, both representing the highest reported for a waveguide PD. The ability to fine tune the output power splitting of the MMI coupler allows for optimization of source laser relative-intensity noise suppression.

I. INTRODUCTION

Balanced photodiodes (BPDs) are used in a number of systems including microwave photonic links and coherent communications systems [1], [2], [3]. In microwave photonic links, differential detection with a BPD can be used to suppress relative-intensity noise (RIN) leading to a lower overall noise figure and improved dynamic range. To optimize the RIN suppression, the photodiodes (PDs) in the BPD pair should be precisely matched both electrically and optically, and the incident optical power on each PD should be equal. Also for high dynamic range microwave photonic links, such as that in [4], it is desirable that the PDs demonstrate a high 1 dB compression current and high third-order output intercept point (OIP3).

We previously demonstrated the concept of current injection tuning in a multimode interference (MMI) coupler/splitter in a BPD in [5]. The output power splitting tunability of the MMI coupler allows for optimization of source laser RIN suppression, and increased fabrication and fiber alignment tolerances. The PDs, which were uni-traveling-carrier PDs (UTC-PDs) demonstrated a 1 dB compression current of greater than 40 mA and OIP3 of 43 dBm at 20 mA and 34 dBm at 40 mA. Here we have optimized the design of the tunable MMI coupler and significantly improved the performance of the UTC-PDs. The coupler can be fine tuned with low levels of injected current while exhibiting low excess loss over a broad wavelength range. The individual UTC-PDs demonstrate a 1 dB compression current of 80.5 mA and a OIP3 of 46.1 dBm at 60 mA and 44.2 dBm at 80 mA. These represent the highest

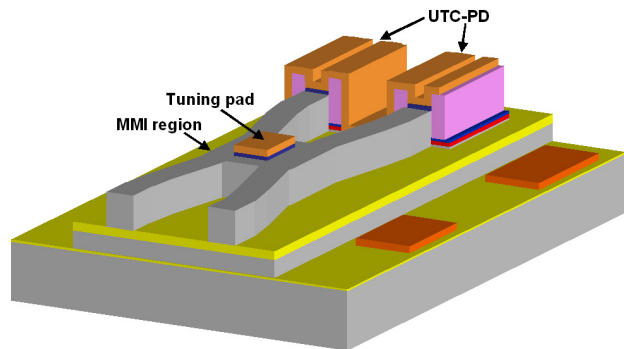


Fig. 1. Plan view schematic of UTC-BPD.

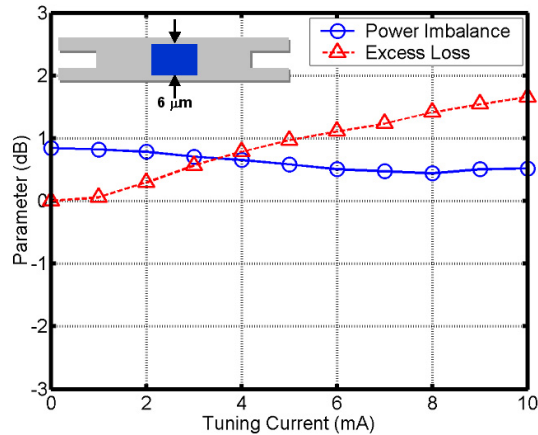
reported 1 dB compression current and OIP3 for a waveguide PD. In the balanced configuration, the OIP3 is subsequently 52.1 dBm and 50.2 dBm at 60 mA and 80 mA respectively.

II. BALANCED PHOTODIODE DESIGN AND FABRICATION

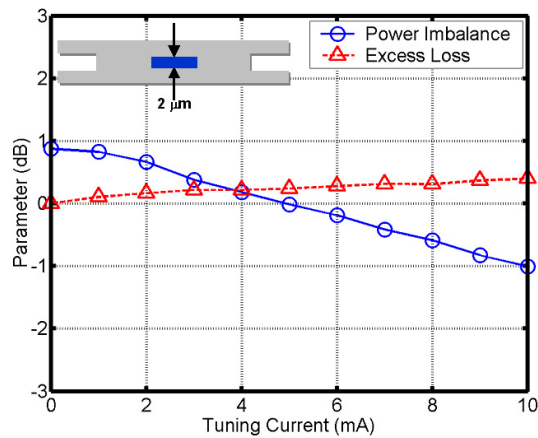
The waveguide BPD, shown in Fig. 1, consists of a pair of high power UTC-PDs, a compact tunable MMI coupler/splitter, and additional passive interconnection elements including waveguide bends and tapers. The UTC-PD structure sits on top of an *InGaAsP* waveguide layer. The monolithic integration fabrication sequence consisted of a photodetection region formation step followed by a p-cladding and p-contact layer regrowth step. The components were all fabricated in a surface ridge architecture. The structure was grown on a semi-insulating *InP* substrate. To realize the balanced configuration, the two adjacent waveguide UTC-PDs were electrically isolated using etching and a high energy ion implantation technique, and subsequently connected in series using a monolithic metal interconnect.

A. Tunable Multimode Interference Coupler

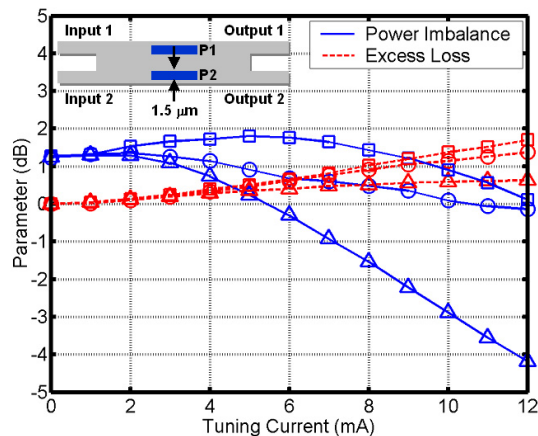
The coupler used was a general interference MMI coupler. The imaging length of a MMI coupler is extremely sensitive to the multimode region width [6]. Additionally, the imaging characteristics are dependent on the excitation at the input



(a) Design 1. The tuning pad is $100\ \mu\text{m}$ long, $6\ \mu\text{m}$ wide, and is placed in the center of the MMI region.



(b) Design 2. The tuning pad is $100\ \mu\text{m}$ long, $2\ \mu\text{m}$ wide, and is placed in the center of the MMI region.



(c) Design 3. The tuning pads are each $100\ \mu\text{m}$ long, $1.5\ \mu\text{m}$ wide, and are placed in the center of the MMI region along the length and $1\ \mu\text{m}$ from the edges along the width.

Fig. 2. Power imbalance and excess loss as a function of tuning current for the three different tuning pad geometries.

of the multimode region, which can be altered by fiber coupling misalignment. MMI couplers with tunable output power splitting ratios can increase the design, fabrication, and fiber alignment tolerances for devices that require well-defined splitting ratios [7]. Tunable MMI couplers can also be used for fine tuning the output power splitting ratio. This allows for optimization of source laser RIN suppression in a BPD.

Tuning the splitting of a MMI coupler exploits the fact that within the multimode region, the input field is reproduced in single or multiple images at periodic intervals along the direction of propagation. The interference of the self-images at one interval leads to the formation of new self-images at the next interval. By modifying the refractive index locally within one interval where self-images occur, the phase relations between the self-images at the next interval will be changed thereby altering the final output images.

A straightforward way to realize a tunable MMI coupler is to change the refractive index in locations where the most distinct self-images occur such as halfway along the length of the MMI. With a beam propagation method simulation, the lateral positions of these self-images at the halfway point can be identified by the points with high field intensity. If the refractive index near the middle two self-images is changed with respect to the refractive index near the outer two self-images, or vice-versa, the output power splitting ratio will be altered.

The refractive index of the material within the MMI can be changed in a number of ways including carrier-induced techniques such as the plasma effect, which leads to a negative refractive index change [8], [9]. Reasonable refractive index changes can be achieved with only modest carrier densities therefore fairly low levels of free carrier absorption are induced, which would otherwise reduce the net tuning effect in the MMI coupler. In order to inject carriers and tune the refractive index, a metal contact pad was integrated as shown in Fig. 1.

Tuning pads with three different geometries were fabricated and characterized. In all cases the length of the tuning pad was $100\ \mu\text{m}$ where the total MMI region length was $350\ \mu\text{m}$, and the tuning pads were placed in the center along the length of the MMI region. The width of the MMI region was $8\ \mu\text{m}$. Design 1 incorporated a single tuning pad that was $6\ \mu\text{m}$ wide and placed in the center of the MMI region along the width. Design 2 incorporated a single tuning pad that was $2\ \mu\text{m}$ wide and identically placed. Lastly, design 3 incorporated two $1.5\ \mu\text{m}$ wide tuning pads placed $1\ \mu\text{m}$ from the edges so that the spacing between the contacts was $3\ \mu\text{m}$.

B. Uni-Traveling Carrier Photodiode

The UTC-PD was utilized because this type of PD demonstrates both high speed and high current operation [10]. In a UTC-PD light is absorbed in an undepleted p-type narrow bandgap layer (absorber) and photogenerated electrons subsequently diffuse to a wide bandgap drift layer (collector). Because electrons are the only active carriers and electrons have a higher drift velocity than holes, space charge saturation

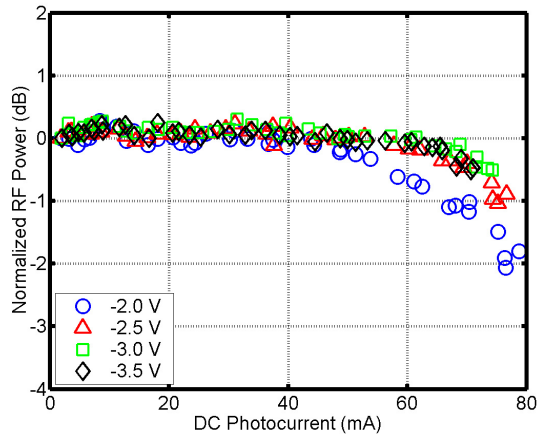


Fig. 3. Normalized RF power as a function of DC photocurrent at 1 GHz for varying bias voltages. The data is normalized to an ideal line with a slope of 20 dB/decade.

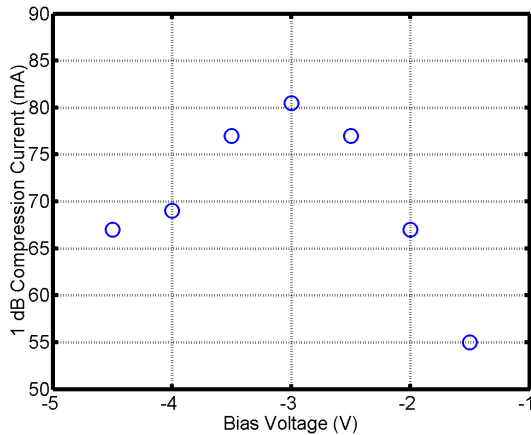


Fig. 4. 1 dB compression current as a function of bias voltage at 1 GHz.

effects are reduced in comparison to a traditional PIN photodiode (PD).

The UTC-PD structures were grown above the *InGaAsP* optical waveguide core and passive regions were formed by selectively removing the PD layers. The thickness of the field termination layer, a highly n-doped *InP* layer between the waveguide and PD layers, could be tailored to adjust the overlap of the optical mode with the absorber layer. A lower overlap factor results in a longer absorption profile and in turn a more uniform distribution of generated photocarriers along the length of the PD. This reduces the space charge saturation at the front end and improves the overall performance. As long as the field termination layer is not made considerably thick, only a slight increase in series resistance would be incurred in increasing the thickness of this layer.

The UTC-PDs used in the BPD have a p-*InGaAs* absorber that is 75 nm thick and is uniformly doped to a concentration of $4\text{E}18\text{ cm}^{-3}$, an *InP* collector that is 200 nm thick and is unintentionally doped, and a n-*InP* field termination layer

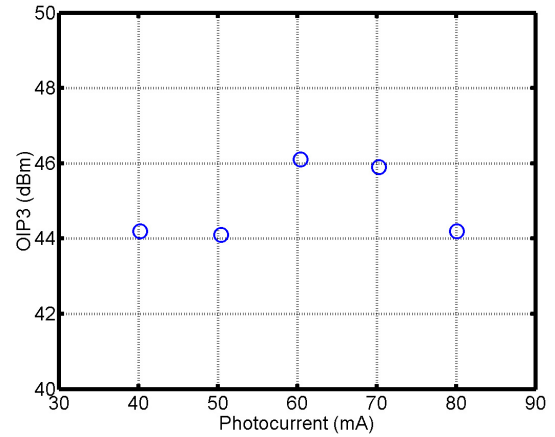


Fig. 5. Two-tone OIP3 as a function of photocurrent level.

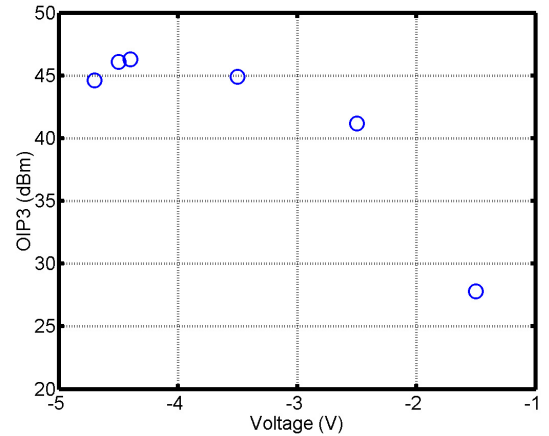


Fig. 6. Two-tone OIP3 as a function of bias voltage for a photocurrent level of 60 mA.

that is 70 nm thick and is doped to a concentration of $2\text{E}18\text{ cm}^{-3}$.

III. RESULTS AND DISCUSSION

For the MMI couplers, 50:50 splitting was achieved over a wide wavelength range. To test the tuning properties of the MMI couplers, the fiber was intentionally misaligned to force an imbalance with a magnitude of around 1 dB with no current injected, and then current was injected to tune to a power imbalance of 0 dB. Here the power imbalance is defined as $10\log(P_{OUT2}/P_{OUT1})$. The imbalance was measured with light coupled to one input access waveguide.

Figure 2 shows the measured power imbalance and excess loss as a function of tuning current for all three MMI tuning pad designs. The excess loss is the excess total transmission loss incurred as a result of increasing the tuning current and modifying the splitting properties of the MMI coupler. With the fiber misaligned, the excess loss increased with tuning current for all of the designs. Recall that these MMI couplers performed optimally with no current injected. The intentional

misalignment of the fiber changed the excitation at the input to the MMI region. The purpose of this experiment was to simulate a fiber misalignment for a packaged device, and test the viability of tuning the MMI splitting with current injection using the different tunable MMI designs. This situation could also simulate a BPD with PDs that are not identical.

For design 1, the splitting improved as the injected current was increased, however 50:50 splitting, or a power imbalance of 0 dB, was not achieved within the current range applied. Additionally, the excess loss was fairly significant. For design 2, with 5 mA of current, the splitting was tuned to a power imbalance of 0 dB from an imbalance with a magnitude slightly less than 1 dB while very little excess loss was induced. For design 3, with two tuning pads, current could be injected into each pad simultaneously, or into one pad only. In Fig. 2(c), the input and output access waveguides and the contact pads are labeled. Light was coupled to input 1 only and the fiber was misaligned so that a larger fraction of the output power was measured at output 2, and the power imbalance was slightly greater than 1 dB. Current was then injected into contact pad P2 only (circles in the figure), P1 only (triangles in the figure), and into both pads simultaneously (squares in the figure). For current injected into P2 only, the power imbalance could be tuned to 0 dB, however 12 mA of current was required and greater than 1 dB of excess loss was induced. For current into P1 only, the power imbalance could be tuned to 0 dB with only 5.4 mA of current and less than 0.5 dB of excess loss. For current into both P1 and P2, the power imbalance initially increased and then decreased to 0 dB at a current of 12 mA.

To characterize the UTC-PDs, the 1 dB compression current and OIP3 were measured. The 1 dB compression current was measured at various biases. Fig. 3 shows the normalized RF power as a function of DC photocurrent at 1 GHz. The response is fairly flat to greater than 60 mA and then begins to decrease gradually. The 1 dB compression current for this PD is 80.5 mA at a bias of -3.0 V. This high compression current is attributed to the low front-end saturation resulting from the relatively thick field termination layer. Figure 4 shows the 1 dB compression current as a function of bias voltage. The 1 dB compression current reaches a maximum at -3.0 V.

Third-order intermodulation distortion (IMD3) measurements were carried out using a three-tone setup as in [11]. For these measurements the fundamental frequencies used were $f_1 = 980$ MHz, $f_2 = 1$ GHz, and $f_3 = 1.015$ GHz. Figure 5 shows the two-tone OIP3 as a function of DC photocurrent. At 60 mA and a bias of -4.5 V, the OIP3 was 46.1 dBm. This is the highest reported OIP3 for a WG-PD. Although high at all the measured photocurrent levels, the OIP3 was highest at 60 mA. The OIP3 at 80 mA, the highest photocurrent level measured, was 44.2 dBm with a bias of -3.6 V. The bias was lowered at 80 mA to prevent thermal runaway. Figure 6 shows the two-tone OIP3 as a function of bias voltage at a photocurrent level of 60 mA. The OIP3 is highest at a bias of -4.4 V, and remains higher than 40 dBm for biases as low as -2.5 V. At a bias of -1.5 V, the OIP3 drops below 30 dBm.

IV. CONCLUSIONS

We have demonstrated a UTC-BPD with a tunable MMI coupler for fine tuning the output power splitting ratio. With a carefully designed tuning pad geometry, the power imbalance can be tuned from 1 dB to 0 dB with little excess loss. The UTC-PDs demonstrate a 1 dB compression current of 80.5 mA and a OIP3 of 46.1 dBm at 60 mA and 44.2 dBm at 80 mA. The 1 dB compression current and the OIP3 values represent the highest reported for a waveguide PD.

ACKNOWLEDGMENT

This research was supported by the DARPA PHOR-FRONT program under United States Air Force contract number FA8750-05-C-0265.

REFERENCES

- [1] T. E. Darcie and A. Moye, "Modulation-Dependent Limits to Intensity-Noise Suppression in Microwave-Photonic Links," *IEEE Photonics Technology Letters*, vol. 17, pp. 2185–2187, 2005.
- [2] P. J. Winzer and H. Kim, "Degradations in Balanced DPSK Receivers," *IEEE Photonics Technology Letters*, vol. 15, pp. 1282–1284, 2003.
- [3] A. Joshi, D. Becker, C. Wree, and D. Mohr, "Coherent Optical Receiver System with Balanced Photodetection," in *Proc. of SPIE*, vol. 6243, 2006.
- [4] J. Klamkin, L. A. Johansson, A. Ramaswamy, J. E. Bowers, S. P. Denbaars, and L. A. Coldren, "Monolithically integrated coherent receiver for highly linear microwave photonic links," in *IEEE Lasers and Electro-optics Conference*, 2007.
- [5] J. Klamkin, A. Ramaswamy, H.-F. Chou, M. N. Sysak, J. W. Raring, N. Parthasarathy, S. P. DenBaars, J. E. Bowers, and L. A. Coldren, "Monolithically integrated balanced uni-traveling-carrier photodiode with tunable MMI coupler for microwave photonic circuits," in *Conference on Optoelectronic and Microelectronic Materials and Devices*, 2006.
- [6] L. B. Soldano and E. C. M. Pennings, "Optical Multi-Mode Interference Devices Based on Self-Imaging: Principles and Applications," *Journal of Lightwave Technology*, vol. 13, pp. 615–627, 1995.
- [7] J. Leuthold and C. H. Joyner, "Multimode Interference Couplers with Tunable Power Splitting Ratios," *Journal of Lightwave Technology*, vol. 19, pp. 700–707, 2001.
- [8] B. R. Bennett, R. A. Soref, and J. A. D. Alamo, "Carrier-Induced Change in Refractive Index of InP, GaAs, and InGaAsP," *IEEE Journal of Quantum Electronics*, vol. 26, pp. 113–122, 1990.
- [9] J.-P. Weber, "Optimization of the Carrier-Induced Effective Index Change in InGaAsP Waveguides—Application to Tunable Bragg Filters," *IEEE Journal of Quantum Electronics*, vol. 30, pp. 1801–1816, 1994.
- [10] T. Ishibashi, T. Furuta, H. Fushimi, S. Kodama, H. Ito, T. Nagatsuma, N. Shimizu, and Y. Miyamoto, "InP/InGaAs Uni-Traveling-Carrier Photodiodes," *IEICE Transactions on Electronics*, vol. E83-C, no. 6, pp. 938–949, June 2000.
- [11] A. Ramaswamy, J. Klamkin, N. Nunoya, L. A. Johansson, L. A. Coldren, and J. E. Bowers, "Three-Tone Characterization of High-Linearity Waveguide Uni-Traveling-Carrier Photodiodes," in *IEEE Lasers and Electro-Optics Society Conference*, 2008.

Experimental Analysis of Two Measurement Techniques to Characterize Photodiode Linearity

Anand Ramaswamy, Nobuhiro Nunoya, Molly Piels, Leif A. Johansson, Larry A. Coldren and John E. Bowers
Electrical & Computer Engineering Department, University of California, Santa Barbara, CA 93106, USA

Alexander S. Hastings and Keith J. Williams
Naval Research Laboratory, Code 5650, Washington, D.C. 20375, USA

Jonathan Klamkin
Lincoln Laboratory, Massachusetts Institute of Technology, 244 Wood St, Lexington, M.A. 02420, USA

anand@ece.ucsb.edu

Abstract—As photodiodes become more linear, accurately characterizing their linearity becomes very challenging. We compare the IMD3 results from a standard two tone measurement to those from a more complex three tone measurement technique. A Ge n-i-p waveguide photodetector on Silicon-on-Insulator (SOI) substrate is used for the comparison. Additionally, we analyze, via simulation, the limitations of the measurement system in determining the distortion of highly linear photodiodes.

I. INTRODUCTION

High performance analog optical links require photodiodes that have high power handling capability as well as high linearity [1]. Surface illuminated photodiodes with over 700mA of photocurrent [2] and 3rd order Output Intercept Points (OIP3) in excess of 50dBm have been reported [3]. UTC based waveguide detectors with OIP3's >40dBm have also been reported [4]. Improvements in photodiode linearity create significant measurement challenges. Namely, distortion from the measurement system influences and in some cases limits the measured third order intermodulation distortion (IMD3). Currently, various techniques are used to determine the IMD3 of photodiodes [3, 5, 6]. When two closely spaced pure radio frequency (RF) tones are incident on the device, the resulting IMD3 measured should emanate entirely from the distortion of the photodiode. One way to get a pure RF tone with 100% modulation depth is through a two-laser heterodyne system [7]. However, generating a second tone that is close in frequency to the first tone would require an additional pair of lasers. Moreover, all four lasers need to be closely matched in wavelength and immune to thermal and other drifts. The latter requirement necessitates the lasers in each pair be locked to each other, further complicating the measurement setup.

An alternative to optical heterodyning is using external intensity modulators to generate two RF tones by modulating the output of two c.w. lasers. Although this greatly simplifies

the measurement setup, it introduces nonlinearities into the measurement through the intensity modulators and RF signal generators. An alternate approach to the two tone measurement technique is to use three tones to measure IMD3 [6, 8]. In this technique, some of the third order non linear distortion components generated in the device under test (DUT) are independent of the harmonics originating in the optical modulators and signal generators.

In this work, we take a Ge n-i-p waveguide photodetector on SOI [9] and use both the above modulator techniques to measure its IMD3. It is observed that the two approaches yield OIP3 results that are consistent with each other. Next, we show mathematically that as the OIP3 of a photodiode increases the results from the two techniques diverge. We find that the two-tone technique is sensitive to non-linearities in the optical source whereas the same is not true of the three-tone technique. This establishes the three-tone measurement technique as the preferred technique for measuring very linear photodiodes.

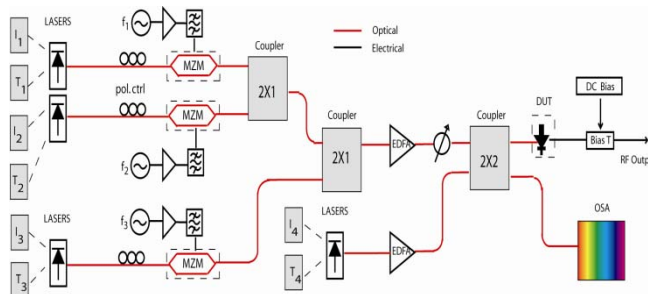


Figure 1. Experimental setup: three-tone measurement

II. EXPERIMENT

Figure 1 shows a schematic of the three tone experimental setup. The output of three CW lasers with differing

wavelengths ($\Delta\lambda \sim 0.5\text{-}7\text{nm}$) are modulated separately at frequencies $f_1=980\text{MHz}$, $f_2=1\text{GHz}$ and $f_3=1.015\text{GHz}$. The modulators are biased at quadrature to minimize second harmonics. The three optical signals carrying RF modulation are combined and amplified by an Erbium Doped Fiber Amplifier (EDFA). Experimentally second order intermodulation distortion has been observed due to the coupling of the gain tilt of an EDFA with frequency chirp of the modulated input signal [10]. However, in this experiment we use x-cut y propagating LiNbO_3 modulators whose chirp parameters are experimentally determined to be ~ 0.1 [11]-a factor of 10 less than that of directly modulated semiconductor lasers [12]. Hence, the EDFA induced distortion can be assumed to be negligible. An attenuator is used at the output of the EDFA to control the modulation index of the three tones. A fourth CW laser is used to ensure that the optical power and hence, photocurrent in the device remains unchanged as the optical modulation index is varied. For this experiment the optical modulation index is varied between approximately 20-30%. The third order intermodulation distortion components are measured at frequencies $(f_1+f_2) - f_3$, $(f_1+f_3) - f_2$ and $(f_2+f_3) - f_1$ as shown in Figure 2. It is important to note that in a three tone linearity measurement such as this, IMD3 from the interaction of two tones is also generated. In other words, in theory, distortion components can be observed at $2f_i - f_k$ ($i,k=\{1,2,3\}; i\neq k$).

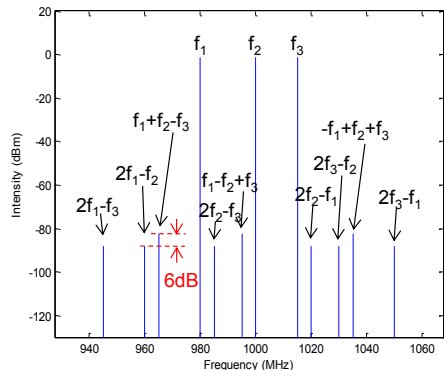


Figure 2. Illustration of IMD3 components in a three-tone experiment

As outlined in [6] the three-tone IMD3 is 6dB larger than the ideally measured two-tone IMD3. This can be inferred from the expressions below:

$$\text{Fundamental } (f_i): \quad m + \frac{15h_3}{4} \left(\frac{m}{h_1} \right)^3 \approx m \quad (1)$$

$$\text{IMD3}(2f_i - f_k): \quad \frac{3h_3}{4} \left(\frac{m}{h_1} \right)^3 \quad (2)$$

$$\text{IMD3}(f_i - (f_j + f_k)): \quad \frac{6h_3}{4} \left(\frac{m}{h_1} \right)^3 \quad (3)$$

As the power in the fundamental tone (1) goes up by 1 dB, the power in both the two-tone (2) and three-tone IMD3 components (3) go up by 3dB. Note that the two-tone and

three tone IMD3's differ by a factor of 2 (or 6dB in Electrical Power). The three-tone IP3 is 3dB smaller than the two-tone IP3 [6]. Hence, a factor of 3dB is added to the three-tone IP3 to relate this to the more commonly used two-tone IP3.

III. EXPERIMENTAL RESULTS

The device used for this experiment is a $7.4\mu\text{m} \times 500\mu\text{m}$ evanescently coupled Ge waveguide photodetector that is grown on top of a Si rib waveguide. The 3dB bandwidth of the device is $\sim 4.5\text{GHz}$. Details of the device design and fabrication can be found in [9].

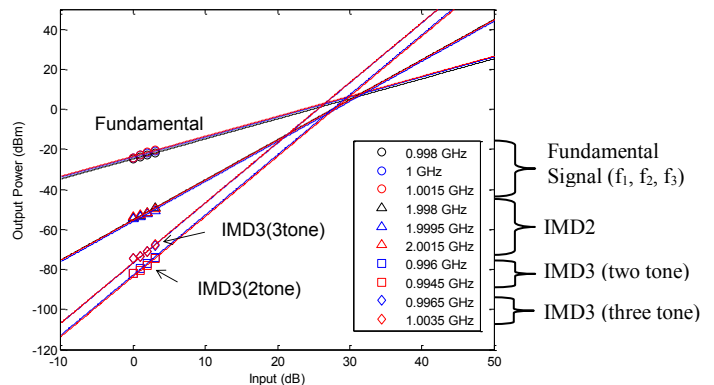


Figure 3. Sample experimental plot from a three-tone measurement (photocurrent = 20mA; bias voltage across photodiode = 2V)

Figure 3 plots the output RF power (in dBm) in the fundamental signals, third order distortion components (both two-tone and three-tone) and second order intermodulation distortion components (IMD2) versus the change in input RF power (dB) into the device. As mentioned in the previous section, the change in input RF power essentially corresponds to a change in optical modulation index, which is experimentally determined to be between 20-30%. Note that for the first time, both the two-tone and three-tone characterization of a photodiode's IMD3 are simultaneously measured. This provides for an accurate comparison of the measurement techniques since the various experimental conditions (e.g. optical modulation index, input RF power etc.) in the measurement system remain relatively constant during the course of the measurement.

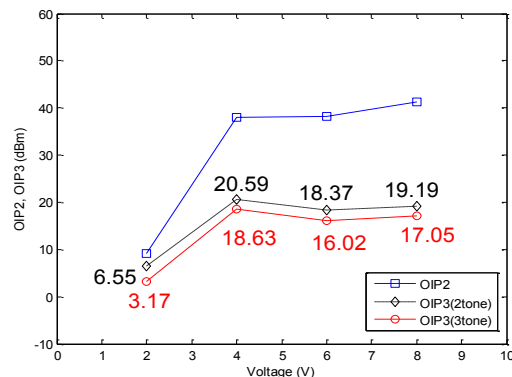


Figure 4. OIP2, OIP3 as a function of reverse bias (photocurrent = 20mA)

Figure 4 summarizes the experimental OIP3 and OIP2 results as a function of reverse bias at a photocurrent of 20mA. Although the difference between the two-tone OIP3 and three-tone OIP3 is not quite the theoretical 3dB, it clearly follows the theoretical trend. This is important because in Section IV it will be shown via simulation that when the linearity of the device is very high (and the distortion of the measurement system begins to dominate), the two tone and three tone techniques yield very different OIP3 values.

IV. NON-LINEARITIES OF MEASUREMENT SYSTEM

In this section we study the effect on OIP3 due to distortion in the optical source carrying the modulated RF tones. A model is developed for the three tone experimental setup shown in Figure 1. If the input signal from the signal generator to the modulator is given as $V_{RF}=V_o(\sin\omega t)$ and we assume a Taylor series expansion for the phase shift in the modulator we get:

$$\phi_{RF} = \left(\frac{\pi}{V_{\pi}}\right) (c_1 V_{RF} + c_2 V_{RF}^2 + c_3 V_{RF}^3 + \dots) \quad (4)$$

where V_{π} is assumed to be 5.0V. Additionally, when the modulators are biased at quadrature, the output power (P_{out}) is related to the input power as follows:

$$P_{out} = \left(\frac{P_{in}}{2}\right) (1 - \phi_{RF}) \quad (5)$$

Similarly, for the photodiode under test, the input optical power has two components: P_{DC} and P_{RF} and correspondingly, the output photocurrent has two components – a DC one given by $I_{DC}=a_1 P_{DC}$ and an RF one given by:

$$I_{RF} = a_1 P_{RF} + a_2 P_{RF}^2 + a_3 P_{RF}^3 + \dots \quad (6)$$

Figure 5 plots the IMD3 and IMD2 calculated using this model. The modulator is assumed to be linear ($c_2=0$ and $c_3=0$) and the non-linear coefficients assumed in the detector are indicated in Figure 6. From this calculation, the two-tone and three -tone OIP3 are found to be 42.218dBm and 39.208dBm. Since, these OIP3 values are similar to experimentally observed values [4] the range of relative non-linear coefficients of the photodiode used in this calculation (and subsequent calculations) can be assumed to be reasonably close to the devices in [4].

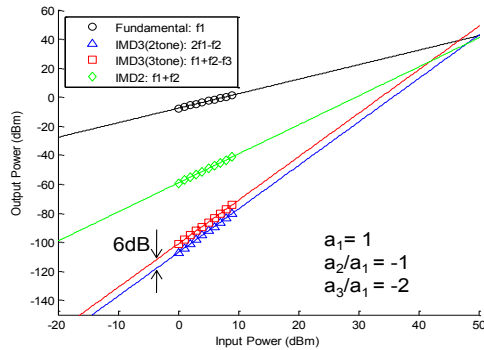


Figure 5. Calculated IMD3 and IMD2 ($P_{dc}= 40mW$)

Next, we introduce distortion in the optical source as follows: $c_2/ c_1=-0.01$ and $c_3/ c_1=-0.001$. Figure 6 plots the OIP3 for both the two-tone and three-tone case as the second order non linear coefficient (a_2) in the photodiode is varied, while keeping a_3 fixed. It can be seen that depending on the magnitude and sign of a_2 of the photodiode the calculated two-tone OIP3 can be either be ~ 6 dB greater or ~ 3 dB less than its actual value. Further, the three-tone OIP3 remains constant even as a_2 is varied. In Figure 7 the third order non-linear coefficient (a_3) in the photodiode is varied while keeping a_2 fixed. Again it can be clearly seen that the two-tone and three-tone OIP3 deviate from their 3dB difference as given by equations (2) and (3).

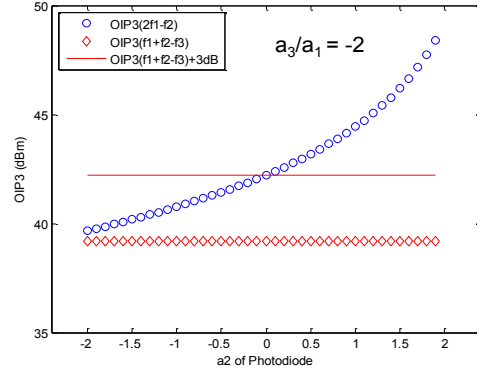


Figure 6. OIP3 dependence on a_2 of photodiode

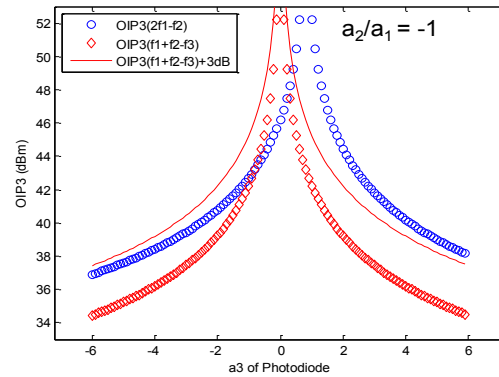


Figure 7. OIP3 dependence on a_3 of photodiode

The deviation of the two-tone OIP3 from the actual OIP3 value is a result of the interaction between the non-linear coefficients of the optical source (c_2 and c_3) and the 2nd order non linear coefficient of the photodiode (a_2). To confirm this, in Figure 8, $a_2/ a_1=-1$ is fixed and the OIP3 (both two-tone and three-tone) is plotted as a function of a_3 while keeping the optical source perfectly linear ($c_2, c_3=0$). Furthermore, in Figure 9 we reintroduce the earlier distortion in the optical source, but set $a_2=0$, thereby eliminating any interaction between the photodiode 2nd order non-linearity and the modulator. In both cases, it can be observed that the two-tone and three-tone results maintain the 3 dB difference as expected from (2) and (3).

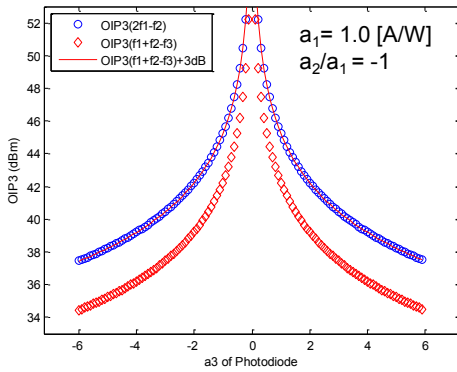


Figure 8. OIP3 dependence on a_3 of photodiode with perfectly linear optical source ($c_2, c_3=0$)

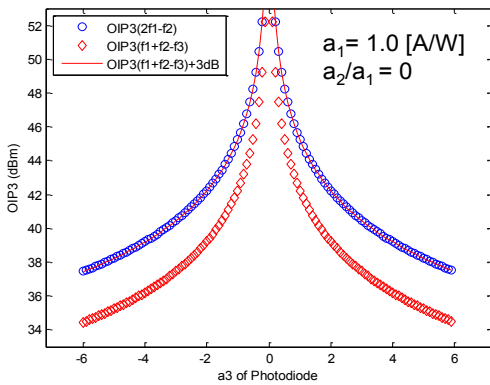


Figure 9. OIP3 dependence on a_3 of photodiode with $a_2/a_1=0$ but not a perfectly linear optical source ($c_2/c_1 = -0.01$ and $c_3/c_1 = -0.001$)

However, in reality there will be some second-order distortion coming from the optical source either due to a poor driver amplifier or improper biasing. Even if the intensity modulators are made out of a highly linear material (e.g. LiNbO₃), as in the case of this experiment, and the modulators are biased at quadrature (to minimize c_2), there will still be some residual second-order distortion due to thermal drift of the bias point. Additionally, having $a_2=0$ in the photodiode is not possible, so the two-tone measurement system will always add a certain nonlinearity (or at least an uncertainty) to the measurement. Thus the three-tone measurement system should be used to eliminate possible errors coming from nonzero a_2, c_2 and c_3 . This is particularly true as the linearity of detectors approach numbers in excess of 40dBm.

V. CONCLUSION

In this paper we have performed a detailed experimental characterization of two different linearity measurement techniques on the same photodiode for the first time. Using a Ge n-i-p waveguide photodetector on a Silicon-on-Insulator (SOI) substrate we have simultaneously measured both the three-tone OIP3 and the two-tone OIP3. Comparing these results, we find that at a photocurrent of 20mA, the difference between the two-tone and three-tone OIP3 is approximately

2-3dB, which is close to the 3dB predicted theoretically. Additionally, to show the need to adopt the more complex but more accurate three-tone measurement technique, we have modeled the measurement setup, introducing nonlinearities from both the optical modulator and RF signal generator. We find that the 2nd and 3rd order non-linear components (c_2, c_3) of the optical modulators affect the two-tone OIP3 measured in the detector because they interact with the photodiode non-linear coefficients (a_2 and a_3). On the other hand, the three-tone OIP3 remains unaffected by distortion in the optical source. Thus, as the linearity of photodiodes continues to increase, it is necessary to use a measurement technique such as the three-tone system to accurately characterize photodiode nonlinearities.

ACKNOWLEDGMENT

The authors would like to thank useful discussions with Ronald Esman, Steve Pappert, Jim Hunter and Nadir Dagli. Further acknowledgement should be provided to Tao Yin from Intel Corp. for providing the SiGe detector on which these measurements were made. This material is based upon work supported by the DARPA-PHORFRONT program under United States Air Force contract number FA8750-05-C-0265.

REFERENCES

- [1] K. J. Williams and R. D. Esman, "Design Considerations for High-Current Photodetectors," *J. Lightw. Technol.*, Vol. 17, no. 8, pp. 1443 - 1454, Aug. 1999.
- [2] D. A. Tulchinsky *et al.*, "High Current Photodetectors as Efficient, Linear and High-Power RF Output Stages," *J. Lightw. Technol.*, Vol. 26, no. 4, pp. 408 - 416, Feb. 2008.
- [3] A. Beling, H. Pan, H. Chen and J. C. Campbell, "Measurement and Modeling of a High-Linearity Modified Uni-Traveling Carrier Photodiode," *IEEE Photon. Technol. Lett.*, Vol. 20, no. 14, pp 1219 - 1221, Jul. 2008.
- [4] J. Klamkin *et al.*, "Uni-Traveling-Carrier Waveguide Photodiodes with >40 dBm OIP3 for up to 80 mA of Photocurrent," *Device Research Conference (DRC)*, Late News, Jun. 2008.
- [5] A. Joshi, S. Datta and D. Becker, "GRIN Lens Coupled Top Illuminated Highly Linear InGaAs Photodiodes," *IEEE Photon. Technol. Lett.*, Vol. 20, no. 17, pp 1500 - 1502, Sep. 2008.
- [6] T. Ohno *et al.*, "Measurement of Intermodulation Distortion in a Unitraveling-Carrier Refracting-Facet Photodiode and a p-i-n Refracting-Facet Photodiode," *IEEE Photon. Technol. Lett.*, Vol. 14, no. 3, pp 375 - 377, Mar. 2008.
- [7] R.D. Esman and K. J. Williams "Measurement of Harmonic Distortion in Microwave Photodetectors," *IEEE Photon. Technol. Lett.*, Vol. 2, no. 7, pp 502 - 504, Jul. 1990.
- [8] T. Ozeki and E. Hara, "Measurement of nonlinear distortion in photodiodes," *Elec. Lett.*, Vol. 12, pp. 80-81, 1976.
- [9] T. Yin, *et al.*, "31 GHz Ge n-i-p waveguide photodetectors on Silicon-on-Insulator substrate," *Opt. Exp.*, Vol. 15, Issue 21, pp. 13965-13971, Oct. 2007.
- [10] K. Kikushima and H. Yoshinaga, "Distortion Due to Gain Tilt of Erbium-Doped Fiber Amplifiers," *IEEE Photon. Technol. Lett.*, Vol. 3, no. 10, pp 945 - 947, Oct. 1991.
- [11] N. Courjal and J.M. Dudley, "Extinction-ratio-independent method for chirp measurements of Mach-Zender modulators," *Opt. Exp.*, Vol. 12, Issue 3, pp. 442-448, Feb. 2004.
- [12] F. Koyama and K. Iga, "Frequency Chirping in External Modulators," *J. Lightw. Technol.*, Vol. 6, no. 1, pp. 87-93, Jan 1988.

Monolithic Integration on InP: Functionalities and Applications in RF Photonics

MWP 2009
October 14, 2009

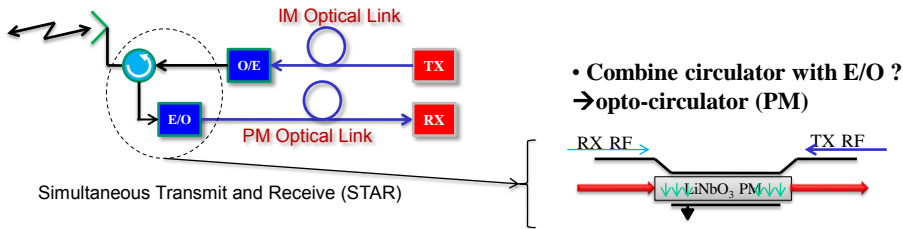
L. A. Coldren
(with many inputs from L. Johansson & M. Rodwell)

ECE and Materials Departments
University of California, Santa Barbara, CA 93106
coldren@ece.ucsb.edu

Outline/Contents

- **Example application: Antenna Remoting**
- **Optical Phase Modulation**
 - Potential for high S/N and SFDR links
 - Need for linear phase demodulators
- **Optical Phase-Locked Loops (OPLLs)**
 - Need for close integration of PICs and EICs
 - Application for linear phase demodulation
 - LIDAR applications
 - Application for remote mmW/THz generation
- **Integration for Linear Optical Transmitters**
- **Other Examples of Advanced InP Integration Technology**

Example Application: Antenna Remoting

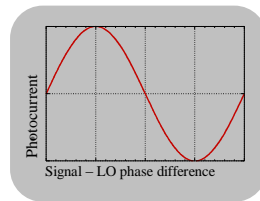
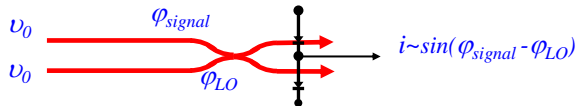


- Combine circulator with E/O ?
→ opto-circulator (PM)

- Phase Modulation (PM) in downlink enhances signal-to-noise and linearity
 - > 100% modulation depth with linearity possible with LEO PM - E/O
- Can also address STAR issues → need to isolate RX from TX and protect LNA
 - Even with perfect circulator and adaptive cancellation get transient large signals to RX
 - Phase modulator preferred → large input results in large phase modulation depth, not converted to large amplitude at remote receiver
 - E/O acts as "opto-isolator"; traveling-wave E/O can combine circulator functionality
- **Now problem gets shifted to creating a linear optical receiver for high-dynamic range phase-modulated signals as well as linear TX link**

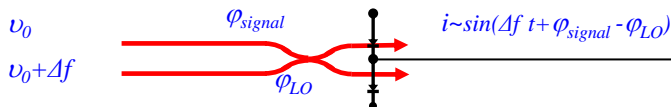
Coldren MWP 101409

Optical Phase Demodulation



Optical Homodyning

- Zero offset optical mixing
- Photocurrent \sim sine (optical phase)



RF phase recovery

Optical Heterodyning

- Optical mixing at offset frequency
- Optical phase \rightarrow RF phase
- Mixed signal circuit phase recovery (in essence a time measurement)

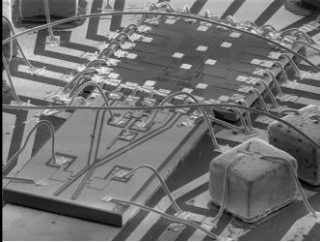
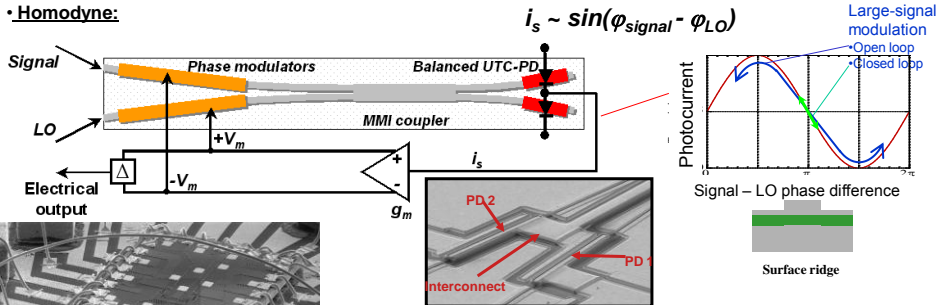
Coldren MWP 101409

Coherent Receiver for Phase Modulated Signals



OPLL—NEED for PICs & close integration/EICs

• Homodyne:



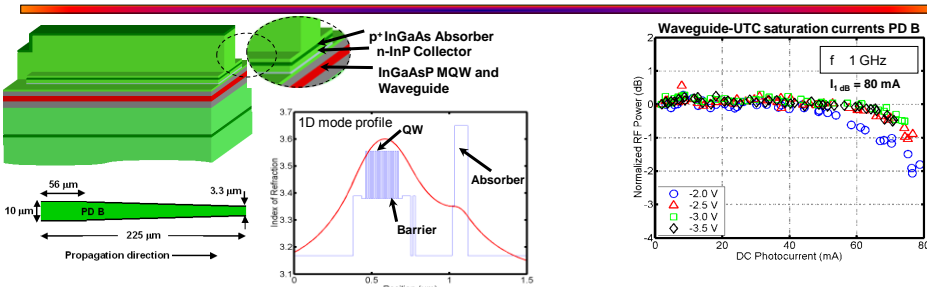
- Signal mixed with LO to demodulate optical phase
 - Detected photocurrent signal-LO phase difference
 - Response is sinusoidal
- With feedback, output reduced by the loop gain: $1/(1+T)$
 - Hybrid integrated EIC provides amplification
 - Operation within linear regime
 - NEED VERY SHORT FEEDBACK PATH



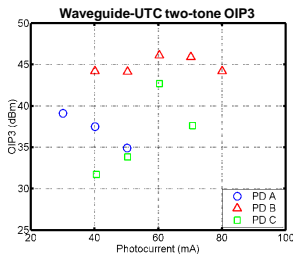
Coldren MWP 101409

L.A. Johansson, H.F. Chou, A. Ramaswamy, L. A. Coldren, and J.E. Bowers, "Coherent optical receiver for linear optical phase demodulation," *Proc. MTT-S Microwave Sym.*, Tu3D-01 (June, 2007).

Integrated Coherent Receiver Results

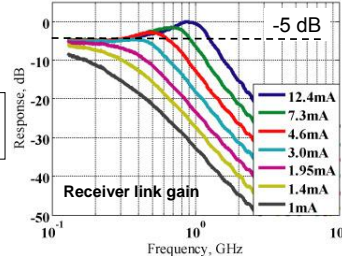


→ Record OIP3 for waveguide PD
= 46.1 dBm at 60 mA (PD B)



• For more on UTCs,
See MWP'09 paper We.2.2

- 1.4 GHz OPLL BW—Loop delay limited
- SFDR = 131 dB-Hz^{2/3} @ 300 MHz

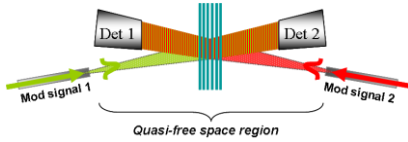


J. Klamkin, et al, *JSTQE*, 44 (4) pp354-359 (Apr., 2008).



A. Ramaswamy, et al, *JLT*, 26 (1) pp209-216 (Jan., 2008).

Ultra-Compact Receiver Approaches



* Chen et al. OFC 2008

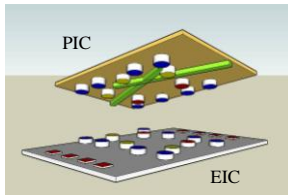
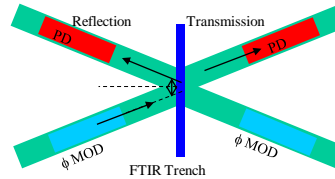
Grating-based beam splitter

- “Standard” fabrication process
- 10 μm splitting length
- Beam distortion issue



Trench-based beam splitter

- Frustrated total internal reflection (FTIR)
- Submicron splitting length
- Sensitive to fabrication



Coldren MWP 101409

Flip-Chip Bonding

- Shortest interconnection
- Eliminate peripheral wirebond and shorten metal routing
- High-density \rightarrow thermal vias needed

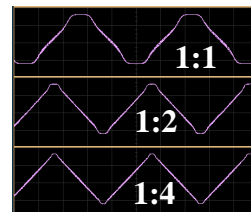
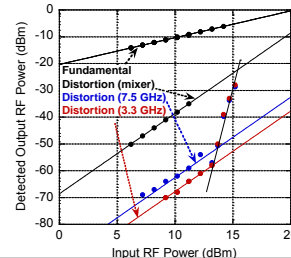
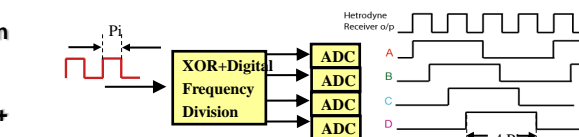
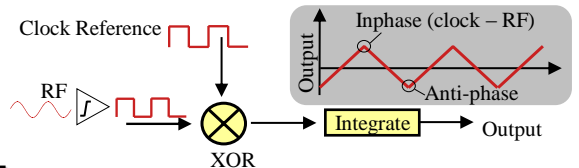
OFC – March 23, 2009

Linear Coherent PM Receiver – Mixed signal approach



Heterodyne:

- XOR linear receiver
- Combine strengths of photonics (linear phase modulation) and electronics (mixed-signal circuits)
- Optical \rightarrow RF frequency down-conversion
- Perform linear phase detection using electronics
- Frequency division for increased linear phase range + subsampling
- Digitally recover full spectral content

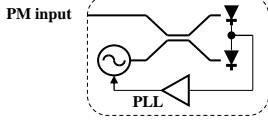


Coldren MWP 101409

Additional OPLL Applications/Challenges

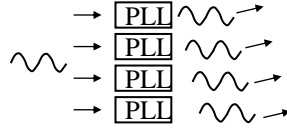


Coherent receiver



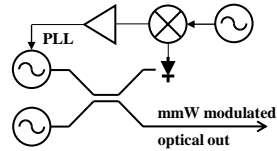
- Costa's Loop for BPSK, QPSK demodulation
- No requirement for complex DSP circuits
- Challenge: Develop receivers for high speed (>100Gbaud) or high constellations (n-QAM)
- Matched with development of coherent sources

LIDAR



- Very rich/challenging area
- Locking tunable lasers
- Arrays of locked OPLLs
- Swept microwave reference
- Time / Phase encoding of directed output
- Need for rapid scanning and locking rates

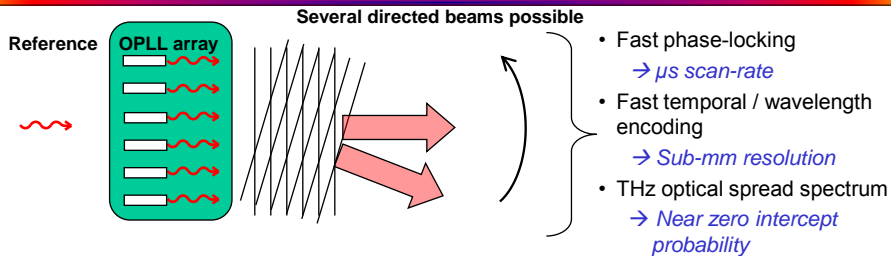
mmW / THz generation



- Locking of two tunable lasers
- Requires Integration of high-speed UTC photodiode
- Speed determined by UTC photodiode and feedback electronics: Can be very high
- Combined with antenna designs for complete TRX links with free-space path

Coldren MWP 101409

Application Goal - LIDAR



- **Optical LIDAR using array of phase-locked widely-tunable lasers**
 - Ultra Agile
 - Beam-steering – No moving parts
 - Precise scan rate – defined by synthesized microwave sweeper
 - Fast and accurate
- **Not possible using prior art**
 - Addition of frequency locking with phase locking for scan/locking speed
 - Resolution and accuracy only possible with close integration of widely-tunable PICs and high-speed EICs

Coldren MWP 101409

OP(& Frequency)LL performance metrics: Speed of operation/capture range—Integrated OPFLL



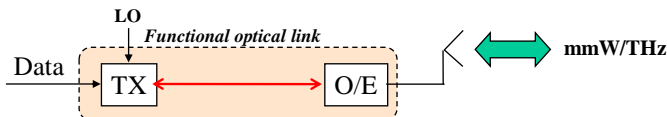
	State-of-art PLL	Integrated OPFLL
• Search range:	100 GHz	100 GHz
• Loop Bandwidth:	1 MHz	2 GHz (PLL mode), 120 MHz (FLL mode)
• Lock-in Bandwidth:	/- 3 MHz	/-100 GHz
• Search points:	$1.7 \cdot 10^4$	1
• Search rate:	0.16 μ s / point	1.3 ns / point
• Time to lock:	2.65 ms	1.3 ns (2×10^6 faster)
• Frequency scan range	100 GHz	100 GHz
• Frequency scan time	16 ms	4.0 ns (4×10^6)

(PLL slew-rate limit)
 $df/dt \propto f_u^2$ (f_u is the unity gain bandwidth)

- High-bandwidth electronics
- Small loop delays \rightarrow OE integration

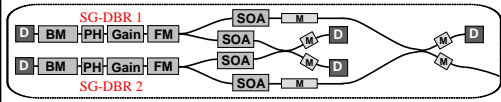
Coldren MWP 101409

Application goal: mmW/THz

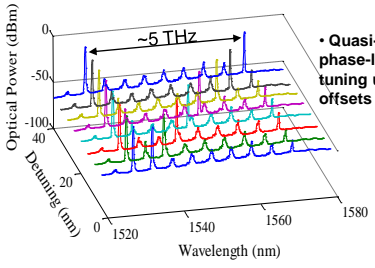
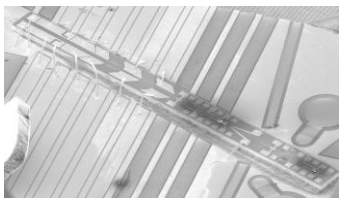
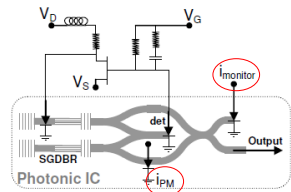


- Transparent photonic extension of RF path
 - Limited reach of mmW/THz
 - Long reach of SSB modulated optical carrier
- Current technology requires ultra-high-speed optical modulators with high-linearity & low loss.
- Offset phase-locking of two semiconductor lasers provides better source for remote mmW/THz generation
 - Data modulation at base band
 - Offset lock using rf mixer in electronics
 - (or) Offset lock using optical phase modulator on PIC
 - Multiply offset via higher order PM lines or other optical comb source

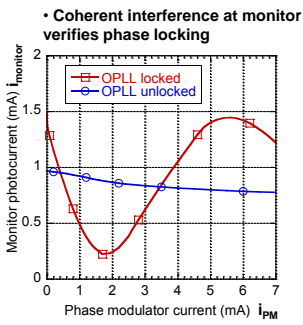
Phase-Locked SGDBRs/OPLL



D Photodetector
M Modulator



• Quasi-continuous phase-locked digital tuning up to 5 THz offsets possible



• Coherent interference at monitor verifies phase locking

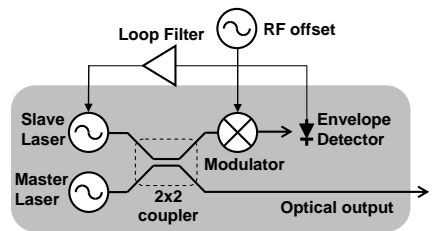
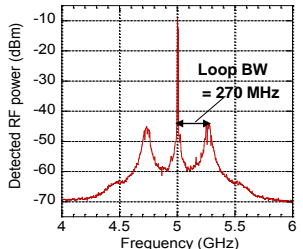
Coldren MWP 101409

S. Ristic, et al, *OFC '09*, PDPB3, San Diego, (Mar., 2009)

OPLL'd SGDBRs—Heterodyne



- ▶ EA modulator used to generate 5 GHz offset frequency
- ▶ Slave laser locked to modulation sideband
- ▶ Coherent beat observed
 - 0.03 rad² phase error variance in +/-2GHz BW estimated from captured spectrum
- ▶ Up to 20 GHz offset locking demonstrated



Ristic et al: *JLT* v.28 no.4, 2010, in press, also at *MWP2009*

paper **Th 1.5**



Coldren MWP 101409

Novel Linear Transmitter Concepts (IM)

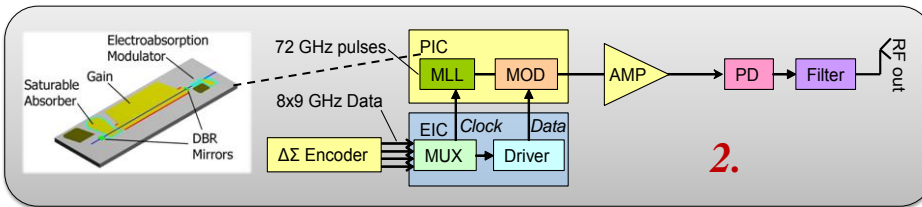
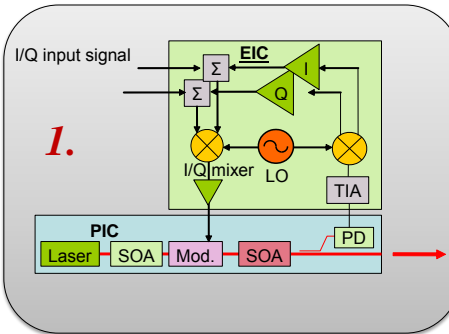


1. Cartesian Feedback transmitter

- Build on PHOR-FRONT technology
- Feedback linearized architecture

2. Delta-Sigma optical transmitter

- 1-bit oversampled $\Delta\Sigma$ DAC with optical components
- 4th order $\Delta\Sigma$ modulator will generate 66dB SQNR at 18 GHz (9x oversampling, 2GHz IBW)
- MLL integrated with High-speed EAM for oversampling

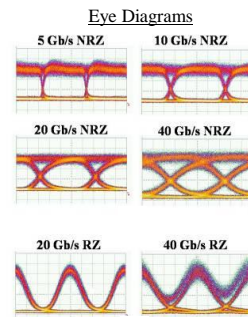
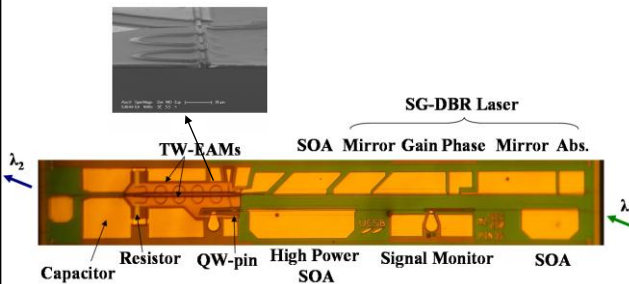
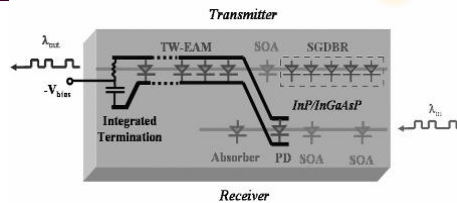


Coldren MWP 101409

Examples of PIC Technology: SOA-PIN & SGDBR-TW/EAM transceiver



- Data format and rate transparent 5-40Gb/s
- No filters required (same λ in and out possible)
- On-chip signal monitor
- Two-stage SOA pre-amp for high sensitivity, efficiency and linearity
- Traveling-wave EAM with on chip loads
- Only DC biases applied to chip—photocurrent directly drives EAM
- 40 nm wavelength tuning range



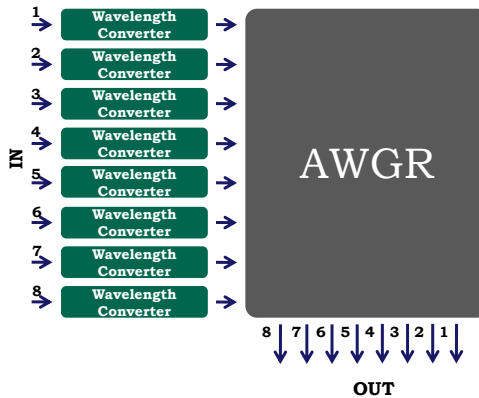
Coldren MWP 101409

M. Dummer et al. Invited Paper Th.2.C.1, ECOC 2008.

Examples of PIC Technology: Space Switching with Wavelength Converters



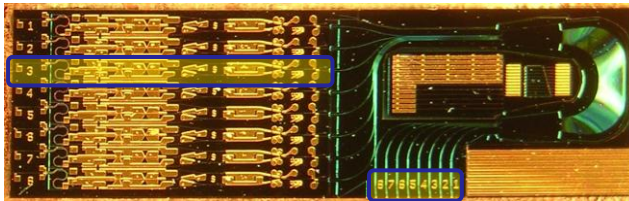
- Routing (space switching) with wavelength converters + dispersive elements such as arrayed waveguide routers AWGRs.
- Separates active switching engine (WC) from passive fabric (AWGR) to reduce power density in the fabric



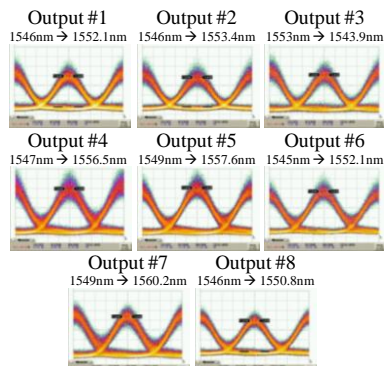
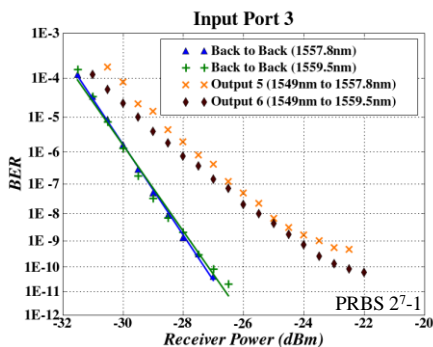
Monolithic Tunable Optical Router (MOTOR)

Coldren MWP 101409

MOTOR Results : Constant Input Port: 40 Gbps RZ

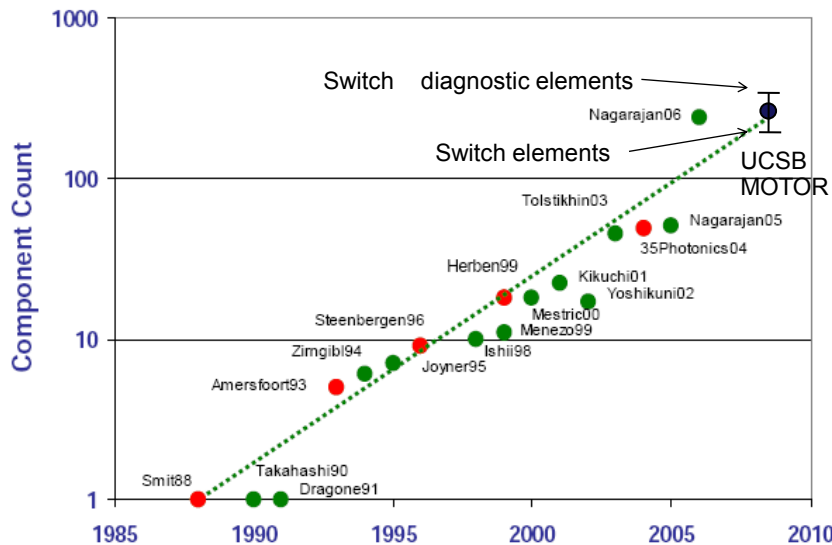


- Power penalty at BER 1E-9 for PRBS 2⁷-1 data at 40 Gbps 3.5 dB (no AR coating)



Coldren MWP 101409

Growth of Functional Photonic ICs



Coldren MWP 101409

Adapted from Prof. Meint Smit, Lecture at UCSB, Nov 7, 2008. + Nicholes, et. al., *OFC'09* PDPB1, 2009.

Conclusions



- Closely integrated Photonic ICs (PICs) with Electronic ICs (EICs) can provide high-bandwidth Optical Phase Locked Loops (OPLLs) for a wide variety of linear coherent optical sensing and communication functions
- Monolithic integration technology on InP has reached a level of maturity that many optical circuit elements can now be successfully combined on a single chip to enable such functionalities.
- Examples of the above have been illustrated.

Coldren MWP 101409

I. PIC Technology and Devices

D. Ring-resonator-based Filters and Logic Elements

PROGRAMMABLE PHOTONIC FILTERS FABRICATED WITH DEEPLY ETCHED WAVEGUIDES

Erik J. Norberg[†], Robert S. Guzzon[†], Steven C. Nicholes^{*}, John S. Parker[†] and Larry A. Coldren[†]

[†]*Department of Electrical and Computer Engineering*
^{*}*Department of Materials*
 University of California, Santa Barbara 93106

Abstract

Novel monolithic programmable optical filters are proposed and demonstrated. Deeply-etched waveguides are used throughout. Unit cells, incorporating a ring resonator in one arm of a Mach-Zehnder, have given programmable poles and zeros; cascaded unit cells have yielded flat-topped band-pass filter characteristics.

I. Introduction

Programmable optical filters have the potential to improve latency in real-time signal processing applications compared to digital approaches. The idea of programmable optical filters was suggested over two decades ago [1], however their complexity, control, and stability have all been limited by the inability to integrate the optical components on a chip. More recently, channel selection and add/drop multiplexer filters have been shown for WDM applications using micro ring resonators as well as larger ring geometries [2-6]. We propose a family of IIR (infinite-impulse-response) and FIR (finite-impulse response) optical filters that can be constructed from arrays of unit cells that incorporate a ring resonator within one branch of a Mach-Zehnder interferometer (MZI). These can be used as “channelizing” or “matched” filters to prefilter massive amounts of incoming analog data in nearly real time to identify signal bands or signatures that are worthy of further more detailed digital signal processing. This analog filter application is very challenging in that it requires fully programmable filters with much broader wavelength and bandwidth tunability than channel selection filters. Therefore these filters would consist of many sections with many ring resonators. Here we discuss the building blocks of these filters consisting of one and two unit cells.

II. Material Platform and Waveguide Design

The device design is based on a standard InGaAsP active/passive Offset Quantum Well (OQW) platform with a 300nm 1.3Q waveguide layer and 7 OQWs with a total confinement factor of 7.1% [7]. A single blanket regrowth of p-cladding following active/passive definition was utilized. In order to minimize radiation loss from waveguide bends and simultaneously keep the fabrication as simple as possible, the device uses a deeply etched waveguide design. Fig.1a shows the mode profile for the deep etch design. Since the mode has a large contact area with the waveguide sidewalls, the fabrication of smooth anisotropic sidewalls becomes

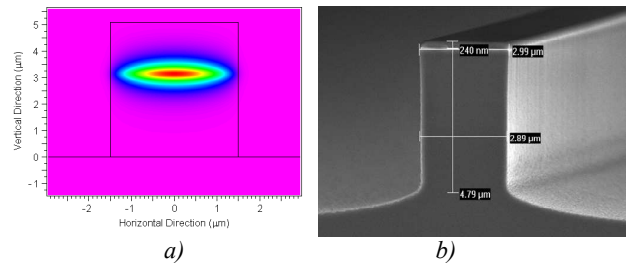


Fig.1 a) Simulated mode profile for deep etched ridge. b) SEM image of deep etched ridge waveguide.

extremely crucial to avoid optical scattering loss and surface recombination currents.

Photolithography and a dual mask process using a 55nm Cr layer on top of 500nm SiO₂ was employed to define the waveguide mask. The deep etching was then carried out in an ICP system using a Cl₂:H₂:Ar chemistry and a Si carrier wafer. Previous papers have reported the use of this etch chemistry and the importance of using a Si-carrier for dry etching InGaAsP [8],[9]. In this work the etch conditions were optimized to give anisotropic and smooth sidewalls. Fig.1 shows a cross section of a deep etched waveguide.

Using the cleave-back method on deeply etched active and active/passive ridge lasers, the waveguide loss was extracted, and the results are summarized in Table 1. Both the loss numbers and threshold current densities are very encouraging. Comparing the passive loss to that of 3μm surface ridges formed with a crystallographic wet etch (1.9 cm⁻¹ measured) suggests that there is not significant scattering loss added from the sidewalls. The low threshold current densities for the 3μm ridges confirm that the surface recombination current at the

Table.1 Loss coefficients and threshold current data for deeply etched waveguides measured under pulsed conditions.

Ridge width [μm]	α_i [cm ⁻¹]	α_p [cm ⁻¹]	Threshold current density / well [A/cm ²], (Laser length>1500μm)
3.0	8.5	2.2	75.7±7.8
1.8	11.4	-	129±12.4

sidewalls is not a major issue for this ridge width. However, the higher threshold current densities for the narrower 1.8 μm ridges imply a larger portion of the injected current goes into surface recombination. For this reason, all active gain sections in the device design have waveguides of 3 μm ; while the waveguide is tapered down to 1.8 μm at the input of couplers to reduce the coupling length.

Gain measurements from deeply etched SOAs show large signal gains of about 260 dB/cm (60 cm⁻¹) with an output 1-dB saturation of 8.4 dBm. This gain is about 25% higher than what we have seen using the same OQW platform with surface ridge waveguides of the same width.

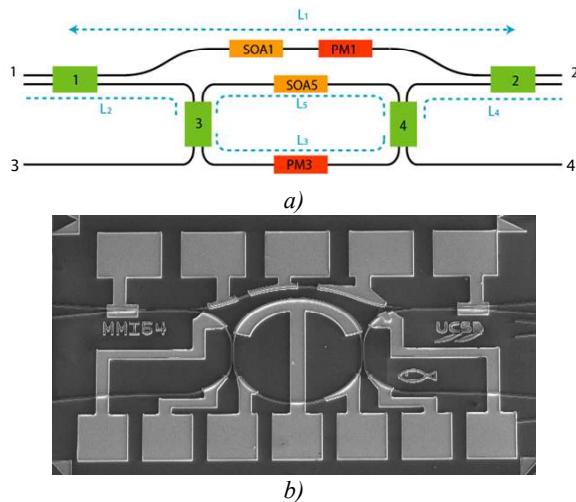


Fig.2 a) Schematic and b) SEM picture of the Single Ring Unit cell.

III. Device Design

A. Single Ring Unit Cell

The simplest filter design incorporates one ring and a parallel “feed-forward” waveguide. This is the Single Ring Unit Cell, shown fabricated in the SEM picture, Fig.2b; a schematic drawing is also shown in Fig.2a. When a signal is input to port 1, it encounters two interfering branches, one of which contains a ring resonator. A first-order pole response is created by the ring. A first-order zero response is created by the Mach-Zehnder Interferometer that is formed from the independent paths of the ring and the feed-forward waveguide. Thus, FIR and IIR filter responses can be synthesized between ports 1 and 2 as well as between other pairs of ports. The response of this unit cell is tuned in amplitude via active SOA regions in each path. The phase is tuned by carrier injection into passive waveguide sections via the free-carrier-absorption effect. We have formulated the scattering parameters for the single ring unit cell, shown here in a simplified form for an input to port 1 and an output at port 2.

$$S_{21} = AG_{ff}e^{-j(\beta L_1 + \Phi_{ff})} + \frac{Be^{-j[\beta(L_2 + L_3 + L_4) + \Phi_{ring}]}}{1 - CG_{ring}e^{-j[\beta(L_3 + L_5) + \Phi_{ring}]}} \quad (1)$$

The A, B, and C coefficients include the loss from various elements in the structure including waveguide, MMI transmission, and MMI coupling loss. G_{ff} and G_{ring} are the gain provided by the SOA for the feed-forward and ring respectively. The response of the zero can be isolated by applying a reverse bias to the SOA in the ring, and likewise the response of the pole can be isolated by applying a reverse bias to the SOA in the feed-forward waveguide.

In the fabricated device, the resonator has a length of 915 μm and the length difference of the MZI arms is 330 μm , corresponding to an FSR of 0.7nm (87GHz) and 2nm (249GHz) respectively. In addition to the active SOAs and passive phase tuning pads, a number of short passive pads or “taps” were included, Fig.2b. By reverse biasing these taps in different places along the unit cell, the individual components can be better understood. By calibrating the quantum efficiency of the taps using separate test structures, the taps can ultimately be used as sensors which together with feedback loops can stabilize the filter operation.

B. Cascaded Unit Cells

When two single ring unit cells are cascaded, a system with 3 coupled rings is created. The transfer function of this system has 6 total poles. 3 are created by individual rings, while 3 are manifest in the coupling between rings. 2 of the coupling poles are formed by the “figure-eight” path formed by 2 rings, and 1 is created by the similar combination of 3 rings. Cascaded coupled ring unit cells were fabricated together with the single ring unit cells, shown in Fig. 3. The fabricated device has a resonator length of 1500 μm . The design – like the Single Ring Unit Cell – includes passive contacts that act as phase modulators or “taps.”

The possibilities for the response from the coupled ring system is great, as the poles and zeros can be tuned via the SOAs and phase modulators. In general, many unit cells can be cascaded, allowing for the synthesis of complex filters. For example, a flat-topped bandpass response of any order can be synthesized for an input to port 1 and an output at port 2 by applying a reverse bias to the feed-forward SOAs (SOA1 in the schematic), and applying a forward bias the ring SOAs. This coupled-ring bandpass filter could be suitable for WDM add/drop filter applications [3]. To synthesize a narrow bandwidth filter, reverse and forward biases are applied to the SOAs in alternating rings, effectively cascading the poles from every other ring. For example in our 3-ring system, this is accomplished by reverse biasing the SOA in the center ring. With the rings no longer coupled, their poles can be located at the same wavelength to create a sharp filter response. The MZI structures created by the feed-forward waveguides can be tuned to eliminate neighboring poles and improve the effective FSR of the filter.

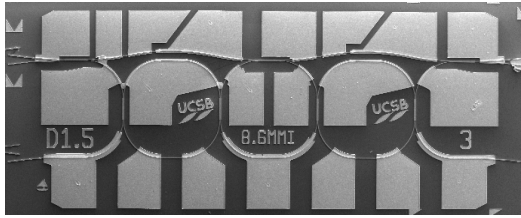


Fig.3 SEM of a Cascaded Unit Cell including 3 coupled rings.

IV. Results

A. Single Ring Unit Cell

Measurements of the filters were made by fiber coupling broadband light from an Amplified Spontaneous Emission (ASE) source into the chip and fiber coupling the output into an Optical Spectrum Analyzer (OSA). All testing was performed CW at room temperature. An MZI response was generated by reverse biasing the ring SOA to -9V to shut off the resonator; the feed-forward SOA was also reversed biased at -4V in order to balance the coupling loss induced by the path going through the resonator. The resulting MZI zero shows an extinction ratio of 15dB, and the S_{21} simulation (1) was fitted with $AG_{ff}=0.8B$, $G_{ring}=0$, Fig. 4a. The pole response was measured between ports 3 & 4 with the ring SOA biased at 17mA ($I_{th}=20mA$), resulting in an extinction ratio of 15dB with a pole FWHM of 0.067nm (8.5GHz), corresponding to a resonator Q-value of 23,000, as shown in Fig. 4b. Simulations fits a pole value of $CG_{ring}=0.76$ with $G_{ff}=0$.

B. Cascaded Unit Cells

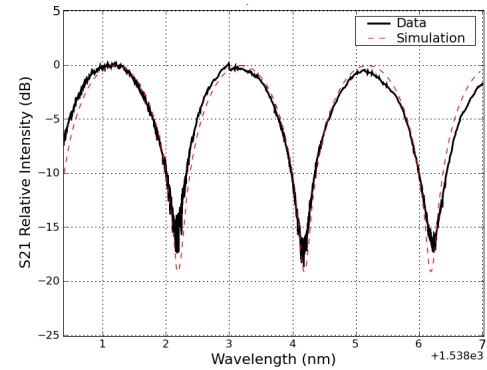
Fig. 5 shows a simple 2nd-order pole response measured from the device illustrated in Fig. 3. This was created by turning off the feed-forward waveguides and the third ring by applying a reverse bias to their respective SOAs; the remaining two 2 rings were tuned to create a band-pass filter with a 0.302 nm (37.7 GHz) FWHM. Given the strong 3 dB interstage coupling in this filter, a relatively wide-bandwidth, low-extinction passband results.

IV. Conclusion

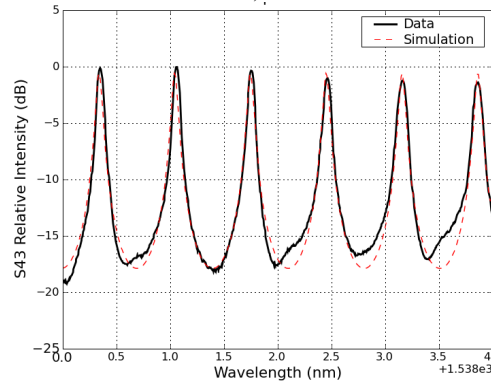
We have designed and fabricated the building blocks for a novel programmable filter entirely based on deep etching. By optimizing ICP etch conditions in $Cl_2:H_2:Ar$ chemistry we have achieved low loss passive waveguides and high active gain. Basic filter characteristics are demonstrated, including a high-Q single-ring-resonator pole response and a MZI zero response. By monolithically cascading unit cells, a band-pass filter was realized.

Acknowledgements

This work was supported by the DARPA-PhASER Project. A portion of this work was done in the UCSB nanofabrication facility, part of the NSF funded NNIN network.



a)



b)

Fig.4 Measured Single Unit Cell responses with superimposed S_{21} simulations using (1). a) MZI zero response; b) Resonator pole response.

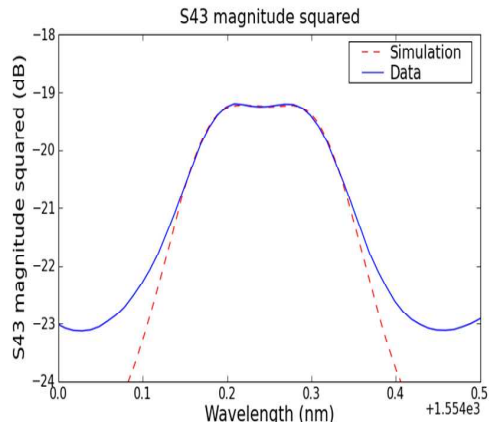


Fig.5 Measured and simulated throughput from 2-coupled-ring bandpass filter tuned to ~ 0.1 dB ripple with a 0.302 nm (37.7 GHz) FWHM.

References

- [1] J. E. Bowers, S. A. Newton, W. V. Sorin, and H. J. Shaw, "Filter Response of Single Mode Fiber Recirculating Delay Lines," *Elec. Letts*, **18**, 110, (1982).
- [2] S. Matsuo, Y. Ohiso, K. Tateno, T. Segawa, M. Kohtoku,

and S. Oku, "A high-speed tunable optical filter using a semiconductor double-ring resonator," *IPRM*, 14th, 467-470, (2002).

[3] D. Rabus, M. Hamacher, U. Troppenz, and H. Heidrich, "Optical filters based on ring resonators with integrated semiconductor optical amplifiers in GaInAsP-InP," *JSTQE*, **8**, 1405-1411(2002).

[4] S. Choi, Z. Peng, Q. Yang, E. H. Hwang, and P. Dapkus, "A high-Q wavelength filter based on buried heterostructure ring resonators integrated with a semiconductor optical amplifier," *IEEE Photonics Technology Letters*, **17**, 2101-2103 (2005).

[5] A. Agarwal et al. "Fully programmable ring-resonator-based integrated photonic circuit for phase coherent applications," *J. Lightwave Technology*, **24**, 77-87 (2006).

[6] Y. Ma, S. Chang, S. Chang, and S. Ho. "Improved optical filter responses in cascaded InGaAsP/InP microdisk resonators," *Electronics Letters*, **37**, 564-565 (2001).

[7] E. J. Skogen, J. W. Raring, G. B. Morrison, C. S. Wang, V. Lal, M. L. Masanovic, and L. A. Coldren, "Monolithically integrated active components: a quantum-well intermixing approach," *IEEE JSTQE*, **11** (2), 343-355, (2005).

[8] Sean L. Rommel, "Effect of H₂ on the etch profile of InP/InGaAsP alloys in Cl₂/Ar/H₂ inductively coupled plasma reactive ion etching chemistries for photonic device fabrication," *J. Vac. Sci. Technol. B*, **20** (4), (Jul/Aug 2002).

[9] S. Bouchoule et al., "Sidewall passivation assisted by a silicon coverplate during Cl₂-H₂ and HBr inductively coupled plasma etching of InP for photonic devices," *J. Vac. Sci. Technol. B*, **26** (2), (Mar/Apr 2008).

InGaAsP/InP based Flattened Ring Resonators with Etched Beam Splitters

Erik J. Norberg, John S. Parker, Uppili Krishnamachari, Robert S. Guzzon and Larry A. Coldren
 ECE Department, University of California at Santa Barbara, Santa Barbara, CA 93106-9560
 Tel: 805-893-8465, Fax: 805-893-4500, E-mail: norberg@ece.ucsb.edu

Abstract: A novel flattened ring resonator design utilizing Etched Beam Splitters (EBS) in InGaAsP/InP is proposed and demonstrated. A multiple-thickness hard mask that compensates for RIE-lag realizes waveguides and EBS gaps in a single etch step.

©2009 Optical Society of America

OCIS codes: 230.5750 Resonators, 250.5300 Photonic integrated circuits

1. Introduction

Ring resonators are a basic building block in filters needed for DWM applications and analog signal processing, resonators should ideally have small footprint and be easily integrateable with other PIC structures. The problem when scaling down resonators lies with the coupler since the length of the coupler ultimately limits the total ring length. Directional couplers are most often used when the resonator sizes are reduced; however when the ring size shrinks, the coupler region and amount of cross coupling reduces accordingly. In order to have enough cross coupling the inter waveguide distance must be made extremely small. For lateral directional couplers this implies the use of electron-beam lithography and more difficult fabrication; and even when using sub-micron features the directional couplers have cross-coupling limited to only a few percent. A solution to this problem is the Etched Beam Splitter (EBS)[1,2], an extremely compact coupler that allow the full range of cross/bar coupling ratios. Byungchae et al. have previously demonstrated an EBS in the AlGaAs/GaAs system with passive micro-ring resonators [3]. In order to achieve integration with conventional InP PIC technology, we have extended to the InGaAsP material system and report in this work for the first time on active ring resonator devices with EBS used for input/output coupling.

2. Flattened Ring Resonator Design and Simulations

Ring resonators are most often based on bent waveguides, when reducing the size of the resonator the bend radius decreases accordingly, whence a need for higher confinement is crucial to avoid radiation losses. In our design we therefore use a deeply etched waveguide to highly confine the mode laterally. But to obtain smaller ring circumferences without extremely small bend radii, we propose a novel flattened ring design, figure 1a). This design is a natural extension of the EBS coupler into a ring resonator, where the length of the ring is defined by the incident angle at the EBS coupler together with the bend radius of the waveguides, $L = \Theta R\pi / 45$. It has the major advantage of a reduced bend radius as compared to circular or racetrack type resonators that utilize directional couplers, the reduced bend radius translates into less optical scattering loss.

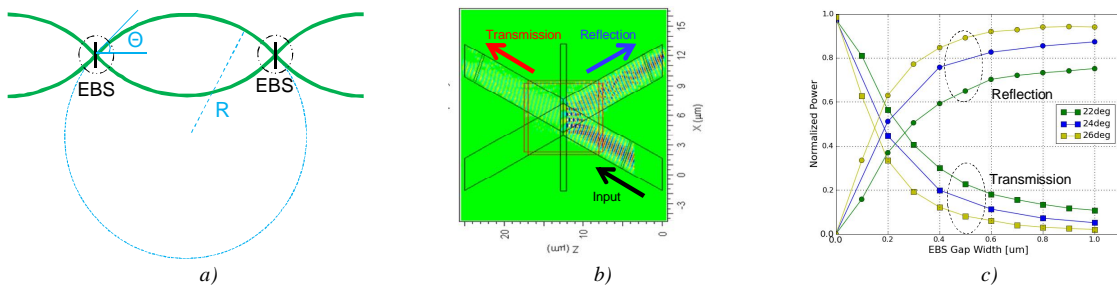


Fig 1. a) Schematic illustration of flattened ring resonator design. b) EBS design and 2D-FDTD simulation. c) Simulated power splitting as a function of incident angle and gap width.

The EBS design proposed in this work is the first based on high confinement waveguides, previous work have investigated EBS in weak guides [1,2]. Utilizing an EBS gap of air offers the smallest critical angle (18°), and thus the largest bend radius for a fixed resonator length. The EBS design is shown in figure 1b), varying the gap width and incident angle adjusts the amount of power reflected or transmitted through the process of Frustrated Total-Internal Reflection (FTIR) [4]; simulation results from 2D-FDTD is shown in figure 1c), the complete range of

power splitting is evident. For the EBS design, a given incident angle has an optimal shift between input and output waveguides, as expected due to the Goos-Hanchen shift [5].

3. Fabrication of EBS in InGaAsP/InP

There have been a few papers that investigated ICP etching of InGaAsP using $\text{Cl}_2:\text{H}_2:\text{Ar}$ chemistry [6,7]. We have previously optimized the conditions of this etch to yield smooth and straight sidewalls for deeply etched waveguides, for which low passive loss was demonstrated [8]. In this work we have further developed the etch to yield higher aspect ratio for the EBS gaps; we found $\text{Cl}_2:\text{H}_2:\text{Ar} = 7.6:11.4:2$, 800W ICP, 125W RIE and 8mT to be the optimal conditions. Surprisingly, better results was achieved with 8mT rather than lower pressures (~1.5mT), this is attributed to a Si-passivation layer being responsible for the anisotropy [7], and not a low etch pressure as in the case of many other RIE etch chemistries.

The FDTD simulations show that the loss in the EBS is very sensitive to rotational misalignment of the EBS gap with respect to the waveguides, for this reason we simultaneously define the EBS gaps and the waveguides. using standard photolithography. In the process of high-aspect-ratio deep etching, an aspect dependent etch rate (RIE-lag) is present, this is a well documented effect [9], and very hard to avoid by only varying etch parameters. This limits the EBS gap depth that can be achieved while keeping the waveguides in other areas at reasonable heights (< 6 μm); the etch depth of the EBS gap might be less than half of that in planar areas, figure 2a). We address the RIE-lag problem by using a novel multiple-thickness hard mask. First, both EBS and waveguides are patterned into a 500nm SiO_2 mask using standard photolithography, secondly, using a lift off technique with low temp SiO_2 deposition a second layer of SiO_2 is added everywhere except around the EBS, figure 2b). When the ICP deep etch takes place, the EBS region effectively etches for a longer time then the waveguides and hence the RIE-lag effect is compensated as illustrated in figure 2c). With the conditions given above the selectively is 1:20 for $\text{SiO}_2:\text{InP}$, thus a second deposition of 150nm SiO_2 translates into an extra 3 μm of etch depth in the EBS region; for a 0.4 μm wide EBS gap the depth is increased from 2 μm to 3 μm , a critical improvement in order for the optical mode to see the TIR mirror as the waveguide layer is located at a depth of 1.8 μm from the top.

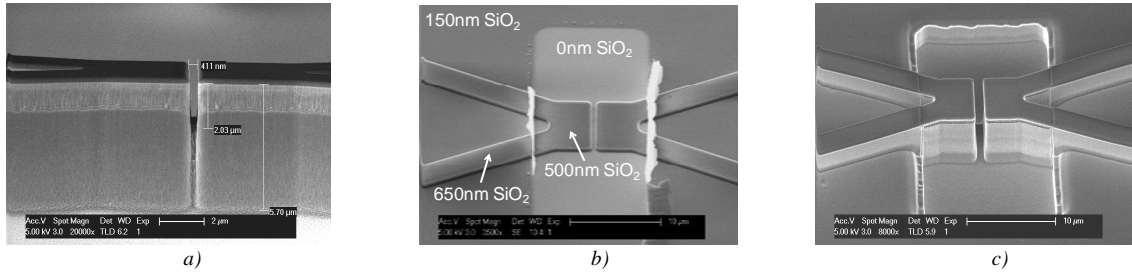


Fig 2. a) RIE-lag limits the EBS gap depth. b) Multiple-thickness SiO_2 mask effectively delays the waveguide deep etch. c) RIE-lag is reduced yielding higher aspect ratio EBS gaps

After the simultaneous deep etch of the EBS and the waveguides, only a single non-critical extra lithography step is needed in order to fully integrate the EBS couplers with our standard active PIC fabrication process; this is the removal of SiN on the EBS mirrors, figure 3.

4. Active Flattened Ring Resonators

In this work we used an InGaAsP Active/Passive Offset Quantum Well (OQW) platform with a 300nm 1.3Q waveguide layer and 7 OQWs with a total confinement factor of 7.1% [10]. The resonator design utilized 3 μm wide waveguides with a bend radius of 500 μm and EBS with an incident angle of 24°; this yields a total resonator length of 838 μm . The resonator has a 375 μm long gain region and two passive metal contacts for current injected phase tuning, figure 3.

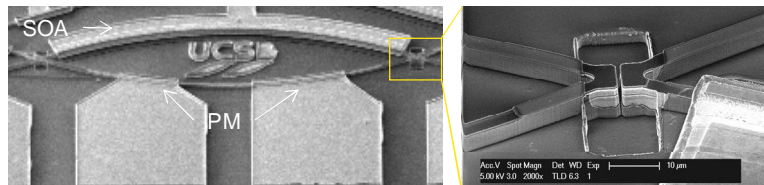


Fig.3 Fabricated active flattened ring resonator with an SOA, two Phase Modulators (PM) and EBS for in/out coupling

All measurement was done in room temperature CW, for *LIV* measurements an on chip passive pad outside the ring was used as photodetector, the quantum efficiency of this is very low, thus the optical power indicated in figure 4a) is arbitrary. The lasing spectra were captured using a lensed fiber to an Optical Spectrum Analyzer (OSA), it shows single mode lasing with a SMSR up to ~35dB, figure 4b). The threshold currents decreases as a function of EBS gap width as less output coupling is provided, the data is based on 22 devices with three different gap widths.

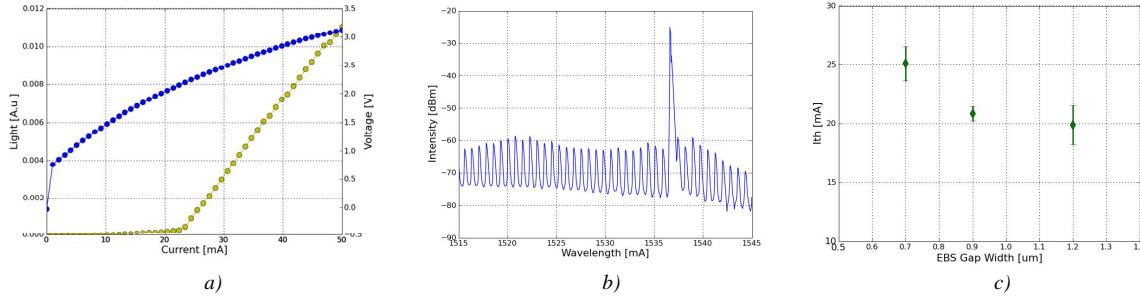


Fig.4 a) *LIV* characteristic for an EBS ring resonator. b) Lasing spectra for same device at 65mA. c) Threshold currents as a function of EBS gap width, mean values and standard deviations indicated.

These proof of concept results verify that the material structure, etching technology, and device designs are capable of providing state-of-the-art ring-resonator results with nearly arbitrary input/output coupling levels. From the low CW threshold current densities and de-embedded losses observed in these and other experiments, we can project that much smaller circumference rings should operate cw at room temperature, and results on such rings as well as more details on the EBS couplers will be presented in the oral presentation.

5. Conclusions

In this paper we have proposed a new micro-ring resonator design based on deeply etched flattened rings; the EBS design has been optimized using 2D-FDTD simulation. A novel hard masking process was demonstrated, which produced high aspect ratio EBS gaps together with deeply etched waveguides in a single etch step. The EBS fabrication is fully compatible with other InGaAsP-based PIC structures; active EBS-coupled flattened-ring resonators are demonstrated for the first time.

Acknowledgements

This work was supported by DARPA through the PhASER project; a portion of the work was done in the UCSB nanofabrication facility, part of the NSF funded NNIN network.

References

- [1] B. Kim and N. Dagli, "Compact Micro Resonators with Etched Beam Splitters and Total Internal Reflection Mirrors," Conference Proceedings. IPR2006, IWB3, April 2006.
- [2] L. Li, G. P. Nordin, J. M. English, and J. Jiang, "Small-area bends and beamsplitters for low-index-contrast waveguides," *Optics Express*, **11** (3), 282-290 (2003).
- [3] B. Kim, Y. Chang and N. Dagli, "Compact Ring Resonators using Conventional Waveguides, Etched Beam Splitters and Total Internal Reflection Mirrors," Conference Proceedings. OFC2009, March 2009.
- [4] S. Zhu, A. W. Yu, D. Hawley, and R. Roy, "Frustrated total internal reflection: a demonstration and review," *Am. J. Phys.* **54**, 601-607 (1986).
- [5] R. H. Renard, "Total reflection: a new evaluation of the Goos-Hänchen shift," *J. Opt. Soc. Am.* **54**, 1190-1197 (1964).
- [6] Sean L. Rommel, "Effect of H₂ on the etch profile of InP/InGaAsP alloys in Cl₂/Ar/H₂ inductively coupled plasma reactive ion etching chemistries for photonic device fabrication," *J. Vac. Sci. Technol. B*, **20** (4), (Jul/Aug 2002).
- [7] S. Bouchoule et al., "Sidewall passivation assisted by a silicon coverplate during Cl₂-H₂ and HBr inductively coupled plasma etching of InP for photonic devices," *J. Vac. Sci. Technol. B*, **26** (2), (Mar/Apr 2008).
- [8] E. Norberg, R. Guzzon and L. Coldren, "Programmable Photonic Filters Fabricated with Deeply Etched Waveguides," Conference Proceedings. IPRM2009, May 2009.
- [9] D. Keil and E. Anderson, "Characterization of reactive ion etch lag scaling," *J. Vac. Sci. Technol. B*, **19** (6), (Nov/Dec 2001).
- [10] E. J. Skogen, J. W. Raring, G. B. Morrison, C. S. Wang, V. Lal, M. L. Masanovic, and L. A. Coldren, "Monolithically integrated active components: a quantum-well intermixing approach," *IEEE JSTQE*, **11** (2) 343-355, (2005).

Single Port Optical Switching in Integrated Ring Resonators

John S. Parker, Yung-Jr Hung, Erik J. Norberg, Robert S. Guzzon, Larry A. Coldren

Electrical and Computer Engineering Department, University of California, Santa Barbara, CA 93106-9560

E-mail: JParker@ece.ucsb.edu

Abstract: We have experimentally investigated single-port injection-triggered switching in a new class of semiconductor ring lasers with integrated gain, phase and passive waveguide sections as a building-block for all-optical signal processing such as high-speed analog-to-digital conversion.

©2009 Optical Society of America

OCIS codes: (250.3140) Integrated optoelectronic circuits; (140.3560) Lasers, ring

1. Introduction

Semiconductor ring lasers (SRLs) are attractive components for all-optical signal processing. They typically lase bidirectional at low drive current and unidirectional at high current due to gain suppression between the competing clockwise (CW) and counter-clockwise (CCW) modes. This unidirectionality can potentially be utilized for bistable operation by switching between the lasing directions. Bistable switching has been demonstrated for various ring designs including circular [1], racetrack [2], and triangular with TIR mirrors [3], and in a variety of laser structures including InGaAs/InGaAlAs/InP [2], GaAs/AlGaAs [4], and InP/AlGaInAs [5]. Current research in the field by Hill et al. has shown switching speeds can be as fast as 20 ps [6], and by Calabretta et al. that switching can be directionally independent [7].

Recently high speed all-optical signal processing designs have been proposed such as a >100 GHz analog-to-digital converter as a milestone for future photonic integrated circuit (PIC) applications [8]. These systems rely on all-optical switching and can gain advantage from monolithically-integrated coupled SRLs for low power consumption, faster operation speeds, and high-order functionality without the need for additional cleaved facets. Such complex structures can benefit greatly from SRLs with phase pads for independent tuning of each laser and tap pads to monitor the power within each coupled SRL during operation. We have evaluated single-port injection triggered switching of SRLs with gain, phase, and tap pads as a building block for all-optical signal processing.

In this paper, we present an initial investigation of the switching mechanism between the CW and CCW modes in a new class of SRLs under injection from a single tunable laser from the same port. We found switching between both lasing directions can be achieved by changing wavelength while using only one port. Such findings are critical for SRL use in integrated photonic devices where much of the prior research on directional switching has been shown for injections into two counter-propagating ports [5,9]. The use of a single switching port greatly simplifies device design by reducing operation complexity with the potential to reduce the device area, the number of components including SRLs, and thus increase speeds for such devices as the >100 GHz all-optical analog-to-digital converter.

2. Material platform and Waveguide Design

The experimental devices integrated active and passive waveguide sections together using an offset quantum-well (OQW) integration platform [10], in the InGaAsP/InP materials system. The common passive waveguide consisted of a 300 nm thick 1.3 μm Q-layer, and the active sections added 7 QWs with a total confinement factor of 7.1% on top of this. Deeply etched waveguides of $\sim 5 \mu\text{m}$ were used to minimize radiation loss and allow for tight bending radii, although the minimum used was 100 μm . The deep etching was achieved using an ICP RIE system with an $\text{Cl}_2:\text{H}_2:\text{Ar}$ gas mixture to fabricate smooth and vertical sidewalls that are crucial to creating low loss bends. As recommended by Bouchoule et al., it was necessary to place the sample on a Si carrier wafer during the etch to assist in the formation of passivation compounds for smooth sidewalls [11].

The ring has a circumference of 1150 μm with 390 μm active Semiconductor-Optical-Amplifier (SOA) for gain, a 100 μm passive phase adjust pad, and a 100 μm passive tap pad to measure the power inside the ring during lasing. The waveguides are tapered from 3 μm at the SOA for high gain to 1.8 μm at the coupler to allow for shorter 100 μm couplers to be used. Two coupler variations, a 3dB Multimode-Interference (MMI) and a ~ 6 dB zero-gap directional coupler, are used in the ring designs. An SEM photo of the finished ring with metal p-contacts is shown in Fig. 1 with an MMI coupler. The two coupler designs and their coupling dependence on wavelength are shown in Fig 1b. and Fig 1c. The MMI coupler provides better coupling uniformity across wavelengths while the zero-gap directional coupler varies from 8dB to 5dB cross-coupling.

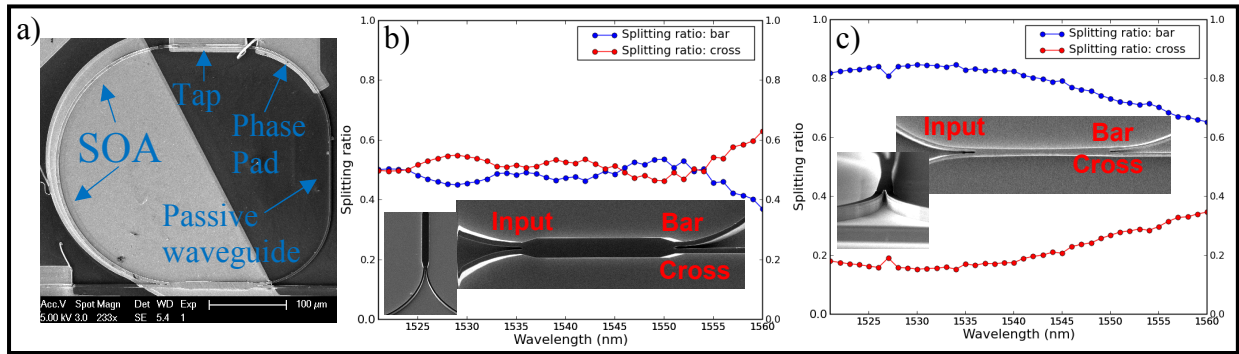


Fig. 1a. SEM of fabricated SRL with MMI coupler, 1b/c. MMI/zero-gap coupler splitting ratio vs. wavelength

3. Switching Results

Inherent bistability in the SRL can be observed as the drive current is increased as shown in Fig. 2. Bidirectional lasing occurs just above threshold, however the SRL becomes unidirectional as the current is increased to 75 mA where the CW mode is dominant and suppresses the CCW mode. At 90 mA this state is reversed and the CCW becomes dominant suppressing the CW up to the peak current at 175 mA. To observe injection triggered switching, the SRL was biased to 160 mA to assure strong suppression between the two modes and high output power levels.

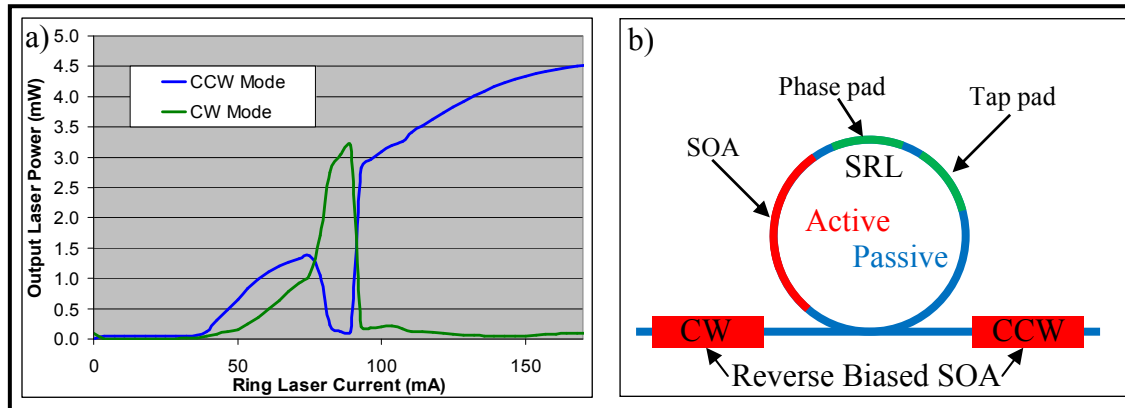


Fig. 2a. Bistable SRL Power vs. Current plot, 2b. Schematic of device

The bistable switching observed for a single injection port is wavelength dependent, while there are several specific wavelengths that can induce switching. The unidirectional ring lasing power inside the cavity with a 3 dB coupler was 9.5 dBm (6.5 dBm on-chip output power) with an injected switching power into the cavity of -25dBm. Low power switching can be achieved with triggering powers ~35dBm less than lasing power. The FSR of the cavity was 0.55 nm at 1.55 μ m lasing operation, and a detuning of 0.04 nm between the CW and CCW modes was observed on an optical spectrum analyzer (OSA). Figure 3a shows the output SRL spectrum from a single port when each of the modes is dominant showing an on/off power extinction ratio of 18 dB.

To test the switch's wavelength dependence, the tunable laser was swept in 0.01 nm increments while the two reverse biased SOAs were used to monitor the power in each direction as the ring switched from CW to CCW and then back to CW as shown in Fig. 3b. Switching occurred when the injected tunable laser was 0.01 nm from one of the side peaks of each mode's lasing spectrum. Therefore all potential switches occur at (for integer $n \leq 3$, where $\lambda_{o,CW}$ and $\lambda_{o,CCW}$ are typically detuned by ~ 0.04 nm):

$$\lambda_{CW \text{ Switch} / CCW \text{ Switch}} = \lambda_{o, CW / CCW} \pm (n \times FSR). \quad (1)$$

However, as shown by Fig. 3b at 1557.15 nm and 1557.85 nm a complete switching does not always occur. The number of complete switching wavelengths was improved by slowing the sweep speed and increasing the injected power. Further improvements to switching may be realized by using a narrow linewidth injection source to maximize the energy coupled into a single mode. Once switched, the stability of the CW and CCW states was verified for over an hour with no external injection. Additionally, for both stable states the lasing mode comb was shifted by 0.3 nm using the phase pads and the temperature changed by $\pm 10^\circ$ C using a thermo-electric cooler

without triggering a switch. Switching results are reported here for operation at 20° C indicating that near-room temperature operation of such devices is possible.

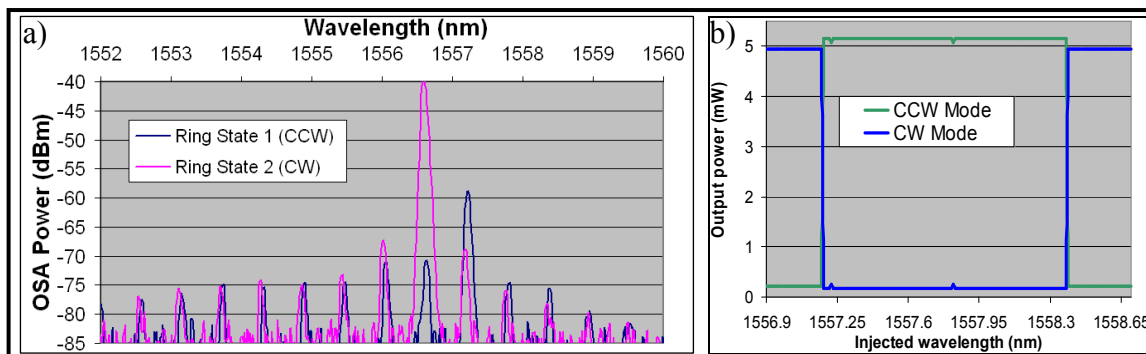


Figure 3a. Lasing spectrum overlay of CW and CCW modes, 3b. Directional switching plot

4. Conclusion

We have characterized single port switching in a new class of SRLs containing gain, phase, and passive waveguide sections for greater control and flexibility in coupled SRL systems. The switching is highly wavelength dependent, in which 0.01 nm matching between the injected wavelength and the SRL lasing peaks is crucial for consistent switching. The required switching power was ~35 dB below the SRL lasing power. This new class of integrated SRL is a promising building-block for all-optical signal processing where each SRL requires independent phase adjustment and optical power monitoring inside the cavity. We have used a fabrication and material platform that is extendable to more complex PICs and these building blocks are fully compatible with other InGaAsP/InP PIC devices. Additionally, their scalability to smaller sizes is mainly coupler limited. Future work might use these building blocks to integrate on-chip tunable sources, detectors, and coupled rings for even greater capability.

5. Acknowledgements

This work was supported by the Office of Naval Research, and a portion of this work was done in the UCSB nanofabrication facility, part of the NSF funded NNIN network.

6. References

- [1] M. Sorel, P.J.R. Laybourn, G. Giuliani, and S. Donati, "Unidirectional bistability in semiconductor waveguide ring lasers," *Appl. Phys. Lett.* **80**, 3051-3053 (2002).
- [2] S. Yu, Z. Wang, G. Yuan et al., "Optically triggered monostable and bistable flip-flop operation of a monolithic semiconductor ring laser," in *Photonics in Switching*, (IEEE, San Francisco, USA, 2007), pp. 115-116.
- [3] M.F. Booth, A. Schremer, and J.M. Ballantyne, "Spatial beam switching and bistability in a diode ring laser," *Appl. Phys. Lett.* **76**, 1095-1097 (2000).
- [4] M. Sorel, G. Giuliani, A. Scire, R. Miglierina, S. Donati, and P.J.R. Laybourn, "Operating regimes of GaAs-AlGaAs semiconductor ring lasers: experiment and model," *JQE* **39**, 1187-1195 (2003).
- [5] G. Yuan, Z. Wang, B. Li, M.I. Memon, and S. Yu, "Theoretical and experimental studies on bistability in semiconductor ring lasers with two optical injections," *JQE* **14**, 903-910 (2008).
- [6] M.T. Hill, H.J.S. Dorren, T. de Vries et al., "A fast low-power optical memory based on coupled micro-ring lasers," *Nature* **432**, 206-208 (2004).
- [7] N. Calabretta, S. Beri, L. Gelens et al., "Experimental investigation of semiconductor ring lasers under optical injection," in *ECIO*, (Eindhoven University of Technology, Eindhoven, the Netherlands, 2008), pp. 151-154.
- [8] M. Sayeh and A. Siahmakoun, "All optical binary delta-sigma modulator," in *Photonic Applications in Devices and Communication Systems*, (SPIE, Toronto, Canada, 2005), pp. 59700-59707.
- [9] B. Li, M.I. Memon, G. Mezosi, G. Yuan, Z. Wang, M. Sorel, and S. Yu, "All-optical response of semiconductor ring laser to dual-optical injections," *PTL* **20**, 770-772 (2008).
- [10] E.J. Skogen, J.W. Raring, G.B. Morrison, C.S. Wang, V. Lal, M.L. Masanovic, and L.A. Coldren, "Monolithically integrated active components: a quantum-well intermixing approach," *JSTQE* **11**, 343-355 (2005).
- [11] S. Bouchoule, G. Patriarche, S. Guilet, L. Gatilova, L. argeau, and P. Chabert, "Sidewall passivation assisted by a silicon coverplate during Cl₂-H₂ and HBr inductively coupled plasma etching of InP for photonic devices," *J. Vac. Sci. Technol. B* **26**, 666-674 (2008).

I. PIC Technology and Devices

E. Optical-Phase-Locked-Loop PICs

Integrated Optical Phase-Locked Loop

S. Ristic, A. Bhardwaj, M.J. Rodwell, L.A. Coldren and L.A. Johansson

*Electrical and Computer Engineering Department, University of California, Santa Barbara, CA 93106
ristic@ece.ucsb.edu*

Abstract: We demonstrate the first integrated optical phase-lock loop (OPLL) photonic IC, containing two SG-DBR lasers with >5 THz tuning range, a balanced detector pair and output modulators. A proof-of-concept homodyne OPLL demonstration has been performed.

©2007 Optical Society of America

OCIS codes: (250.3140) Integrated optoelectronic circuits, (060.1660), Coherent communications (060.5060), (060.2360) Fiber optics links and subsystems.

1. Introduction

Optical phase-locked loops (OPLLs) are routinely constructed using low-linewidth solid state or external cavity lasers. They are more challenging to build using wide linewidth semiconductor lasers due to the required short feedback delay. Past semiconductor laser OPLL demonstrations have typically used miniature bulk optics to meet these latency requirements [1,2]. In this paper, we demonstrate for the first time, an integrated optical phase-lock loop photonic integrated circuit in which all required optical components are integrated, including lasers, waveguides, couplers and photodetectors, as well as optical modulators. This eliminates the latency and instability from free-space or fiber optical paths to allow a very fast and robust OPLL.

Moreover, the OPLL photonic IC is built using widely-tunable lasers with over 5 THz wavelength range. This is key to several applications. First, it allows the development of homodyne coherent receivers in the form of Costa's loop, without the requirement for complex, power hungry DSP electronics to manage laser phase noise. The relative simplicity of the Costa's loop will also allow scaling to high data rates, >100Gbps. Second, an OPLL with 5 THz wavelength tuning range will allow coherent beam forming for sub-mm resolution LIDAR applications. Third, together with a THz photodetector, it will allow optical heterodyne signal generation with a DC to 5 THz frequency range with maintained coherence. Applying optical phase or amplitude modulation to one optical line will now generate a coherent phase or amplitude modulated THz signal. This is the target application for this paper. The photonic integrated circuit is described in section 2 and a proof-of-concept homodyne OPLL demonstration is described in section 3.

2. Optical Phase Lock Loop Photonic Integrated Circuit

A diagram of the PIC is shown in Fig. 1, and the corresponding SEM image is shown in Fig. 2, left. The PIC epitaxial structure has been grown on an S-doped InP substrate by MOCVD. The integration platform used here is often referred to as "Offset Quantum Well Platform" and has been described in more detail in [3] and references therein. In this platform, the light is guided by a 300 nm 1.4Q surface-ridge-waveguide core layer, which forms a basis for "passive" components: waveguides, Multimode Interference Splitters/Couplers (MMIs), and Franz-Keldysh modulators. Above this layer, the epitaxial material structure contains a 119-nm Multiple-Quantum-Well Region (MQW) region that forms a basis for "active" components: gain sections in SGDBR lasers, SOAs, as well as photodetectors. The "active" MQW region is defined by wet etching, as the very first processing step, followed by grating patterning/etching, waveguide p-cladding re-growth, and the rest of the steps, main of which are: surface-ridge wet etching, top N-contact wet etching and deposition, BCB patterning for modulators and detectors, P-metal pads, P-metal via etching, P-metal deposition, wafer thinning, and back-side N-metal deposition.

Light from each of the two SGDBR lasers is first divided by a 90- μm -long 1 X 2 MMI splitter into two equal-power components, and all four components are amplified by four 400- μm -long SOAs. One of these two components from either laser is used for the feedback loop, and the other is used for the PIC output. The half-power component from either laser that is used in the feedback loop first enters a 340- μm -long 2 X 2 MMI coupler (with tuning pads), which is, in turn, followed by a balanced receiver, containing two 250- μm -long phase modulators. These phase modulators are followed by a pair of 50- μm -long active photodetectors that can be used as a balanced receiver. The residual light that is not absorbed in the photodetectors will additionally be absorbed in 200- μm -long curved (7°) active sections with grounded pads. The P-metal electrodes for both types of detectors are supported by

PDPB3.pdf

BCB and are connected to $100\ \mu\text{m} \times 100\ \mu\text{m}$ RF pads, which are laid out in a G-S-G-S-G-S-G configuration ($150\ \mu\text{m}$ pitch) on either side of the PIC for direct probing.

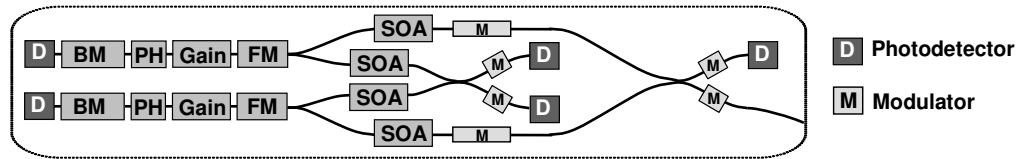


Fig. 1. Functional schematic of chip.

Each of the other two half-power components from the 1×2 MMI splitter (directed toward the output) is first passed through a $400\text{-}\mu\text{m}$ -long phase modulator before entering a $340\text{-}\mu\text{m}$ -long 2×2 MMI coupler (with tuning pads). These two modulators connect to the same RF pads as the photodetectors mentioned above. Following the 2×2 MMI coupler, light passes through a $250\text{-}\mu\text{m}$ -long additional amplitude modulators in each branch that can be used for electronic monitoring of the PIC's output. Similar to the feedback loop, one of the modulators is followed by a photodetector (also for electronic monitoring of the output), while the other is followed by a 7° curved output waveguide with AR coated facet. The back sides of the SG-DBR lasers are also AR coated. The output modulators connect to RF pads that are identical to those in the feedback loop. Total length of the PIC is about $6.6\ \text{mm}$ and its width is about $450\ \mu\text{m}$.

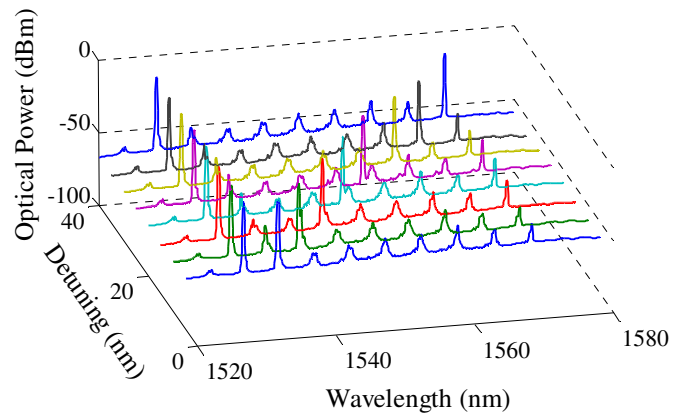
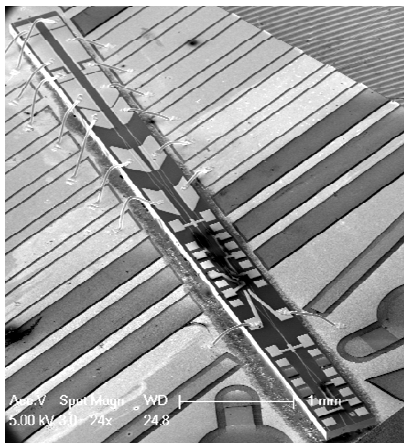


Fig. 2. Left) SEM of Integrated OPLL PIC. Right) Output spectra from heterodyne optical source.

The SG-DBR lasers have more than 40nm wavelength quasi-continuous tuning range. By keeping one laser at fixed frequency and tuning the second laser, a heterodyne optical output signal is generated from the photonic IC where the heterodyne difference frequency can be selected over the full 0 to $5\ \text{THz}$ frequency range, corresponding to the 40nm tuning range. This is illustrated by Fig. 2, right, where a series of optical spectra are captured to illustrate the output frequency range.

3. Proof-of-Concept OPLL Demonstration

A simplified schematic of the proof-of-concept OPLL arrangement is shown in Fig. 3, left. One of the integrated photodetectors is used to detect the beat signal between the two SG-DBR lasers. The detected photocurrent is then used to generate the wavelength tuning current applied to the phase section of one of the SG-DBR lasers, now acting as a current-controlled oscillator. A FET-transistor is required to translate the reverse biased detector current, to a forward biased phase section injection current. The detector load is tailored to generate a second order loop transfer function with lag compensation. In addition, the phase section is terminated by an inductor to compensate for the 3-dB bandwidth of the FM response of the SG-DBR laser (around 100MHz). The resulting loop bandwidth is around 300MHz . The free-running heterodyne beat signal is shown in Fig. 3, center, on a linear amplitude scale. The FWHM of the beat signal is around $300\ \text{MHz}$. However, it has been shown that the linewidth of SG-DBR lasers is dominated by low-frequency jitter [4], and as such, the phase noise can be well suppressed by a 300MHz loop bandwidth, as evidenced by the results below.

By splitting off part of the output of each laser before heterodyne detection, the phase and amplitude of each locked laser can be individually controlled. The two laser signals are then combined a second time, but now the heterodyne beat signal will carry any applied phase or amplitude modulation. In other words, this source has the potential to translate optical vector modulation to modulation on a coherent mmW or THz beat signal. For this homodyne OPLL demonstration, an applied phase modulation is applied by injecting a current into the phase modulator, resulting in a change in detected photocurrent in the on-chip monitor photodiode. This confirms successful optical phase locking of the two lasers. The finite extinction is a result of imbalanced detected power from the two lasers. In contrast, changing the modulator phase when the OPLL is unlocked, results only in the observation of residual amplitude modulation of the phase modulator, as also seen in Fig. 3, right.

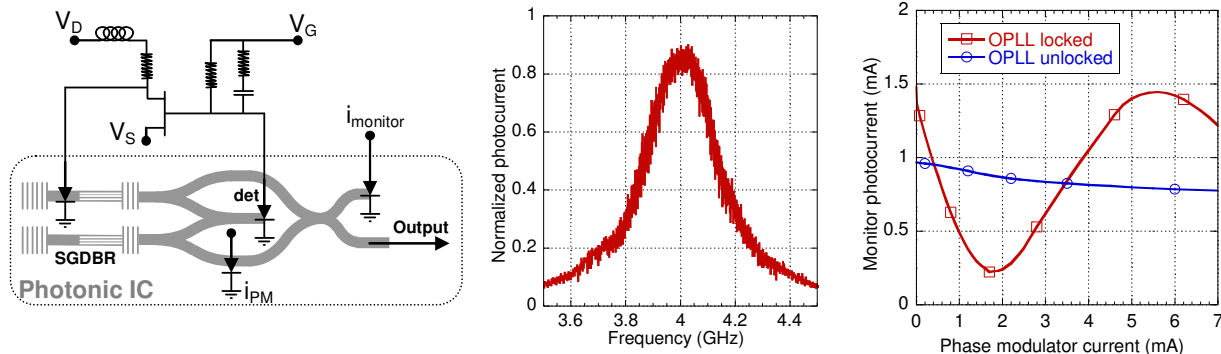


Fig.3. Left) Schematic of proof-of-concept OPLL demo. Center) Free-running laser heterodyne signal. Right) Interference between two locked lasers

4. Conclusion

In this paper we have demonstrated a monolithically integrated optical phase-locked loop photonic circuit in which all required optical components are integrated, including lasers, waveguides, couplers and photodetectors. This device includes widely tunable lasers with 5 THz tuning range and a capacity to apply modulation to a single optical line, translating optical vector modulation to an optical heterodyne signal. A simple proof-of-concept homodyne OPLL demonstration has been performed, confirming the suitability of SG-DBR lasers as a VCO laser in an OPLL. Future mmW heterodyne OPLL versions will fully utilize balanced detection, already in place on the photonic IC and integrated feedback electronics to increase the loop bandwidth and reduce laser amplitude noise fed back into the loop, for lower resulting phase noise.

Acknowledgements

This work is supported by DARPA under United States Air Force Contract #FA8760-08-1-7856. A portion of this work was done in the UCSB nanofabrication facility, part of the NSF funded NNIN network.

References

- [1] R. T. Ramos and A.J. Seeds, "Fast heterodyne optical phase-lock loop using double quantum well laser diodes", *Elec. Lett.*, vol. 28, pp. 82-83, 1992.
- [2] L.N. Langley, M.D. Elkin, C. Edge, M.J. Wale, U. Gliese, X. Huang and A.J. Seeds, "Packaged semiconductor laser optical phase-locked loop (OPLL) for photonic generation, processing and transmission of microwave signals", *IEEE Trans. Microwave Theory Tech.*, vol. 47, pp. 1257-1264, 1999.
- [3] J. W. Raring, M. N. Sysak, A. Tauke-Pederetti, M. Dummer, E. J. Skogen, J. S. Barton, S. P. DenBaars, and L. A. Coldren, "Advanced Integration Schemes for High-Functionality/High-Performance Photonic Integrated Circuits," in *Nanophotonic Packaging Proc. of SPIE Photonics West*, paper no. 6126 -19, San Jose, CA (January 21-26, 2006)
- [4] S. Nakagawa, G. Fish, A. Dahl, P. Koh, C. Schow, M. Mack, L. Wang, R. Yu, "Phase noise of widely-tunable SG-DBR laser", *Optical Fiber Communications Conference*, 2003. 23-28 March 2003 Pages: 461-462 vol.2.

Heterodyne Locking of an Integrated Optical Phase-Locked Loop

S. Ristic¹, A. Bhardwaj¹, M. J. Rodwell¹, L. A. Coldren^{1,2}, and L. A. Johansson¹

¹Department of Electrical and Computer Engineering

²Materials Department

University of California, Santa Barbara

Santa Barbara, USA

ristic@ece.ucsb.edu

Abstract—We demonstrate proof-of-concept heterodyne locking of the first optical phase-locked loop photonic integrated circuit. The circuit contains two sampled-grating distributed reflector lasers monolithically integrated with optical amplifiers, multimode interference splitters/couplers, and high-speed modulators and photodetectors.

I. INTRODUCTION

An optical phase-locked loop (OPLL) is a control system that exhibits both essential similarities and fundamental differences when compared to its RF counterpart. In an RF phase-locked loop (PLL), a mixer is used to detect a phase difference between an input signal and an output of a local voltage-controlled oscillator (VCO). The mixer produces a phase error signal that is filtered and applied to the VCO, tuning its output frequency to have a fixed phase relation with the input signal frequency. In an OPLL, however, a photodetector detects a phase difference between an input optical signal and an output of a local current-injection tunable laser, which effectively plays a role of a current-controlled oscillator (CCO) and is a direct equivalent of the VCO [1]. The phase error signal produced by the photodetector is filtered and applied to the CCO, tuning its output frequency to have a fixed phase relation with the input optical signal frequency. This locking can be implemented in a homodyne fashion, where the frequencies of the input light and the CCO output light are the same, or in a heterodyne fashion, where these frequencies are different (also referred to as offset locking). Because in heterodyne locking the photodetector produces a beat signal at an offset frequency, the beat signal is usually down-converted by mixing with an RF reference at the same frequency in order to generate the phase error signal that tunes the CCO.

There are many applications that utilize homodyne and heterodyne locking. For example, homodyne locking provides high receiver sensitivities [2] and can be used for coherent demodulation in double-sideband suppressed carrier (DSB-

SC) communications [3]. Heterodyne locking of several “slave” lasers at the same frequency, which is offset relative to a reference “master” laser’s frequency, can be used to produce a high-power coherent beam combination (CBC) [4]. In addition, heterodyne locking of two lasers has been successfully demonstrated in producing coherent optical beats with frequencies in the GHz region [5]. This single-sideband source can find many applications in microwave photonics.

Unlike an RF PLL, an OPLL is not easily locked. In an RF PLL, the RF oscillator is spectrally pure, and the feedback loop bandwidth is relatively large in comparison to the frequency of the input signal. The large loop bandwidth can easily compensate for the small phase noise of the RF oscillator. In an OPLL, however, the tunable laser linewidth can be in the MHz range, and the feedback loop bandwidth is small compared to the frequency of the input signal, which is ~ 193 THz (1550 nm). The feedback loop bandwidth is typically smaller, and its latency is larger, compared to the RF PLL because of the large size of optical components and interconnects. Consequently, for successful locking of an OPLL, researchers have used either a very narrow linewidth lasers (kHz range) with large and slow feedback loops [6], or wide linewidth semiconductor lasers with very compact bulk optics necessary to achieve small loop latencies [5], [7].

Recently, we have demonstrated homodyne locking of the first OPLL photonic integrated circuit (OPLL-PIC) [8]. The OPLL-PIC is monolithically integrated, and its compactness allows the use of wide linewidth tunable semiconductor lasers. The small OPLL-PIC is robust and provides for easy packaging. In this work, we demonstrate proof-of-concept heterodyne locking the OPLL-PIC.

II. AN OPTICAL PHASE-LOCKED LOOP PHOTONIC INTEGRATED CIRCUIT

Fig. 1 shows a schematic of an OPLL-PIC and the external feedback electronics used in the heterodyne experiment. In

This work is supported by DARPA under United States Air Force Contract #FA8760-08-1-7856.

this section, we describe the OPLL-PIC. The details about the feedback loop and the heterodyne locking experiment are presented in Section III.

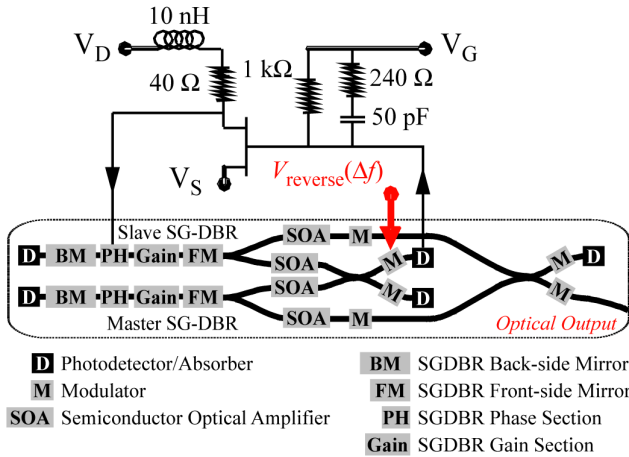


Figure 1. A schematic of the OPLL-PIC and the electronic feedback circuit used in a heterodyne locking experiment.

The monolithically integrated OPLL-PIC contains two widely tunable sampled-grating distributed reflector (SG-DBR) lasers, as well as semiconductor optical amplifiers (SOAs), multimode interference splitters/couplers (MMIs), and high-speed modulators and photodetectors. Light from each SG-DBR laser is split equally using a $90\text{-}\mu\text{m}$ -long 1×2 MMI, and each of the four output components is amplified using a $400\text{-}\mu\text{m}$ -long SOA. After amplification, the outputs from the two SG-DBR lasers are combined in two different $340\text{-}\mu\text{m}$ -long tunable 2×2 MMIs. One of the two MMIs is part of the OPLL-PIC feedback loop, and it has a $250\text{-}\mu\text{m}$ -long high-speed modulator followed by a $50\text{-}\mu\text{m}$ -long high-speed photodetector on each of its two output waveguides. The two photodetectors are used to provide the phase error signal to the feedback loop and can be used either separately or in a balanced pair configuration. The other MMI is part of the OPLL-PIC output. This MMI has a high-speed modulator on each of its two input waveguides, and similar to the feedback MMI, it also has a high-speed modulator on each of the two output waveguides. The output MMI, however, has a high-speed photodetector following a high-speed modulator only on one of its two output waveguides. This photodetector is used to monitor the coherent output beat signal in the electrical domain. The other output waveguide of the MMI is used to monitor the output beat signal from the output of the OPLL-PIC in the optical domain. The output waveguides are curved (7°) and their facets are anti-reflection coated in order to minimize reflections. The length of the OPLL-PIC is 6.6 mm , and the width is 0.45 mm . Fig. 2 shows a scanning electron microscope (SEM) image of the OPLL-PIC mounted on a carrier and wire-bonded. As can be seen in Fig. 2, there are four $100\ \mu\text{m} \times 100\ \mu\text{m}$ G-S-G-S-G-S-G RF pads ($150\ \mu\text{m}$ pitch) used for direct probing of the high-speed modulators and photodetectors in both feedback and output sections of the OPLL-PIC.

Our monolithic integration platform is referred to as the “Offset Quantum Well Platform” [9]. The epitaxial structure is grown on a 2-inch S-doped InP wafer using Metalorganic Chemical Vapor Deposition (MOCVD). An “active” 119-nm -thick multiple-quantum-well (MQW) region that provides gain is grown on top of a “passive” 300-nm -thick $1.4Q$ layer. The passive layer is used to guide light as well as provide modulation either via carrier plasma effect, in the forward-bias operation of the modulator diodes and phase sections of the SG-DBR lasers, or via the Franz-Keldysh effect, in the reverse-bias operation of the modulator diodes. The active devices (SOAs, SG-DBR gain sections, and photodetectors) are defined by wet etching, after which the gratings in the back-side and front-side SG-DBR laser mirrors are defined by Electron Beam Lithography. Subsequently, the p-cladding regrowth is done, and surface-ridge waveguides are wet etched. The rest of the main fabrication steps include dry etching and deposition of top-side n-contacts (used for high-speed modulators and photodetectors), BCB patterning for high-speed modulators and photodetectors, p-contact metallization, proton implant isolation of passive waveguide sections between devices, wafer thinning, and back-side n-contact metallization (used for all of the low-speed devices).

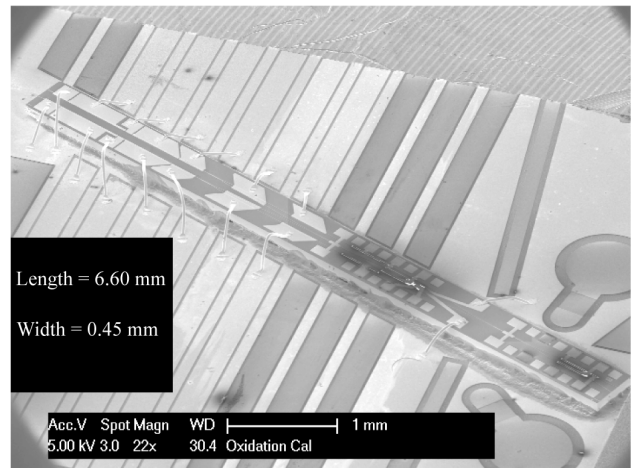


Figure 2. An SEM image of a fully fabricated OPLL-PIC after mounting on a test-carrier and wire-bonding.

III. HETERODYNE LOCKING DEMONSTRATION

As shown in Fig. 1, in the heterodyne locking of two SG-DBR lasers, one laser plays the role of the CCO (the slave laser), and its frequency is tuned by current injection into the phase section [10]. SG-DBR lasers offer several key advantages for OPLL applications. Their tuning sensitivities are $\sim 20\text{ GHz/mA}$, and they are an order of magnitude larger than those of the semiconductor lasers typically used in OPLL applications [5]. Their large sensitivities provide large loop gains and make OPLLs more stable. In addition, SG-DBR lasers have more than 40 nm ($>5\text{ THz}$) of quasi-continuous wavelength tuning range. Consequently, the OPLL-PIC can generate coherent optical beams at very high frequencies and can also provide broadband wavelength operation in homodyne applications. Fig. 3 illustrates this point, where a discrete incremental detuning of one integrated, unlocked SG-

DBR laser relative to the other is plotted. Lastly, unlike distributed feedback (DFB) lasers [5], SG-DBR lasers do not exhibit phase sign inversion when tuned via current injection into the phase section. It is hard to compensate this phase inversion using feedback electronics.

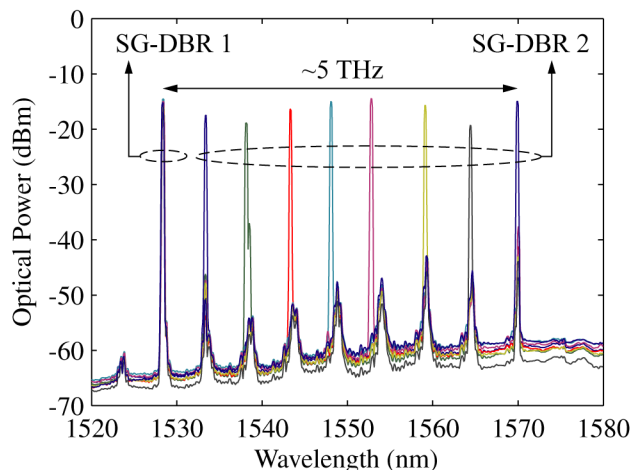


Figure 3. Optical spectra corresponding to incremental discrete detuning between the two on-chip unlocked SG-DBR lasers.

The relatively large linewidth that is characteristic of the SG-DBR laser is dominated by low-frequency jitter [11] and therefore can be well compensated by using the compact feedback loops achievable with monolithic integration. We measure linewidths of our lasers to be between 10 MHz and 50 MHz using a 30- μ s-delay self-homodyne technique. Fig. 4 shows the combined linewidth of two integrated unlocked SG-DBR lasers to be \sim 300 MHz when measured using an external photodetector and electrical spectrum analyzer.

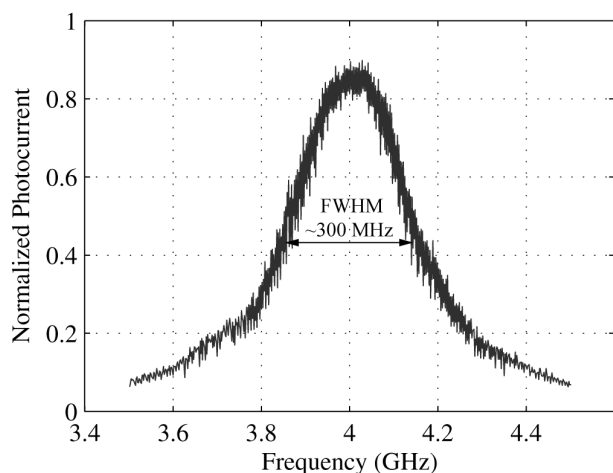


Figure 4. Combined linewidth of two unlocked integrated SG-DBR lasers.

In the heterodyne locking of the first integrated OPLL, we do not use an external mixer, which, as explained in Introduction, is a common practice [1]. Rather, for a proof-of-concept demonstration, we utilize sideband locking. In this scheme, the frequencies of the two SG-DBR lasers are detuned by the amount corresponding to the desired coherent beat frequency, *i.e.*, Δf . The combined laser outputs are then

modulated with a high-speed modulator at the output of the feedback 2x2 MMI at the same frequency Δf . As shown in Fig. 1, the modulator is voltage-driven in the reverse bias regime, where the drive voltage (V_{reverse}) is applied using a microwave synthesizer. As the detuning frequency and the modulation frequencies are the same, a sideband of one laser occurs at the same frequency as the center frequency of the other laser, and sideband locking becomes possible. A phase error current signal is generated in the photodetector and provided as an input to the feedback electronic circuit, where it is amplified and filtered. Subsequently, the phase error current signal is applied to the phase section of the slave SG-DBR laser, adjusting its output frequency to have a fixed phase relation to the output frequency of the master SG-DBR laser.

A FET transistor in the feedback loop is used to amplify and adjust the polarity of the phase error current signal from the photodetector so that it can be used to drive the phase section of the slave laser. The total load seen by the feedback photodetector is designed to provide a second-order transfer function with lag compensation. The LR circuit is designed to have a zero at a frequency close to the pole in the FM frequency response of the slave laser, making it a more controllable device. The 3-dB point in the FM frequency response of the SG-DBR laser is \sim 70 MHz. Since the laser itself acts as an integrator, the remaining RC circuit is required to provide only a single pole. This is achieved with the larger of the two resistors that dominates at low frequencies. The smaller resistor dominates at frequencies closer to the 3-dB point and provides a zero that is necessary to improve stability of the loop at the frequencies where the gain becomes unity. The resulting bandwidth of the loop is \sim 300 MHz, which, as we show below, is sufficient for locking an SG-DBR laser, in large part due to the fact that the phase noise of SG-DBR lasers is dominated by low-frequency jitter.

Figs. 5(a) and 5(b) show oscilloscope traces of the OPLL-PIC optical output before and after locking it with a 5 GHz microwave signal, which is also used to trigger the oscilloscope. Locking is achieved by gradually bringing the detuning frequency closer to the modulation frequency. As shown in Fig. 5(a), before locking, the phase noise is so large that only the envelope of the beat is observed. When the OPLL is locked, most of the power from the beat is in the locked state, as shown in Fig. 5(b). Occasional cycle slipping of the OPLL is evident in the jitter shown in Fig. 5(b). Fig. 6 shows the corresponding phase noise spectrum of a locked OPLL-PIC, measured using an external photodetector and an electrical spectrum analyzer. The phase noise reaches maxima at frequencies \sim 300 MHz below and above the 5 GHz offset frequency because the loop becomes unstable when operating at frequencies exceeding its bandwidth (\sim 300 MHz).

There is a significant noise penalty associated with the sideband locking scheme because the power in the sidebands is a fraction of the power in the main lobes, producing an inefficient mixing in the photodetector. For the same reason, the modulation power needed for successful locking in our experiment is around 10 dBm. The noise penalty could be decreased by using an external RF mixer, which is a more complicated setup. In the future work, feedback electronics

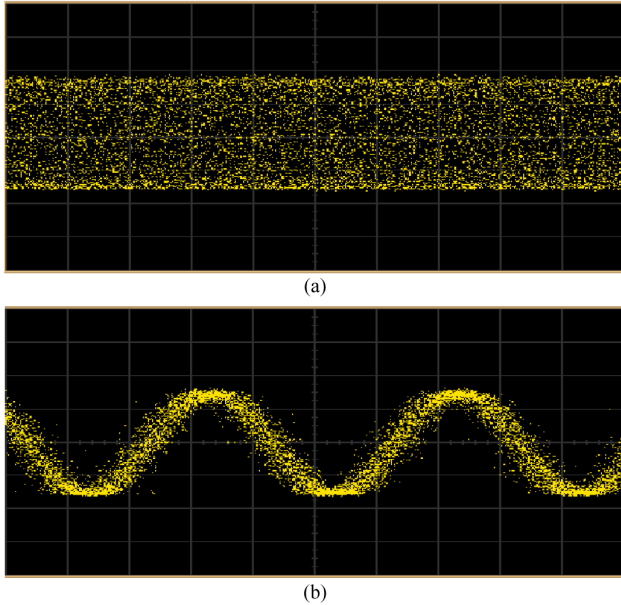


Figure 5. Oscilloscope traces of the OPLL-PIC optical output (a) before and (b) after heterodyne locking of the SG-DBR lasers at a 5GHz frequency offset. Both traces are 500 ps long.

will be integrated to further improve the loop bandwidth and decrease the phase noise. In addition, the on-chip feedback photodetectors will be used in a balanced configuration, which should decrease the phase noise penalty due to laser amplitude noise.

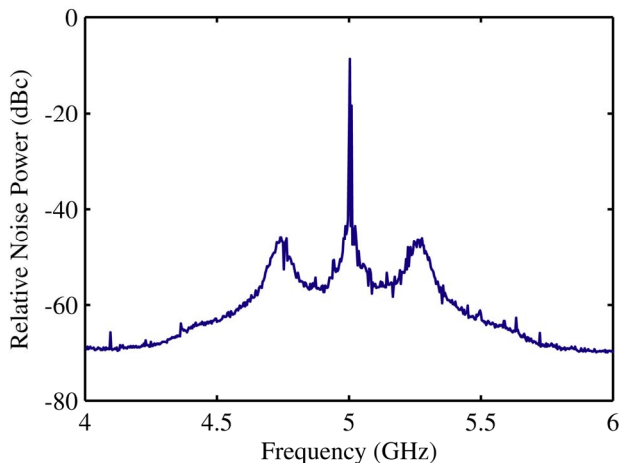


Figure 6. Phase noise spectrum of the OPLL-PIC output corresponding to heterodyne locking of the two SG-DBR lasers at a 5 GHz frequency offset.

IV. CONCLUSION

In this paper, we have demonstrated a proof-of-concept heterodyne locking of the first integrated OPLL. The OPLL-PIC contains two SG-DBR lasers monolithically integrated with SOAs, MMIs, and high-speed modulator and photodetectors. The monolithic integration enables small-

latency (large-bandwidth) feedback loops, necessary to compensate for wide linewidths of SG-DBR lasers, and semiconductor lasers in general. SG-DBR lasers offer large tuning sensitivities, they are well-behaved when used as CCOs, as they do not suffer from the phase inversion problem, and they offer wide wavelength tuning ranges, *i.e.*, large coherent beat frequencies. The OPLL-PIC contains on-chip modulators that can be used for modulation of a coherent millimeter-wave beat. The technology is robust, has a small footprint, and provides for easy packaging. Future improvements of the OPLL will be achieved by using both feedback detectors as a balanced receiver pair in order to reduce laser amplitude noise, which increases the phase noise of the OPLL. In addition, more sophisticated, integrated feedback electronics will be used in order to further decrease the feedback loop latency, thereby decreasing the phase noise of the OPLL.

ACKNOWLEDGMENT

A portion of this work was done in the UCSB nanofabrication facility, part of the NSF funded NNIN network.

REFERENCES

- [1] R. C. Steele "Optical phase-locked loop using semiconductor laser diodes," *Electron. Lett.*, vol. 19, no. 2, pp. 69–71, Jan. 20, 1983.
- [2] W. R. Leeb, H. K. Philipp, and A. L. Scholtz, "Homodyne receiver for ASK signals at 10- μ m wavelength," *Appl. Opt.*, vol. 23, no. 4, pp. 523–524, Feb. 15, 1984.
- [3] H. K. Philipp, A. L. Scholtz, E. Bonek, and W. R. Leeb, "Costas loop experiments for a 10.6 μ m communications receiver," *IEEE Trans. Commun.*, vol. COM-31, no. 8, pp. 1000–1002, Aug. 1983.
- [4] N. Satyan, W. Liang, A. Kewitsch, G. Rakuljic, and A. Yariv, "Coherent power combination of semiconductor lasers using optical phase-lock loops," *IEEE J. Sel. Top. Quant. Electron.*, vol. 15, no. 2, pp. 240–247, Mar./Apr. 2009.
- [5] L. N. Langley, M. D. Elkin, C. Edge, M. J. Wale, U. Gliese, X. Huang, and A. J. Seeds, "Packaged semiconductor laser optical phase-locked loop (OPLL) for photonic generation, processing and transmission of microwave signals," *IEEE Trans. Microwave Theory Technol.*, vol. 47, no. 7, pp. 1257–1264, July 1999.
- [6] L. A. Johansson and A. J. Seeds, "Millimeter-wave modulated optical signal generation with high spectral purity and wide locking bandwidth using a fiber-integrated optical phase-lock loop," *IEEE Photon. Tech. Lett.*, vol. 12, no. 6, pp. 690–692, Jun. 2000.
- [7] R. T. Ramos and A. J. Seeds, "Fast heterodyne optical phase-lock loop using double quantum well laser diodes," *Electron. Lett.*, vol. 28, no. 1, pp. 82–83, Jan. 1992.
- [8] S. Ristic, A. Bhardwaj, M. J. Rodwell, L. A. Coldren, and L. A. Johansson, "Integrated Optical Phase-Locked Loop," *Optical Fiber Communications Conf. (OFC). Postdeadline Tech. Dig. Opt. Soc. Amer.*, PDPB3, 2009.
- [9] J. W. Raring *et al.*, "Advanced integration schemes for high-functionality/high-performance photonic integrated circuits," presented at the Proc. SPIE, San Jose, CA, Jan. 23–25, 2006, Paper 61260H.
- [10] L. A. Coldren, "Monolithic tunable diode lasers," *IEEE J. Select. Topics Quantum Electron.*, vol. 6, no. 6, pp. 988–999, Nov./Dec. 2000.
- [11] S. Nakagawa *et al.*, "Phase noise of widely-tunable SG-DBR laser," in *Optical Fiber Communications Conf. (OFC). (Trends in Optics and Photonics Series Vol. 86)Tech. Dig. (IEEE Cat. 03CH37403). Opt. Soc. Amer.*, vol. 2, Wash., DC, 2003, pp. 461–462.

II. Vertical-Cavity Surface-Emitting Lasers (VCSELs) & MBE Technology

Efficient, High-Data-Rate, Tapered Oxide-Aperture Vertical-Cavity Surface-Emitting Lasers

Yu-Chia Chang, and Larry A. Coldren, *Fellow, IEEE*

(Invited Paper)

Abstract—New advances in high-efficiency, high-speed 980 nm vertical-cavity surface-emitting lasers (VCSELs) are presented. The tapered oxide aperture was optimized to provide additional mode confinement without sacrificing its static low-loss performance. The pad capacitance was reduced by using BCB, removing the n -contact layer, and shrinking the pad dimension. The mesa capacitance was also lowered by using a thicker oxide aperture and deep oxidation layers. With all these improvements, our devices demonstrated >20 GHz bandwidth, the highest for 980 nm VCSELs, and 35 Gb/s operation at only 10 mW power dissipation, corresponding to the highest reported data-rate/power-dissipation ratio of 3.5 Gbps/mW.

Index Terms—Oxidation, optical interconnects, optical modulation, semiconductor lasers, Vertical-cavity surface-emitting lasers (VCSELs).

I. INTRODUCTION

IN the past several years, vertical-cavity surface-emitting lasers (VCSELs) have received renewed interest due to their applications in optical interconnects, which are becoming widely used, partially because of possible reductions in system power dissipation. Due to the intensive worldwide research efforts, the performance of VCSELs, particularly in high-speed aspect, has made tremendous progress in just the past few years. In 2006, 25 Gb/s operation was first reported by N. Suzuki *et al.* [1]. In 2007, data rates of 30, 35, 40 Gb/s were consecutively demonstrated by K. Yashiki *et al.* [2], the authors [3], and T. Anan [4], respectively. In the year of 2007, data rate of VCSEL was pushed from 25 to 40 Gb/s, a significant progress.

Table I summarizes the state-of-the-art high-speed VCSEL structures and results in three different wavelengths. At 850 nm, 30 Gb/s was reported by R. Johnson in 2008 [5]. At 980 nm, 35 Gb/s was our results. At 1.1 μm , 40 Gb/s was reported by T. Anan. By examining the structures of these record VCSELs, we can see what the requirements to achieve high-speed operation are. Thick low-dielectric-constant materials such as silicon oxide, Benzocyclobutene (BCB), and polyimide have to be used for reducing the pad capacitance. The mesa capacitance has to be lowered by either ion implantation or deep oxidation layers. The optical modes need to be confined by oxide aperture or buried tunnel junction. On the other hand, there are unique features for each device. For example, highly-strained InGaAs/GaAs quantum wells (QWs) are used in Anan's devices to achieve high differential gain.

Manuscript received November 3, 2008; Revised December 3, 2008. This work was supported by DARPA via ARL.

The authors are with the Department of Electrical and Computer Engineering, University of California, Santa Barbara, CA 93106 USA (phone: 805-893-7065; fax: 805-893-4500; e-mail: yuchia@engineering.ucsb.edu).

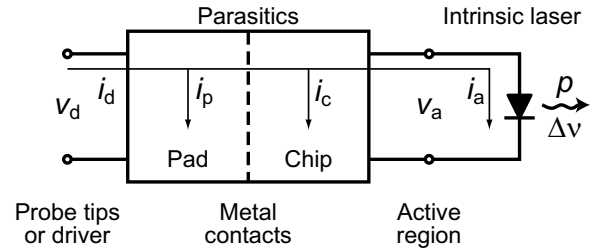


Fig. 1. Cascaded two-port model of diode laser.

Compared with the other two devices that operate best at ~ 6 μm , our devices can be much smaller due to their lower cavity losses associated with the lens-like tapered aperture [6]. Therefore, the threshold current of our devices is much lower at 0.14 mA for a 3 μm diameter device, and because the resonance frequency varies inversely with the square-root of the photon volume, our devices are fast at small biases, achieving a 20 GHz bandwidth at just 2 mA. In addition, smaller devices with low cavity losses are more power efficient, which is very important for optical interconnect applications. A data rate of 35 Gb/s was demonstrated at 4.4 mA with only 10 mW power dissipation, corresponding a record data-rate/power-dissipation ratio of 3.5 Gbps/mW. All these results are enabled by carefully designing the tapered oxide aperture for low loss and high confinement, optimizing the distributed Bragg reflector (DBR) mirror, incorporating the deep oxidation layers, and reducing the pad capacitance.

The paper is organized as follows: Section II presents the theoretical background for directly-modulated VCSELs. The device designs are covered in Section III. Section IV shows the device fabrication. The results and discussion are given in Section V. Finally, Section VI concludes the paper.

II. THEORETICAL BACKGROUND

For directly-current-modulated VCSELs, the bandwidth is determined by the intrinsic laser properties as well as the extrinsic parasitics. To make our discussion easier, we will consider them separately using the cascaded two-port model [7], shown in Fig. 1, to isolate the parasitics from the intrinsic laser. The intrinsic laser is defined as the active region approximately in the apertured area where carriers and photons interact via absorption and emission. The parasitics, defined between the intrinsic laser and driving circuit, are split into the pad parasitics and chip parasitics at the metal contacts.

The input variables of the VCSEL are the drive voltage, v_d , and current, i_d . The voltage and current seen by the intrinsic

TABLE I
STATE-OF-THE-ART HIGH-SPEED VCSELS

Wavelength (nm)	Authors	Features	Achievements
850	R. Johnson <i>et al.</i> [5]	<ul style="list-style-type: none"> • Thick silicon oxide • Proton implantation • Oxide aperture 	<ul style="list-style-type: none"> • $I_{th}=0.75$ mA for 6 μm devices • 19 GHz bandwidth • 30 Gb/s operation at 8 mA
980	Y.-C. Chang <i>et al.</i> [3]	<ul style="list-style-type: none"> • BCB • Deep oxidation layers • Low-loss high-confinement tapered oxide aperture 	<ul style="list-style-type: none"> • $I_{th}=0.14$ mA for 3 μm devices • >20 GHz bandwidth • 35 Gb/s operation at 4.4 mA
1100	T. Anan [4]	<ul style="list-style-type: none"> • Polyimide • Ion implantation • Buried tunnel junction • Optimized active region 	<ul style="list-style-type: none"> • $I_{th}<1$ mA for 6 μm devices • 24 GHz bandwidth • 40 Gb/s operation at 5 mA

laser are v_a and i_a , respectively. The output variables are the output power, p , and frequency shift, $\Delta\nu$. For short-distance optical interconnects, dispersion is negligible and $\Delta\nu$ will not be discussed. The currents entering the pad and chip parasitics are i_p and i_c , respectively.

A. Intrinsic laser limitations

The dynamic behaviors of diode laser are commonly analyzed using small-signal frequency response. For diode laser, the modulation response can be approximated as [8]:

$$H_{\text{int}}(\omega) \equiv \frac{p(\omega)}{i_a} = \frac{A}{\omega_r^2 - \omega^2 + j\omega\gamma} \quad (1)$$

where A is an amplitude factor, ω is the angular modulation frequency, $\omega_r = 2\pi f_r$ is the relaxation resonance frequency, and γ is the damping factor.

The relaxation resonance frequency is the natural oscillation frequency between the carriers and photons in the laser cavity and can be approximately expressed as

$$\omega_r = \left[\frac{v_g a N_p}{\tau_p} \right]^{1/2} = \left[\frac{v_g a}{q V_p} \eta_i (I - I_{th}) \right]^{1/2} \quad (2)$$

where v_g is the group velocity, a is the differential gain at threshold, N_p is the photon density, τ_p is the photon lifetime, q is the electronic charge, V_p is the mode volume, η_i is the injection efficiency, I is the bias current, and I_{th} is the threshold current.

The relaxation resonance frequency basically determines how fast an intrinsic laser can be modulated, provided the damping is not severe. To improve the high-speed performance, the relaxation resonance frequency must be increased. As shown in Eq. (2), higher differential gain and larger photon density increase the relaxation resonance frequency. Several approaches have been shown to increase the differential gain, such as using quantum dots active region [9], adding strain in the QW [10], and p -doping the active region [11]. The photon density can be increased by increasing the current that contributes to the photon number, $\eta_i(I - I_{th})$, and/or reducing the mode volume. The mode volume can be reduced using dielectric DBRs [2] in the longitudinal direction and photonic crystals [12] in the lateral direction.

Since the relaxation resonance frequency increases with the bias current, a figure-of-merit to evaluate how efficient an intrinsic laser can be modulated is the D -factor [13]:

$$D \equiv \frac{f_r}{(I - I_{th})^{1/2}} = \frac{1}{2\pi} \left[\frac{v_g a}{q V_p} \eta_i \right]^{1/2}$$

To evaluate the device's overall high-speed performance, modulation current efficiency factor (MCEF) is used:

$$\text{MCEF} \equiv \frac{f_{3\text{dB}}}{(I - I_{th})^{1/2}}$$

where $f_{3\text{dB}}$ is the 3-dB frequency. If the parasitics and damping are small, $\text{MCEF} \approx 1.55D$.

The damping factor, γ , is given as:

$$\gamma = v_g a N_p \left[1 + \frac{\Gamma a_p}{a} \right] + \frac{1}{\tau_{\Delta N}} + \frac{\Gamma R'_{sp}}{N_p} \quad (3)$$

where Γ is the confinement factor, $a_p = -\partial g / \partial N_p$, $\tau_{\Delta N}$ is the differential carrier lifetime, and R'_{sp} is the spontaneous emission rate into the modes. At high photon density, the first term on the right hand side dominates, and γ increases proportional to N_p and hence f_r^2 . The proportionality between γ and f_r^2 is the K -factor, which determines the theoretical maximum 3-dB frequency:

$$f_{3\text{dB}}|_{\text{max}} = \sqrt{2} \frac{2\pi}{K}$$

B. Extrinsic parasitic limitations

When dealing with high-frequency devices, parasitics are always a concern. Parasitics divert the modulated current i_d from entering the intrinsic laser due to i_p and i_c . In most cases, it is desirable to minimize the parasitics so that the intrinsic bandwidth can be achieved.

Fig. 2 shows a cross-sectional schematic of an oxide-confined VCSEL superimposed with its parasitic elements. The pad capacitance, C_p , represents all the capacitances between the signal and ground from the probe tips/driver to the metal contacts. The value of C_p varies from tens to hundreds of femto-farads, depending on the pad layout and the materials between the pads. Typical high-speed VCSELS employ thick low-dielectric-constant materials such as polyimide or BCB underneath the signal pad to reduce C_p . The pad resistance,

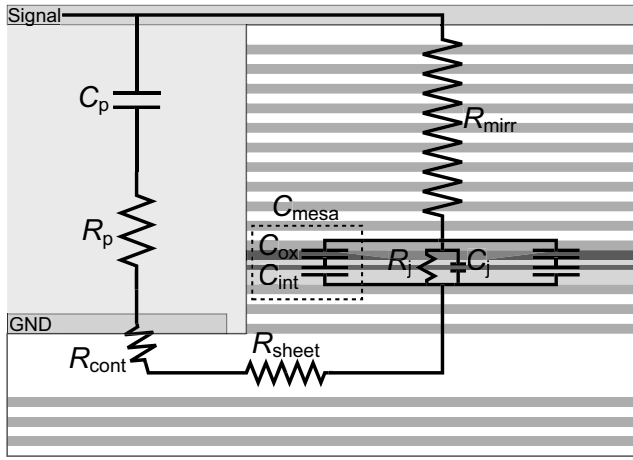


Fig. 2. Cross-sectional schematic of VCSEL superimposed with its parasitics.

R_p , accounts for the pad loss. Since it is usually relatively small, in the ohm range, compared with the impedance of C_p at the frequency of interest, it is sometimes omitted in the small-signal model.

The mirror resistance, R_{mirr} , includes the resistances from both the n - and p -DBRs. R_{sheet} represents the sheet resistance in the n -contact layer, and R_{cont} is the contact resistance for both contacts. All these resistances, usually dominated by R_{mirr} , can be grouped together into $R_m = R_{\text{mirr}} + R_{\text{sheet}} + R_{\text{cont}}$ in the small-signal model. The mesa capacitance, C_{mesa} , is the oxide capacitance, C_{ox} , in series with the capacitance associated with the intrinsic region below the aperture, C_{int} . C_{mesa} depends on the pillar size and the thicknesses of the oxide and intrinsic layer.

The capacitance, C_j , represents the diode junction capacitance in the apertured area where current flows. It is the sum of the depletion capacitance and diffusion capacitance. Under normal forward bias condition, C_j is dominated by the diffusion capacitance, which models the modulation of the carriers stored in the intrinsic separate-confinement heterostructure (SCH) region [14]. It has been shown that the diffusion capacitance not only depends on the carrier lifetime but also depends on the length/grade of the intrinsic SCH region [15]. By decreasing the doping setback and grading the SCH, the diffusion capacitance can be reduced. To simplify our model, C_{mesa} and C_j are grouped together into $C_m = C_{\text{mesa}} + C_j$. Lastly, the intrinsic laser is represented by the junction resistance, R_j .

Fig. 3 illustrates the small-signal model of VCSEL and the RF driving source. Here we have implicitly assumed that VCSEL is driven by the instrument. The RF driving source consists of a voltage source, v_s , and a characteristic impedance of Z_0 , which is included to account for the power reflection due to impedance mismatch.

The effects of the parasitics can be described by the transfer function, $H_{\text{ext}}(\omega)$ [16]:

$$H_{\text{ext}}(\omega) \equiv \frac{\text{current flowing into the intrinsic diode}}{\text{voltage from the voltage source}} = \frac{i_a(\omega)}{v_s}$$

The frequency at which $|H_{\text{ext}}(\omega)|^2 / |H_{\text{ext}}(0)|^2 = 1/2$ is

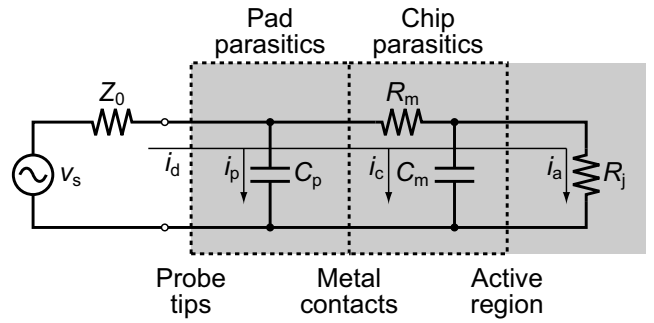


Fig. 3. Small-signal model with the driving source. The VCSEL is grayed.

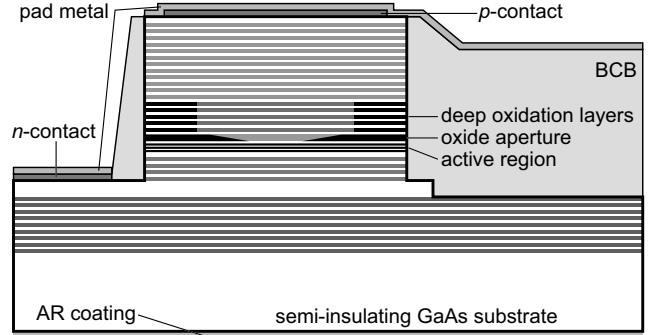


Fig. 4. schematic cross-section of our devices.

defined as the parasitic 3-dB frequency, ω_{rc} . This transfer function can be approximated by a single-pole low-pass filter function:

$$H_{\text{ext}}(\omega) = \frac{B}{1 + j(\omega)/(\omega_0)} \quad (4)$$

where B is a proportional constant and ω_0 is the parasitic roll-off frequency, which may be different from ω_{rc} .

The overall electrical modulation frequency response, $H(\omega)$, is given as:

$$\begin{aligned} H(\omega) &\equiv \left| \frac{p(\omega)}{v_s} \right|^2 = \left| \frac{i_a(\omega)}{v_s} \cdot \frac{p(\omega)}{i_a(\omega)} \right|^2 = |H_{\text{ext}}(\omega) \cdot H_{\text{int}}(\omega)|^2 \\ &= \left(\frac{B^2}{1 + (\omega/\omega_0)^2} \frac{A^2}{(\omega_r^2 - \omega^2)^2 + \gamma^2 \omega^2} \right) \end{aligned} \quad (5)$$

which gives the commonly used three-poles formula for fitting the frequency response to extract ω_r , γ , and ω_0 .

III. DEVICE STRUCTURE

Our devices are n -intracavity, bottom-emitting, oxide-confined VCSELs emitting at 980 nm wavelength as shown in Fig. 4. For 980 nm emission, strained InGaAs/GaAs QW, which has lower transparency and higher differential gain, can be used. Bottom emission offers the possibility of backside microlenses, which can collimate the output beams and thus improve the alignment tolerance and reduce the packaging costs [17]. In addition, direct driver integration can be realized using flip-chip bonding, which eliminates the parasitics associated with the bonding wires.

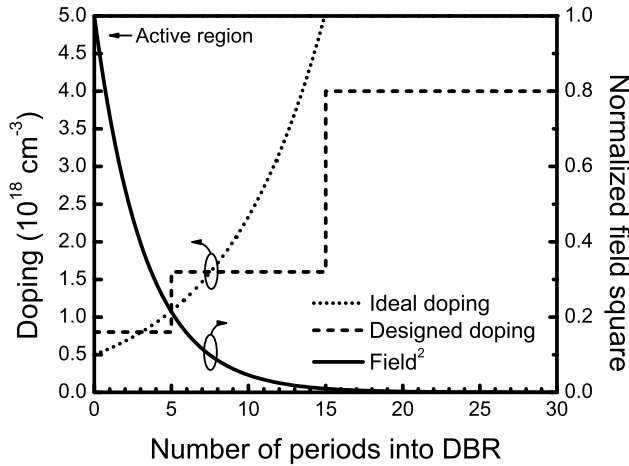


Fig. 5. Average doping profile for each DBR period.

Our devices have a 14-period undoped GaAs/AlAs DBR, followed by a five-quarter wavelength thick silicon-doped n -GaAs contact layer, and a 4-period n -type GaAs/Al_{0.9}Ga_{0.1}As DBR. The highly-doped n -contact layer is placed four periods away from the cavity in consideration of optical loss and longitudinal mode confinement. The active region has three InGaAs/GaAs QWs embedded in the SCH layer. On top of the SCH is the oxide aperture, followed by a 30-period carbon-doped p -mirror, which has 5 periods of GaAs/Al_{0.93}Ga_{0.07}As DBR for the deep oxidation layers and 25 periods of GaAs/Al_{0.85}Ga_{0.15}As DBR. The top layer is a highly-doped p -contact layer.

In the remaining part of this section, we will discuss the components of our VCSELs, namely the DBR mirror, oxide aperture, deep oxidation layers, and cavity structure.

A. DBR mirror

A major trade-off in designing VCSELs is the electrical resistance and optical loss by the free carrier concentration, controlled by the doping. Due to higher free carrier absorption loss and lower mobility of holes, p -mirror usually employs more sophisticated design scheme, and we will focus on its design here.

First, the average doping concentration for each DBR period is determined by maintaining a constant loss-resistance product across the whole p -mirror. For the first-order approximation, the ideal doping concentration, $\rho(z)$, should be [18]

$$\rho(z) \propto \psi(z)^{-1/2}$$

where $\psi(z)$ is the electric field square profile and can be determined using one-dimensional transfer matrix calculation. Fig. 5 plots the average doping concentration for each DBR period in our devices. Three different doping levels were used to approximate the calculated ideal doping profile. The doping is the lowest near the active region, where the electric field is the highest, for maintaining reasonable optical losses. As moving towards the top contact layer, the doping increases to reduce the resistance.

Once the average doping concentration has been determined, the doping profile within the period can be designed.

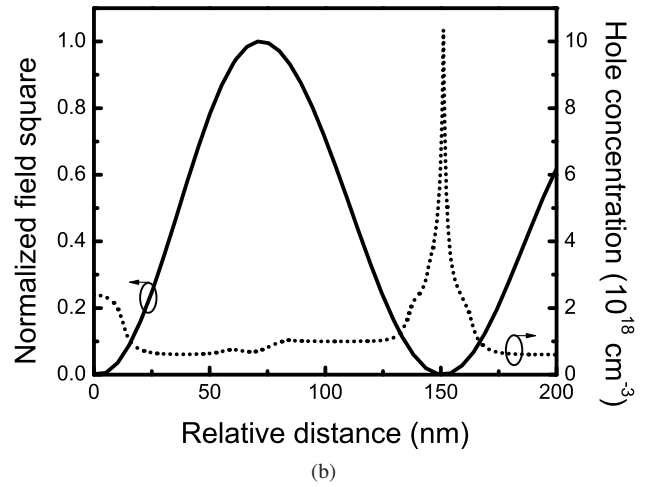
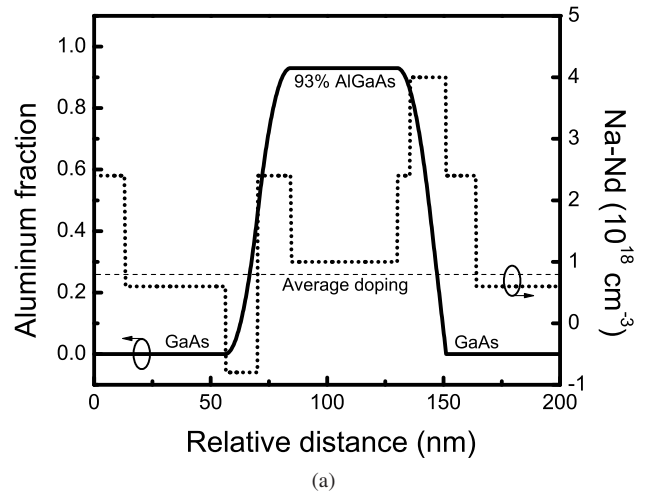


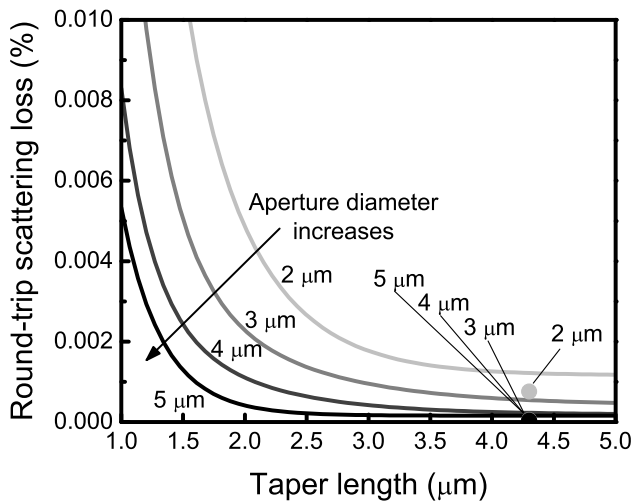
Fig. 6. (a) Grading and doping and (b) normalized electric field square and simulated hole concentration in one DBR period.

Bandgap-engineering was used to eliminate the hetero-barriers in the valence band at the interfaces and simultaneously maintain minimal optical losses. Fig. 6 shows our low-doped DBR design. The horizontal dash line in Fig. 6(a) is the average doping concentration obtained from Fig. 5. The doping in GaAs and AlGaAs layers are slightly adjusted to compensate the difference in the mobility.

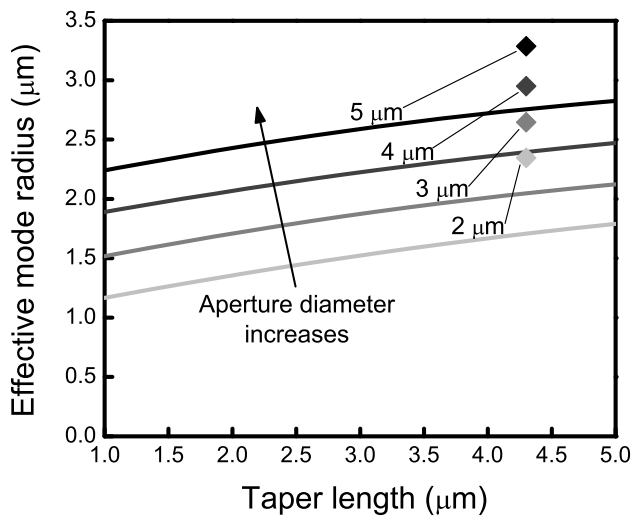
We can also take advantages of the standing-wave effects in VCSELs. At the standing-wave peaks, bi-parabolic grade and modulation doping was used to flatten the valence band [19]. No excess holes are produced with this scheme so that the optical loss is minimized. On the other hand, uni-parabolic scheme was used at the standing-wave nulls [20]. The abrupt change of the slope of the composition at 150 nm creates an accumulation of holes, which improves the resistance without adding extra optical loss.

B. Oxide aperture

Tapered oxide apertures, which have been demonstrated to have low optical scattering losses [6], are used in our devices for electrical and optical confinement. The thickness of the aperture was increased from the standard quarter-wavelength



(a)



(b)

Fig. 7. (a) Round-trip optical scattering loss and (b) effective mode radius versus taper length for different device sizes, ranging from 2 to 5 μm in diameter. These curves were calculated assuming the effective indices in the unoxidized and fully oxidized sections are 3.254 and 3.113, respectively. Superimposed are the simulated results for the original taper aperture, plotted as circles (scattering loss) in (a) and diamonds (effective mode radius) in (b).

thick to half-wavelength thick for lowering the chip parasitic capacitance.

As discussed earlier, the mode volume has to be reduced to efficiently achieve high-speed operation. However, there is a trade-off between the optical scattering loss and mode confinement. Blunter taper provides better mode confinement but also creates more loss. In order to find the optimal design, simulations based on the model given in Ref. [6] were performed and the results are plotted in Fig. 7 [21].

Fig. 7(a) shows the simulated round-trip optical scattering loss for different taper lengths and the aperture diameters of interest, ranging from 2 to 5 μm . As expected, the optical scattering loss increases rapidly as the taper length goes below the critical length L_c , which is smaller for larger diameter devices. Taper length of 4 μm was conservatively chosen so that the scattering losses for all the devices are

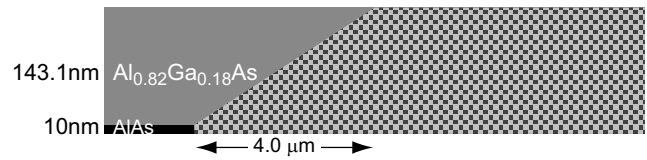


Fig. 8. Tapered oxide aperture design in our devices.

still within the flat region. The circles in the figure are the simulated results for our original aperture, which has a quarter-wavelength thickness and 4.3 μm taper length. The original aperture was optimized for low optical scattering loss and has experimentally demonstrated negligible optical scattering loss down to 1.5 μm diameter devices. As can be seen, the optical scattering loss does not increase considerably from our original aperture design.

On the other hand, the mode confinement does improve greatly compared with the original aperture. Fig. 7(b) plots the corresponding effective mode radius, which is defined as the $1/e^2$ radius for an equivalent Gaussian mode with the same total power and peak amplitude. The diamonds in the figure are the results of our original aperture. Take 3 μm devices as an example, the effective mode radius reduced from 2.64 to 2.01 μm . This corresponds to a 1.73 times mode volume reduction and a 31% increase in D -factor.

Fig. 8 shows our aperture design, which consists of a 10 nm pure AlAs layer and a 143.1 nm $\text{Al}_{0.82}\text{Ga}_{0.18}\text{As}$ layer. This design gives a taper length of $\sim 4 \mu\text{m}$.

C. Deep oxidation layers

Due to the alternating layers in the DBRs, VCSELs inherently have higher series resistances, and if no precaution is taken, the bandwidth is likely to be parasitic-limited. One approach to relieve the parasitic limitation is to reduce the capacitance, specifically C_{mesa} . However, the thicknesses of the oxide aperture and the intrinsic semiconductor below the oxide are restricted by the cavity design and can not be easily increased. In order to lower C_{mesa} , additional thick non-conducting layers have to be created inside the mesa, and this is commonly done using proton implantation. For bottom-emitting VCSELs with semiconductor top mirror, energy of several hundreds electron volt is needed for the protons to reach the active region. This in turn requires fairly thick masking layers to block these high-energy protons, which inevitably complicates the fabrication process and increases the costs.

Another approach to form the non-conducting layers is to use oxidation. One example is to use double oxide apertures [22], which have different optical waveguiding than the single aperture and need to be considered. We proposed the deep oxidation layers [23], which can be formed simultaneously with the oxide aperture. By increasing the Aluminum fraction of the AlGaAs layers for the first several DBR periods in the top mirror, these layers will penetrate further during oxidation as shown in Fig. 9. These deeply oxidized layers effectively increase the equivalent capacitor thickness and thus reduce the capacitance.

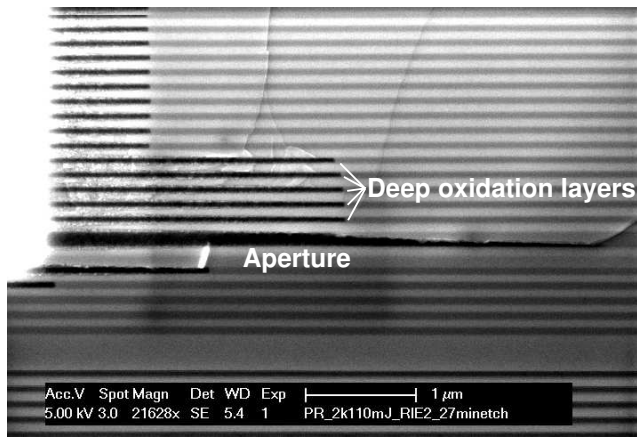


Fig. 9. Cross-sectional SEM showing five deep oxidation layers and the oxide aperture.

There are several advantages with this approach. First, it is simple and can be easily incorporated into any oxide-confined VCSEL with a semiconductor top mirror. Second, no process modification is required. Third, the index contrast in the unoxidized region where optical modes exist also increases due to these higher Aluminum content layers, which improves the longitudinal mode confinement. Fourth, compared with proton implantation, this approach requires thinner non-conducting layers to achieve the same C_{mesa} due to the smaller dielectric constant of the oxide than the semiconductor. This is favorable in consideration of the resistance because of the distance that the current has to funnel is reduced.

In order not to perturb the optical modes, the length of the deep oxidation layers was conservatively chosen to be 5 μm , which can be achieved with $\text{Al}_{0.93}\text{Ga}_{0.07}\text{As}$ layers in our device structure. Five deep oxidation layers were incorporated in our devices.

D. Cavity

Fig. 10 shows the cavity design of our devices. The active region is sandwiched by two $\text{Al}_{0.3}\text{Ga}_{0.7}\text{As}$ SCH layers. The thickness of the bottom SCH is 111 nm, and the n -doping ($\sim 2 \times 10^{17} \text{ cm}^{-3}$) is setback 50 nm to minimize the carrier transport effects [24] and maintain a reasonable loss. The top SCH layer has a thickness of 20 nm and is undoped to reduce the current spreading underneath the oxide aperture [25]. However, the layers which form the oxide aperture are doped p -type at $\sim 6 \times 10^{17} \text{ cm}^{-3}$ to reduce the resistance from the apertured area.

IV. DEVICE FABRICATION

The sample was grown on a semi-insulating GaAs (100) substrate by molecular beam epitaxy. The fabrication flow is shown in Fig. 11. The fabrication began by etching cylindrical mesas ranging from 21 to 30 μm in diameter to expose the n -GaAs contact layer using reactive ion etch. The oxide apertures were then formed by wet oxidation, resulting in a $\sim 9 \mu\text{m}$ oxide aperture with $\sim 4 \mu\text{m}$ taper length. The deep oxidation layers were also formed at the same time. Ti/Pt/Au

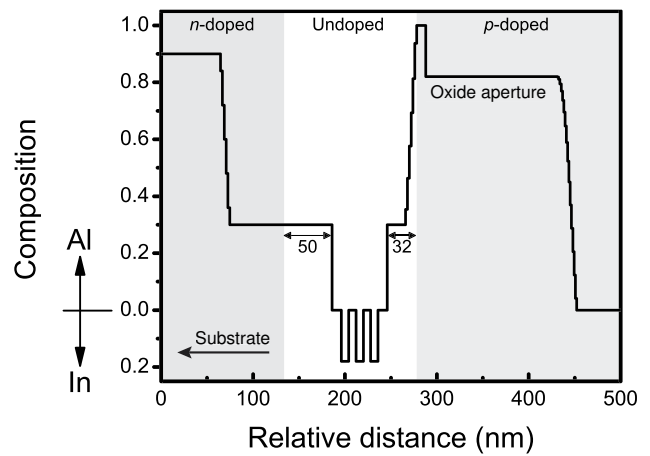


Fig. 10. Cavity structure of our devices.

and AuGe/Ni/Au were evaporated for the p - and n -contacts, respectively. The part of the n -GaAs contact layer (ground) that lies beneath the p -pad (signal) is removed to reduce the pad capacitance. BCB, sandwiched between silicon nitride, was patterned and fully cured. Then vias were opened to expose the contacts, followed by depositing Ti/Au as pad metal. The signal pad is only $40 \times 70 \mu\text{m}^2$ for low capacitance. Finally antireflection coating was applied to reduce backside reflection. Fig. 12 shows a top-view SEM of the fabricated device.

V. DEVICE RESULTS

A. L-I-V-P curves

Fig. 13 plots the voltage, output power, and power dissipation against current (L-I-V-P) curves for the 3 μm diameter device. The device has a slope efficiency of 0.67 W/A, corresponding to a differential quantum efficiency (DQE) of 54%. The threshold current is only 0.144 mA, comparatively low for typical high-speed VCSELs which have diameters from 5 to 8 μm . The low threshold current along with high slope efficiency indicates that the internal loss in our devices is low. This means that our tapered oxide aperture does not introduce excess optical scattering losses even down to 3 μm diameter devices.

The threshold voltage, a good measure of the excess voltage drop from the hetero-barriers of the DBRs, is 1.47 V. It is very low for such a small device, only 220 meV larger than the photon energy. This low threshold voltage is the consequence of our optimized p -doping scheme as well as the low threshold current. The series resistance is approximately 250 Ω at 4.4 mA. The series resistance is relatively high due to the deep oxidation layers which restrict the current conducting area. The thermal impedance is 3.3 $^{\circ}\text{C}/\text{mW}$. At a bias current of 4.4 mA, the power dissipation and temperature rise are 10 mW and 33 $^{\circ}\text{C}$, respectively. This device has a peak wall-plug efficiency of 31% at 1 mA and a maximum output power of 3.1 mW at a bias current of 7 mA.

Fig. 14 plots the threshold current and DQE versus the stage temperature for another 3 μm device which has a slightly lower DQE at 20 $^{\circ}\text{C}$. Even though the gain-cavity offset in our

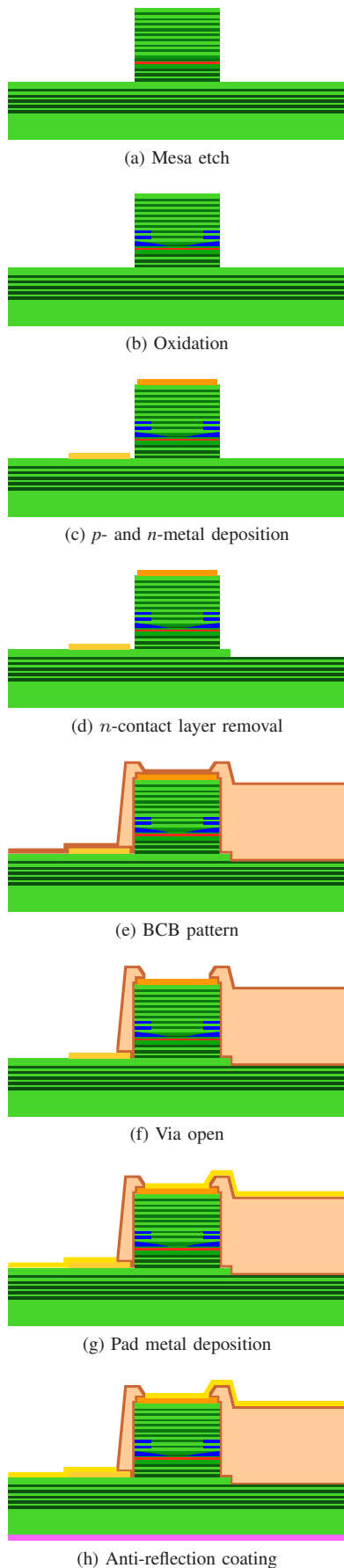


Fig. 11. Process flow.

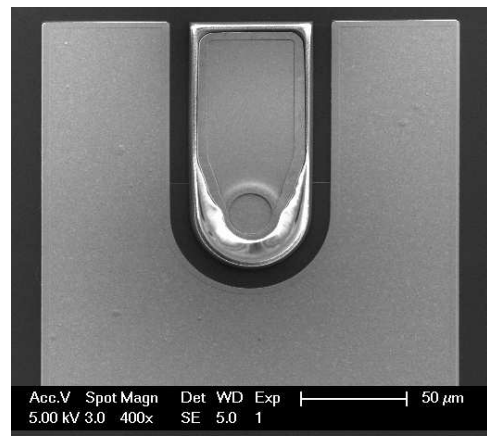


Fig. 12. Top-view SEM of the fabricated device.

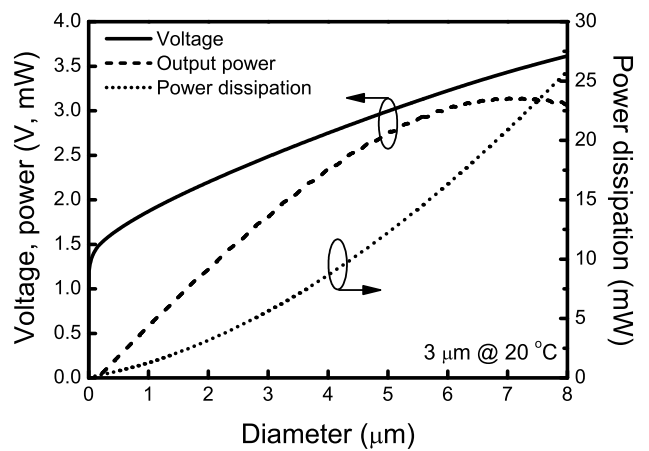


Fig. 13. L-I-V-P curves for 3 μm devices at 20°C.

devices was not optimized for high-temperature operation [26], they perform relatively well at elevated temperatures. The threshold current increases from 0.13 mA at 20°C to 0.34 mA at 110°C, corresponding to a 2.6 times increase. The DQE decreases from 50% at 20°C to 38% at 110°C, corresponding

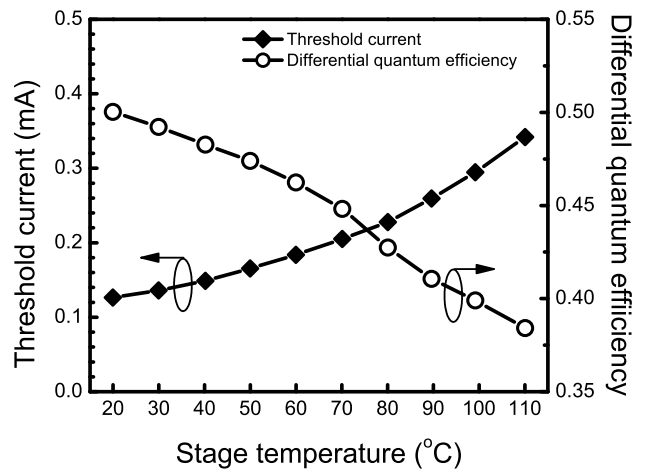


Fig. 14. Threshold current and differential quantum efficiency versus stage temperature for 3 μm diameter devices.

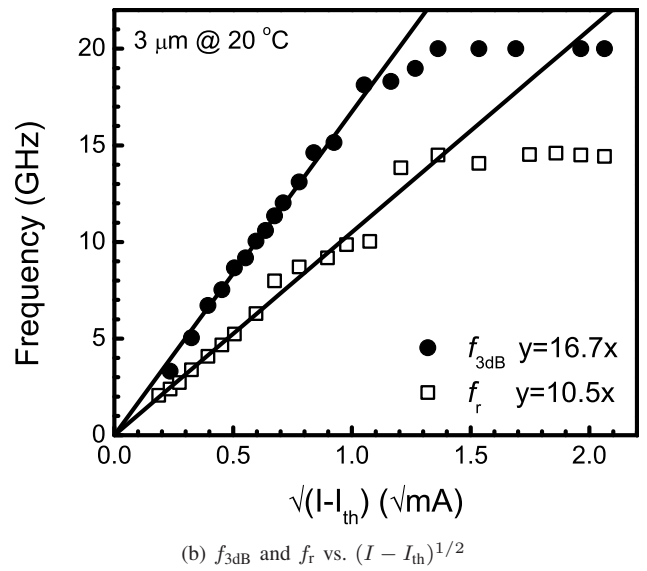
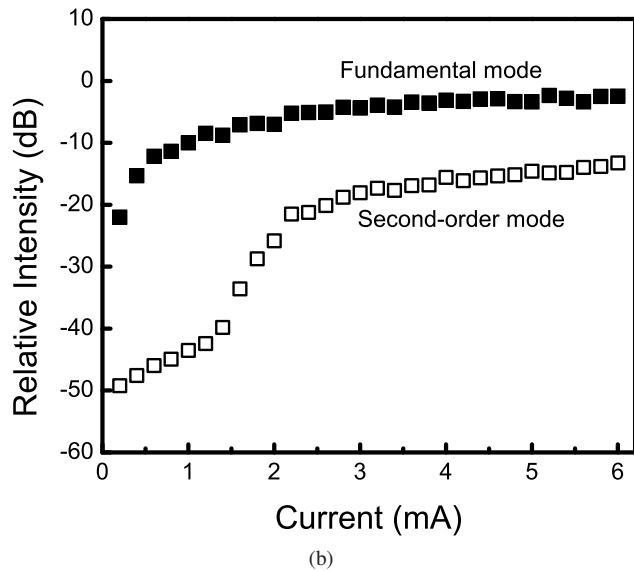
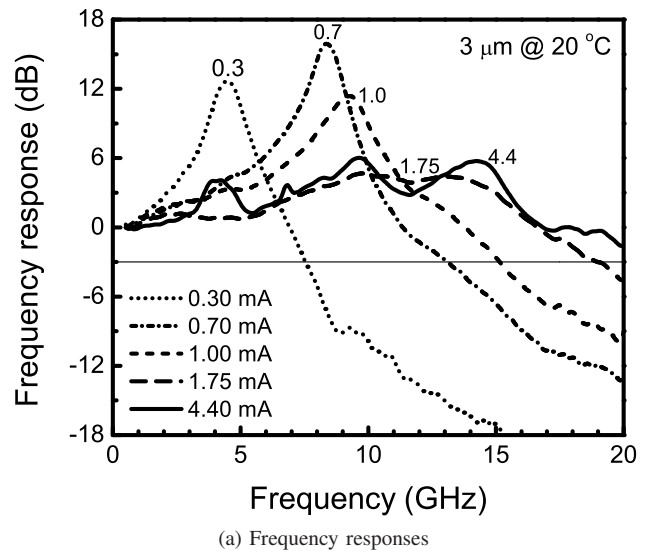
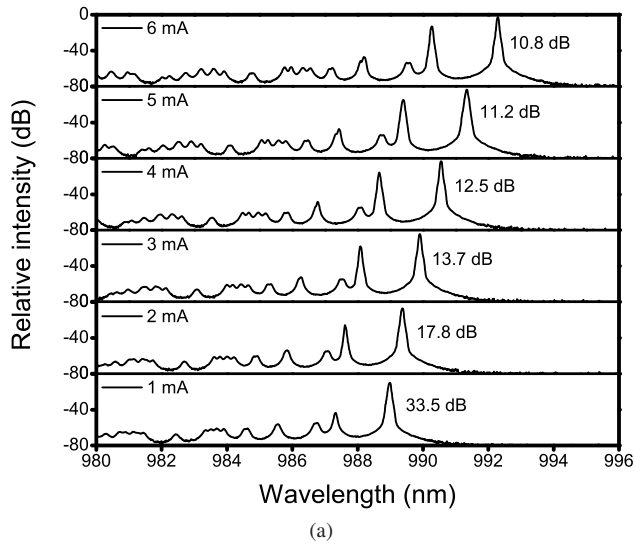


Fig. 15. (a) Spectra with the corresponding SMSR labeled for 3 μm device at different bias currents. (b) The intensities for the fundamental and second-order modes versus bias current.

Fig. 16. (a) Normalized electrical frequency responses at different bias currents for 3 μm diameter device. (b) Relaxation resonance frequency (f_r), determined from relative intensity noise measurements, and 3 dB frequency (f_{3dB}) versus $(I - I_{th})^{1/2}$.

to a 25% reduction.

B. Spectrum

Fig. 15(a) shows the spectra for the 3 μm device at different bias currents. The device lases multi mode, side mode suppression ratio (SMSR) < 30 dB, except for the lowest bias current at 1 mA. To see how the distribution of power between modes evolves as the current increases, Fig. 15(b) plots the intensities of the fundamental and second-order modes as a function of the bias current. The intensity of the fundamental mode increases quickly for the current smaller than 0.5 mA and then slowly saturates. On the other hand, the second-order mode increases rapidly as the current increases from 1.4 to 2 mA. Single-mode operation is only maintained below 1.4 mA, and the device practically operates with two modes in the bias condition of interest. Consequently, the photon density of the fundamental mode does not scale with current after 1.5 mA,

when the second-order mode begins to consume a significant fraction of the additional current. This results in a reduction in the obtainable relaxation resonance frequency as will be discussed in the next section.

C. Small-signal modulation bandwidth

Fig. 16(a) plots the small-signal modulation responses for the 3 μm device at different bias currents. To ensure the device was actually operated with small-signal modulation, the input RF power was chosen to be -40 dBm.

As shown in the figure, bandwidth of 15 GHz, which should enable 20 Gb/s operation, is achieved with a bias current of 1 mA. The corresponding power consumption and dissipation are only 1.87 and 1.29 mW, respectively. The estimated temperature rise at this bias current is less than 5°C and should have negligible thermal impacts on the device performance. Bandwidth exceeding 20 GHz has also been demonstrated

for currents larger than 2 mA. Although this is the record bandwidth for 980 nm VCSELs to date, the high-current data clearly show a saturation effect which accompanies the build-up of power in higher order modes as the total photon density spreads from the fundamental mode to these higher order modes. Simple small-signal modeling fitted only to the lower-current data indicates bandwidths in excess of 25 GHz if the higher order modes are not allowed. The ripples in the Fig. 16(a) higher-current data are believed to be due to multimode effects, because they were not significant at lower currents, but it is also possible that some optical reflections still remain in the test system.

Fig. 16(b) plots the relaxation resonance frequency and 3-dB frequency versus the square root of the current above threshold. The extracted D -factor is $10.5 \text{ GHz}/\text{mA}^{1/2}$, higher than typical high-speed VCSELs. This is because our tapered oxide aperture effectively confines the mode laterally. The MCEF is $16.7 \text{ GHz}/\text{mA}^{1/2}$, which is very close to the highest reported value of $16.8 \text{ GHz}/\text{mA}^{1/2}$ for QW-based VCSELs [27]. The ratio of the slopes of $f_{3\text{dB}}$ to f_r is 1.59, close to the theoretical value of 1.55, indicating that the damping is not severe in our devices at low bias currents. This also has been revealed in Fig. 16(a) as the resonance peaks are quite strong.

Since our devices were not optimized for high-temperature operation, the threshold current increases, and the injection efficiency and differential gain decrease at elevated temperatures. However, according to the static performance shown in Fig. 14, we expect our devices would not degrade significantly up to the commonly specified 85°C .

D. Impedance

To understand how the parasitics affect the high-speed performance of our devices, the values of the parasitic elements need to be determined. This is commonly done by curve fitting the measured S_{11} data to the small-signal model, shown in Fig. 3. It should be noted that to reduce the number of the fitting parameters, this model was simplified by assuming the resistances between the oxide aperture layer and the deep oxidation layers are relatively small compared with R_j so that all the capacitances in the mesa can be grouped together into C_m .

In the small-signal model, C_p and R_m are assumed to be bias independent, which neglects the heating effects, and C_m and R_j are assumed to be bias dependent. The following procedure was used to do the fitting. First, all the parasitic elements are allowed to vary for each bias current, and the estimated ranges of C_p and R_m can be obtained. Then C_p and R_m are determined so that they give the best overall fitting for all the currents. Finally, C_m and R_j can be obtained using the fitted C_p and R_m .

For the $3 \mu\text{m}$ device, the fitted C_p and R_m are 29 fF and 103Ω , respectively. Table II lists the extracted C_m and R_j and the calculated parasitic 3-dB frequency f_{rc} for different bias currents. C_m increases with current due to the increased diffusion capacitance, and R_j decreases as current increases. Due to the small size of our device, R_j and R_m are inherently larger than typical high-speed VCSELs which have larger

TABLE II
EXTRACTED C_m AND R_j AND CALCULATED PARASITIC 3-DB FREQUENCY f_{rc} FOR $3 \mu\text{m}$ DEVICE AT DIFFERENT BIAS CURRENTS.

Current (mA)	1.0	2.0	3.0	4.5	6.0
R_j (Ω)	274.4	192.7	168.2	146.5	126.7
C_m (fF)	57.1	66.7	75.4	87.9	100.0
f_{rc} (GHz)	27.0	25.9	24.6	22.8	21.8

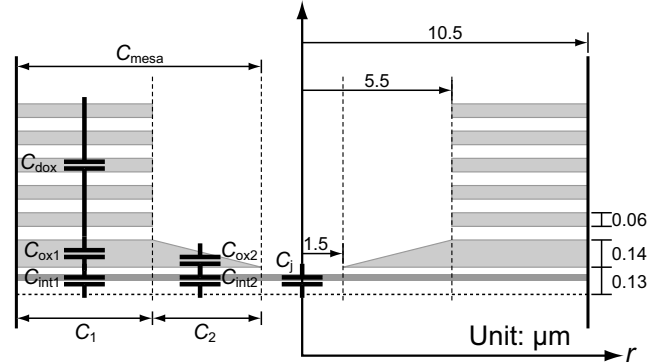


Fig. 17. Various components for C_m in our devices. The lengths are labeled for $3 \mu\text{m}$ diameter devices.

device sizes. To compensate this, the capacitive elements in our devices were minimized so that most the modulation current can enter the intrinsic laser. By removing the n -contact layer, inserting BCB, and reducing the pad dimension, C_p was greatly reduced. With the incorporation of the deep oxidation layers and thicker oxide aperture, C_m is also relatively small.

To understand how these two features reduce C_m , a simple calculation based on the schematic shown in Fig. 17 was performed. Assume the dielectric constants of the oxide and semiconductor are 4 and 12.2 [28], respectively. For the region of $10.5 \geq r > 5.5 \mu\text{m}$, the capacitance C_1 is C_{dox} (from the deep oxidation layers), C_{ox} , and C_{int} connected in series. Using the parallel plate capacitance approximation, C_{dox} , C_{ox} , and C_{int} are calculated to be 29.7, 63.5, and 208.7 fF, respectively. For the region of $5.5 \geq r > 1.5 \mu\text{m}$, the capacitance C_2 is calculated to be 46.4 fF.

By increasing the aperture thickness from quarter-wavelength to half-wavelength with the same taper length, we were able to reduce C_m from 118.3 to 76.8 fF. Assuming everything else remains unchanged, this corresponds to an increase of f_{rc} from 12.9 to 17.3 GHz, a 34% increase. The inclusion of the deep oxidation layers further lowers C_m from 76.8 to 46.4 fF, corresponding to an increase of f_{rc} from 17.3 to 22.8 GHz. By implementing a thicker oxide aperture as well as the deep oxidation layers, we were able to greatly reduce the chip parasitic capacitance. However, our devices are still partially limited by the parasitics as f_{rc} is in the range of 22–27 GHz.

In order to further reduce the chip parasitic capacitance, C_j has to be lowered. For typical edge-emitters which are usually operated at tens of milliamperes, R_j is very small and C_j is negligible. However, for VCSELs which require less current to operate, C_j cannot be neglected. Fig. 18 plots the extracted C_m as a function of the bias current. All the data fit in a line.

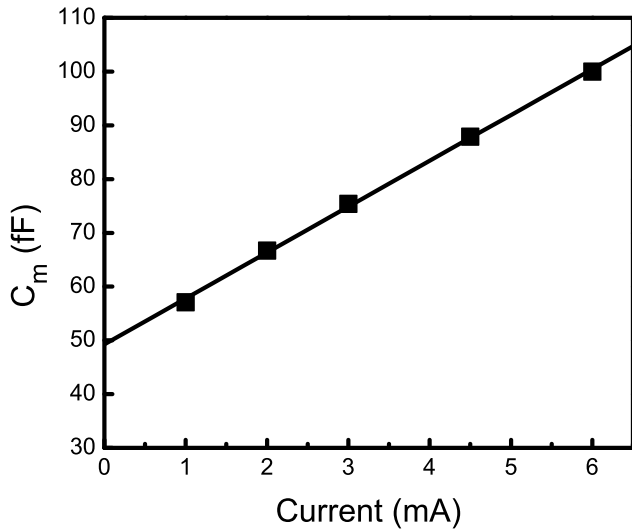


Fig. 18. Extracted C_m versus the bias current for 3 μm device.

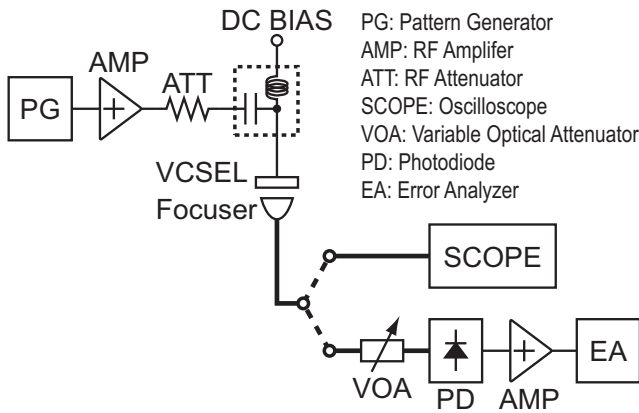


Fig. 19. Experiment setup for bit error rate and eye diagram.

Similar trend has also been found in the literature [29] and can be explained using the following simple argument.

$$C \equiv \frac{dQ}{dV} = \frac{di \cdot \Delta t}{dv} = \frac{di \cdot \Delta t}{di \cdot (V_T/I_{\text{bias}})} \propto I_{\text{bias}} \quad (6)$$

where di and dv are the small-signal modulation current and voltage, respectively, and V_T is the thermal voltage, ~ 26 meV at room temperature. Here we have assumed ideal diode equation for the relation between di and dv .

For the bias current of 4.5 mA, which is close to the condition for the large-signal modulation experiments, a considerable portion of C_m comes from C_j . Therefore, carefully designing the SCH region is needed to lower the parasitics.

E. Bit error rate and eye diagram

Fig. 19 shows the test setup for large-signal modulation experiments. The non-return-to-zero (NRZ) signal with $2^7 - 1$ word length from the pattern generator (SHF 12100A) was amplified using a 38 GHz SHF 806E amplifier with 26 dB gain and then attenuated 6 dB using a fixed attenuator to reduce the voltage swing to $\sim 0.84 V_{\text{p-p}}$. The RF signal was combined with the DC bias through a 65 GHz Anritsu V255

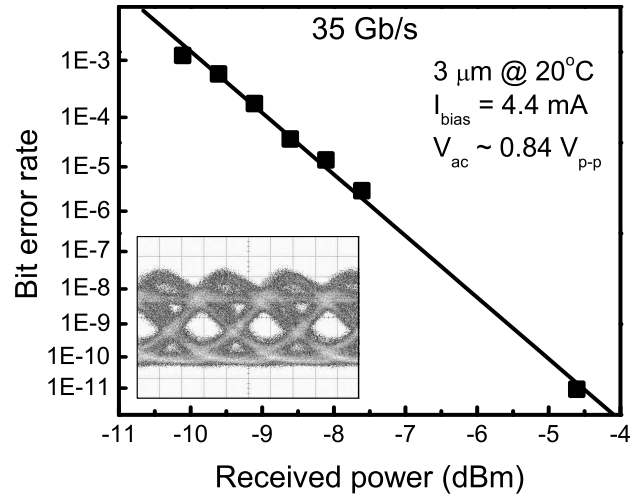


Fig. 20. Bit error curve at 35 Gb/s for 3 μm diameter device. The device was biased at 4.4 mA and a RF voltage swing of 0.84 $V_{\text{p-p}}$ was used. The inset shows the corresponding optical eye diagram with an extinction ratio of 5.4 dB.

bias tee and fed to the device using a 67 GHz ground-signal-ground RF probe. The output power was collected into a one-meter standard 9/125 fiber attached with a dual-lens focuser. Standard telecom 9/125 fiber was used for equipment compatibility. The eye diagram was measured using an Agilent 86109A oscilloscope with an internal 30 GHz photodiode. To measure the bit error rate (BER), the optical signal was attenuated using a variable optical attenuator (VOA) and then fed to a 25 GHz New Focus 1414 photodiode coupled with a 40 GHz SHF 810 amplifier and finally sent to the error analyzer (SHF 11100A). The coupling efficiency under the BER testing was approximately 27%, estimated by the photocurrent from the photodiode and the L-I curve.

Fig. 20 shows the BER curve at 35 Gb/s for the 3 μm device. The bias current was 4.4 mA. The inset of the figure shows the optical eye diagram at 35 Gb/s and the eye is clearly open with an extinction ratio of 5.4 dB. In the BER curve, all the data points except the lowest one were taken with a VOA. Due to the ~ 3 dB insertion loss of the VOA, the BER in the range of 10^{-11} and 10^{-7} could not be measured. Thus, the lowest data point at a received power of -4.7 dBm was taken without the VOA. At a bias current of 4.4 mA, the power consumption and dissipation, excluding the RF driver circuitry, are only 12.5 and 10 mW, respectively. This corresponds to a data-rate/power-dissipation ratio of 3.5 Gps/mW.

One concern with small devices is the high current density which can cause reliability problems. At 4.4 mA where the BER testing was performed, the current density, $J = I/\text{Area}$, is indeed quite high at over 60 kA/cm². The rationale to, or trying to, go with small devices is that ideally, the relaxation resonance frequency should be independent of the size of the device. This can be seen if we rewrite Eq. (2) as

$$\omega_r = \left[\frac{\Gamma v_g a}{q L_a A} \eta_i A (J - J_{\text{th}}) \right]^{1/2} = \left[\frac{\Gamma v_g a}{q L_a} \eta_i (J - J_{\text{th}}) \right]^{1/2}$$

where A is the apertured area, L_a is the total thickness of the QWs, and $J_{\text{th}} = I_{\text{th}}/A$. Here we have assumed that the

confinement factor Γ is size-independent. Moreover, small devices require less power to operate. As shown earlier, our 3 μm devices can achieve a 15 GHz bandwidth at 1 mA, corresponding to a current density of 14 kA/cm^2 . Further optimization of the devices and testing setup may bring the current density of 60 kA/cm^2 down to a more reasonable value.

VI. CONCLUSION

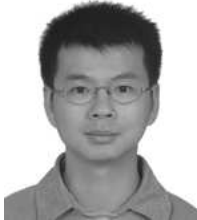
High-efficiency, high-speed, oxide-confined 980 nm VCSELs are demonstrated. We first considered the factors that determine the bandwidth and tried to address them in our device design. To improve the intrinsic laser response, an optimized tapered oxide aperture was used for better mode confinement and higher photon density. The parasitic limitations were lowered by using the deep oxidation layers, thicker oxide apertures, and reducing the pad capacitance. These designs enabled us to use smaller 3 μm devices, which have a threshold current of 0.14 mA. In addition, our devices achieved >20 GHz bandwidth for current >2 mA and 35 Gb/s operation at only 10 mW power dissipation, corresponding to a data-rate/power-dissipation ratio of 3.5 Gbps/mW. By analyzing the results, we also pointed out some potential improvements such as single modeness and the reduction of the junction capacitance.

ACKNOWLEDGMENT

The authors would like to thank Professor J. E. Bowers and Professor D. J. Blumenthal for supporting the RF equipment and Dr. C. S. Wang, Dr. L. A. Johansson, H. N. Poulsen, and Dr. Y.-H. Kuo for helping with the RF test setup. The comments from the reviewers are also gratefully appreciated.

REFERENCES

- N. Suzuki, H. Hatakeyama, K. Fukatsu, T. Anan, K. Yashiki, and M. Tsuji, "25-Gbps operation of 1.1- μm -range InGaAs VCSELs for high-speed optical interconnections," in *Proc. Optical Fiber Communication Conf.*, 2006, Paper no. OFA4.
- K. Yashiki, N. Suzuki, K. Fukatsu, T. Anan, H. Hatakeyama, and M. Tsuji, "1.1- μm -range tunnel junction VCSELs with 27-GHz relaxation oscillation frequency," in *Proc. Optical Fiber Communication Conf.*, 2007, Paper no. OMK1.
- Y.-C. Chang, C. S. Wang, and L. A. Coldren, "High-efficiency, high-speed VCSELs with 35 Gbit/s error-free operation," *Electron. Lett.*, vol. 43, no. 19, pp. 1022–1023, 2007.
- T. Anan, N. Suzuki, K. Yashiki, K. Fukatsu, H. Hatakeyama, T. Akagawa, K. Tokutome, and M. Tsuji, "High-speed ingaas VCSELs for optical interconnects," in *Proc. International Symposium on VCSELs and Integrated Photonics*, 2007, Paper no. E3.
- R. H. Johnson and D. M. Kuchta, "30 Gb/s directly modulated 850 nm datacom VCSELs," in *Conf. on Lasers and Electro-Optics*, 2008, Paper no. CPDB2.
- E. R. Hegblom, D. I. Babic, B. J. Thibeault, and L. A. Coldren, "Scattering losses from dielectric apertures in vertical-cavity lasers," *IEEE J. Sel. Topics Quantum Electron.*, vol. 3, no. 2, pp. 379–389, 1997.
- R. S. Tucker, "High-speed modulation of semiconductor lasers," *J. Lightw. Technol.*, vol. 3, no. 6, pp. 1180–1192, 1985.
- L. A. Coldren and S. W. Corzine, *Diode lasers and photonic integrated circuits*. Wiley, 1995.
- Y. Arakawa and A. Yariv, "Quantum well lasers—gain, spectra, dynamics," *IEEE J. Quantum Electron.*, vol. 22, no. 9, pp. 1887–1899, 1986.
- I. Suemune, "Theoretical study of differential gain in strained quantum well structures," *IEEE J. Quantum Electron.*, vol. 27, no. 5, pp. 1149–1159, 1991.
- J. D. Ralston, S. Weisser, I. Esquivias, E. C. Larkins, J. Rosenzweig, P. J. Tasker, and J. Fleissner, "Control of differential gain, nonlinear gain and damping factor for high-speed application of GaAs-based MQW lasers," *IEEE J. Quantum Electron.*, vol. 29, no. 6, pp. 1648–1659, 1993.
- P. O. Leisher, C. Chen, J. D. Sulkin, M. S. B. Alias, K. A. M. Sharif, and K. D. Choquette, "High modulation bandwidth implant-confined photonic crystal vertical-cavity surface-emitting lasers," *IEEE Photon. Technol. Lett.*, vol. 19, no. 9, pp. 1541–1543, 2007.
- D. Tauber, G. Wang, R. S. Geels, J. E. Bowers, and L. A. Coldren, "Large and small signal dynamics of vertical cavity surface emitting lasers," *Appl. Phys. Lett.*, vol. 62, no. 4, pp. 325–327, 1993.
- Y. Liu, W.-C. Ng, F. Oyafuso, B. Klein, and K. Hess, "Simulating the modulation response of VCSELs: the effects of diffusion capacitance and spatial hole-burning," *IEE Proc. Optoelectron.*, vol. 149, no. 4, pp. 182–188, 2002.
- J. Strologas and K. Hess, "Diffusion capacitance and laser diodes," *IEEE Trans. Electron Devices*, vol. 51, no. 3, pp. 506–509, 2004.
- K. Y. Lau and A. Yariv, "Ultra-high speed semiconductor lasers," *IEEE J. Quantum Electron.*, vol. 21, no. 2, pp. 121–138, 1985.
- D. A. Louderback, O. Sjölund, E. R. Hegblom, J. Ko, and L. A. Coldren, "Flip-chip bonded arrays of monolithically integrated, microlensed vertical-cavity lasers and resonant photodetectors," *IEEE Photon. Technol. Lett.*, vol. 11, pp. 304–306, 1999.
- E. R. Hegblom, "Engineering oxide apertures in vertical cavity lasers," Ph.D. dissertation, Univ. of California, Santa Barbara, Mar. 1999.
- M. G. Peters, B. J. Thibeault, D. B. Young, J. W. Scott, F. H. Peters, A. C. Gossard, and L. A. Coldren, "Band-gap engineered digital alloy interfaces for lower resistance vertical-cavity surface-emitting lasers," *Appl. Phys. Lett.*, vol. 63, no. 25, pp. 3411–3413, 1993.
- K. L. Lear and R. P. Schneider, Jr., "Uniparabolic mirror grading for vertical cavity surface emitting lasers," *Appl. Phys. Lett.*, vol. 68, no. 5, pp. 605–607, 1996.
- Y.-C. Chang and L. A. Coldren, "Optimization of VCSEL structure for high-speed operation," in *Semiconductor Laser Conference, 2006. Conference Digest. 2008 IEEE 20th International*, Sorrento, Italy, Sep. 14–18 2008, Paper no. ThA1.
- P. Westbergh, J. Gustavsson, A. Haglund, H. Sunnerud, and A. Larsson, "Large aperture 850 nm VCSELs operating at bit rates up to 25 Gbit/s," *Electron. Lett.*, vol. 44, no. 15, pp. 907–908, 2008.
- Y.-C. Chang, C. S. Wang, L. A. Johansson, and L. A. Coldren, "High-efficiency, high-speed VCSELs with deep oxidation layers," *Electron. Lett.*, vol. 42, no. 22, pp. 1281–1282, 2006.
- R. Nagarajan, M. Ishikawa, T. Fukushima, R. S. Geels, and J. E. Bowers, "High speed quantum-well lasers and carrier transport effects," *IEEE J. Quantum Electron.*, vol. 28, no. 10, pp. 1990–2008, 1992.
- E. R. Hegblom, N. M. Margalit, B. Thibeault, L. A. Coldren, and J. E. Bowers, "Current spreading in apertured vertical-cavity lasers," *Proc. IEEE*, vol. 3003, pp. 176–180, 1997.
- D. B. Young, J. W. Scott, F. H. Peters, M. G. Peters, M. L. Majewski, B. J. Thibeault, S. W. Corzine, and L. A. Coldren, "Enhanced performance of offset-gain high-barrier vertical-cavity surface-emitting lasers," *IEEE J. Quantum Electron.*, vol. 29, no. 6, pp. 2013–2022, 1993.
- K. L. Lear, A. Mar, K. D. Choquette, S. P. Kilcoyne, R. P. J. Schneider, and K. M. Geib, "High-frequency modulation of oxide-confined vertical cavity surface emitting lasers," *Electron. Lett.*, vol. 32, no. 5, pp. 457–458, 1996.
- S. Adachi, "GaAs, AlAs, and $\text{Al}_x\text{Ga}_{1-x}\text{As}$: Material parameters for use in research and device applications," *J. Appl. Phys.*, vol. 58, no. 3, pp. R1–R29, 1985.
- A. N. AL-Omari and K. L. Lear, "Polyimide-planarized vertical-cavity surface-emitting lasers with 17.0-GHz bandwidth," *IEEE Photon. Technol. Lett.*, vol. 16, no. 4, pp. 969–971, 2004.



Yu-Chia Chang received the B.S. degree in electrical engineering and M.S. degree in electro-optical engineering from National Taiwan University in 1997 and 1999, respectively. He worked for BenQ Inc., Taiwan during 1999–2001 and National Taiwan University during 2001–2002. He is currently working toward the Ph.D. degree in electrical and computer engineering at the University of California, Santa Barbara.

His current research interests are the design, growth, fabrication, and characterization of high-efficiency, high-speed vertical-cavity surface-emitting lasers for optical interconnect applications.



Larry A. Coldren (S'67–M'72–SM'77–F'82) is the Fred Kavli Professor of Optoelectronics and Sensors at the University of California, Santa Barbara, CA. He received the Ph.D. degree in Electrical Engineering from Stanford University in 1972. After 13 years in the research area at Bell Laboratories, he joined UC-Santa Barbara in 1984 where he now holds appointments in Materials and Electrical & Computer Engineering, and is Director of the Optoelectronics Technology Center. In 1990 he co-founded Optical Concepts, later acquired as Gore

Photonics, to develop novel VCSEL technology; and in 1998 he co-founded Agility Communications, later acquired by JDSU, to develop widely-tunable integrated transmitters.

At Bell Labs Coldren initially worked on waveguided surface-acoustic-wave signal processing devices and coupled-resonator filters. He later developed tunable coupled-cavity lasers using novel reactive-ion etching (RIE) technology that he created for the then new InP-based materials. At UCSB he continued work on multiple-section tunable lasers, in 1988 inventing the widely-tunable multi-element mirror concept, which is now used in some JDSU products. During the late eighties he also developed efficient vertical-cavity multiple-quantum-well modulators, which led to novel vertical-cavity surface-emitting laser (VCSEL) designs that provided unparalleled levels of performance. Prof. Coldren continues to be active in developing new photonic integrated circuit (PIC) and VCSEL technology, including the underlying materials growth and fabrication techniques. In recent years, for example, he has been involved in the creation of efficient all-epitaxial InP-based and high-modulation speed GaAs-based VCSELs as well as a variety of InP-based PICs incorporating numerous optical elements for widely-tunable integrated transmitters, receivers, and wavelength converters operating up to 40 Gb/s.

Professor Coldren has authored or co-authored over 900 conference and journal papers, 5 book chapters, 1 textbook, and has been issued 62 patents. He has presented dozens of invited and plenary talks at major conferences, he is a Fellow of the IEEE, OSA, and IEE, the recipient of the 2004 John Tyndall Award, and a member of the National Academy of Engineering.

High-efficiency, high-speed VCSELs for optical interconnects

Yu-Chia Chang · Larry A. Coldren

Received: 20 July 2008 / Accepted: 16 December 2008
© The Author(s) 2009. This article is published with open access at Springerlink.com

Abstract High-efficiency, high-speed, tapered-oxide-apertured vertical-cavity surface-emitting lasers (VCSELs) emitting at 980 nm have been demonstrated. By carefully engineering the tapered oxide aperture, the mode volume can be greatly reduced without adding much optical scattering loss for the device sizes of interest. Consequently, these devices can achieve higher bandwidth at lower current and power dissipation. In addition, the parasitics are reduced by implementing deep oxidation layers and an improved *p*-doping scheme in the top mirror. Our devices show modulation bandwidth exceeding 20 GHz, a record for 980 nm VCSELs. Moreover, 35 Gb/s operation has been achieved at only 10 mW power dissipation. This corresponds to a data-rate/power-dissipation ratio of 3.5 Gbps/mW. Most importantly, our device structure is compatible with existing manufacturing processes and can be easily manufactured in large volume making them attractive for optical interconnects.

PACS 42.55.Px

1 Introduction

Through scaling and integration, the performance of microprocessors is consistently improving to the point that current copper-based interconnects are slowly becoming the bottleneck due to their physical limitations [1]. More and more power and chip real state have been devoted to interconnects. In addition, signal loss, distortion, and cross-talk

in electrical interconnects become worse as frequency increases. In order to keep up the advance of microprocessors, new technology is required.

Optics is a viable alternative to copper interconnects because it offers the advantages of short signal delay, high bandwidth, low power dissipation, and freedom from electromagnetic interference. In the past several years, vertical-cavity surface-emitting lasers (VCSELs) have received renewed interest for potential applications in optical interconnects [2]. Compared with edge emitters, VCSELs have several benefits: they have smaller footprint; they are easier to fabricate in arrays; they support on-wafer testing; they require less power to achieve high-speed operation; and they usually are less expensive to manufacture.

Recently, data rate up to 40 Gb/s with a 24 GHz bandwidth has been demonstrated for 1.1 μm wavelength VCSELs [3]. 30 Gb/s operation has also been reported for 850 nm wavelength VCSELs [4]. Here we present our work on high-efficiency, high-speed VCSELs emitting at 980 nm wavelength. Our devices show >20 GHz bandwidth and 35 Gb/s operation at only 10 mW power dissipation corresponding to a very high data-rate/power-dissipation ratio of 3.5 Gbps/mW.

2 Device structure

In optical interconnects, the transmitters convert signals from electrical to optical domain at comparatively high data rates, usually within compact systems with many active components but limited heat sink. Therefore, these devices must be capable of operating at speeds at least 20 Gb/s, be efficient to minimize power dissipation, be compatible with silicon electronics, and most importantly, be manufacturable in large volume with high yields and low costs.

Y.-C. Chang (✉) · L.A. Coldren
Department of Electrical and Computer Engineering,
University of California, Santa Barbara, CA 93106, USA
e-mail: yuchia@engineering.ucsb.edu

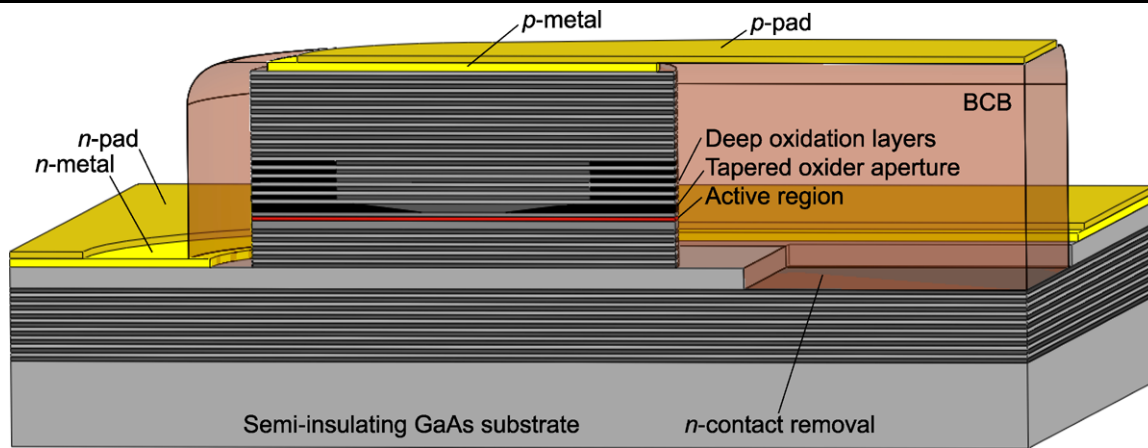


Fig. 1 Cross-sectional schematic of the device

In order to meet these requirements, *n*-intracavity, bottom-emitting, tapered-oxide-apertured structure, shown in Fig. 1, is used. Emission wavelength of 980 nm is chosen so that strained InGaAs/GaAs quantum wells (QWs), which provide higher gain at low carrier densities, can be used. In addition, this wavelength is transparent to GaAs substrate and hence enables us to use bottom-emitting structure. Bottom emission along with *n*-intracavity means that flip-chip bonding can be used to directly integrate VCSEL arrays with silicon electronics. This eliminates the need of individual wire bonding and the parasitics associated with bond wires. Moreover, backside microlenses can be fabricated to collimate output beams, which increase the alignment tolerance and reduce packaging costs [5].

The sample was grown on a semi-insulating GaAs (100) substrate by molecular beam epitaxy. The bottom mirror consists of a 14-period undoped AlAs/GaAs distributed Bragg reflector (DBR) followed by a five-quarter wavelength thick *n*-GaAs contact layer and a 4-period *n*-type Al_{0.9}Ga_{0.1}As/GaAs DBR. The *n*-contact layer is setback 4 periods to reduce the free carrier absorption loss and improve longitudinal mode confinement for high-speed consideration. The active region has three InGaAs/GaAs QWs embedded in a Al_{0.3}Ga_{0.7}As separate confinement heterostructure (SCH) layer to form the cavity.

On top of the SCH is the oxide aperture. To achieve high bandwidth at low power dissipation, we redesigned our tapered oxide aperture for better lateral mode confinement. The aperture thickness increases from quarter-wavelength to half-wavelength thick and the taper length is also reduced from 4.3 to 4 μm . According to our simulation, this aperture yields a 31% improvement in relaxation resonance frequency for 3 μm diameter devices over our original design. In addition, the static performance is not sacrificed because the optical loss does not increase noticeably for device sizes down to 3 μm in diameter.

The top mirror has a 30-period AlGaAs/GaAs DBR. The aluminum fraction of the first 5 periods of DBR is increased from 85 to 93% to form deep oxidation layers [6]. When oxidizing the aperture, these high aluminum content layers oxidized comparatively faster than the other DBR periods forming thicker dielectric layers in the perimeter of the mesa. These oxidized layers effectively increase the equivalent capacitor thickness and reduce the parasitic capacitance. Compared with ion implantation commonly used to reduce the parasitic capacitance, our approach is simple and cost effective.

The parasitics are further reduced using the following approaches: The *p*-doping in the top mirror is carefully optimized to reduce the series resistance without introducing too much optical loss. The pad capacitance is reduced by (a) removing the part of the *n*-contact layer (RF ground) beneath the *p*-pad metal (RF signal), (b) inserting low dielectric constant resin Benzocyclobutene (BCB) underneath the *p*-pad, and (c) shrinking the *p*-pad dimension to $40 \times 70 \mu\text{m}^2$. Details of the fabrication can be found in [7].

3 Device results

Figure 2 shows the voltage, output power, and power dissipation against current curves for a 3 μm diameter device at 20°C.

The lasing wavelength is around 990 nm. The device has a slope efficiency of 0.67 W/A, corresponding to a differential quantum efficiency of 54%. The threshold current is only 0.144 mA, comparatively low for typical high-speed VCSELs with diameters ranging from 5 to 8 μm . This low threshold along with high slope efficiency indicates that our new tapered oxide aperture with shorter taper length does not introduce excess optical loss even down to 3 μm diameter range. The threshold voltage is 1.47 V, very low for such a small device, as it is only 220 meV larger than the photon

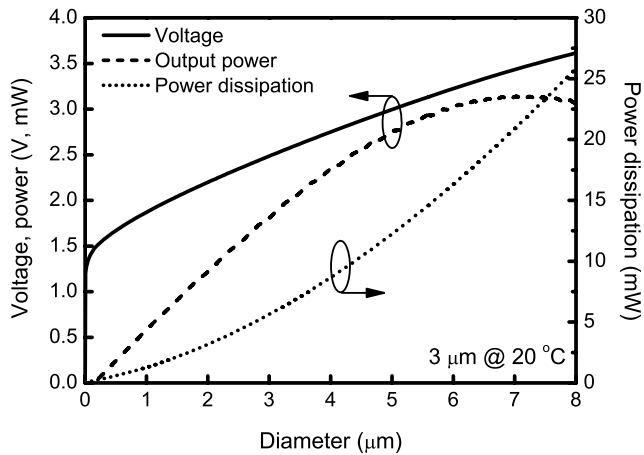


Fig. 2 Voltage, output power, and power dissipation against current curves for 3 μm diameter device at 20°C

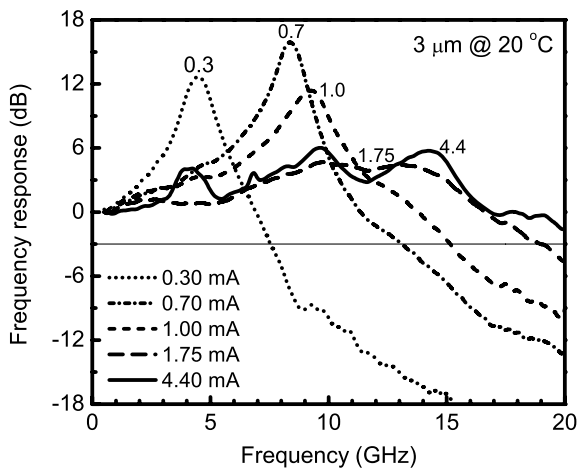


Fig. 3 Frequency responses for 3 μm device at 20°C under different bias currents

energy. This low threshold voltage is the consequence of our optimized p -doping scheme and low threshold current. The series resistance is approximately 250 Ω at a bias current of 4.4 mA, where the large-signal modulation experiments were performed. The thermal impedance is 3.3°C/mW, calculated by measuring the wavelength shift at different stage temperatures and at different biases [8]. At a bias current of 4.4 mA, the power dissipation and temperature rise are 10 mW and 33°C, respectively. The peak wall-plug efficiency, occurring at 1 mA, is 31% and the maximum output power is 3.1 mW.

Figure 3 shows the small-signal modulation responses for a 3 μm device under different bias currents. Bandwidth of 15 GHz is achieved with a bias current of only 1 mA. Limited by the instruments, frequency response could only be measured up to 20 GHz. However, it is evident that bandwidth exceeding 20 GHz has been achieved, highest for 980 nm VCSELs.

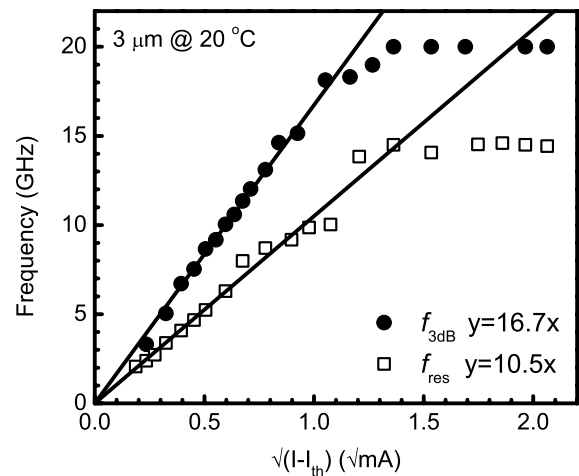


Fig. 4 Relaxation resonance frequency (f_{res}) and 3 dB frequency ($f_{3\text{dB}}$) versus square root of the current above threshold

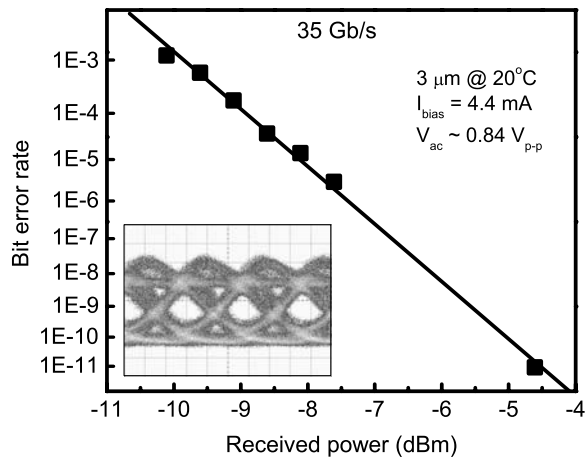


Fig. 5 Bit error rate curve at 35 Gb/s for 3 μm diameter device. This device was biased at 4.4 mA and a RF voltage swing of 0.84 $V_{\text{p-p}}$ was used. The inset shows the corresponding optical eye diagram with an extinction ratio of 5.4 dB

Figure 4 plots the relaxation resonance frequency, f_{res} , and 3 dB frequency, $f_{3\text{dB}}$, as a function of the square root of the current above threshold. The modulation current efficiency factor (MCEF), defined as $f_{3\text{dB}}/\sqrt{(I - I_{\text{th}})}$, is 16.7 GHz/mA^{1/2}, very close to the highest reported value of 16.8 GHz/mA^{1/2} for QW-based VCSELs [9]. This high MCEF is mainly due to better lateral mode confinement, consequence of our improved tapered oxide aperture design. The ratio of the slopes of $f_{3\text{dB}} : f_{\text{res}}$ is 1.59, close to the theoretical value of 1.55, indicating damping is not severe in our devices.

Figure 5 plots the bit error rate (BER) curve at 35 Gb/s for a 3 μm diameter device at 20°C. The experimental setup is given in [10]. The input was a non-return-to-zero (NRZ) signal with $2^7 - 1$ word length. The bias current was 4.4 mA and the RF voltage swing was $\sim 0.84 V_{\text{p-p}}$. The inset of the

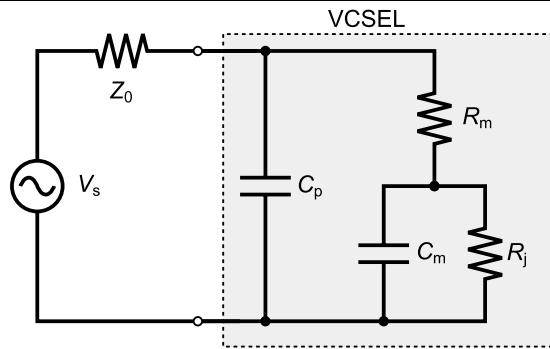


Fig. 6 Small-signal equivalent circuit model for the device. The device is represented by C_p , R_m , C_m , and R_j . V_s is the RF voltage source and $Z_0 = 50 \Omega$ is the characteristic impedance of the instruments

figure shows the corresponding optical eye diagram. The eye is clearly open with an extinction ratio of 5.4 dB. In the BER curve, all the data points except the lowest one were taken with a variable optical attenuator (VOA). Owing to the ~ 3 dB insertion loss of the VOA, the BER in the range of 10^{-4} to 10^{-7} could not be measured. Thus, the lowest data point at a received power of -4.7 dB was taken without the VOA. The BER is 9.2×10^{-12} , gated for 30 min with total 583 errors to ensure the accuracy of the measurement.

Since both high data rate and low power dissipation are desired for optical interconnects, a good figure-of-merit is the data-rate/power-dissipation ratio. At a bias current of 4.4 mA, the power consumption and dissipation of our devices, excluding the RF circuitry, were only 12.5 and 10 mW, respectively. This corresponds to a very high data-rate/power-dissipation ratio of 3.5 Gbps/mW.

Small-signal equivalent circuit model is useful to understand the bandwidth limitation due to parasitics. The circuit model for our devices, shown in Fig. 6, includes four elements: C_p , R_m , C_m , and R_j . The pad capacitance, C_p , represents all the capacitances between the p - and n -contacts outside the mesa. The mesa resistance, R_m , includes the contact resistances, DBR mirror resistances, and spreading sheet resistance associated with the n -contact layer. The mesa capacitance, C_m , includes the capacitances from the deep oxidation layers, oxide aperture, intrinsic layer beneath the aperture, and diode junction. R_j denotes the diode junction resistance for the active region. For the RF driving circuit side, V_s is the RF voltage source and $Z_0 = 50 \Omega$ is the characteristic impedance of the instruments. Z_0 has to be included to account for the RF reflection due to impedance mismatch.

The values for these circuit elements can be determined by fitting S_{11} parameter as a function of frequency and bias current. Table 1 lists the extracted small-signal circuit elements for a 3 μm diameter device.

We have assumed R_m and C_p to be bias independent, which neglects any heating effects. C_m increases with cur-

Table 1 Extracted small-signal circuit elements for 3 μm diameter device at different bias currents. R_m and C_p are fitted to be 102.9 Ω and 29.1 fF. f_{rc} is the parasitic 3 dB frequency

Current (mA)	1.0	2.0	3.0	4.5	6.0
R_j (Ω)	274.4	192.7	168.2	146.5	126.7
C_m (fF)	57.1	66.7	75.4	87.9	100.0
f_{rc} (GHz)	27.0	25.9	24.6	22.8	21.8

rent due to the increased diffusion capacitance and R_j decreases as current increases. Due to smaller size of our devices, R_j and R_m are larger than typical high-speed VCSELs. C_p is very small thanks to n -contact removal, BCB insertion, and pad-size reduction. C_m is also very small, resulting from the incorporation of deep oxidation layers and thicker oxide aperture.

The influence of the parasitics on modulation bandwidth is determined by calculating the transfer function of the current flowing through R_j over V_s . The -3 dB frequency of this transfer function, f_{rc} , is also listed in Table 1. At a bias current of 4.5 mA, f_{rc} is 22.8 GHz, indicating our devices are still partially limited by parasitics.

4 Conclusion

We have fabricated and characterized high-efficiency, high-speed 980 nm VCSELs. These devices are based on a structure that is compatible with existing manufacturing processes and can be easily mass produced. The 3 μm diameter devices demonstrated 35 Gb/s operation at a bias current of 4.4 mA, corresponding to only 10 mW power dissipation. This represents a data-rate/power-dissipation ratio of 3.5 Gbps/mW. Combined with high-speed operation, low power dissipation, and manufacturability, these devices are very attractive for optical interconnects. With improvements in active region design, suppression of higher-order modes, and reduction in parasitics, 40 Gb/s operation and beyond can be expected.

Acknowledgement The work was supported by a MICRO with IBM and gift funds from Agilent.

Open Access This article is distributed under the terms of the Creative Commons Attribution Noncommercial License which permits any noncommercial use, distribution, and reproduction in any medium, provided the original author(s) and source are credited.

References

1. D.A. B Miller, Int. J. Optoelectron. **11**, 155 (1997)
2. L. Schares, J.A. Kash, F.E. Doany, C.L. Schow, C. Schuster, D.M. Kuchta, P.K. Pepeljugoski, J.M. Trewhella, C.W. Baks, R.A. John, L. Shan, Y.H. Kwark, R.A. Budd, P. Chiniwalla,

- F.R. Libsch, J. Rosner, C.K. Tsang, C.S. Patel, J.D. Schaub, R. Dangel, F. Horst, B.J. Offrein, D. Kucharski, D. Guckenberger, S. Hegde, H. Nyikal, C.-K. Lin, A. Tandon, G.R. Trott, M. Nyström, D.P. Bour, M.R.T. Tan, D.W. Dolf, *IEEE J. Sel. Top. Quantum Electron.* **12**, 1032 (2006)
3. T. Anan, in *Proc. International Symposium on VCSELs and Integrated Photonics*, E3 (2007)
4. R.H. Johnson, D.M. Kuchta, in *Conf. Laser and Electro-Optics, CPDB2* (2008)
5. E.M. Strzelecka, G.D. Robinson, M.G. Peters, F.H. Peters, L.A. Coldren, *Electron. Lett.* **31**, 724 (1995)
6. Y.-C. Chang, C.S. Wang, L.A. Coldren, *Electron. Lett.* **42**, 1281 (2006)
7. Y.-C. Chang, C.S. Wang, L.A. Coldren, *Electron. Lett.* **43**, 396 (2007)
8. D.B. Young et al., *IEEE J. Quantum Electron.* **29**, 2013 (1993)
9. K.L. Lear, A. Mar, K.D. Choquette, S.P. Kil-coyne, R.P. Schneider Jr., K.M. Geib, *Electron. Lett.* **32**, 457 (1996)
10. Y.-C. Chang, C.S. Wang, L.A. Coldren, *Electron. Lett.* **43**, 1022 (2007)

Wide-dynamic-range, fast-response CBr₄ doping system for molecular beam epitaxy

Yu-Chia Chang*, Yan Zheng*, John H. English†, Andrew W. Jackson*, and Larry A. Coldren**†

*ECE Dept. and †Materials Dept., University of California, Santa Barbara, CA 93106

Phone: (805) 893-7065, Fax: (805) 893-4500, E-mail: yuchia@engineering.ucsb.edu

Over the past several years, vertical-cavity surface-emitting lasers (VCSELs) have been the subject of intensive worldwide research due to their applications in optical interconnects and optical data links. To improve VCSEL performance, various bandgap-engineering schemes have been implemented in the distributed Bragg reflectors (DBRs) to simultaneously achieve low optical loss and low electrical resistance. This is especially important for *p*-DBRs due to higher free carrier absorption loss and lower mobility of holes. These bandgap-engineered DBRs usually have many different doping levels within a short DBR period. In addition, a very high doping level is needed to minimize the contact resistance. For molecular beam epitaxy (MBE), carbon doping using carbon tetrabromide (CBr₄) has been shown to produce material with better properties than doping with Beryllium, another commonly used *p*-dopant. However, most CBr₄ doping systems currently available cannot quickly and precisely switch between multiple doping levels, which is required for VCSEL growths. Here we report a custom-designed CBr₄ doping system that is suitable for growing sophisticated structures such as VCSELs.

All CBr₄ doping systems mainly perform two basic functions. One is to control the CBr₄ base vapor pressure, which is several hundred millitorr at room temperature, by either directly regulating the vapor pressure or indirectly regulating the CBr₄ temperature. The other is to reduce the CBr₄ vapor pressure, usually by several orders of magnitude, before injecting into the growth chamber to have the desired doping levels. Fig. 1 shows the schematic of our CBr₄ doping system, which consists of the thermoelectric cooler (TEC) system and parallel orifice valve (POV) system to perform these two functions.

The CBr₄ vapor pressure is temperature controlled by using four TECs [1]. One side of the TECs contacts the CBr₄ canister and the other side contacts a water-cooled copper block. The CBr₄ temperature is monitored using a thermocouple welded on the CBr₄ canister and controlled by a PID controller. A Baratron is used to monitor the vapor pressure. To characterize the TEC system, the CBr₄ temperature and vapor pressure were both recorded for three hours as shown in Fig. 2. The temperature was initially maintained at -5°C, then was raised to 20°C after one hour and lowered back to -5°C after another hour. Once stabilized, the temperature and vapor pressure is nearly constant. In Region I, II, and III, the standard deviation for the temperature and vapor pressure is less than 0.1°C and 1% of the mean. The difference in vapor pressures for Region I and III is less than 2%, which indicates that the vapor pressure is fairly reproducible. From -5°C to 20°C, the CBr₄ vapor pressure increases over 10 times. The rise time and fall time (10%-to-90%) for the vapor pressure is ~6.5 and ~1.5 min, respectively.

At a given CBr₄ temperature, the doping is controlled by the POV system, which currently has six different size orifices. These orifices, ranging from 50 to 250 μm in diameter, are used to reduce the CBr₄ vapor pressure injecting into the growth chamber. Upstream of each orifice is an air-operated pneumatic valve. By opening different combinations of pneumatic valves, the doping can be controlled digitally and reproducibly. Since the switching time for these valves is practically negligible, the doping can be changed rapidly. Ideally, if the conductance doubles for every other orifice, almost two orders of magnitude of doping concentration (2⁶=64) can be realized with six orifices. Combined with adjusting the CBr₄ temperature, three orders of magnitude of the doping concentration can be achieved in this system. To evaluate the POV system, a calibration sample which has eight layers with different valve opening combinations was grown, and Fig. 3 shows the doping profile measured by secondary ion mass spectrometry (SIMS). The CBr₄ temperature was maintained at -5°C during the growth. The spike near the surface is due to the carbon contamination from the environment. The doping profile is relatively flat as shown in the figure. If the doping level for opening individual valve of C6, C5, and C4 are summed, the resulting doping level is 1.96×10¹⁸ cm⁻³, which is very close to the doping of 1.98×10¹⁸ cm⁻³ obtained from opening valves C4, C5, and C6 together. This implies that the doping contribution from each valve can indeed be added. The transient response is also evaluated by measuring the CBr₄ beam flux and shows that the typical transient time is less than 10 seconds.

In conclusion, a compact versatile CBr₄ doping system for MBE was designed and built. This system can achieve a wide doping range by using six different size orifices and adjusting the CBr₄ temperature. The doping is controlled by pneumatic valves and can be changed rapidly. These make the system suitable for growing complicated structures such as VCSELs.

[1] Y.-C. Chang et al., *Proc. Electronic Materials Conference*, paper no. Y8, University Park, PA (June 2006)

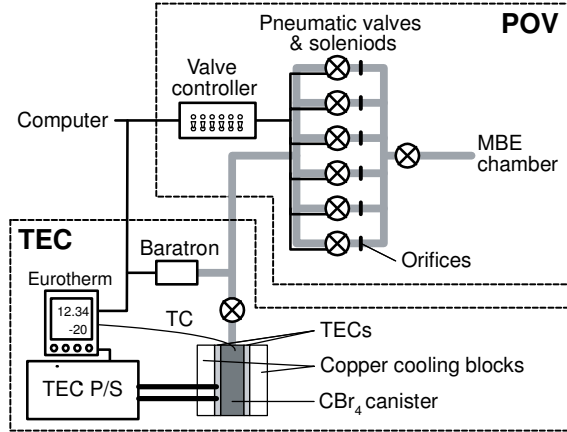


Fig. 1: Schematics of the CBr_4 doping system

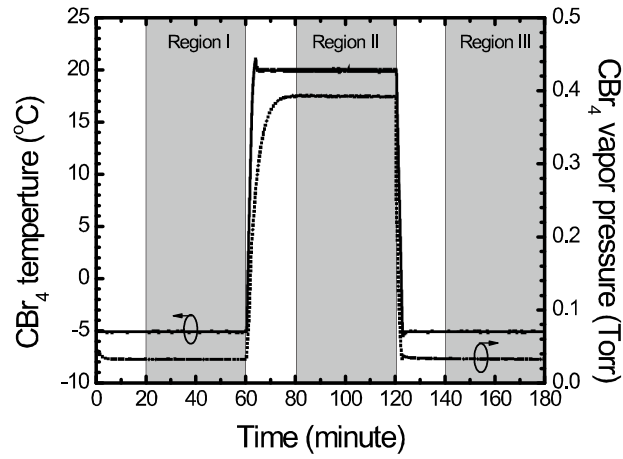


Fig. 2: The CBr_4 temperature and vapor pressure with the temperature setpoint changed between -5°C and 20°C

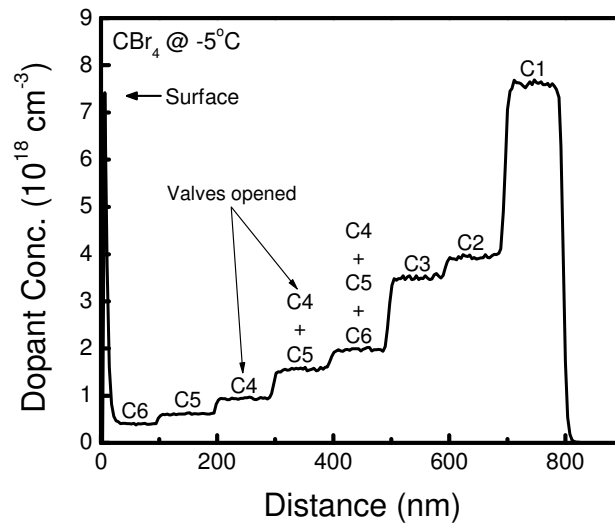


Fig. 3: Doping profile measured by SIMS with eight different valve combinations

III. Cavity QED

Externally Mode-Matched Cavity Quantum Electrodynamics with Charge-Tunable Quantum Dots

M. T. Rakher,^{1,*} N. G. Stoltz,² L. A. Coldren,^{2,3} P. M. Petroff,^{2,3} and D. Bouwmeester^{1,4}

¹*Department of Physics, University of California Santa Barbara, Santa Barbara, California 93106, USA*

²*Materials Department, University of California Santa Barbara, Santa Barbara, California 93106, USA*

³*ECE Department, University of California Santa Barbara, Santa Barbara, California 93106, USA*

⁴*Huygens Laboratory, Leiden University, P.O. Box 9504, 2300 RA Leiden, the Netherlands*

(Received 3 June 2008; published 5 March 2009)

We present coherent reflection spectroscopy on a charge and dc Stark tunable quantum dot embedded in a high-quality and externally mode-matched microcavity. The addition of an exciton to a single-electron-charged quantum dot forms a trion that interacts with the microcavity just below the strong-coupling regime of cavity quantum electrodynamics. Such an integrated, monolithic system is a crucial step towards the implementation of scalable hybrid quantum-information schemes that are based on an efficient interaction between a single photon and a confined electron spin.

DOI: 10.1103/PhysRevLett.102.097403

PACS numbers: 78.67.Hc, 78.55.Cr, 78.90.+t

Hybrid quantum-information schemes combine the coherence properties and ease of manipulation of photons with the scalability and robustness of local quantum systems. Examples of local quantum systems include electron spins in quantum dots, defect centers in diamond, and trapped atoms or ions [1,2]. Hybrid schemes such as quantum repeaters and quantum networks use the coupling between the local quantum system (qubit) and the optical field to reversibly map the quantum state of a photon onto the state of the local system [3–6]. Other hybrid schemes use a joint measurement of emitted photons, which are entangled with their respective local qubit, to perform gate operations on the two spatially separated local systems [7–10]. This latter scheme can be used to create entanglement between many local qubits as needed for cluster-state quantum computation. Implementations based on trapped ions or atoms have reached operation fidelities greater than 80% for 2 remote qubit interactions. However, the overall success probabilities are currently limited to $\approx 10^{-8}$, due to the technical incompatibility of trapping the particles and coupling them efficiently to a single external optical mode [11,12]. Here we present a solid-state system that integrates a trapped, electrically controlled quantum system with near unity coupling efficiency to an external optical mode.

To achieve an efficient coupling, the quantum system must be placed in a high-quality microcavity so that it dominantly interacts with a single optical mode. Furthermore, this cavity mode must be mode matched to an external mode to ensure efficient operation at the single photon level. The ideal operating point for such hybrid schemes is deep in the weak coupling (Purcell) regime of cavity quantum electrodynamics (QED), just below the onset of strong coupling. In addition, for cluster-state and distributed quantum computation, the hybrid system must be scalable. Our system satisfies these requirements in the solid-state. It is composed of self-assembled quantum dots (QDs) (density $\approx 10 \mu\text{m}^{-2}$) at the center of an oxidation-

apertured micropillar cavity with integrated doped layers that enable an external bias to apply an electric field across the QD. This field causes carriers to tunnel in and out [13] of the QD, changing the QD charge state, and induces the quantum confined Stark effect [14], shifting the emitted photon's energy. While cavity QED has been studied using quantum dots for several years, this has been done using a neutral exciton [15,16]. Neutral excitons, bound electron-hole pairs, have been proposed as qubits [17] but seem problematic due to their quick spontaneous decay, ≈ 1 ns in GaAs, and fast dephasing [18]. The local qubit in our system is the spin of a trapped electron [19,20], which interacts with the cavity mode through the addition of an exciton, forming a short-lived trion state. Since the polarization of the emitted photon is correlated with the spin state of the remaining electron, the trion acts as a readout channel of the spin [5]. Additionally, the micropillar cavity geometry is such that the fundamental mode is a doubly degenerate $\text{HE}_{1,1}$ mode, which mode matches well to external modes due to its Gaussian-like shape [21]. Here, we report on two variations of the solid-state cavity QED system, one optimized to operate in the charge-tuning regime, and the other in the Stark-tuning regime.

The demonstration of an electrically gated QD embedded in a high Q cavity mode has become feasible through a series of scientific advances. First, the development of vertical-cavity surface-emitting lasers (VCSELs) with oxide apertures in the GaAs/AlGaAs material system enabled the creation of cavities with small mode volumes, $V_{\text{eff}} = 35(\lambda/n)^3$, while maintaining a very high Q [22]. Second, the addition of single, self-assembled InAs/GaAs QDs embedded at the axial antinode of the cavity mode provided an atomiclike emitter to couple to the optical mode [23]. Third, the use of etched trenches to define the oxidation front, as shown in Fig. 1, enabled both control over the polarization degeneracy of the cavity modes as well as global electrical connection to an array of cavities

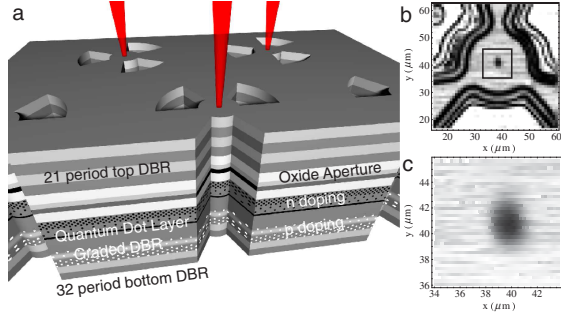


FIG. 1 (color online). (a) Schematic of the scalable cavity QED system based on electrically gated QDs embedded in oxide-apertured micropillars. (b) Two-dimensional reflectivity scan of a micropillar cavity taken with a laser resonant with the cavity mode. The mode in the center can be seen clearly as a dip in the reflected signal. (c) Higher resolution reflectivity scan taken in a $10 \mu\text{m} \times 10 \mu\text{m}$ area containing the mode.

[24]. In the experiments presented here, the oxidation time of the aperture is such to maximize Q while minimizing the mode volume. As shown in Figs. 1(b) and 1(c), the cavity mode is to a good approximation Gaussian in lateral profile and fits to a waist of $2.2 \mu\text{m}$, in agreement with measurements of the spacing between transverse modes [23].

Using a voltage source to drop an electric field over the QD active region is complicated by the presence of nearby material interfaces at each distributed Bragg reflector (DBR) period and at the oxide aperture region. These interfaces trap charges and result in the formation of charge domains, which reduce the field dropped across the QD region and obstruct controlled charging and Stark tuning [24]. To overcome these problems, a novel p - i - n device structure was developed in which the intrinsic region does not include the oxide aperture and the nearby p -doped $\text{Al}_{0.9}\text{Ga}_{0.1}\text{As}$ DBR period is Al-content graded to and from the adjacent GaAs layers as shown in Fig. 1(a). The Al-content grading prevents the formation of triangular potential wells that arise at abrupt $\text{Al}_{0.9}\text{Ga}_{0.1}\text{As}/\text{GaAs}$ interfaces. Furthermore, all doping concentrations are graded such that they are easily contacted by countersink etching without introducing unnecessary dopants near the QDs. The two variations of the solid-state cavity QED system presented here have nominally the same growth structure, but the average doping levels for the charge-tuning system are $3.5 \times 10^{18} \text{ cm}^{-3}$ ($2.5 \times 10^{18} \text{ cm}^{-3}$) for the n -doped (p -doped) layer whereas for the Stark tuning system they are $7.0 \times 10^{17} \text{ cm}^{-3}$ ($7.5 \times 10^{17} \text{ cm}^{-3}$).

To investigate the intracavity charging, we first characterized QDs outside of the cavities in the surrounding mirror region, where the Purcell effect is negligible. We monitored the photoluminescence spectrum (using a 1.25 m monochromator coupled with a CCD array) under 150 fs, 860 nm Ti:sapphire laser excitation with 50 nW average power as the applied bias is varied. A typical trace for a single QD is shown in Fig. 2(a). Near 18 V applied bias, the

QD emission abruptly changes 6 meV to lower energy. This is the characteristic energy separation for the transition between the neutral exciton, X^0 , and the singly electron-charged exciton, X^- [13,25]. To verify the charge designations as X^0 and X^- , we also measured the time-resolved decay of the photoluminescence. The result is shown in Fig. 2(b), with curves taken at biases below (above) 18 V labeled as dashed (straight). Because of the presence of optically dark states, the X^0 decay traces have a distinctive biexponential behavior, whereas the X^- decay are single exponentials [24,26].

The same lifetime measurement is performed for QDs in the cavity region which are on resonance with a polarization-degenerate fundamental mode as shown in Fig. 2(c) (this was possible for approximately 10% of cavities), and the results qualitatively replicate that of the bulk QDs. However, the effect of the high Q cavity strongly reduces the emission lifetime by the Purcell effect. For some X^- cases, this lifetime approaches 150 ps, the timing resolution of our experiment. Nonetheless, a deconvolved lifetime of 137 ± 21 ps was obtained for the fastest X^- transition and 321 ± 15 ps for the X^0 . This yields a Purcell enhancement, $F_p = \tau_o/\tau_{\text{cav}}$, of approximately 7 for the X^- . We measure that on average ($F_p = 2.8 \pm 0.22$ for 4 X^0 transitions and 5.9 ± 0.96 for 6 X^-) the Purcell enhancement is stronger for X^- than for X^0 . Because both transitions have similar lifetimes in the DBR region, resulting from similar oscillator strengths, one would expect both to have similar Purcell effects. However, this is not found experimentally and may be due to a better matching of the transition dipole moment to the cavity mode polar-

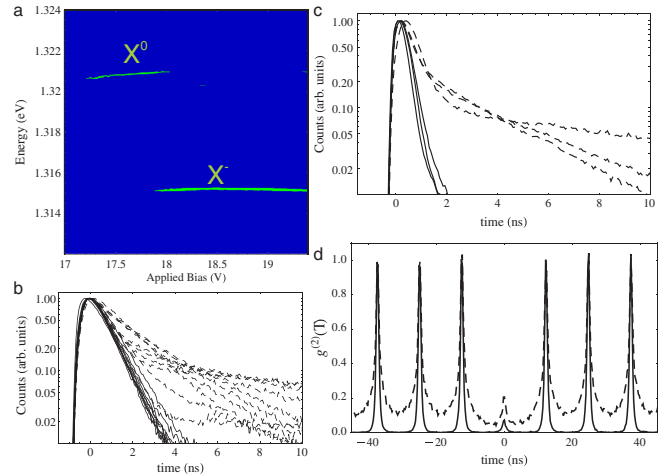


FIG. 2 (color online). (a) Photoluminescence spectra as a function of applied bias for a QD in the mirror region at 4 K. (b) Emission decay traces for 10 QDs in the mirror region. Straight traces are taken with 18.5 V applied bias (X^-) and dashed traces are taken with 17.5 V applied bias (X^0). (c) Emission decay traces for QDs on resonance with cavity modes for several different cavities. The straight (dashed) traces correspond to an X^- (X^0) decay. (d) $g^{(2)}(\tau)$ measurements for an X^- (straight) and X^0 (dashed) transition.

ization for the X^- . This could be explained by theoretical calculations beyond the standard techniques for calculating the optical transitions of a QD [27]. In addition, the second-order photon correlation function, $g^{(2)}(\tau)$, was measured as shown in Fig. 2(d) for an X^0 and an X^- transition. While both clearly demonstrate single photon behavior, the X^- is much cleaner due to its fast, single exponential decay. The measured single photon ($g^{(2)}(0) < 0.25$) count rate was typically $3 \times 10^6 \text{ s}^{-1}$ for an X^- with an 80 MHz pump rate, yielding a 25% extraction efficiency for the QD when corrected for the optical and detection losses of the setup (15%).

While the lifetime measurements indicate that the emission is coupled to the cavity mode, it does not yield a quantitative measure of the coupling strength, g , or the mode-matching efficiency. To do this, one must probe the coupled system coherently and we accomplish this by measuring the reflectivity of the cavity-QD system [15,16]. The reflection spectrum can be derived from the Jaynes-Cummings Hamiltonian using the input-output formalism and under sufficiently weak probing of a symmetric cavity [28–31], can be expressed as

$$R(\omega) = \left| 1 - \frac{\kappa[\gamma - i(\omega - \omega_{\text{QD}})]}{[\gamma - i(\omega - \omega_{\text{QD}})][\kappa - i(\omega - \omega_c)] + g^2} \right|^2, \quad (1)$$

where g is the emitter-cavity coupling, ω_{QD} (ω_c) is the emitter (cavity) resonance, γ is the dipole decay rate, and κ is cavity field decay rate. If there are no QDs coupled to the cavity mode, the spectrum shows a single dip at the cavity resonance with a width equal to the cavity field decay rate, κ , as shown in Fig. 3(a). For this micropillar, a fit to the data yields $\kappa = 24.1 \mu\text{eV}$, corresponding to $Q = 27\,000$. The depth of this dip is a measure of how well the probe beam is mode matched to the cavity, and in this case the coupling efficiency is greater than 96%. This remarkably high efficiency implies that reliable information transfer at the single photon level is feasible and would constitute an increase in the success probability of a two-photon experiment [11,12] by 3–4 orders of magnitude. If a QD is coupled to the microcavity, the reflection spectrum is drastically altered. Figure 3(b) shows the absolute reflection spectrum of the cavity mode interacting with a single QD transition. By fitting this spectrum to Eq. (1), we obtain an emitter-cavity coupling of $g = 9.7 \mu\text{eV}$ and a dipole decay rate of $\gamma = 1.9 \mu\text{eV}$. Since $g/\kappa = 0.402$, the emitter-cavity system is deep in the Purcell (weak-coupling) regime and at the precipice of strong-coupling, $g/\kappa > 0.5$, exactly in the region ideally suited for hybrid quantum-information schemes [5,6,8,9]. The spectrum, with resolution limited by the probe laser linewidth, completely characterizes the system. Additionally, it reveals the natural linewidth of the QD transition with a signal much greater than achieved in transmission or differential transmission. In conclusion, the combination of these results for the cavity QED system in the charge-tuning

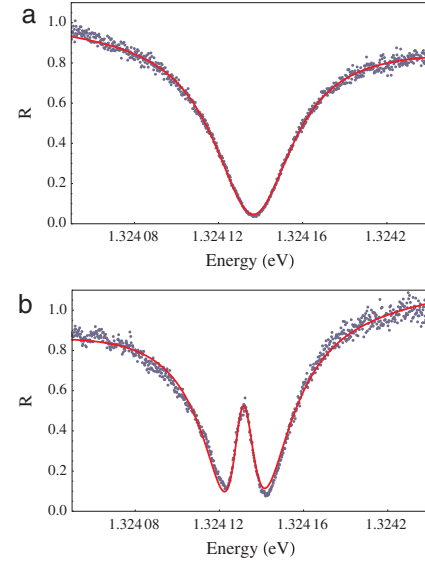


FIG. 3 (color online). (a) Cavity reflection spectrum of an unloaded micropillar cavity measured by recording the reflected signal of a tunable-wavelength laser. Equation (1) with $g = 0$ plus a linear background is used to fit the data. (b) Cavity reflection spectrum of a QD coupled to the micropillar cavity in (a). Eq. (1) plus a linear background is used to fit the data.

regime demonstrates that it is ideal for hybrid quantum-information processing.

We now turn to the Stark-tuning cavity QED system. Since the coupling between the QD and the cavity mode depends on the spectral detuning, an external control is necessary to reach resonance. In QD systems without electrical gating, this control is achieved by adjusting the sample temperature [16]. However, this control typically decreases coherence through higher phonon occupations and is not scalable. An applied electric field can also tune the QD transition via the Stark effect without the negative effects of temperature and in principle can be scalable by gating each cavity separately. In order to illustrate this effect and potential applications, we utilized a polarization nondegenerate cavity mode. As mentioned in Ref. [24], an engineered ellipticity of the aperture lifts the polarization degeneracy, creating two orthogonal linear polarization modes (denoted as H and V) as illustrated in Fig. 4(a). Because the Q factor is very high (40 000), the modes can be spectrally separated by as little as $50 \mu\text{eV}$ and still be resolved. This enables the quantum dot transition to be Stark-shift tuned into resonance with two modes as shown in Fig. 4(b). Note that the dependence is nonlinear with bias as expected for the quantum confined Stark effect [14].

By Stark-shift tuning the QD emission, the Purcell effect is observed on resonance with each mode. Stark-shift tuning as opposed to current induced heating was confirmed by observing a constant QD linewidth over the tuning range. For several applied biases, the QD emission decay curve is measured, see Fig. 4(c), and the extracted lifetime is plotted as a function of spectral position as shown in

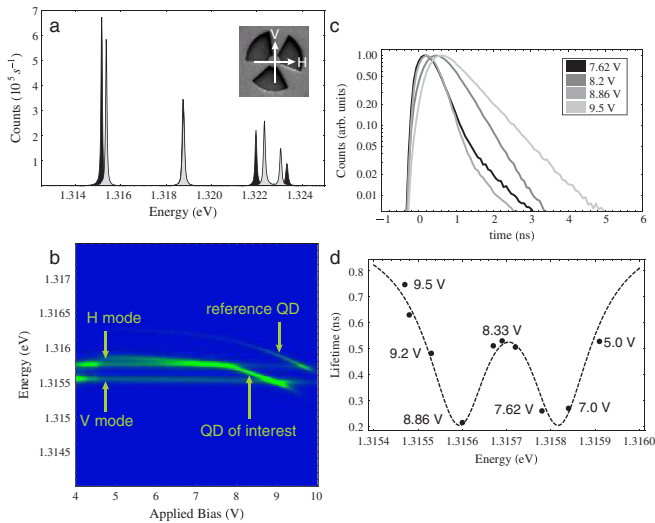


FIG. 4 (color online). (a) Microphotoluminescence spectra of nondegenerate optical modes in a micropillar. H (V) polarized modes are black (grey). Inset: SEM image of a micropillar. (b) Photoluminescence spectra as a function of applied bias for two QDs (labeled QD of interest and reference QD) and two nondegenerate fundamental cavity modes (labeled H mode and V mode). (c) Lifetime traces for a few bias settings; 7.62, 8.2, 8.86, and 9.5 V. (d) Deconvolved lifetimes as a function of emission energy with fit.

Fig. 4(d). The dips in the transition lifetimes measured on resonance are a clear consequence of the Purcell effect. The lifetimes at the resonance of each mode is measured to be 220 ps as shown in Fig. 4(d), approximately 5 times shorter than the bulk lifetime. The appearance of a biexponential, most prevalent for the on resonance biases, in Fig. 4(c) is attributed to a small fraction ($\sim 4\%$) of photons collected from QDs outside the mode volume. Stark-shift tuning when used in addition to charge tuning constitutes a completely bias-controlled, solid-state cavity QED system.

In conclusion, we presented a solid-state cavity QED system which has near ideal properties for photon electron-spin coupling as needed for hybrid quantum-information processing. The unique features of our system are intracavity electron charging, near perfect mode matching, polarization control of the cavity modes, and operation deep in the Purcell regime. In addition, the cavity-QD coupling can be controlled via the Stark effect, which has applications for quantum and classical communication. The combination of this work with spin initialization, manipulation, and readout [25,32,33] as well as techniques for active positioning of quantum dots [34] will bring the implementation of solid-state hybrid quantum-information protocols within reach.

The authors would like to thank M. P. Van Exter and W. Yao for useful discussions. This work was supported by NSF NIRT No. 0304678, DARPA No. MDA 972-01-1-0027, and Marie-Curie EXT-CT-2006-042580.

*mrakher@nist.gov

Present address: National Institute of Standards and Technology, Gaithersburg, MD 20899, USA.

- [1] J. M. Raimond, M. Brune, and S. Haroche, *Rev. Mod. Phys.* **73**, 565 (2001).
- [2] H. Mabuchi and A. C. Doherty, *Science* **298**, 1372 (2002).
- [3] S. J. van Enk, J. I. Cirac, and P. Zoller, *Phys. Rev. Lett.* **78**, 4293 (1997).
- [4] J. I. Cirac, P. Zoller, H. J. Kimble, and H. Mabuchi, *Phys. Rev. Lett.* **78**, 3221 (1997).
- [5] W. Yao, R. Liu, and L. J. Sham, *Phys. Rev. Lett.* **92**, 217402 (2004).
- [6] W. Yao, R. B. Liu, and L. J. Sham, *Phys. Rev. Lett.* **95**, 030504 (2005).
- [7] R. Raussendorf and H. J. Briegel, *Phys. Rev. Lett.* **86**, 5188 (2001).
- [8] Y. L. Lim, A. Beige, and L. C. Kwek, *Phys. Rev. Lett.* **95**, 030505 (2005).
- [9] S. D. Barrett and P. Kok, *Phys. Rev. A* **71**, 060310(R) (2005).
- [10] C. Simon *et al.*, *Phys. Rev. B* **75**, 081302(R) (2007).
- [11] D. L. Moehring *et al.*, *Nature (London)* **449**, 68 (2007).
- [12] W. Rosenfeld, S. Berner, J. Volz, M. Weber, and H. Weinfurter, *Phys. Rev. Lett.* **98**, 050504 (2007).
- [13] R. J. Warburton *et al.*, *Nature (London)* **405**, 926 (2000).
- [14] P. W. Fry *et al.*, *Phys. Rev. Lett.* **84**, 733 (2000).
- [15] K. Srinivasan and O. Painter, *Nature (London)* **450**, 862 (2007).
- [16] D. Englund *et al.*, *Nature (London)* **450**, 857 (2007).
- [17] P. Chen, C. Piermarocchi, and L. J. Sham, *Phys. Rev. Lett.* **87**, 067401 (2001).
- [18] C. Kammerer *et al.*, *Appl. Phys. Lett.* **81**, 2737 (2002).
- [19] A. V. Khaetskii, D. Loss, and L. Glazman, *Phys. Rev. Lett.* **88**, 186802 (2002).
- [20] I. A. Merkulov, A. L. Efros, and M. Rosen, *Phys. Rev. B* **65**, 205309 (2002).
- [21] M. Pelton *et al.*, *IEEE J. Quantum Electron.* **38**, 170 (2002).
- [22] C. Wilmsen, H. Temkin, and L. A. Coldren, *Vertical-Cavity Surface-Emitting Lasers* (Cambridge University Press, Cambridge, England, 1999).
- [23] N. G. Stoltz *et al.*, *Appl. Phys. Lett.* **87**, 031105 (2005).
- [24] S. Strauf *et al.*, *Nat. Photon.* **1**, 704 (2007).
- [25] M. Atature *et al.*, *Science* **312**, 551 (2006).
- [26] J. M. Smith *et al.*, *Phys. Rev. Lett.* **94**, 197402 (2005).
- [27] G. A. Narvaez, G. Bester, and A. Zunger, *Phys. Rev. B* **72**, 245318 (2005).
- [28] J. T. Shen and S. Fan, *Opt. Lett.* **30**, 2001 (2005).
- [29] E. Waks and J. Vuckovic, *Phys. Rev. Lett.* **96**, 153601 (2006).
- [30] E. Waks and J. Vuckovic, *Phys. Rev. A* **73**, 041803(R) (2006).
- [31] A. Auffèves-Garnier, C. Simon, J.-M. Gérard, and J.-P. Poizat, *Phys. Rev. A* **75**, 053823 (2007).
- [32] B. D. Gerardot *et al.*, *Nature (London)* **451**, 441 (2008).
- [33] M. H. Mikkelsen *et al.*, *Nature Phys.* **3**, 770 (2007).
- [34] K. Hennessy *et al.*, *Nature (London)* **445**, 896 (2007).